Studies of phenomena arising from the non-linearity of the Josephson junction

George Long

Royal Holloway University of London

A thesis submitted for the degree of

Doctor of Philosophy

April 2019

Supervisors: Professor Phil Meeson (RHUL) and Dr Jonathan Williams (NPL)

Declaration

I declare that the work in this thesis is my own. Where information has been derived from other sources, I confirm that this has been indicated in the thesis.

George Long

For my family.

Acknowledgements

I would like to thank my supervisor Professor Phil Meeson for the opportunity to work in his research group. I would also like to thank my NPL supervisor Dr Jonathan Williams for his support throughout this work. I would like to thank Dr Connor Shelly for all his help. I would also like to thank my fellow PhD students Jacob Dunstan, Katie Porsch and Tom Dixon. I would also like to thank the National Physical Laboratory (NPL) for sponsoring my studentship. Furthermore, I would also like to thank everyone in the RHUL physics department for making it such a pleasant place to work.

Abstract

Non-linear quantum devices employing superconducting resonators have drawn much attention since the realisation of quantum information processing. I outline the design, fabrication and behaviour of several devices in which niobium half-wavelength coplanar waveguide (CPW) superconducting resonators are modified with the inclusion of Josephson elements. The configuration of the Josephson elements (single junction and RF SQUIDs) and their position in the cavity are varied to explore and exploit both odd and even orders of the non-linear Josephson inductance. The Josephson elements were produced in two distinct ways. The primary focus was the development of shadow evaporated aluminium Josephson junctions deposited within an etched gap in the central conductor of a niobium CPW resonator. The samples were intended to be operated as amplitude bifurcation detectors for low power input signals however unexpected phenomena arose with the observation of well-defined, power-dependent modes appearing in the spectra. The nature and behaviours of these modes are explored and characterised. A secondary objective was the development of samples based on weak-link constrictions (nanobridges) patterned into the niobium resonators central conductor via electron beam lithography and reactive ion etching. These devices focus around a RF SQUID geometry, modifying the current-phase relation of the constriction to take advantage of an even order non-linearity and three-wave mixing. The phenomena arising in these circuits are explored.

Contents

1 Introduction **1**

1.1 This thesis . . . 3

1.2 Thesis layout . . . 4

2 Background Theory **6**

2.1 CPW transmission lines and resonators . . . 6

2.1.1 Coplanar waveguides . . . 9

2.1.2 CPW resonators . . . 11

2.1.2.1 Loaded quality factor . . . 15

2.1.2.2 Superconducting coplanar waveguide resonators . . . 18

2.1.3 Dielectric losses . . . 22

2.1.4 Fano resonance . . . 24

2.2 The Josephson effect . . . 31

2.2.1 Josephson junctions . . . 31

2.2.2 Nanobridges . . . 33

2.2.3 RCSJ model . . . 34

2.2.4 The RF SQUID . . . 37

2.2.5 Non-linearity of the Josephson junction . . . 38

2.3 Wave mixing and associated phenomena in non-linear media . . . 41

2.3.1 Non-linear wave equation . . . 42

2.3.2 The Born approximation . . . 43

2.3.3 Second order non-linear media . . . 43

2.3.3.1 Three-wave mixing . . . 44

2.3.4 Third order non-linear media . . . 47

2.3.4.1 Four-wave mixing . . . 48

2.3.5 Coupled wave theory . . . 49

2.3.6 Microwave parametric media . . . 54

2.3.7 Amplitude bifurcation . . . 59

3 Experimental Method **65**
3.1 The cryostat . . . 65
3.2 Current sensing Johnson noise thermometry . . . 68
3.2.1 Resistive thermometry . . . 68
3.2.2 Johnson noise . . . 70
3.2.3 DC SQUID . . . 70
3.2.4 DC SQUID sensor characterisation . . . 72
3.2.5 Noise resistor . . . 74
3.2.6 Input circuit construction . . . 76
3.2.7 Low temperature thermometry . . . 78
3.2.8 Vibrational noise . . . 81
3.2.9 The noise thermometer program . . . 82
3.3 Experimental wiring . . . 84
3.3.1 Sample holders . . . 87

4 PTB Period Doubling sample **89**

5 Fabrication **95**
5.1 Niobium CPW resonators . . . 95
5.1.1 Resonator design . . . 95
5.1.2 Fabrication of Nb CPW resonators . . . 98
5.1.3 4.18 K measurements of fabricated CPW resonators . . . 102
5.1.4 Power dependence . . . 104
5.2 Aluminium Josephson junctions . . . 104
5.2.1 Design considerations . . . 106
5.2.2 The "T" design . . . 107
5.2.3 Fabrication . . . 109
5.2.3.1 Electron-beam lithography . . . 109
5.2.3.2 Thermal evaporation . . . 110
5.2.4 Fabrication and design development . . . 112
5.2.5 Inconsistency in oxidation . . . 118
5.2.6 Critical current . . . 120
5.2.7 Resist residue . . . 120
5.2.8 Large area junctions . . . 121
5.3 Integration of Nb CPW resonators with Al Josephson junctions . . . 122
5.4 Niobium nanobridges . . . 125
5.4.1 Fabrication . . . 125
5.4.2 Etching . . . 127
5.4.3 Device design . . . 128

6 Measurements of Al Josephson junction Nb CPW resonators 130
6.1 Sample design - SA1 . . . 130
6.2 SA1 . . . 131
6.2.1 4.18 K measurements . . . 132
6.2.2 Low temperature measurements . . . 135
6.3 SA2 . . . 138
6.3.1 Design considerations . . . 138
6.3.2 Prerequisite measurements . . . 140
6.3.3 Initial low temperature measurements . . . 142
6.3.4 Second mode . . . 145
6.3.4.1 Second mode: −107 dBm to −93 dBm . . . 147
6.3.4.2 Second mode: −96 dBm to −77 dBm . . . 151
6.3.4.3 Quality factor . . . 154
6.3.5 Sigma mode . . . 158
6.3.6 Temperature dependence . . . 162
6.3.7 Coupled modes . . . 164
6.3.8 Third mode . . . 167
6.3.9 Summary . . . 168

7 Measurements of Nb nanobridge RF SQUID CPW resonators 169
7.1 Nanobridge RF SQUIDs . . . 169
7.2 SN1 . . . 170
7.2.1 Sample design . . . 170
7.2.2 Fundamental mode . . . 172
7.2.3 Second mode . . . 176
7.2.4 Summary . . . 177
7.3 SN2 . . . 178
7.3.1 Sample design . . . 178
7.3.2 Trial iterations . . . 179
7.3.3 Fundamental mode . . . 180
7.3.4 Four-wave mixing . . . 186
7.3.5 Summary . . . 188

8 Conclusions 190

A Fabrication recipes 196

Bibliography 201

List of Figures

1.1 Schematic and optical images of a tunable Josephson parametric amplifier fabricated by M. A. Castellanos-Beltran et al. [7] 2
1.2 Schematic, optical and SEM images of a travelling-wave Josephson parametric amplifier fabricated by T. C. White et al. [8] 3

2.1 A lumped element equivalent circuit for an incremental length of a transmission line. 6
2.2 Impedance mismatch in a transmission line. 8
2.3 Types of coplanar waveguides. 9
2.4 Cross section of CPW transmission line. 10
2.5 Illustration and distributed element circuit diagram of a CPW half wavelength resonator. 12
2.6 Normalised current distribution squared of the first 3 modes of a $\lambda/2$ resonator as a function of position. 13
2.7 Illustration of the nodes and anti-node present in the current distribution of a CPW resonator. 13
2.8 Fitted transmission spectrum ($|S_{21}|$) of a Nb CPW resonator. 14
2.9 Lumped element parallel LCR representation of a TL resonator and Norton equivalent circuit. 16
2.10 Comparison of resonant frequency and quality factor for superconducting CPW resonators with different coupling capacitances [17]. 17
2.11 BCS denstiy of states and energy gap, for aluminium [19]. 19
2.12 Quasiparticle density as a function of temperature for aluminium [19]. . . . 20
2.13 Numerical evaluation of the Fano function (Equation 2.1.55), showing the change in the functions line-shape with varying asymmetry parameter. . . 24
2.14 Representation of a mechanical oscillators subject to a restoring and damping force. 25
2.15 Evaluation of amplitude and phase response for a damped oscillator subject to a harmonic driving force. 26
2.16 Coupled oscillators. The first oscillators amplitude and phase response to an external driving force of frequency ω. 27

2.17 Coupled oscillators. The second oscillators amplitude and phase response to an extremal driving force. 28
2.18 Coupled oscillators. Effect of coupling constant on the detuning of the resonant frequency of the oscillators. 29
2.19 Coupled oscillators. Response of first oscillator in the case of no damping and finite damping. 29
2.20 Schematic and measurement of a CPW resonator exhibiting a Fano lineshape. Taken from [37]. 30
2.21 Graphical representation of a Josephson junction and a nanobridge. 32
2.22 Andreev/quasiparticle bound state energies $E_{J\pm}$ as a function of the phase difference of the superconducting electrodes δ for different values of tunnelling probability τ. 32
2.23 RCSJ model equivalent circuit of a Josephson junction bias with a current source $I(t)$. 35
2.24 Josephson (tilted washboard) potential. 36
2.25 RF SQUID equivalent circuit. 37
2.26 Simplified circuit diagram of Josephson junction embedded transmission line. 38
2.27 Simplified circuit diagram of an RF SQUID transmission line 39
2.28 Illustration of scattering off a non-linear medium described by the first Born approximation. 43
2.29 Three-wave mixing (TWM) regimes. 46
2.30 Degenerate TWM as a photon interaction process. 46
2.31 Four-wave mixing (FWM)regimes. 49
2.32 Photon flux density as a function of interaction length for an idealised degenerate parametric amplifier. 53
2.33 Non-degenerate parametric amplification, derived from coupled wave theory. 54
2.34 RF SQUID non-linear coefficents as a function of flux. Taken from [57]. . . 57
2.35 Images of period doubling PTB sample. Images taken and adapted from [58] 58
2.36 Measurements of the period doubling bifurcation sample fabricated by PTB. Taken from [58]. 59
2.37 Amplitude of duffing oscillator as a function of driving force and frequency. 61
2.38 Amplitude of duffing oscillator for $F > F_c$. 62
2.39 Solutions to the amplitude of the Duffing oscillator when $F = F_c$ 63

3.1 Photograph of the *Cryoconcept* dilution refrigerator insert. 66
3.2 Image of dilution refrigerator control program. 67
3.3 Image of fridge diagnostics program. 68
3.4 Image of thermometry control program. 69
3.5 Schematic of DC SQUID and V/Φ_e characteristics 71

3.6 Operation of a DC SQUID using a flux locked loop. Adapted from [44]. . . 72
3.7 FFT of the voltage of a DC SQUID with an open input coil. 73
3.8 Gain response function for DC SQUID sensor. 74
3.9 FFT of the voltage of SQUID sensor with a Johnson noise source connected to the input coil. 75
3.10 Pictures of noise thermometry circuit fabricated and installed on a dilution refrigerator. 78
3.11 Johnson noise thermometer vs RuO_2 resistance thermometer over the temperature range of 4 K to 0.03 K. 79
3.12 Cold plate SQUID thermometer temperature comparison 80
3.13 Comparison of Johnson noise signal at 4.18 K and 0.035 K measured using a SQUID sensor. 81
3.14 Peak removal method employed to remove pick up from Johnson noise signal 82
3.15 Image of noise thermometry program. 83
3.16 Schematic representation of the RF circuit installed on the dilution refrigerator for low temperature measurement. 84
3.17 $|S_{21}|$ measurements of the output of RF circuit used for low temperature measurements. 85
3.18 Gain and noise performance of Low Noise Factory LNF-LNC4.8C 4-8 GHz cryogenic low noise amplifier at 5 K provided with purchase. Taken from [62]. 87
3.19 Photographs of sample boxes used to measure superconducting CPW resonators. 88

4.1 PD sample - Representation of PD sample 89
4.2 PD sample - Experimental setup 90
4.3 PD sample - Spectrum analyser outputs showing possible mixing regimes. . 91
4.4 PD sample - Relative change in (A) Signal tone and (B) Idler tone. TWM. 93
4.5 PD sample - Mixing regimes as a function of applied flux and pump power. 93

5.1 Design of quartz chrome optical mask used for optical lithography. 96
5.2 Design of R1 $\lambda/2$ CPW resonator. 96
5.3 Design of R3 and R5 $\lambda/2$ CPW resonator. 97
5.4 Illustration of optical lithography process. 99
5.5 Etching process for an anisotropic etch and an isotropic etch. 101
5.6 Resist beading in a contact photo-lithography process. 101
5.7 $|S_{21}|$ data as a function of frequency for unmodified R3 resonator. 102
5.8 $|S_{21}|$ as a function of frequency measurement for unmodified R3 resonator with asymmetric line-shape 103

5.9 $|S_{21}|$ data as a function of frequency for unmodified R3 resonator for multiple power levels. . . . 104
5.10 Double angle shadow evaporation using a Dolan bridge to form an Al/AlO_x/Al tunnel junction. . . . 105
5.11 SEM image and dose profile of "T" design Josephson junction. Taken from [66]. . . . 108
5.12 SEM image of the sample configuration used for testing Al junctions. . . . 113
5.13 Exposure profile for T design Al Josephson junction. . . . 113
5.14 SEM images of test junctions that failed to form due to insufficient copolymer clearing. . . . 114
5.15 Normal state resistance measurement of "standard" T design Al junctions. 115
5.16 SEM image of T design junction employing secondary exposure. . . . 116
5.17 SEM images of single overlap design junction. . . . 117
5.18 SEM image of multiple junction designs employing the secondary exposure method. . . . 117
5.19 Normal state resistance measurements of different junction designs focused on small area junctions. . . . 119
5.20 SEM images of early (failed) junctions showing resist residue. . . . 121
5.21 SEM imaging of exposed and developed resist bilayer defining large area variants of the T junctions. . . . 121
5.22 Optical image of an approximately 20 μm $\times$ 20 μm gap etched in the central conductor of an R3 Nb CPW resonator using a copolymer mask. . . . 123
5.23 Optical image of a thermally evaporated 50 nm thick Al bridge over a gap etched in the Nb CPW resonators central conductor. . . . 124
5.24 Optical images of an Al junction deposited into an etched gap in a Nb CPW resonator. . . . 125
5.25 Resist bilayer exposure cross section for forming nanobridges. . . . 126
5.26 Nanobridge formed from etching Nb using a PMMA/copolymer bilayer. . . . 127
5.27 A selection of SEM images of Nb etched using SF_6/Ar masked with a PMMA/copolymer bilayer to form narrow constrictions separating two electrodes. . . . 128
5.28 Optical images of a Nb CPW resonator with SQUID array employing etched constrictions. . . . 129
5.29 SEM image of several constrictions etched in the central conductor of a Nb CPW resonator. . . . 129

6.1 Image of Al Josephson junction embedded $\lambda/2$ Nb CPW resonator designated SA1. . . . 132
6.2 SA1 - 4.18 K dilution refrigerator RF circuit 133

6.3 SA1 - $|S_{21}|$ for SA1 at 4.18 K . . . 134
6.4 SA1 - $|S_{21}|$ for different temperatures. . . . 136
6.5 SA1 - $|S_{21}|$ measurements around the fundamental mode . . . 137
6.6 Optical image of R3 Nb CPW resonator in comparison to R1 Nb CPW resonator . . . 139
6.7 Image of Al Josephson junction embedded $\lambda/2$ Nb CPW resonator with an embedded Al junction, designated SA2. . . . 140
6.8 SA2 - $|S_{21}|$ of first four modes at 4.18 K. . . . 141
6.9 SA2 - $|S_{21}|$ of SA2 at 4.18 K. . . . 142
6.10 SA2 - $|S_{21}|$ measurements around the second mode. -107 dBm to -67 dBm 143
6.11 SA2 - $|S_{21}|$ measurements around the fourth mode. . . . 143
6.12 SA2 - S_{21} measurement around the second mode . . . 144
6.13 SA2 - S_{21} measurement around the second mode, wide power sweep. . . . 145
6.14 SA2 - second mode $|S_{21}|$ measurements centred around the second mode. . 146
6.15 SA2 - second mode S_{21} phase data corresponding to $|S_{21}|$ . . . 146
6.16 SA2 - second mode $|S_{21}|$ for a power level of -107 dBm. . . . 147
6.17 SA2 - second mode S_{21} for several different power levels. . . . 148
6.18 SA2 - second mode $|S_{21}|$ from -100 dBm to -93 dBm. . . . 149
6.19 SA2 - second mode $|S_{21}|$ power level of -93 dBm. . . . 149
6.20 SA2 - second mode $|S_{21}|$ around the second mode -96 dBm to -77 dBm. . 151
6.21 SA2 - second mode S_{21} measurements for -96 to -88 dBm. . . . 152
6.22 SA2 - second mode $|S_{21}|$ measurements for -86 to -80 dBm. . . . 153
6.23 SA2 - second mode $|S_{21}|$ for a power level of -78 dBm. . . . 154
6.24 SA2 - quality factor and centre frequency of second mode as a function of power level. . . . 155
6.25 SA2 - second mode $|S_{21}|$ for power level of -87 dBm . . . 155
6.26 SA2 - second mode centre frequency of the dominant peak . . . 156
6.27 SA2 - second mode $|S_{21}|$ for power level of -67 dBm. . . . 156
6.28 SA2 - sigma mode $|S_{21}|$ measurement -93.8 dBm to -91.16 dBm. . . . 158
6.29 SA2 - sigma mode $|S_{21}|$ measurement showing onset for increasing power level. . . . 159
6.30 SA2 - sigma mode S_{21} phase measurement showing onset for increasing power level. . . . 159
6.31 SA2 - sigma mode $|S_{21}|$ measurements for a power level of -86 dBm fit with a Fano function. . . . 160
6.32 SA2 - sigma mode S_{21} measurements for a power interval of -87 dBm to -83 dBm in 1 dBm intervals. . . . 161
6.33 SA2 - sigma mode S_{21} measurements for a power level of -67 dBm. . . . 162

6.34 SA2 - sigma mode $|S_{21}|$ measurements for a power level of -86 dBm at several temperatures. 163
6.35 SA2 - Quality factor of second mode measured at constant power as a function of temperature. 164
6.36 SA2 - coupled mode measurement set-up for probing the response of the second mode when driving the sigma mode. 164
6.37 SA2 - coupled modes measurements of relative change in oscillation of a probe tone at the second mode when driving the sigma mode. $f_p = 3.5466$ GHz, $P_{probe} = -107$ dBm 165
6.38 SA2 - coupled modes measurements of relative change in oscillation of a probe tone at the second mode when driving the sigma mode. $f_p = 3.5466$ GHz $P_{probe} = -117$ dBm 166
6.39 SA2 - $|S_{21}|$ around the second mode for power level of -120 dBm. 167

7.1 SN1 - image of sample. 171
7.2 SN1- $|S_{21}|$ fundamental mode power level of -50 dBm. Fitted for quality factor. 172
7.3 SN - $|S_{21}|$ measurements of the fundamental mode, onset of bifurcation. . . 172
7.4 SN1 - $|S_{21}|$ measurements showing the bifurcation of fundamental mode for a range of power levels. 174
7.5 SN1 - S_{21} measurements showing the bifurcation of fundamental mode for a wide range of power levels. 175
7.6 SN1 - $|S_{21}|$ measurements showing the full range of the bifurcation of fundamental mode observed. 176
7.7 SN1 - $|S_{21}|$ measurements of the second mode for a number of power levels. 177
7.8 Illustration of the sample design of SN2 178
7.9 Image of a sample fabricated a part of a trial iteration of SA2 179
7.10 SN2 - trail iteration $|S_{21}|$ 180
7.11 SN2 - image of the sample 181
7.12 SN2 - $|S_{21}|$ measurements of the fundamental mode at a power level of -72 dBm 181
7.13 SN2 - $|S_{21}|$ measurements of the fundamental mode for a range of power levels from -48.73 dBm to -47.75 dBm 182
7.14 SN2 - $|S_{21}|$ measurements of the fundamental mode for a range of power levels from -49.33 dBm to -43.11 dBm 183
7.15 SN2 - $|S_{21}|$ measurements of the fundamental mode for a range of power levels from -38.31 dBm to -38.28 dBm 183
7.16 SN2 - $|S_{21}|$ measurements of the fundamental mode for a range of power levels from -38.31 dBm to -38.08 dBm 184

7.17 SN2 - $|S_{21}|$ measurements of the fundamental mode for a range of power levels from -24 dBm and -48.5 dBm. 185
7.18 SN2 - $|S_{21}|$ measurements of the Second mode bifurcating. 185
7.19 SN2 - FWM experimental set-up. 187
7.20 SN2 - spectrum analyser outputs, showing various 4WM mixing regimes. . 187
7.21 SN2 - FWM multiple signal powers 188

8.1 Images of segments of traveling-wave parametric amplifiers based on three-wave mixing in a Josephson metamaterial. Taken from [74]. 192
8.2 A SEM image of a nano-SQUID fabricated using focussed ion beam lithography for sensing of magnetic particles [77]. 194

Chapter 1

Introduction

Superconducting quantum circuits present an opportunity to probe fundamental physical relationships as well as manifesting and controlling quantum phenomena to realise new technologies. In recent years quantum information processing has driven development of these devices. Superconducting qubits are an area of intense research. Several different types of superconducting qubits have been experimentally demonstrated ([1], [2], [3], [4]). Although the considerations involved differ, they share one unifying element, the Josephson junction, with its non-linear inductance required to break the degeneracy of the energy spacing of these two level systems. Advances in superconducting qubits has generated a need for low noise microwave amplifiers capable of making "single-shot" measurements of qubit states, among other applications. Once again at the heart of this technology is the uniquely suited Josephson junction.

Several different qubit readout schemes employing Josephson junctions have been demonstrated, making use of the non-linearity presented by the Josephson relation in different ways. Cavity bifurcation amplifiers [5] marry Josephson junctions and superconducting resonators to realise a non-dispersive non-linear oscillator. Biased sufficiently, this oscillator is extremely sensitive to the slightest perturbation, such as a change in the state of a superconducting qubit [6]. When biased around the point of bifurcation a change in the state of the qubit can result in a dramatic switching of the state of the oscillator. Resulting in a sensitive two state amplifier, providing a non-destructive method of probing the state of a qubit.

Josephson parametric amplification is quite different in its approach. Parametric amplification is well known and taken advantage of in the field of optics with materials exhibiting a Kerr non-linearity, a non-linear relationship between the refractive index of the media and the applied electric field. In these materials injection of light at some wavelength can generate a non-linear gain at other wavelengths via the process of three- or four-wave mixing depending on the order of non-linearity of the medium. Josephson parametric amplifiers (JPAs) make use of the non-linear inductance of Josephson junctions to couple a pump to a signal tone, transferring energy between them. The strength

of the coupling of the pump to the signal tone is dependent on the magnitude of the non-linearity. Resonators can be used to enhance the effective non-linearity by increasing the interaction time between the pump tone, signal tone and the parametric non-linearity presented by the Josephson junction mediating the interaction. An example of a resonant Josephson parametric amplifier is shown in Fig. 1.1, designed and fabricated by M. A. Castellanos-Beltran et al. [7]. The device was demonstrated to add less than half a noise quantum to the amplified signal with the ability to squeeze quantum fluctuations.

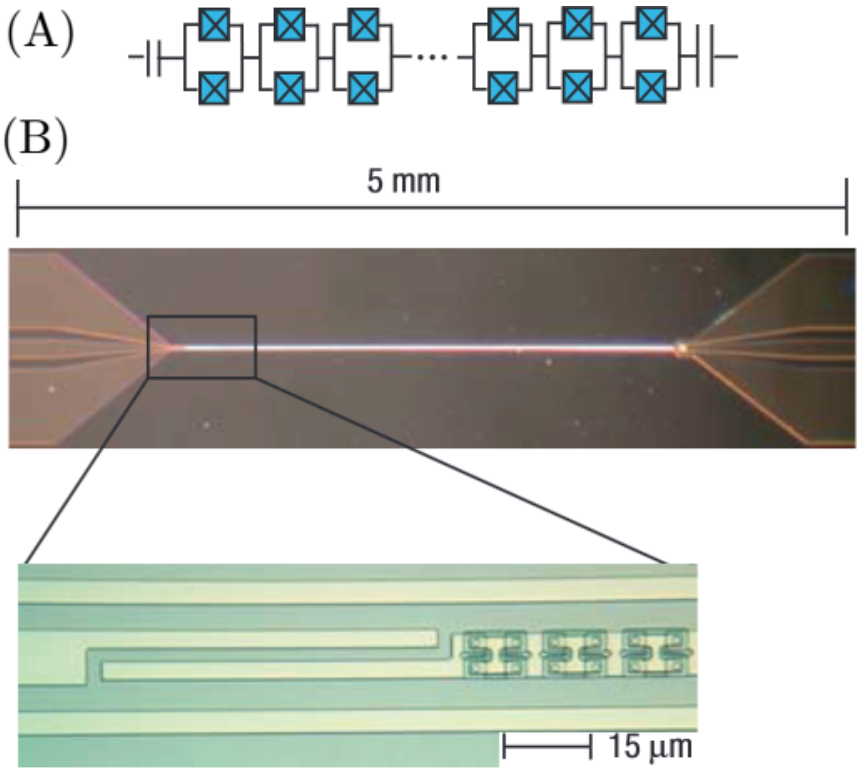

Figure 1.1: Taken from [7]. Schematic diagram and optical images of a tunable Josephson parametric amplifier fabricated by M. A. Castellanos-Beltran et al. A) Schematic of the DC SQUID array which forms the central conductor of a coplanar waveguide. B) Optical images of a resonant JPA employing an array of 480 individual Josephson junctions. These Josephson junctions are embedded in a half-wavelength ($\lambda/2$) cavity by terminating each end of the array with a capacitor. In this device the DC SQUIDs allow the resonant frequency of the resonator to be tuned by an external magnetic flux. This allows the amplifier to be operated over a frequency range of several GHz, overcoming some of the limitations imposed by the resonant structure.

The resonant structure allows for a significant interaction with the parametric non-linearly around the resonant frequency of the amplifier, resulting in high gain at the expense of bandwidth. An alternative way of enhancing the interaction with the parametric non-linearity is to extend the non-linear transmission line itself, removing the bandwidth constraints imposed by a resonant cavity. This type of device is known as a travelling-wave parametric amplifier (TWPA). Such a device was demonstrated by T. C.

White et al. [8], shown in Fig 1.2. This design combines Josephson junctions with shunt capacitors to construct a 50 Ω lumped element non-linear transmission line.

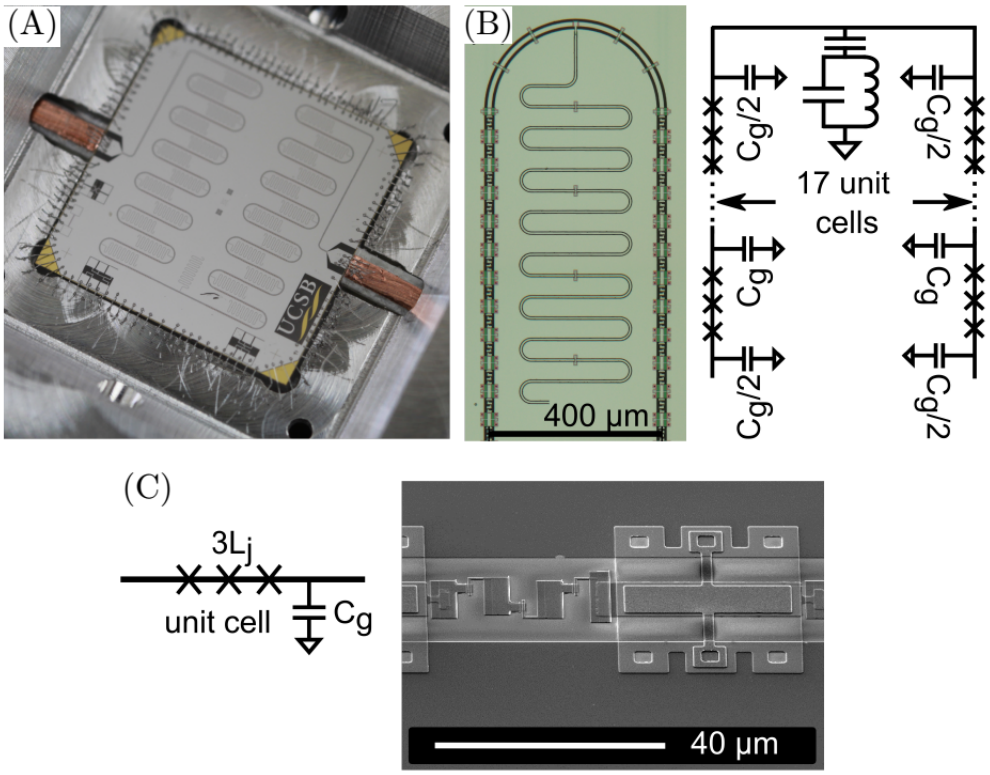

Figure 1.2: Taken from [8]. Josephson TWPA, designed and fabricated by T. C. White et al. A) Photograph of the Josephson TWPA. B) Optical micrograph and circuit diagram. $\frac{\lambda}{4}$ resonators were inserted at regular intervals along the length of the transmission line in order to maintain the phase matching condition between pump and the signal, crucial to achieving high gain. C) Circuit diagram and scanning electron micrograph of a non-linear unit cell, consisting of three Josephson junctions (left) and a shunt parallel plate capacitor (right).

1.1 This thesis

This thesis focuses on the development of non-linear superconducting quantum devices in the form of superconducting coplanar waveguide (CPW) resonators with integrated Josephson elements. A major part of this project was the development of fabrication processes to realise such devices using the Royal Holloway university of London (RHUL) clean room facilities. Specifically the fabrication of low I_c Al/AlO_x/Al tunnel junctions and their subsequent integration with Nb CPW resonators. The combination of these technologies results in a highly reactive non-linear oscillator capable of supporting parametric interactions. Such devices have a wide range of possible applications, depending on the configuration of the integrated Josephson junctions. Low I_c Al Josephson junctions were favoured such as to produce non-linear elements capable of being perturbed suffi-

ciently to exhibit a non-linear response even by the weakest of signals. Over the course of fabrication a method of forming nanobridge constrictions in the central conductor of a Nb CPW resonator was also developed. The main results of this thesis are as follows:

- The development of the fabrication methods to produce small area ($25000 - 40000$ nm^2) Al/AlO$_x$/Al tunnel junctions characterised with a high normal state resistances of several kΩ.
- The fabrication of Nb $\lambda/2$ CPW resonators and the development of methods to integrate them with Al/AlO$_x$/Al tunnel junctions.
- Low temperature measurements of a Nb $\lambda/2$ coplanar waveguide resonator with an integrated Al/AlO$_x$/Al tunnel junction. This resulted in power dependent phenomena consistent with a low I_c Josephson junction interacting with the modes of the resonator. A secondary power dependent mode whose state of oscillation seemingly relates to the state of the embedded junction was also observed.
- The development of the fabrication methods to form nanobridges in the central conductor of a Nb $\lambda/2$ CPW resonator using a novel method involving electron beam lithography and reactive ion etching.
- The design and measurement of Nb $\lambda/2$ coplanar waveguide resonators with etched nanobridge RF SQUIDs at 4.18 K. Observing bifurcations in the state of oscillations consistent with a Duffing like non-linearity and volcano non-linearity. Four-wave mixing is also demonstrated.

1.2 Thesis layout

- Chapter 2 provides an overview of the relevant theoretical background, introducing the most important concepts relating to fabricated devices. These include; the primary considerations involving $\lambda/2$ superconducting CPW resonators, the Josephson junction as a non-linear circuit element and the phenomena associated with non-linear media.
- Chapter 3 details the primary equipment used for low temperature measurement including the dilution refrigerator and RF circuit used to measure devices reported in Chapter 6. A primary focus of this chapter is the implementation of current sensing Johnson noise thermometry on the dilution refrigerator, such as to provide accurate and reliable thermometry at mK temperatures.
- Chapter 4 presents measurements demonstrating three and four-wave mixing using a Nb $\lambda/2$ CPW resonator with embedded Nb trilayer RF SQUIDs designed by A. Zorin and fabricated by Physikalisch-Technische Bundesanstalt (PTB).

- Chapter 5 details the methods developed to fabricate the samples whose measurement is detailed in Chapter 6 and 7. Primarily, the development of a recipe for fabricating Al/AlO_x/Al tunnel junctions with a high normal state resistance suitable for integration with Nb CPW resonators. As well as the methodology used to etch nanobridge constrictions into the central conductor of a Nb CPW resonator.

- Chapter 6 presents measurements of Nb CPW resonators with embedded Al/AlO_x/Al tunnel junctions. This focuses primarily on the observation of power dependent phenomena associated with the inclusion of the Al junction.

- Chapter 7 presents measurements of two Nb CPW resonators with etched nanobridge RF SQUIDs. The first sample utilises a RF SQUID array configuration and exhibits a Duffing type non-linearity. The second sample features single RF SQUIDs and exhibits a volcano non-linearity and four-wave mixing.

- Chapter 8 will provide a brief summary of the main results and future directions.

Chapter 2

Background Theory

This chapter is intended to provide an overview of the theoretical background relevant to future chapters. This chapter is divided into three main sections. Section 2.1 will cover transmission line theory, coplanar waveguides and $\lambda/2$ coplanar waveguide resonators. Section 2.2 will introduce the Josephson junction and how it defines a non-linear element which can be used to form a non-linear superconducting microwave medium. Section 2.3 is focused on non-linear phenomena associated with such a medium.

2.1 CPW transmission lines and resonators

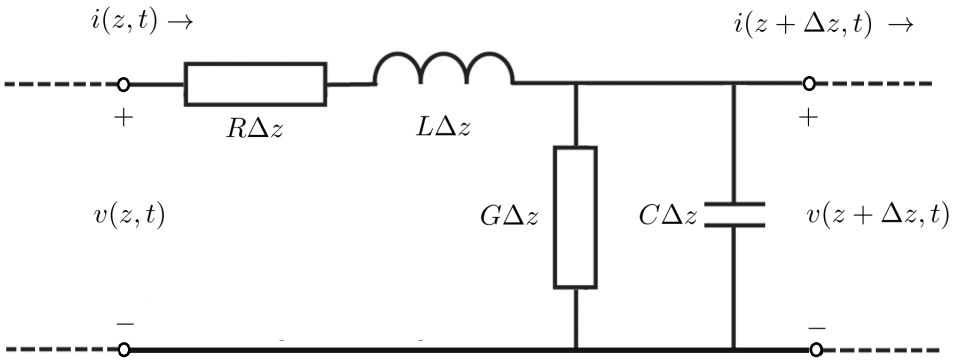

Figure 2.1: A lumped element equivalent circuit for an incremental length of a transmission line.

Microwaves are defined as alternating current signals oscillating with a frequency between 300 MHz and 300 GHz. Due the physical wavelength of microwaves standard circuit analysis techniques which assume that the physical dimensions of a network are much smaller than the electrical wavelength are invalid. Transmission line theory was introduced to model a distributed-parameter network where the currents and voltages can vary in magnitude and phase over the physical length of the device/circuit. A transmission line can be described as a cascade of infinitesimal elements shown in Fig. 2.1, where R is the

series resistance per unit length, L is the series inductance per unit length, G is the shunt conductance per unit length and C is the shunt capacitance per unit length.

Using Kirchhoff's voltage and current laws, in the limit of $\Delta z \to 0$, the following equations can be derived,

$$\frac{\partial v(z,t)}{\partial z} = -Ri(z,t) - L\frac{\partial i(z,t)}{\partial t} \tag{2.1.1}$$

$$\frac{\partial i(z,t)}{\partial z} = -Gv(z,t) - C\frac{\partial v(z,t)}{\partial t} \tag{2.1.2}$$

which are more commonly expressed in the sinusoidal steady-state condition with cosine-based phasors

$$\frac{dV(z)}{dz} = -(R + j\omega L)I(z) \tag{2.1.3}$$

$$\frac{dI(z)}{dz} = -(G + j\omega C)V(z) \tag{2.1.4}$$

These coupled differential equations are known as the telegrapher equations. They can be solved simultaneously to yield the following travelling wave solutions for the voltage and current as a function of z,

$$V(z) = V_0^+ e^{-\gamma z} + V_0^- e^{\gamma z} \tag{2.1.5}$$

$$I(z) = I_0^+ e^{-\gamma z} + I_0^- e^{\gamma z} \tag{2.1.6}$$

where $\gamma = \alpha + j\beta = \sqrt{(R + j\omega L)(G + j\omega L)}$ is the complex propagation constant for a given frequency ω. The $e^{\pm\gamma z}$ term dictates the direction of the propagation of the waves and $V_0^{\pm}$ and $I_0^{\pm}$ are their respective amplitudes. Differentiating Equation 2.1.5 and substituting the result into Equation 2.1.3 yields the following relation.

$$I(z) = \frac{\gamma}{R + j\omega L}[V_0^+ e^{-\gamma z} - V_0^- e^{\gamma z}] \tag{2.1.7}$$

Comparing with Equation 2.1.4, the characteristic impedance can be defined as

$$Z_0 = \frac{R + j\omega L}{\gamma} = \sqrt{\frac{R + j\omega L}{G + j\omega C}} \tag{2.1.8}$$

If we assume that the transmission line is lossless, such that $R = G = 0$, then the propagation constant becomes $\gamma = j\omega\sqrt{LC}$ and the characteristic impedance of the line is given by

$$Z_0 = \sqrt{\frac{L}{C}} \tag{2.1.9}$$

with a phase velocity of the propagating waves given by

$$\nu_p = \frac{1}{\sqrt{LC}} \tag{2.1.10}$$

Impedance matching is primary concern in microwave electronics. In order to achieve maximum power transfer over a transmission line the line impedance must match the source and load impedance. This is illustrated in Fig. 2.2. At points of impedance mismatch power is reflected back toward the source and not delivered to the load. These reflections can also constructively and destructively interfere with the incident waves leading to the formation of standing waves over the length of the transmission line. The microwave engineering community adopted a 50 Ω impedance standardization for microwave systems in the 1930's for consistency across the industry. A value of 50 Ω is chosen as it is a good compromise between power handling and loss [9].

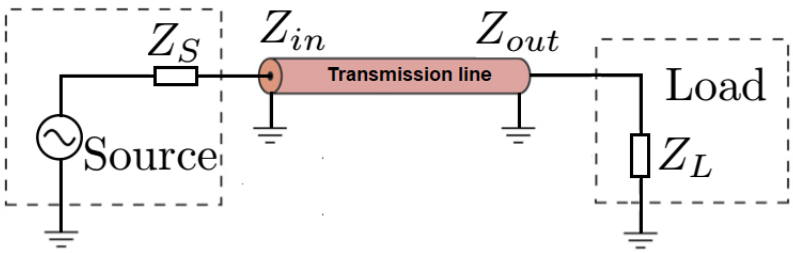

Figure 2.2: A source (Z_s) is connected to a load (Z_L) via the transmission line, in this case modelled as a coaxial cable. A mismatch of the source and the load impedance results in the maximal power not be delivered to the load and is instead reflected back toward the source.

Many of the early microwave devices used waveguides as transmission lines. In the most generic case electromagnetic waves propagating though a waveguide are confined to one (slab waveguide) or two dimensions (fibre or channel waveguide). Total internal reflection results in lossless transmission in the ideal case. However, in general, waveguides are bulky, expensive to produce and do not lend themselves to use in the area of complex microwave circuitry. Coaxial lines, are another commonly used transmission line at microwave frequencies. Comprised of a central conductor surrounded by an insulating layer and a outer conductor shield, they have very high bandwidth and are useful in a large number of applications, however, once again they do not lend themselves to being integrated in complex microwave circuitry. Planar transmissions lines were developed to be used in an ever expanding area of integrated microwave circuits. Some common types

of planar waveguides are shown in Fig. 2.3. The geometries of these planar transmission lines are generally compact and low in cost allowing them to be easily fabricated, while allowing for the incorporation of active components such as transistors and diodes to form complex circuitry.

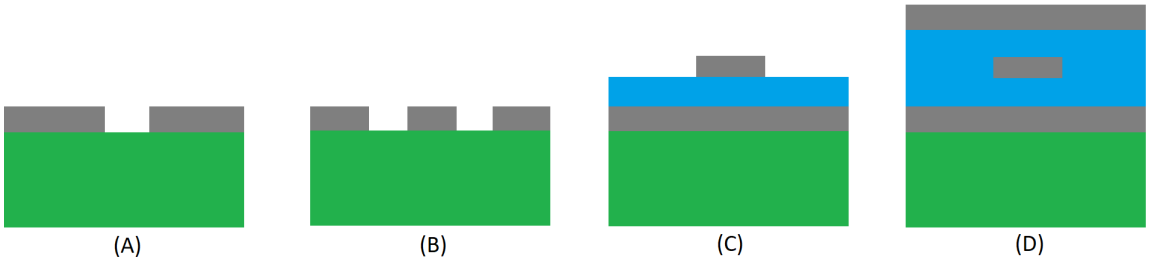

Figure 2.3: Four varieties of planar waveguides. Green - substrate, Grey - conductor, Blue - dielectric. (A) Slot line; (B) Coplanar; (C) Microstrip; (D) Strip line.

2.1.1 Coplanar waveguides

Coplanar waveguides (CPW) were first proposed by C. P. Wen in 1969 [10]. A schematic is given in Fig. 2.4. They are often the favoured type of planar waveguides for use in cQED (circuit quantum electrodynamics) and superconducting microwave devices for a number of reasons, including:

- Operation up to high frequencies of several GHz's
- The ground plane on either side of the central conductor limits cross talk between other lines in local proximity
- Suffer less from radiative loses and dispersion than coplanar slotlines
- CPW designs are easily fabricated in a single step process
- Straightforward implementation of common nano-fabrication techniques to engineer discrete passive or active elements into the transmission line or mounted on its surface
- Characteristic impedance of CPW line is effectively controlled by the parameters W and S, this allows implementation of this transmission line geometry varying in lateral dimensions from the μm to mm length scale.

CPW transmission lines have multiple modes which support the propagation of electromagnetic fields. Focussing on the "even" quasiTEM mode, conformal mapping and partial capacitance techniques can be used to analyse the electromagnetic field distributions in a multi-layered substrate CPW [11].

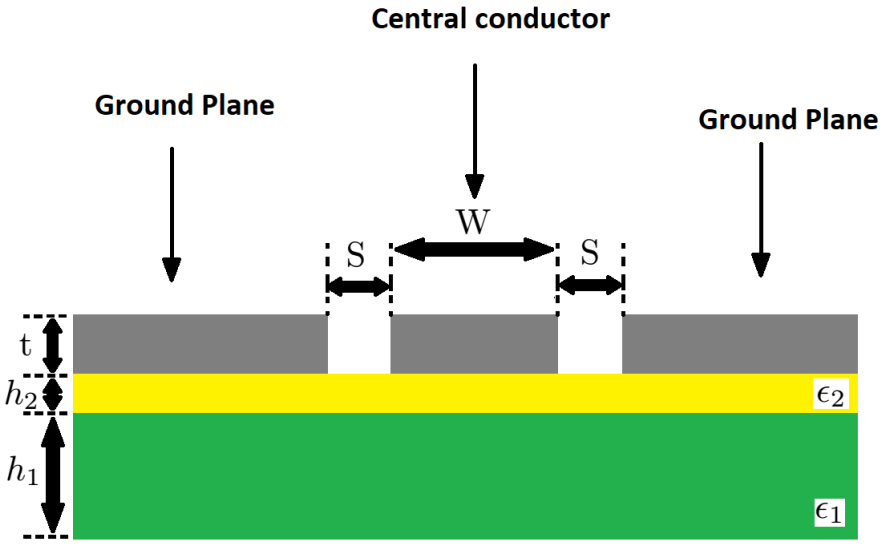

Figure 2.4: Cross section of CPW transmission line, characterised by a central conductor of width W enclosed by a ground plan with a spacing S. Single and multilayer substrates can be used. In this case the substrate is comprised of two layers. Where yellow represents a SiO_2 surface layer with permittivity ϵ_2 and green represents the bulk Si substrate with permittivity ϵ_1. This is a common substrate, typical of what was used to fabricate the CPW devices detailed in Chapter 5.

Conformal mapping involves transforming the geometry of the CPW into another conformation. This technique is detailed in [12] and has shown to be in agreement with finite-element methods [13]. Neglecting kinetic inductance for the time being the inductance per unit length, L_l, of the CPW line with a non-magnetic substrate ($\mu_{eff} = 0$) is given as

$$L_l = \frac{\mu_0}{4}\frac{K(k^{'})}{K(k)} \tag{2.1.11}$$

where μ_0 is the permeability of free space and $K(k^{'})$ and $K(k)$ represent the complete elliptic integrals of the first kind and their respective complementary moduli/arguments

$$k = \frac{W}{W + 2S} \tag{2.1.12}$$

$$k^{'} = \sqrt{1 - k^2} \tag{2.1.13}$$

In order to determine the capacitance per unit length C_l, a partial-capacitance technique can be used to approximate a multilayer substrate with i layers into i single layer substrates each with a modified dielectric constant $\epsilon_{eff}^{(i)}$. Reducing to the case of a double layer substrate ($i = 1, 2$) with dielectric permittivity ϵ_1 and ϵ_2, respectively, the partial capacitance of the i^{th} layer is given by

$$C_i = 2\epsilon_0\epsilon_{eff}^{(i)}\frac{K(k_i)}{K(k_i^{:})} \tag{2.1.14}$$

The total capacitance per unit length is the sum of the partial capacitances for layer 1 and 2, given as

$$C_l = 4\epsilon_0\epsilon_{eff}\frac{K(k_0)}{K(k_0')} \tag{2.1.15}$$

where ϵ_{eff} is a function of ϵ_1 and ϵ_2. Using these relations for the inductance and capacitance per unit length and Equations 2.1.9 and 2.1.10, the characteristics impedance and phase velocity of a CPW transmission line can be defined as

$$Z_0 = \sqrt{\frac{L_l}{C_l}} \tag{2.1.16}$$

$$\nu_p = \frac{1}{\sqrt{L_l C_l}} \tag{2.1.17}$$

To summarise, in the case of a non-magnetic substrate and neglecting kinetic inductance, L_l and C_l are determined from the geometry of the conductors (W and S) and the effective dielectric permittivity ϵ_{eff}. Thus the characteristic impedance of the CPW, Z_0 is effectively determined by the ratio of the width of the central conductor W and the spacing between it and the ground plane S. This feature of CPW's makes their geometry extremely scalable. Central conductor and ground spacing widths can vary from millimetres to microns while maintaining a ratio $\frac{S}{W}$ which defines a 50 Ω impedance given the ϵ_r of the dielectric used (in the case impedance matching is required). This allows for vast flexibility/scalability in device design and integration of CPW transmission lines. Furthermore, in the context of cQED, the ability to reduce their dimensions offers the ability to construct resonant structures with large vacuum fields [14].

2.1.2 CPW resonators

A simplistic top down view of a $\lambda/2$ CPW resonator is shown in Fig. 2.5(A). The resonator is defined by the interruption of the central conductor of a CPW transmission line with two series capacitors which constitute boundary conditions on the electromagnetic fields defined by their lengths of the separation. This type of resonator is analogous to a Fabry-Pèrot resonator/interferometer, where capacitors replace the partially reflective optical surfaces.

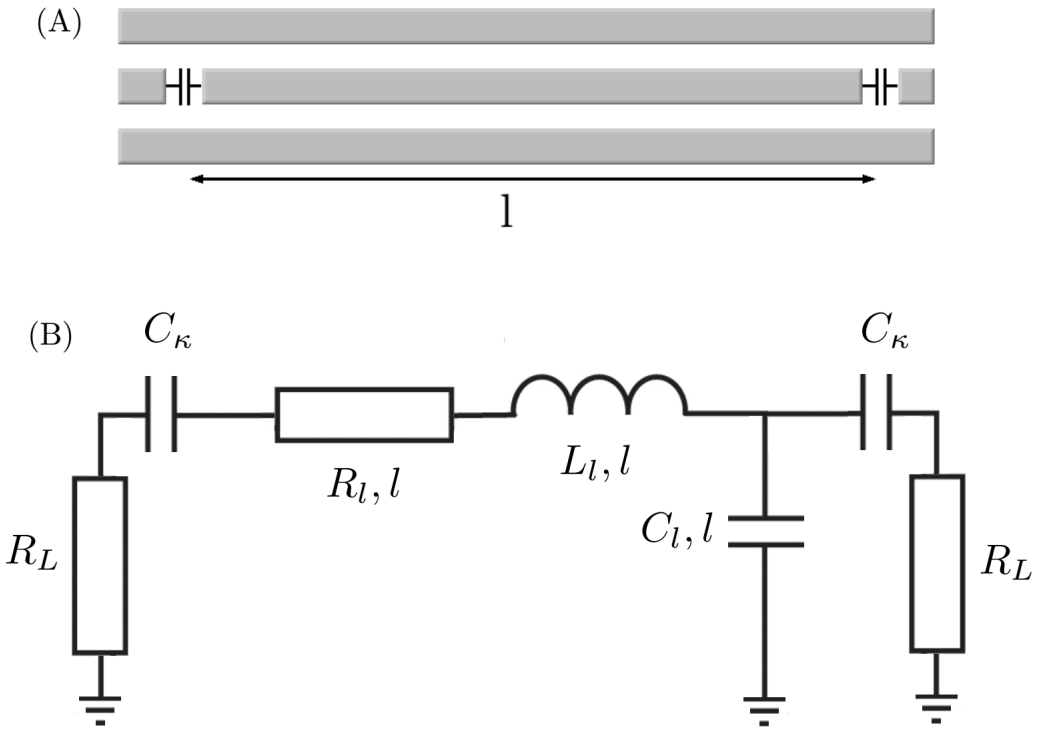

Figure 2.5: (A) A simplistic top down view of a CPW transmission line where the central conductor has been interrupted by series capacitors to form the resonator. (B) Distributed element representation of a transmission line resonator, where R_l, L_l and C_l are the resistance, inductance and capacitance to ground, per unit length of the CPW discussed in the previous section. C_κ and R_L represents the capacitive coupling and the resistive loading, respectively.

The length of the resonator corresponds to a half wavelength ($\frac{\lambda}{2}$) of the intended resonant frequency, f_1. The n^{th} mode of the resonator, f_n, is related via the phase velocity $\nu_{ph} = \frac{c}{\sqrt{eff}}$, and is given as

$$f_n = (n)\frac{c}{\sqrt{\epsilon_{eff}}}\frac{1}{2l} \tag{2.1.18}$$

where n is an integer mode number, with $n = 1$ corresponding to the fundamental mode of the resonator. Fig. 2.6 shows the normalised current distribution squared for the first three modes ($n = 1, 2, 3$) of an idealised resonator. Fig 2.7 shows an arbitrary element embedded at the centre ($\lambda/4$ point) of a $\lambda/2$ resonator. In this case the position of the element corresponds with an antinode (maximum) in the current distribution of the fundamental mode and a node in the current distribution of the second mode. Excitation of the fundamental mode will result in an effective oscillating current bias over the element.

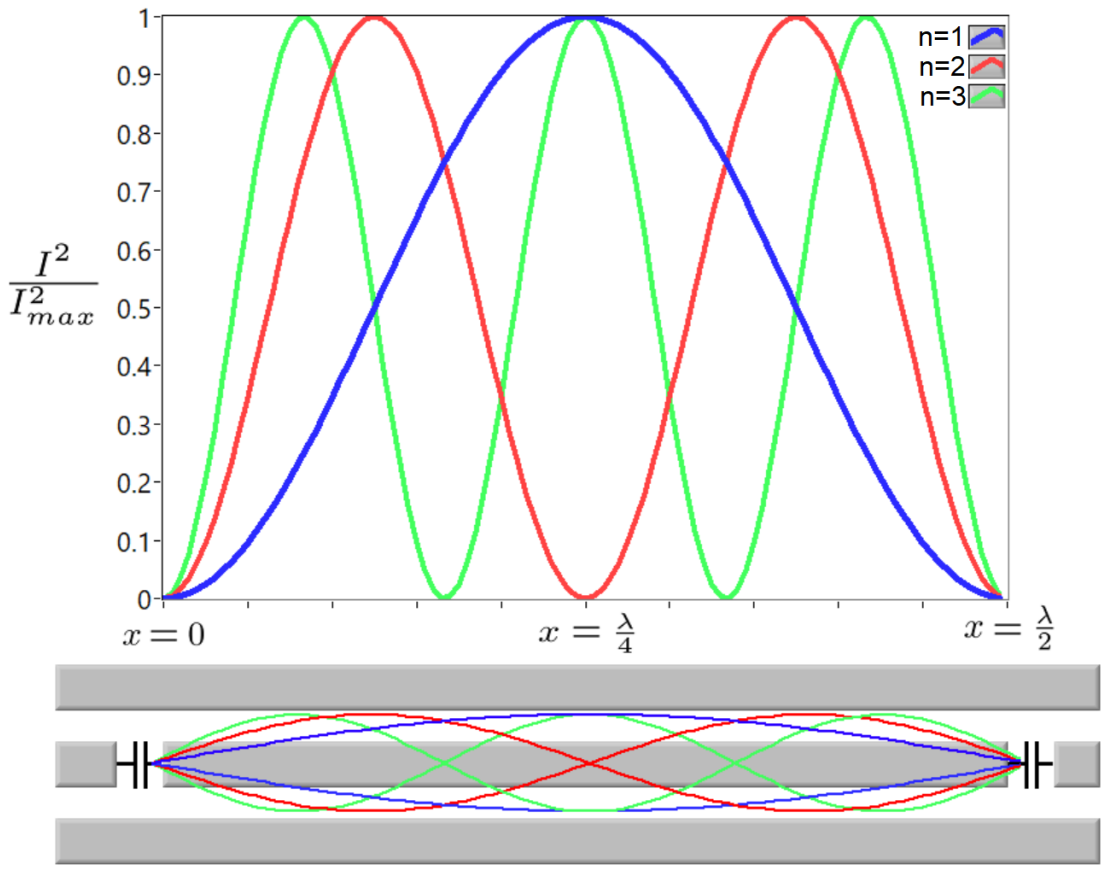

Figure 2.6: Normalised current distribution squared of the first 3 modes of a $\lambda/2$ resonator as a function of position x. Blue - fundamental; Red - second mode; Green - third mode.

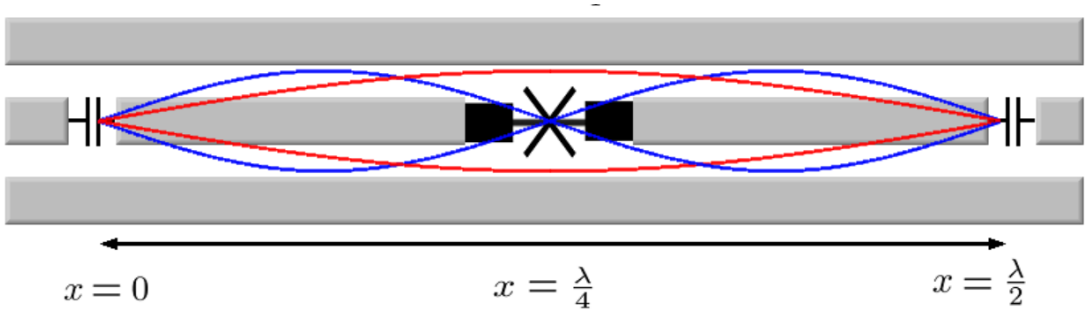

Figure 2.7: Fundamental (red) and second mode (blue) of $\lambda/2$ resonator with a discrete element ($\times$) inserted at the $\lambda/4$ point. Due to the central position of the element in the resonator, the fundamental mode is coupled to the element and the second mode is uncoupled.

The transmission spectrum around the fundamental mode $f_{n=1}$, which for convention we will refer to as f_0, of a niobium CPW resonator with a fundamental frequency of approximately 6 GHz is shown in Fig. 2.8. In general CPW resonators exhibit a Lorentzian (Breit-Wigner) line-shape characterised by a maximum at the resonant frequency f_0 and

a bandwidth δf, together defining the quality factor of the resonance, given as $Q = \frac{f_0}{\delta f}$. Several methods exist to measure the resonant frequency and quality factor from transmission data, a comparison of the most common methods can be found in [15]. In the case of Fig. 2.8, the quality factor is obtained via a non-linear least squares fit used to fit the data to a generalised Lorentzian fitting function, given as

$$F_{Lor} = A_1 + A_2 f + \frac{|S_{max}| + A_3 f}{\sqrt{1 + 4(\frac{f - f_0}{\delta f})^2}} \tag{2.1.19}$$

where $A_1 + A_2 f$ defines a sloped background, the A_3 factor adds a skew and $|S_{max}|$ defines the maximum magnitude of transmission. This function will be used to describe CPW resonators in later chapters.

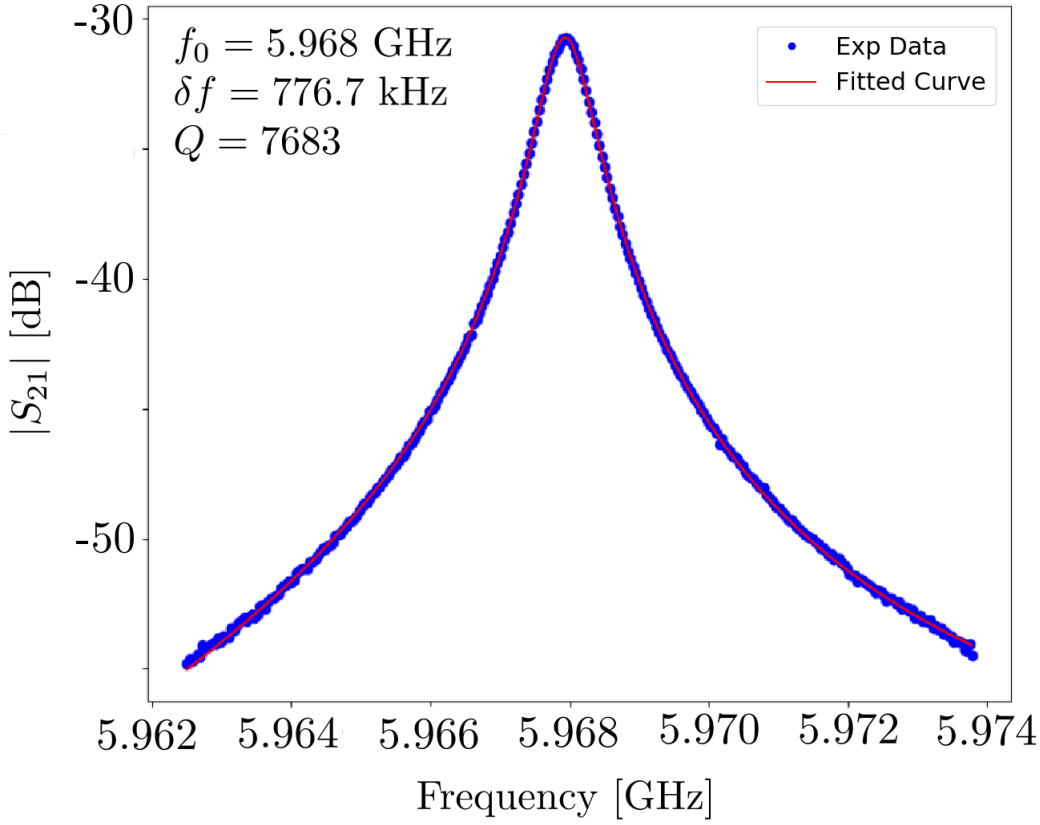

Figure 2.8: Example of the transmission spectrum ($|S_{21}|$) of a CPW resonator. In this case a Nb $\lambda/2$ CPW resonator measured at 4.18 K fabricated at RHUL using the techniques and procedures outlined in Chapter 5.

S_{21} refers to the forward scattering parameter in a 2 port network, often used to characterise frequency dependent transmission through microwave devices. The data shown in Fig. 2.8 was acquired using a 2 port vector network analyser (VNA), which measures the amplitude of incident and reflected voltage waves for the respective ports of the device, resulting in a scattering matrix, given as

$$\begin{pmatrix} V_1^- \\ V_2^- \end{pmatrix} = \begin{pmatrix} S_{11} & S_{12} \\ S_{21} & S_{22} \end{pmatrix} \begin{pmatrix} V_1^+ \\ V_2^+ \end{pmatrix} \tag{2.1.20}$$

where $V_{1,2}^+$ and $V_{1,2}^-$ are the amplitudes of the incident and reflected voltage waves for the respective ports.

The overall quality factor of the CPW resonator is dependent on a number of parameters and in the case of independent channels of dissipation can be given as

$$\frac{1}{Q} = \frac{1}{Q_{coupling}} + \frac{1}{Q_{resistive}} + \frac{1}{Q_{radiative}} + \frac{1}{Q_{dielectric}} \tag{2.1.21}$$

where the respective terms correspond to the available dissipation mechanisms in a generalised CPW resonator. We will briefly look at each term individually in order to understand in what way these dissipation mechanism manifest in a superconducting CPW resonator such as that shown in Fig. 2.8, primarily focusing on $Q_{coupling}$, $Q_{resistive}$ and $Q_{dielectric}$. We will neglect as in general $Q_{radiative}$ it is small when compared to the other loss mechanisms.

2.1.2.1 Loaded quality factor

In order to understand how the coupling of the input and output lines to a CPW resonator affects its behaviour, it is worth defining a few useful representations of a transmission line (TL) resonator. Fig. 2.5(B) shows a distributed device representations of a transmission line resonator with a resonant frequency ω_0, where R_l, C_l and L_l are the resistance, capacitance and inductance per unit length. The impedance, Z_{TL} of the TL resonator, as is given in [16], is

$$Z_{TL} = Z_0 \frac{1 + i\tan(\beta l)\tanh(\alpha l)}{\tanh(\alpha l) + i\tan(\beta l)} \tag{2.1.22}$$

where α is the attenuation constant and $\beta = n\omega_0\nu_{ph}$ is the phase constant. If the loss is small such that $\alpha l \ll 1$ for frequencies ω close to $n\omega_0$ (near resonance), the impedance can be approximated as

$$Z_{TL} \approx \frac{Z_0}{\alpha l + i\frac{\pi}{\omega_0}(\omega - \omega_n)} \tag{2.1.23}$$

where

$$\omega_n = n\omega_0 = \frac{1}{\sqrt{L_n C}} \tag{2.1.24}$$

$$L_n = \frac{2L_l l}{n^2\pi^2} \tag{2.1.25}$$

$$C = \frac{C_l l}{2} \tag{2.1.26}$$

Following the analysis set out by [17], the behaviour of a TL resonator can be approximated as a lumped element parallel LCR oscillator , shown in Fig. 2.9(A), with impedance given as

$$Z_{LCR} = \Big(\frac{1}{i\omega L_n} + i\omega C + \frac{1}{R}\Big)^{-1} \tag{2.1.27}$$

where

$$R = \frac{Z_0}{\alpha l} \tag{2.1.28}$$

for frequencies close to resonance ($\omega \approx \omega_n$) the impedance can be approximated as

$$Z_{LCR} \approx \frac{R}{1 + 2iRC(\omega - \omega_n)} \tag{2.1.29}$$

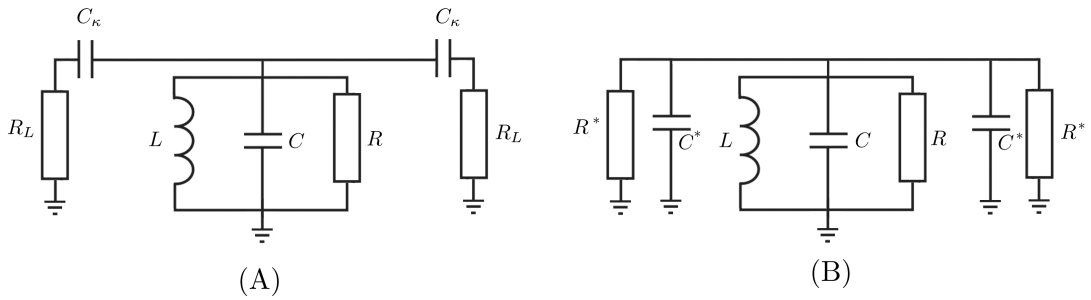

Figure 2.9: (A) Lumped element parallel LCR representation of a TL resonator. (B) The Norton equivalent circuit for this TL resonator representation.

The internal quality factor of the resonator $Q_{internal}$ (in the absence of the coupling to the input and output line) is given as

$$Q_{internal} = R\sqrt{\frac{C}{L_n}} = \omega_n RC \tag{2.1.30}$$

The coupling of the transmission line resonator to the input and output generally results in a reduction of the quality factor due to resistive loading of the input and output lines. The coupling capacitance also results in a frequency shift of the resonant modes. The effect of the coupling to the input and output lines can be explored by using a Norton equivalent circuit of the parallel LCR oscillator, shown in Fig. 2.9(B). The series R_L and C_κ are transformed into a Norton equivalent parallel connection, with the modified resistance and capacitance given as

$$R^\star = \frac{1 + \omega_n^2 C_\kappa^2 R_L^2}{\omega^2 C_\kappa^2 R_L} \tag{2.1.31}$$

$$C^\star = \frac{C_\kappa}{1 + \omega^2 C_\kappa^2 R_L^2} \tag{2.1.32}$$

considering the case where the coupling capacitance of the input and output are equal, the "loaded" quality factor, Q_L, is modified by the parallel combination of C and $C^\star$ and R and $R^\star$ and is given as

$$Q_L = \omega_n^\star \frac{C + 2C^\star}{1/R + 2/R^\star} \tag{2.1.33}$$

where $\omega_n^\star$ is the shifted frequency of the n$^{\text{th}}$ resonant mode, given as

$$\omega_n^\star = \frac{1}{\sqrt{L_n(C + 2C^\star)}} \tag{2.1.34}$$

Manipulating the coupling capacitance C_k allows for Q_L of a CPW resonator to be varied over multiple orders of magnitude. Using small coupling capacitances results in an under-coupled resonator with a high loaded quality factor. In the context of cQED, such a resonator would be suitable for storing photons for long time scales, applicable for "quantum memory" devices. A high capacitive coupling results in an overcoupled resonator with low quality factors. Once again considering cQED, such a resonator could be used for fast measurement of quantum systems such as qubits.

ID	Coupling	C_κ (fF)	f_0 (GHz)	Q_L
A	8+8 finger	56.4	2.2678	3.7×10^2
B	7+7 finger	48.6	2.2763	4.9×10^2
C	6+6 finger	42.9	2.2848	7.5×10^2
D	5+5 finger	35.4	2.2943	1.1×10^3
E	4+4 finger	26.4	2.3086	1.7×10^3
F	3+3 finger	18.0	2.3164	3.9×10^3

ID	Coupling	C_κ (fF)	f_0 (GHz)	Q_L
G	2+2 finger	11.3	2.3259	9.8×10^3
H	1+1 finger	3.98	2.3343	7.5×10^4
I	10 μm gap	0.44	2.3430	2.0×10^5
J	20 μm gap	0.38	2.3448	2.0×10^5
K	30 μm gap	0.32	2.3459	2.3×10^5
L	50 μm gap	0.24	2.3464	2.3×10^5

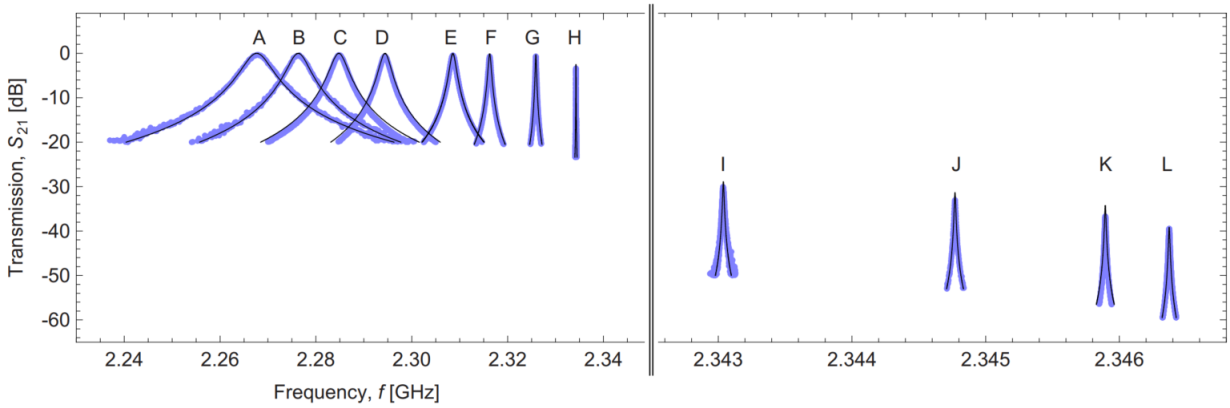

Figure 2.10: Taken from [17]. Comparison of resonant frequency and quality factor for superconducting CPW resonators with different coupling capacitances. Upper - table of individual Al CPW resonator characteristics. Lower - transmission spectra ($|S_{21}|$) of resonators measured at a temperature of 0.02 K. The effect of the input/output loading can be observed in the quality factor and centre frequencies of the respective fundamental modes.

Coupling capacitors are often defined in CPW resonators by forming a gap in the central conductor of a CPW transmission line, referred to as gap capacitors. Higher capacitive

coupling can be realised by employing interdigitated (finger) capacitors interrupting the central conductor. Göppl et al. [17] fabricated a multitude of identical superconducting CPW resonators with varying magnitudes of symmetric capacitive coupling. The resulting transmission data for these resonators is shown in Fig. 2.10.

Although we have been discussing symmetric coupling capacitance, asymmetric coupling capacitors can also be used. By manipulating the capacitance of one port relative to the other a preferred output can be defined. In Chapter 5 we will discuss fabrication and measurement of both asymmetric and symmetric coupled Nb CPW resonator with differing loaded quality factors.

2.1.2.2 Superconducting coplanar waveguide resonators

In the previous section we saw how the capacitive and resistive loading of a TL resonator results in modification to the quality factor and resonant frequency of the oscillator. Up to this point we have regarded superconductors simply as a convenient lossless medium, however, in order to understand resistive losses and the inductive contributions associated with a superconducting coplanar waveguide (SCPW) resonator it is required to define a more formal understanding of superconductivity.

BCS superconductivity

Superconductivity is a state of matter defined by the loss of electrical resistivity and the expulsion of magnetic fields, commonly referred to as the Meissner effect. In BCS theory [18], superconductivity is mediated by bosonic electron pairs (Cooper pairs), the attractive interaction binding the two negatively charged electrons is provided by phonons originating from electromagnetic interactions between the electrons and the lattice ions. Upon the onset of superconductivity the attractive interaction between electrons allows them to lower their energy to that corresponding to the BCS ground state of the system. The bosonic Cooper pairs are exempt from Pauli's exclusion principle, as such multiple Cooper pairs can occupy the same quantum state, leading to a coherent bosonic condensate resulting in the formation of an energy gap in the density of states. This energy gap corresponds to the reduction in energy between the normal and superconducting electron states, respectively. The normalized BCS density of states is shown in Fig.2.11(A).

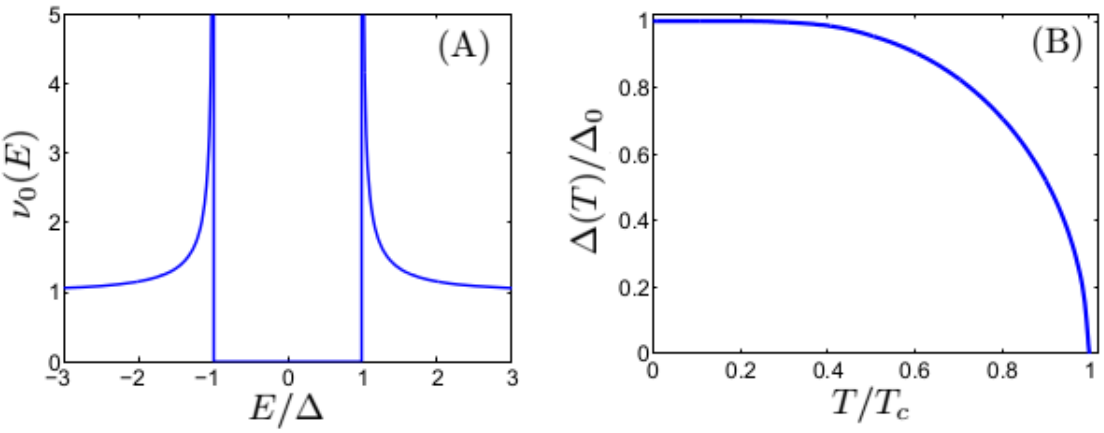

Figure 2.11: Taken from [19]. For aluminium; (A) Normalized BCS density of states. (B) BCS energy gap as a function of temperature.

The energy gap of a superconductor, Δ, is temperature dependent (Fig. 2.11(B)) and related to the transition temperature of the superconducting material T_C by $\Delta_0 \approx 1.76 k_B T_C$, where Δ_0 is the energy gap at $T = 0$ K. BCS theory gives the density of states of a superconducting material below its transition temperature as

$$N(E) = N(0)\nu_0(E) \tag{2.1.35}$$

where

$$\nu_0(E) = |Re(\frac{E/\Delta}{\sqrt{(E/\Delta)^2 - 1}})| \tag{2.1.36}$$

$N(0)$ is the two-spin density of states at the Fermi level for the material above its transition temperature T_c (normal state).

The coherence length, ξ, defines the characteristic length scale for which the density of Cooper pairs changes appreciably. It can also be interpreted as the width of a boundary between a normal and superconducting phase. At zero temperature ξ is given as

$$\xi_0 = \hbar v_f / \pi \Delta_0 \tag{2.1.37}$$

where v_f is the Fermi velocity. Another notable parameter is the London penetration depth, λ, which can be approximated at zero temperature as [20],

$$\lambda(0) = 1.05 \times 10^{-3} \sqrt{\rho(T_c)/T_c} \tag{2.1.38}$$

where $\rho(T_c)$ denotes the resistivity at T_c. The penetration depth characterises the depth at which a magnetic field incident on the superconducting material has fallen to $1/e$ of its value at the surface.

Quasiparticles

Quasiparticles refer to excited states within the superconductor, neither completely electrons or holes these states can be treated as a quantum superposition of both a hole and electron state [21]. Quasiparticles in a superconductor can arise due to several different mechanisms, such as thermal excitation of Cooper pairs in the BCS ground state. The density of quasiparticles in a superconductor in equilibrium at temperature T_S can be found by considering the integral of quasiparticle occupation vs energy

$$n(T_S) = 2N(0) \int_0^\infty f_S(E)\nu_0(E)\, dE \tag{2.1.39}$$

where $f_S(E)$ Fermi distribution function, which for quasiparticles with a positive energy f_S relates to occupied states and for quasiparticles with negative energy, f_S, relates to unoccupied states. Fig. 2.12 shows the quasiparticle density as a function of the temperature of a superconductor.

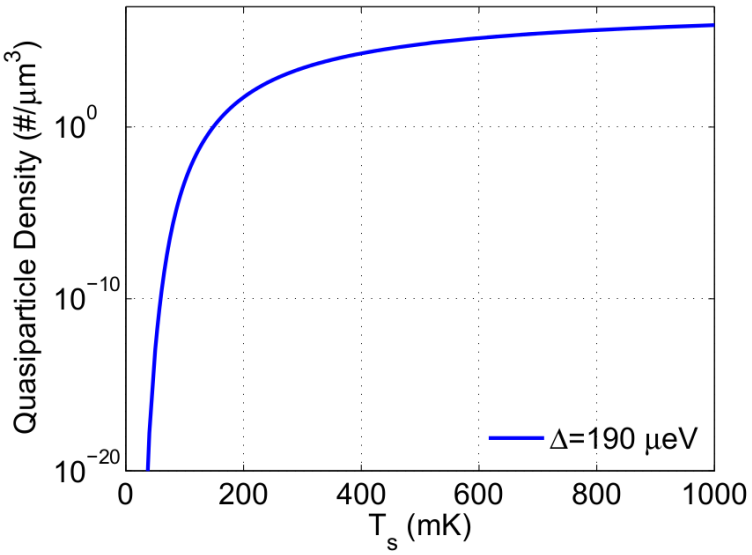

Figure 2.12: Taken from [19]. Quasiparticle density as a function of T_S for aluminium.

Mattis-Bardeen theory

The presence of a non-zero quasiparticle population results in superconductors exhibiting finite dissipation when carrying alternating (AC) electric fields. This is due to the acceleration and deceleration of the quasiparticles in the electric field and their subsequent scattering from impurities resulting in ohmic loses. Following from [21], a two fluid model can be used to describe the response of the superconductor in alternating fields where the conduction is described by the superposition of a superconducting electron fluid of density n_S and a normal (quasiparticle) fluid of density n_n. The two fluids are assumed to have different relaxation times, τ_s and τ_n, respectively. Furthermore, it is assumed

that $\tau_s = \infty$ such that the superconducting electrons do not scatter. In the case that the frequency of the applied field E with frequency $\omega \ll 1/\tau_n$ (an assumption generally valid for microwave frequencies), the quasiparticles give a parallel ohmic conduction channel within the superconductor, defined by a current density $\overrightarrow{J}_n$, given as

$$\overrightarrow{J}_n = (n_n e^2 \tau_n / m_e) \overrightarrow{E} \tag{2.1.40}$$

Using the Drude model allows for an approximate description of the combined AC response of the parallel channels to a field of the form $Ee^{i\omega t}$ to be expressed as a complex conductivity given as

$$\sigma(\omega) = \sigma_1(\omega) + i\sigma_2(\omega) \tag{2.1.41}$$

where

$$\sigma_1(\omega) = \frac{n_n e^2 \tau_n}{m} \tag{2.1.42}$$

$$\sigma_2(\omega) = \frac{n_s e^2}{m\omega} \tag{2.1.43}$$

σ_1 accounts for ohmic loses due to the scattering of quasiparticles. σ_2 is an inductive term which accounts for the inertia of the Cooper pairs in the electric field, we will discuss this further in the next section. The conductivity is thus a function of the quasiparticle population and thus depends on the temperature of the superconductor. As such we would expect the quality factor of a superconducting resonator to have temperature dependence relating to dissipation and changes in inductance corresponding to the quasiparticle density. Mattis and Bardeen [22] developed a theory in which the value of σ_1 and σ_2 can be calculated with respect to the normal state ($T > T_c$) conductivity σ_n for a superconductor at temperature T, given as

$$\frac{\sigma_1}{\sigma_n} = \frac{2}{\hbar\omega} \int_{\Delta}^{\infty} \frac{(E^2 + \Delta^2 + E\hbar\omega)(f(E) - f(E+\hbar\omega))}{\sqrt{E^2 - \Delta^2}\sqrt{(E+\hbar\omega)^2 - \Delta^2}} dE \tag{2.1.44}$$

$$+ \frac{2}{\hbar\omega} \int_{\Delta-\hbar\omega}^{-\Delta} \frac{(E^2 + \Delta^2 + E\hbar\omega)(1 - 2f(E+\hbar\omega))}{\sqrt{E^2 - \Delta^2}\sqrt{(E+\hbar\omega)^2 - \Delta^2}} dE \tag{2.1.45}$$

$$\tag{2.1.46}$$

$$\frac{\sigma_2}{\sigma_n} = \frac{1}{\hbar\omega} \int_{\Delta-\hbar\omega}^{\Delta} \frac{(E^2 + \Delta^2 + E\hbar\omega)(1 - 2f(E+\hbar\omega))}{\sqrt{\Delta^2 - E^2}\sqrt{(E+\hbar\omega)^2 - \Delta^2}} dE \tag{2.1.47}$$

Inductance of superconducting CPW

We have already discussed the geometric contribution to the inductance of a CPW line. In this section we will discuss the inductive contribution related to the kinetic inductance of the itinerant Cooper pairs in the superconducting medium. Kinetic inductance arises

from a non-zero relaxation time when considering the motion of the charge carrier in a conductor, manifesting itself as the imaginary term in the complex conductance seen in the previous section. In normal conductors, the kinetic inductance can often be completely neglected due to the numerous relaxation mechanisms available to the charge carriers and thus short relaxation times. However, in the case of superconductors the inductive contribution of the kinetic inductance, owing to the inertia of the Cooper pairs, can be significant. Thus, in-order to describe the total inductance for superconducting CPW L_l both the geometric L_l^m and kinetic L_l^k must be considered:

$$L_l = L_l^m + L_l^k(T) \tag{2.1.48}$$

where for a SCPW geometry L_l^k is given as [23],

$$L_l^k = \mu_0 \lambda(T)^2 \frac{g(W,S,t)}{\alpha} \tag{2.1.49}$$

where $g(W,S,t)/\alpha$ is a term related to the geometry of the CPW line, S and W and the thickness of the conductor (t). $\lambda(T)$ is the temperature dependent penetration depth of the superconducting material. The kinetic inductance of the material is intimately related to the surface impedance of the superconductor, often characterised by two regimes, which relate the coherence length of the superconductor, ξ, with the mean free path of electrons moving on the surface l_{mf}. The two regimes are defined as the clean limit:

$$\xi << l_{mf} \tag{2.1.50}$$

and the dirty limit:

$$\xi >> l_{mf} \tag{2.1.51}$$

Depending on the superconducting material and the corresponding London penetration depth the contribution can be negligible or significant. The innate kinetic conductance of superconductors is also non-linear in current I, as such a SCPW constitutes non-linear inductor, to a varying degree depending on the specific superconductor.

2.1.3 Dielectric losses

Dielectric losses concern the absorption/dissipation of electrical energy by a dielectric medium subject to an AC electric field. The dielectric constant is a complex number

$$\epsilon_r = \epsilon_r^{'} - i\epsilon_r^{''} \tag{2.1.52}$$

where the imaginary term $i\epsilon_r^{''}$ represents the loss in the medium. Generally, in the high temperature/power case the dissipation is due to damping of vibrating dipole moments of the atoms/molecules of the dielectric material in the oscillating field. Considering a

lossless medium, or if a DC field is applied instead of an AC, the complex component is zero and the dielectric constant is given by the real part. The loss of a dielectric medium is often characterised by the loss tangent $\tan(\delta)$, given as

$$\tan(\delta) = \frac{\epsilon_r''}{\epsilon_r'} \tag{2.1.53}$$

with a corresponding quality factor of

$$Q_{dielectric} = \frac{1}{\tan\delta} \tag{2.1.54}$$

Dielectric losses are generally negligible in most situations, however, in the case of SCPW operating at low powers and temperatures they have been associated with a myriad of different mechanisms which result in a significant impact to the cQED devices. Dielectic losses in SCPW's and other cQED devices employing dielectrics (Josephson junctions) have been subject to a great number of investigations [24],[25],[26]. SCPW resonators are often employed to study dielectric loss due to its presence being clearly identifiable at low powers, depending on the geometry and material of SCPW [27].

Generally dielectric loses are largely attributed to defects characterised as quantum two level systems (TLS). These TLS's can be present in bulk dielectric substrate, at material interfaces, or on the surface of the devices itself such as native oxides. TLS's in the oxide barrier of Josephson junction's being of particular concern. The term TLS is broad and can address a number of different mechanisms associated with loss. In the general case TLS's are described by the standard tunnelling model (STM) [28],[29] which describes the quantum mechanical tunnelling of electrons between adjacent lattice sites at low temperatures. The TLS can be regarded as a two level system that absorbs energy that is then dissipated in the environment and generating 1/f noise in electrical material. This model has been employed in the context of electrons tunnelling in insulation barriers, such as surface oxides and Josephson junction, and other tunnelling events at material interfaces. It has been found that not only do TLS's couple to the system of interest (like the fundamental mode of a SCPW) they also interact with other TLS's. With these interactions needing to be accounted for in the STM model to accurately predict their noise charactricsistics and dependence at low temperatures [30].

Advances in engineering, such as thin film deposition technology, and fabrication methodology have made progress limiting the impact of TLS's. For example, it has recently been shown that simple annealing treatment leads to a reduction of 1/f frequency noise in a NbN SCPW resonator by an order of magnitude [31]. The annealing step achieves this by desorption of surface spins, caused by the dissociation of ambient water molecules on the surface of the resonator.

2.1.4 Fano resonance

CPW resonator sometimes exhibit non-Lorentzian line-shapes. An interesting example of this is the Fano line-shape which will become relevant in later chapters referring to experimental observation of resonances with this characteristic asymmetric appearance. Fano resonances occur when a discrete quantum state (super-radiant mode) interferes with continuum band of states (sub-radiant mode) [32]. The line-shape (we will focus on transmission spectra) is given by the Fano formula:

$$F_{Fano}(\omega) = \frac{q + (2\frac{\omega-\omega_0}{\delta\omega})^2}{1 + (2\frac{\omega-\omega_0}{\delta\omega})^2} \tag{2.1.55}$$

where ω_0 and $\delta\omega$ are the resonant frequency and width respectively and q is the Fano (or asymmetry) parameter which is related to the phase shift between the interfering discrete state and the continuum. Fig. 2.13 shows the Fano line-shape for varying values of q. In the limit $q \to \pm\infty$ a Lorentzian line-shape is recovered as the discrete state is no longer coupled to the continuum. In the region of $-1 \lesssim q \lesssim 1$ a high asymmetric line-shape is observed with a sharp transition from transmission to reflection centred around the resonant frequency. These spectral features have attracted interest, specifically in the photonics community in applications such as spectroscopy [33] and switching [34]. Fano resonances manifested in cQED devices have also been investigated, such as in case of Fano resonance in open quantum dot systems with applications for spin filtering [35].

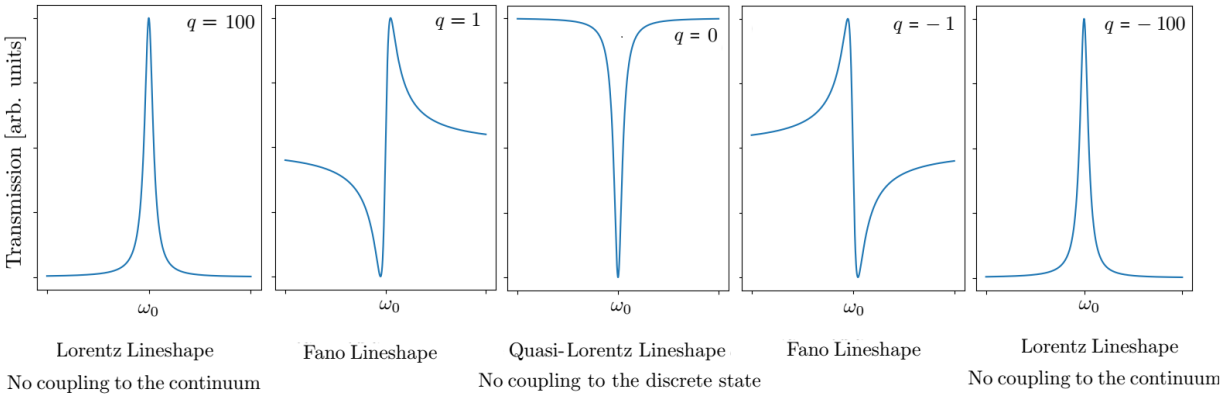

Figure 2.13: Numerical evaluation of the Fano function (Equation 2.1.55), showing the change in the function's line-shape with varying asymmetry parameter. In this case $\omega_0 \gg \delta\omega$.

An intuitive explanation of Fano resonance is given in [36] in which an analogous classical harmonic oscillator system is studied.

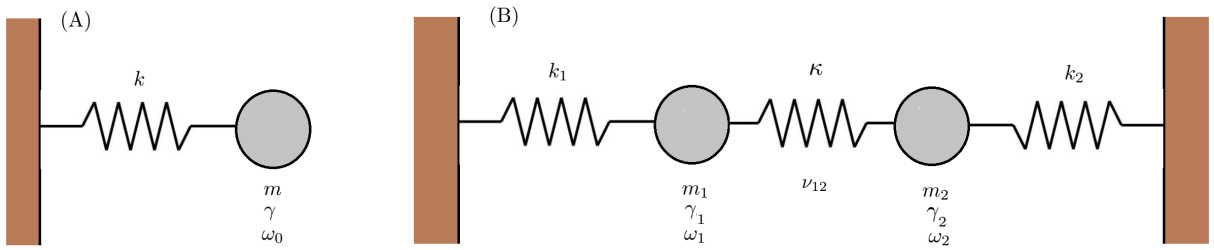

Figure 2.14: (A) Representation of a mechanical oscillator subject to a restoring and damping force. (B) A set of coupled mechanical oscillators, in this case coupled via a third spring κ.

Considering the situation shown in Fig. 2.14(A) representing a single mechanical oscillator subject to a linear restoring and resistive dampening force. In the case the oscillator is driven by a harmonic force ($F = A\cos\omega t$) the equation of motion can be written as

$$\ddot{x} + \gamma\dot{x} + \omega_0^2 x = A\cos\omega t \tag{2.1.56}$$

where ω_0 is the resonant frequency of the oscillator defined by the mass of the oscillator m, the spring constant k and the damping parameter γ. The general solution is given as the sum of the particular solution x_p and the complementary solution x_c, in this case given as

$$x_c(t) = e^{-\gamma t/2}(q_1 e^{i\Omega t} + q_2 e^{-i\Omega t}) \tag{2.1.57}$$

$x_c(t)$ characterises the exponential decay of the transient motion of the damped oscillator after the application of the driving force. In this case we are only interested in the partial solution x_p describing its motion after the transient decay. x_p can be found by rewriting the driving force in complex representation ($F_D = \frac{1}{2}A(e^{i\omega t} + e^{-i\omega t})$). Considering the solutions corresponding to positive frequencies, Equation 2.1.56 can be rewritten as

$$\ddot{x}^+ + \gamma\dot{x}^+ + \omega_0^2 x^+ = a e^{i\omega t} \tag{2.1.58}$$

where $a = A/2$. The solution is given as $x^+(t) = ce^{i\omega t}$, where the complex amplitude $c(\omega)$ is

$$c(\omega) = \frac{a}{\omega_0^2 - \omega^2 + i\gamma\omega} \tag{2.1.59}$$

with modulus $|c(\omega)|$ and phase $\phi(\omega)$

$$|c(\omega)| = \frac{a}{\sqrt{(\omega_0^2 - \omega^2)^2 + \gamma^2\omega^2}} \tag{2.1.60}$$

$$\phi(\omega) = tan^{-1}(\frac{\omega\gamma}{\omega_0^2 - \omega^2}) \tag{2.1.61}$$

Fig. 2.15 shows the amplitude $|c(\omega)|$ and phase ϕ response of the oscillator as the driving force is swept through the resonant frequency.

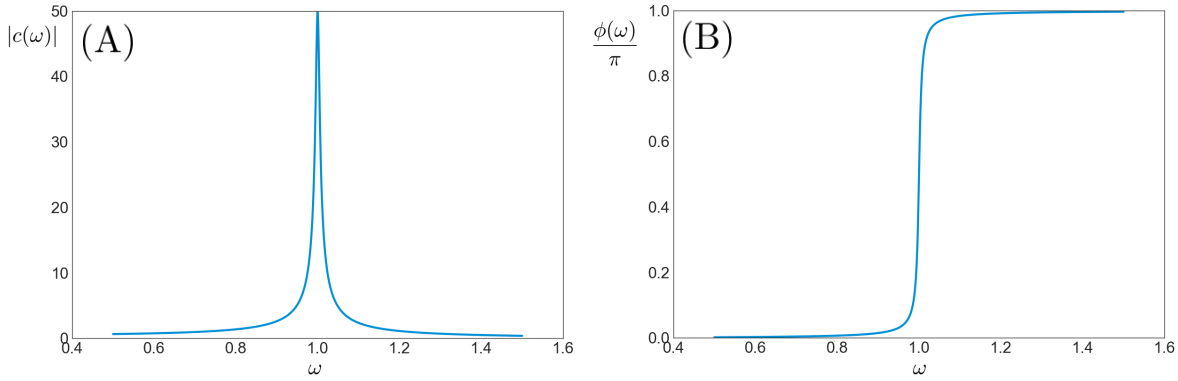

Figure 2.15: Evaluation of $|c(\omega)|$ and ϕ for a damped oscillator subject to a harmonic driving force. In this case $\gamma = 0.02$ (lightly damped). (A) Amplitude response has Lorentzian line-shape. (B) Characteristic π phase change as the driving force is swept through the resonant frequency. ω is divided by ω_0 such that the x-axis is in units of the natural/resonant frequency.

Fig. 2.14(B) shows a system of coupled oscillators, where the coupling is represented by a third spring. Considering the situation where an external harmonic driving force is applied to the first oscillator (1) and no external force is applied to the second oscillator (2). Similarly to the situation of the single oscillator, we will concern ourselves with the complex amplitude response of the partial solution x_p to describe the behaviour of the oscillator around resonance, neglecting the complementary solution as we are only interested in the behaviour of the amplitudes of the oscillators after the transient motion decays. The equations of motion of the coupled oscillator system can be written as

$$\ddot{x}_1 + \gamma\dot{x}_1 + \omega_1^2 x_1 + \nu_{12}x_2 = a_1 e^{i\omega t} \tag{2.1.62}$$

$$\ddot{x}_2 + \gamma\dot{x}_2 + \omega_2^2 x_2 + \nu_{12}x_1 = 0 \tag{2.1.63}$$

where the quantity ν_{12} describes the coupling of the oscillators. In the absence of coupling and with no external driving acting on the oscillators ($\nu_{12} = a_1 = 0$), the free oscillators move independently of each other with given natural resonant frequencies ω_1 and ω_2. If the oscillators are coupled there are two eigenmodes available, the two oscillators can swing back and forth in unison, or they can move in opposite directions. Assuming that there is no damping, such that $\gamma_1 = \gamma_2 = 0$, Equation 2.1.62 and 2.1.63 can be rewritten as

$$\ddot{x}_1 + \omega_1^2 x_1 + \nu_{12}x_2 = 0 \tag{2.1.64}$$

$$\ddot{x}_2 + \omega_2^2 x_2 + \nu_{12}x_1 = 0 \tag{2.1.65}$$

the eigenmodes of this coupled oscillator system are given as

$$(\omega_1^2 - \omega^2)(\omega_2^2 - \omega^2) - \nu_{12}^2 = 0 \tag{2.1.66}$$

If the coupling is weak such that $\omega_2^2 - \omega_1^2 \gg \nu_{12}$ then the eigenmodes of the coupled oscillators ($\tilde{\omega}_1$ and $\tilde{\omega}_2$) are slightly shifted from the uncoupled state and can be approximated as

$$\tilde{\omega}_1 \approx \omega_1^2 - \frac{\nu_{12}^2}{\omega_2^2 - \omega_1^2} \tilde{\omega}_2 \approx \omega_2^2 - \frac{\nu_{12}^2}{\omega_2^2 - \omega_1^2} \tag{2.1.67}$$

Returning to the general case given in Equations 2.1.62 and 2.1.63, the steady state solutions when $\gamma_1, \gamma_2, a_1 \neq 0$, are given as

$$x_1 = c_1 e^{i\omega t} \tag{2.1.68}$$

$$x_2 = c_2 e^{i\omega t} \tag{2.1.69}$$

where

$$c_1(\omega) = \frac{\omega_2^2 - \omega^2 + i\gamma_2\omega}{(\omega_1^2 - \omega^2 + i\gamma_1\omega)(\omega_2^2 - \omega^2 + i\gamma_2\omega) - \nu_{12}^2} a_1 \tag{2.1.70}$$

$$c_2(\omega) = \frac{\nu_{12}}{(\omega_1^2 - \omega^2 + i\gamma_1\omega)(\omega_2^2 - \omega^2 + i\gamma_2\omega) - \nu_{12}^2} a_1 \tag{2.1.71}$$

The phase of the oscillators is given as

$$c_1(\omega) = |c_1(\omega)| e^{-i\phi_1(\omega)} \tag{2.1.72}$$

$$c_2(\omega) = |c_2(\omega)| e^{-i\phi_2(\omega)} \tag{2.1.73}$$

and the phase differences between the oscillators is

$$\phi_2 - \phi_1 = \pi - \cot\left(\frac{\gamma_2\omega}{\omega_2^2 - \omega^2}\right) \tag{2.1.74}$$

The responses of the respective oscillators for the case where $\omega_1 = 1$, $\omega_2 = 1.2$,$\gamma_1 = 0.02$, $\gamma_2 = 0$ and $\nu_{12} = 0.1$ is shown in Fig. 2.16 and 2.17.

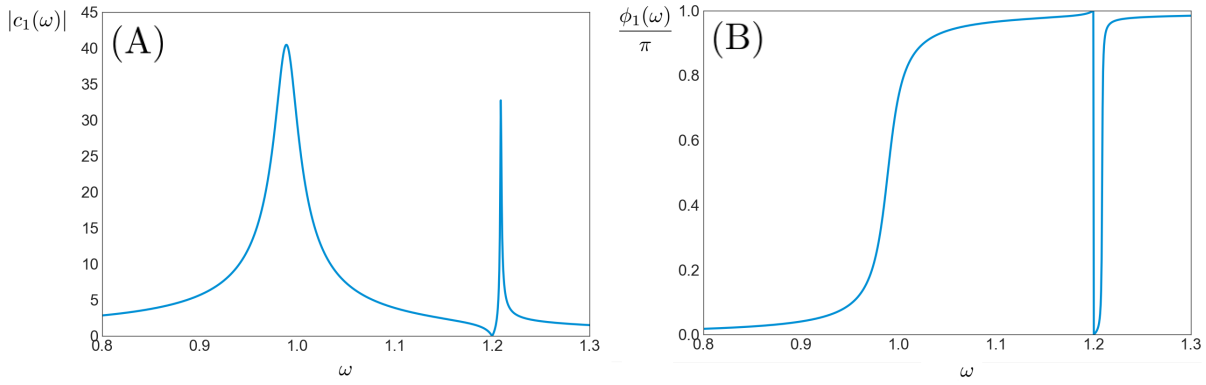

Figure 2.16: Response of the first oscillator $|c_1(\omega)|$ and ϕ_1 to an external driving force of frequency ω. (A) The influence of the second oscillator can be observed as the drive frequency is swept through ω_2, with a zero frequency state at 1.2 followed by a peak, forming an asymmetric line-shape. The response can be observed in (B) where the phase sharply drops by π at $\omega = \omega_2 = 1.2$ before recovering as the drive is moved to higher frequencies.

Referring to Fig. 2.16, showing the amplitude and phase response of the first oscillator as the frequency of the applied force is swept. The coupling to the second oscillator has resulted in a second asymmetric resonance in $|c_1(\omega)|$ around $\omega \approx 1.2$. The resonance around $\omega \approx 1$ is symmetric, similar to that seen in the uncoupled case (2.15), however, now the position of the resonant peak corresponding to the eigen-frequency $\tilde{\omega_1}$ has been shifted to just below $\omega = \omega_1 = 1$, the natural frequency of the uncoupled oscillator. This detuning of the eigenfrequencies of the coupled oscillator is determined by the coupling parameter ν_{12}, for a higher coupling factors the shift away from the uncoupled natural frequency of the oscillator is more significant, as demonstrated in Fig. 2.18. Referring back to Fig. 2.16, the peak around ω_1 has also broadened in comparison with the uncoupled case. The asymmetric feature around the resonant frequency of the second oscillator in $|c_1(\omega)|$ is characteristics by an amplitude zero state at ω_{zero} prior to a peak. At ω_{zero} there is a sharp drop in ϕ_1 by π.

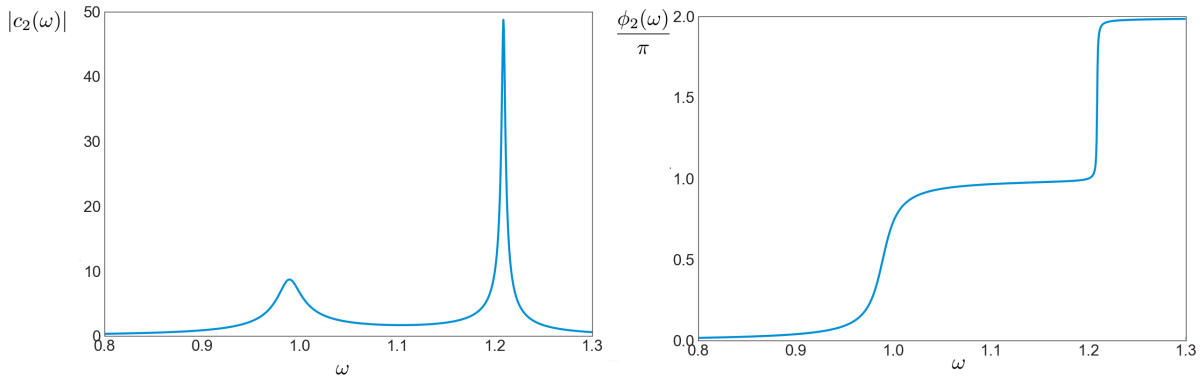

Figure 2.17: Response of the second oscillator $|c_2(\omega)|$ and $\phi_2(\omega)$ to an extremal driving force of frequency ω acting on the first oscillator.

Referring to Fig. 2.17, the response of the second oscillator, here two symmetric resonant peaks can be seen in $|c_2(\omega)|$ with corresponding changes in the phase ϕ_2 as the frequency of the drive passes through the resonances. Comparing Fig. 2.16 and 2.17 it can be seen that at $\omega = \omega_{zero}$ the two oscillators are out of phase. The amplitude zero state at this frequency owes to the motion of the first oscillator being quenched by the action of the second oscillator.

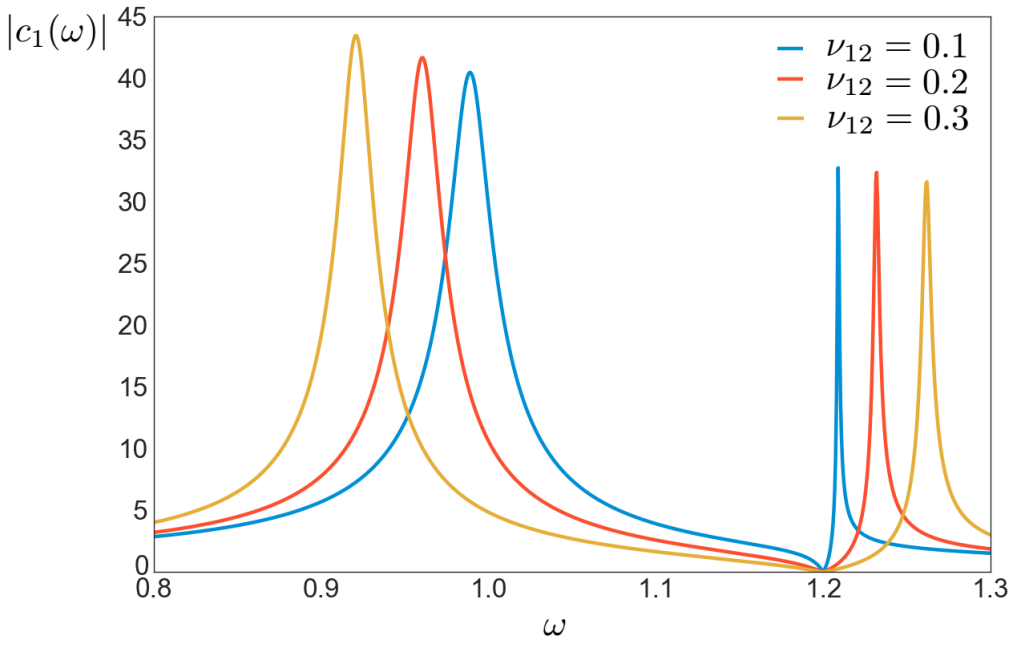

Figure 2.18: Response of first oscillator $|c_1(\omega)|$ where $\omega_1 = 1$, $\omega_2 = 1.2$,$\gamma_1 = 0.02$ and $\gamma_2 = 0$ for an increasing strength of coupling to the second oscillator.

In the case of finite damping of the second oscillator, shown in Fig. 2.19, the zero-frequency of the first oscillator is shifted to the complex-energy plane. The consequence of this is that the response of the first oscillator at ω_{zero} gains a finite amplitude.

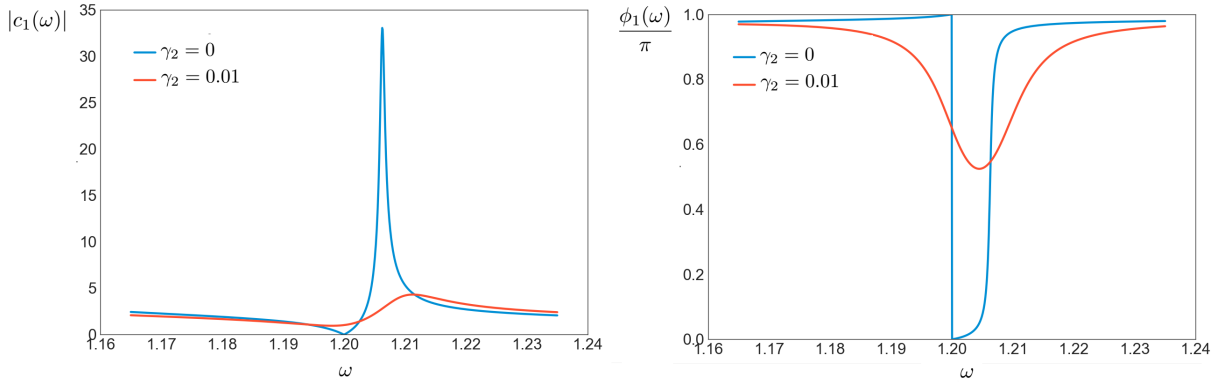

Figure 2.19: Response of first oscillator $|c_1(\omega)|$ and phase ϕ_1 around ω_2, where $\omega_1 = 1$, $\omega_2 = 1.2$ and $\gamma_1 = 0.02$ for the case when there is no damping of the second oscillator (blue) and finite damping $\gamma_2 = 0.01$ (red). In the case of $\gamma_2 = 0.01$ $|c_1(\omega)|$ gains a finite amplitude at ω_{zero}.

As previously mentioned Fano resonances have been observed in a number of cQED devices. A particular case, specific to SCPW resonators, that I would like to highlight is detailed in [37]. The device being reported is a Nb CPW resonator with DC bias lines inserted at low impedance points of second mode (corresponding to a full wave length),

which will be referred to as the mainline resonance. An image of the device and the resulting transmission spectra around the mainline resonance is shown in Fig. 2.20(A). The resonator incorporates DC bias lines (ports 3 and 4) inserted at $l/4$ and $3l/4$ points of the central conductor of the mainline (port 1 to port 2), where l is the length of the resonator. This allows for current bias over the mainline useful for many applications such as current biasing embedded active elements. However, for current purposes we are only concerned with a secondary effect their device exhibited shown in Fig. 2.20(B). This device has 4 ports such that there is a corresponding 4×4 scattering matrix. When the mainline resonance is measured via port 1 and port 2 (S_{21}), a Lorentzian line-shape is observed, similar to that of the Nb resonator shown in Fig. 2.8. However, when measuring transmission via the DC bias lines inputs provided by ports 3 and 4 (S_{31} and S_{41}) a Fano line-shape is observed. In this case the discrete mode is the mainline resonance and the continuum is arising from a broad resonance associate with the DC bias lines, significant when using them as inputs. In this manner, the DC bias lines are acting as additional resonators whose resonant frequencies are shifted far from the mainline resonant frequency. The authors suggest that there are two pathways viable to the photons fed via the bias lines, they can couple directly to the broad modes created by the bias lines, or couple to the main resonance and then to the bias line. Interference between these two pathways is destructive on one side of the main resonance and constructive on the other. We will revisit Fano resonances and coupled modes in later chapters when discussing measurements of fabricated samples.

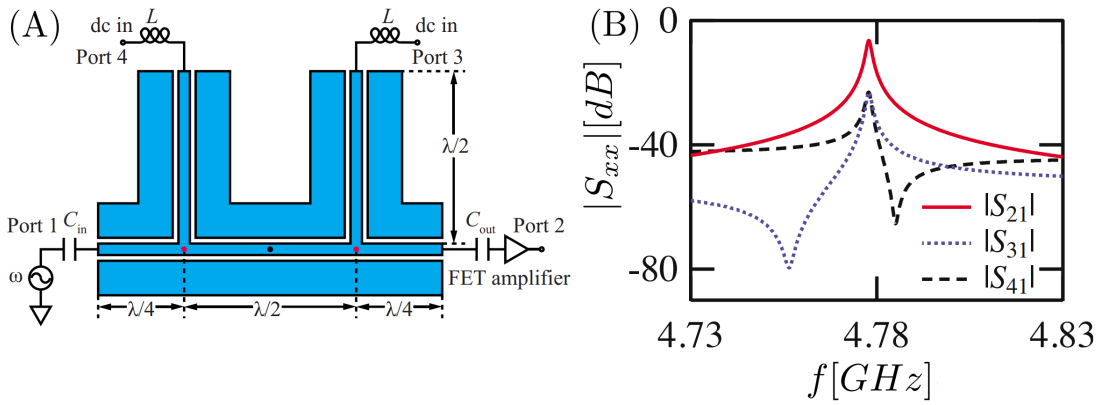

Figure 2.20: Taken from [37]. (A) Schematic representation of the Nb CPW being studied. In this case the "mainline" resonance is chosen to be a full wavelength λ ($n = 2$) due to the insertion of the flux bias line damping the fundamental $\lambda/2$ mode. (B) Transmission spectra around the mainline resonance. $|S_{21}|$ shows a Lorentzian line-shape whereas $|S_{31}|$ and $|S_{41}|$ show an asymmetric line-shape characteristic of a Fano resonance. The asymmetry parameter (q) is also different between $|S_{31}|$ and $|S_{41}|$ indicating a different phase shift between the continuum and discrete state when feeding via port 3 or port 4.

2.2 The Josephson effect

In this section we will introduce the Josephson junction, characterised by a non-linear current-phase relation. We will use the RCSJ model to define a model for a junction easily married with common circuit analysis techniques. This allows for the simple integration (and analysis) of a Josephson junction and a transmission line/gap coupled TL resonator, constituting a non-linear medium. We will also discuss how the current-phase relation can be modulated using an RF SQUID geometry, allowing for the purely odd (cubic) function to be modified to include even terms allowing the realisation of different associated phenomena. In order to build an intuitive understanding of these phenomena and the conditions in which they are manifested, we will borrow from the long established field of non-linear optics. We will discuss the Born approximation and the derivation of coupled wave equations describing the behaviour of propagating waves subject to parametric interactions mediated by the non-linear response of the medium. We will then apply this understanding to microwave transmission lines and resonators employing Josephson junctions, such as Josephson parametric amplifier's (JPA's) and mixers. We will also look at the behaviour of a classical driven oscillator subject to non-linear restoring force to understand the nature of bifurcations in the state of oscillation of a resonant SCPW employing Josephson junctions.

2.2.1 Josephson junctions

The Josephson effect was first predicted by Brian Josephson [38]. A Josephson junction, shown in Fig. 2.21(A), defines a weak coupling between two superconducting condensates separated by a weak link using a thin insulating barrier. The current I and voltage V characteristic of the constriction relates to the gauge invariant phase difference, $\delta = \phi_L - \phi_R$, of the phase ($\phi_{L/R}$) of the wave-functions of the respective superconducting electrodes.

A common way to understand charge transport in a Josephson junction, detailed in [39], is the consideration of bound Andreev states, owing to the energy gap Δ in the DOS of the superconducting electrodes. As such, no states of energy within Δ of the Fermi energy can exist within the electrodes. This constitutes a boundary condition on either side of the junction which results in quasiparticle bound states of energies $E_{J\pm}$. The phenomenon can be understood by describing electrical transport through the junction as a sum of independent conduction channels, where each conduction channel has a transmission probability (τ_i), such that the total current through the junction is given as $I = \sum_i I(\tau_i)$. Considering a plane wave incident on a tunnel junction, where the junction barrier is described as a delta function, the energies of the bound states can be

found to be

$$E_J = \pm\Delta[1 - \tau\sin^2(\delta/2)]^{\frac{1}{2}} \tag{2.2.1}$$

A plot of $E_{J\pm}$ as a function of δ is shown in Fig. 2.22.

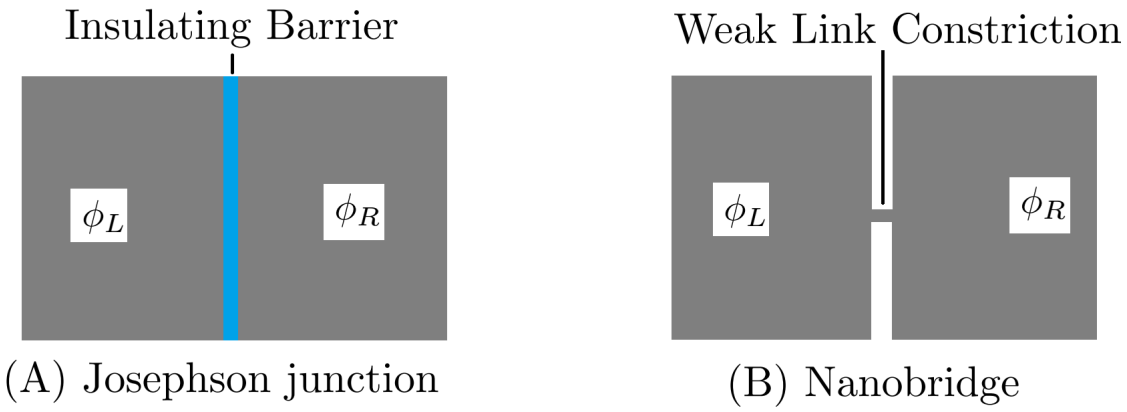

Figure 2.21: The Josephson effect is manifested via a weak coupling between two superconducting condensates separated by a weak link. (A) Josephson junction employing a thin insulting barrier to act as a weak link between the condensates. (B) Nanobridges also define a weak link in the form of a constriction the order of the coherence length of the superconducting material.

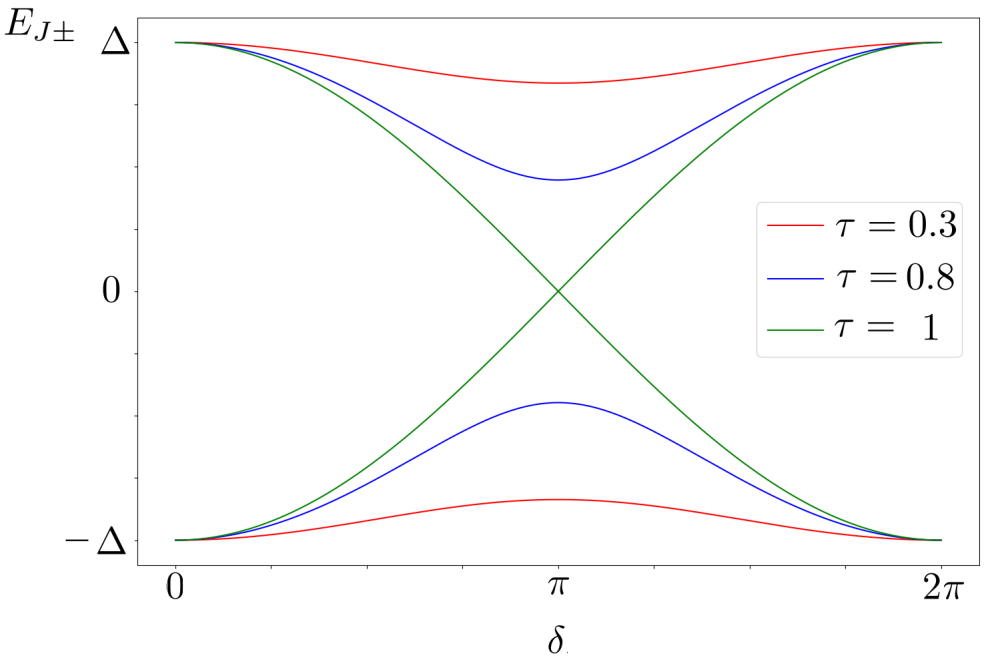

Figure 2.22: Andreev/quasiparticle bound state energies $E_{J\pm}$ as a function of the phase difference of the superconducting electrodes δ for different values of tunnelling probability τ. Quasiparticles are generated from vertical transition from the lower E_{J-} band to the upper E_{J+} band.

At $T = 0$ all states below ϵ_F will be filled and all states above the Fermi energy will be empty. An excitation in the lower band leads to the creation of a corresponding hole state. In this case the current through the junction, the Josephson current I_J, can be given as

$$I_J = I_c \sin\delta \tag{2.2.2}$$

I_c is commonly refereed to as the critical current of the junction, given by the Ambegaokar-Baratoff formula

$$I_c = \frac{\pi}{2}\frac{\Delta(T)}{eR_N}\tanh\Big(\frac{\Delta(T)}{2k_BT}\Big) \tag{2.2.3}$$

where $\Delta(T)$ is the superconducting gap at temperature T and R_N is the normal state resistance of the junction. For $I < I_c$ current can flow in the absence of voltage V over the junction. If a voltage, V, is put across the electrodes the phase varies with time, given as

$$V = \frac{\Phi_0}{2\pi}\frac{d\delta}{dt} \tag{2.2.4}$$

where $\Phi_0 = h/2e$ is the flux quantum. Differentiating Equation 2.2.2 and substituting the result into Equation 2.2.4 yields

$$V = \frac{\Phi_0}{2\pi}\frac{1}{I_c\cos\phi}\frac{dI_J}{dt} \tag{2.2.5}$$

This relation effectively describes an inductor ($V \propto \frac{dI}{dt}$). As such the inductance of the Josephson junction, L_J, can be defined as

$$L_J = \frac{\Phi_0}{2\pi}\frac{1}{I_c\cos\phi} \tag{2.2.6}$$

2.2.2 Nanobridges

Although this chapter is primarily focused on "traditional" Josephson junctions defined by an insulating barrier separating two superconducting electrodes, it is worth briefly introducing another method of manifesting the Josephson effect. A weak link constriction or nanobridge is shown in Fig. 2.21(B). Nanobridges define a weak separation of two superconducting electrodes similar to Josephson junctions. In the case of a Josephson junction the insulating barrier separating the superconducting electrodes is thin enough so that electrons can quantum mechanically tunnel through the barrier. Nanobridges define a similar weak link by joining the two electrodes with a narrow superconducting constriction (bridge). The width of the constriction must be of the order of the coherence

length, ξ, of the superconductor. The current-phase relation and critical current of this nanobridge junction is highly dependent on the geometry of the constriction and the electrodes [40].

Weak links have been of interest since the realisation of the Josephson effect. Well-defined nanobridges fabricated using electron beam lithography (EBL) were demonstrated as early as the 1980's [41]. Fabricating such structures with dimensionality of order ξ (Nb $\xi = 38$ nm) is far from trivial and as such has impeded their development in comparison with tunnel junctions. However, modern advances in engineering and fabrication technologies (high resolution EBL and focussed ion beam lithography) have made fabricating such geometries more reliable. As such nanobridges are seeing increasing usage in the place of tunnel junctions, where applicable. Although fabrication difficulty is often dependent on the equipment available, generally nanobridges are simpler to implement than tunnel junctions, because they remove the need for a double angle evaporation or controlled oxide growth. The lack of an oxide insulating barrier (or additional material interfaces) also reduces the likelihood of parasitic TLS's, as discussed in Section 2.1.3, reducing loss mechanisms incurred when incorporating into other devices. Nanobridges also lack any junction capacitance, which can be an advantage in certain situations, with capacitive shunting a design option if required. The current-phase relation of a nanobridge junction can differ in functionality depending on the geometry compared with the well-defined sinusoidal current-phase relation in tunnel junctions. The current-phase relation can vary from a distorted sinusoid to an almost linear function in extreme situations ($I \propto \delta$) [42]. Another consequence of the nanobridges geometry are the constraints it brings to the thermal conductance of the weak link. Above I_c the link is dissipative, resulting in ohmic heating. With the limited conduction pathways available to the constriction, thermal hysteresis in their current-phase characteristics can be observed [43]. This is similar to the capacitive hysteresis which we will encounter when we overview the resistively and capacitively shunted junction model in the next section.

We will revisit nanobridges in Chapter 5 where a method of fabricating such constrictions in the central conductor of a Nb CPW resonator is detailed. Chapter 7 will detail the measurement of fabricated devices including the observation of non-linear phenomena associated with their inclusion in the CPW resonator.

2.2.3 RCSJ model

The current/voltage behaviour of a Josephson junction can be modelled effectively as a circuit element by employing the resistively and capacitively shunted junction model (RCSJ) [44], where a Josephson junction is represented by an equivalent circuit shown in Fig. 2.23.

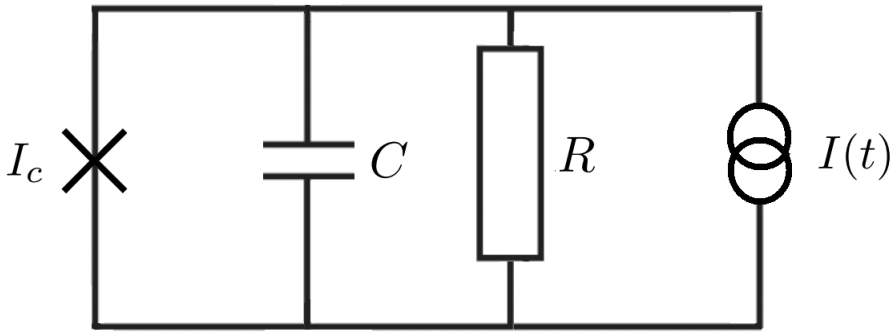

Figure 2.23: RCSJ model equivalent circuit of a Josephson junction bias with a current source $I(t)$. The junction, with characteristic parameters I_c and L_J, is represented with a cross.

The Josephson element is in parallel with a capacitor C and a resistor R. The capacitance can be either self-capacitance owing to insulting barrier forming the junction or an engineered shunt capacitance to control the dynamics of the junctions behaviour. The resistive element can also serve several purposes, it can approximate an ohmic resistance owing to a non-zero quasiparticles density or characterise the real part of the characteristic impedance of a microwave transmission line, and by extension the source impedance. Similarity to shunt capacitances tailored shunt resistors can also be fabricated onto the junction to manipulate its behaviour. Applying Kirchhoff's laws to the circuit shown in Fig. 2.23 yields

$$C\dot{V} + \frac{V}{R} + I_c \sin\delta = I \tag{2.2.7}$$

Substituting in Equation 2.2.4 (the AC Josephson relation) results in the equation of motion for the phase difference δ over the junction, given by

$$\frac{\Phi_0}{2\pi} C\ddot{\delta} + \frac{\Phi_0}{2\pi}\frac{1}{R}\dot{\delta} = I - I_c \sin\delta = -\frac{2\pi}{\Phi_0}\frac{\partial U_J}{\partial \delta} \tag{2.2.8}$$

where the Josephson potential U_J is defined as

$$U_J \equiv \frac{\Phi_0}{2\pi}(I_c(1-\cos\delta) - I\delta) = E_J(1 - \cos\delta - i\delta) \tag{2.2.9}$$

$i = I/I_0$ is the normalised bias current. U_J is shown in Fig. 2.24 and is commonly refereed to as the tilted washboard potential.

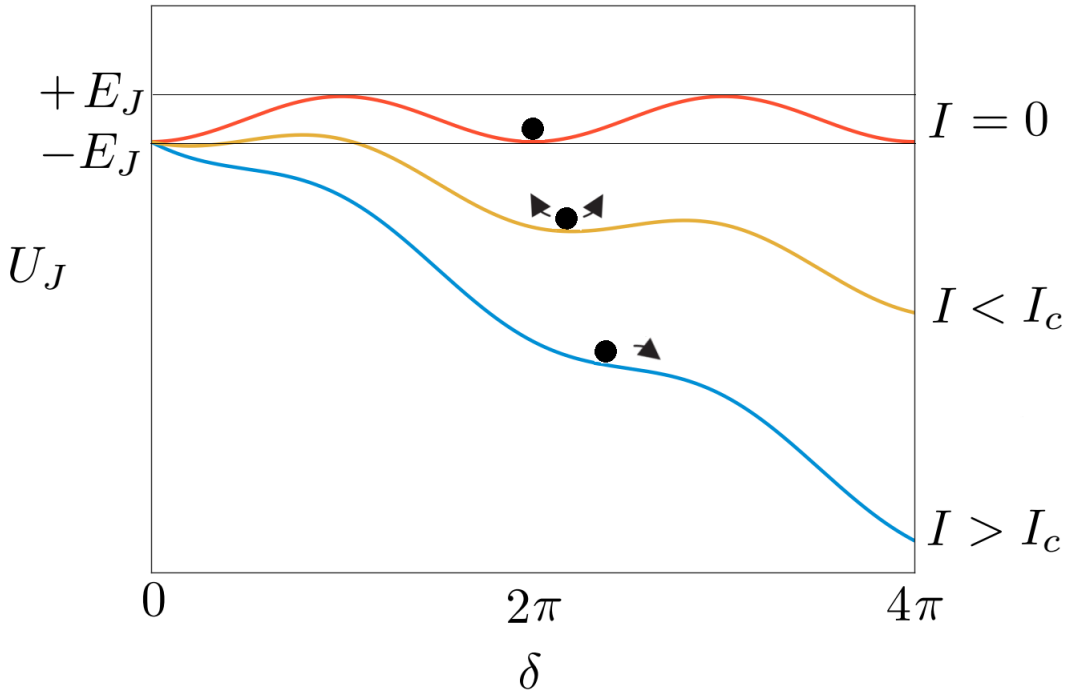

Figure 2.24: The tilted washboard potential. Red ($I = 0$), yellow ($I < I_c$) and blue ($I > I_c$). The black circle represents a mechanical point mass on the potential where the arrows correspond to its motion.

The behaviour of δ can be characterised with a mechanical analogy of a point mass moving on the potential. In this case resistance and capacitance represent the frictional force and the mass of the particle, respectively. For the case when $I < I_c$, the particle is confined to a local minimum in the potential, oscillating with plasma frequency ω_p such that the time averaged DC voltage is zero. When $I > I_c$, the minimum disappears and the phase difference over the junction evolves with time resulting in a voltage over the junction. Once I is reduced below I_c the minima in the potential reappear and the particle becomes trapped again. The point at which the particle is confined is determined by its inertia, defined by the capacitance and resistance. This is encapsulated by the Stewart-McCumber parameter ([45], [46]), βc, which describes the damping of the junction.

$$\beta_c \equiv \frac{2\pi}{\Phi_0} I_c R^2 C. \tag{2.2.10}$$

In the over-damped limit, the inertia of the particle can be considered to be negligible corresponding to a negligible junction capacitance. As such the particle gets trapped instantly once the bias has been reduced below I_c and the resulting I/V characteristics are non-hysteretic. In the under-damped limit, the inertia of the particle is not negligible corresponding to a high junction capacitance, such that bias must be reduced below I_c in order for the particle to be confined and the zero voltage state recovered. As such an under-damped junction's IV characteristics are hysteretic.

2.2.4 The RF SQUID

An equivalent circuit for an RF SQUID (superconducting quantum interference devices) using the RCSJ model is shown in Fig. 2.25.

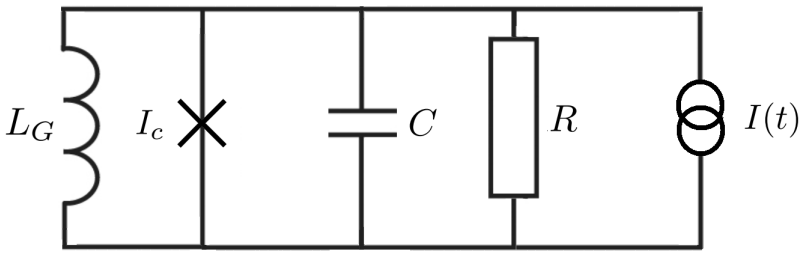

Figure 2.25: RF SQUID equivalent circuit. In this case the SQUID loop is represented by geometric inductance L_G.

The RF SQUID is formed by a superconducting loop, of geometric inductance L_G, interrupted by a single Josephson junction. Due to quantisation of the magnetic flux Φ threading the superconducting loop, the phase over the junction is given as

$$2\pi n \pm \delta = 2\pi \frac{\Phi}{\Phi_0} \tag{2.2.11}$$

The total flux in the loop must also consider the contribution of a circulating current I

$$\Phi = \Phi_{ext} - L_G I \tag{2.2.12}$$

A circulating current is induced by a phase drop over the junction, such that

$$\Phi = \Phi_{ext} - L_G I_c \sin\delta \tag{2.2.13}$$

Using Equation 2.2.11 this can be written in terms of δ as

$$\delta = \delta_{ext} - \frac{2\pi L_G}{\Phi_0} I_c \sin\delta \tag{2.2.14}$$

$$= \delta_{ext} - \beta_L \sin\delta \tag{2.2.15}$$

where β_L defines the SQUID screening parameter

$$\beta_L \equiv \frac{2\pi L_G I_c}{\Phi_0} \tag{2.2.16}$$

In this configuration the current-phase relation of the RF SQUID is dependent on the external flux threading the loop and the geometric inductance L_G. The total inductance L is given as

$$L = \frac{L_G}{1 + \beta_L \cos\delta} \tag{2.2.17}$$

The value of β_L is critical to determining the behaviour of the RF SQUID. In the case when $\beta_L < 1$, the total flux in the SQUID, Φ, is a single-valued function of the external flux Φ_{ext}. However, for $\beta_L > 1$, $\Phi(\Phi_{ext})$ becomes hysteretic, such that the Φ can take two values. In this hysteretic state the SQUID makes transitions between the two stable states dissipating energy at a rate that is periodic in Φ [47].

2.2.5 Non-linearity of the Josephson junction

The non-linearity of the current-phase relation of a Josephson junction for a small phase difference δ can be simply illustrated via a Taylor expansion of Equation 2.2.2

$$\frac{I_J}{I_c} = \delta - \frac{\delta^3}{6} + \frac{\delta^5}{120} - .... \tag{2.2.18}$$

with a similarly non-linear current dependent inductance L_J, which can be approximated from Equation 2.2.6 as

$$L_J(I) = \frac{\Phi_0}{2\pi I_c}\left[1 + \frac{1}{2}\frac{I_J^2}{I_c^2}\right] \tag{2.2.19}$$

Embedding a transmission line with Josephson junctions, shown in Fig. 2.26, results in a non-linear medium where the propagating waves are subject to parametric interactions mediated by the non-linear inductance of the Josephson junctions. The effective strength of the non-linearity in this configuration is determined by I_c. If I_c is low, a non-linear response can be observed even for very low currents (low drive powers).

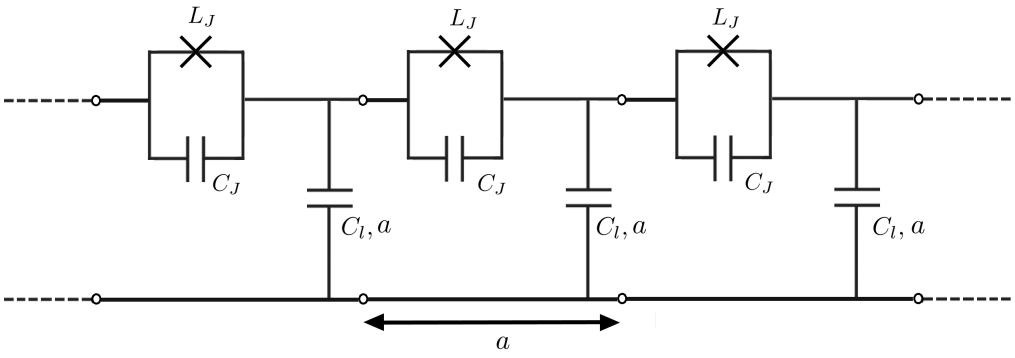

Figure 2.26: Josephson junction embedded transmission line. The shunt resistance of the junction and the inductance of the TL has been neglected. The length of each "cell" (a) represents the length of the individual Josephson components integrated into the transmission line. C_l is the capacitance per unit length of the TL.

This non-linear transmission line is analogous to a Kerr medium in the field of optics, characterised by the cubic dependence of a centrosymmetric non-linearity. A DC SQUID, similar to the RF SQUID where a superconducting loop is in this case is interrupted by two Josephson junctions, can be used to realise an equivalent centrosymmetric non-linearity.

The DC SQUID has many practical benefits as a non-linear circuit element allowing for the inductance to be controlled via an external flux. For current purposes we will focus on the Josephson junction embedded transmission line, the DC SQUID will be discussed in more detail in Chapter 3.

By applying an appropriate bias to the junction the order and magnitude of the non-linearity presented by the current-phase relation can be modified. This is achievable with the RF SQUID geometry previously discussed. If we consider the case that a DC flux is applied to the SQUID loop such that there is a constant current bias I_0 over the junction, where $I_0 < I_c$, this results in a DC phase drop over the junction given by $\delta_0 = \arcsin(I_0/I_C)$. Considering a second small AC phase difference x representative of small oscillation of δ around δ_0, the total phase difference over the junction is given as the sum of the DC and AC components $\delta = \delta_0 + x$, the current-phase relation can be expanded into

$$\frac{I}{I_c} = \sin\delta = \sin(\delta_0 + x) = \sin\delta_0 \cos x + \cos\delta_0 \sin x \tag{2.2.20}$$

Once again using a Taylor expansion in the limit of $x << 1$, and in this case truncating the series expansion for higher orders, the current-phase relation in this situation can be given as

$$\frac{I}{I_c} \approx \sin\delta_0(1 - \frac{x^2}{2}) + \cos\delta_0(x - \frac{x^3}{6}) \tag{2.2.21}$$

The current-phase relation has now been modified by the bias such as to have quadratic as well as cubic non-linear terms, allowing for the manifestation of phenomena associated with the odd Kerr non-linearity, but now also interactions available due to the presence of the even non-linear terms. This can be realised in a RF SQUID transmission line, shown in Fig. 2.27.

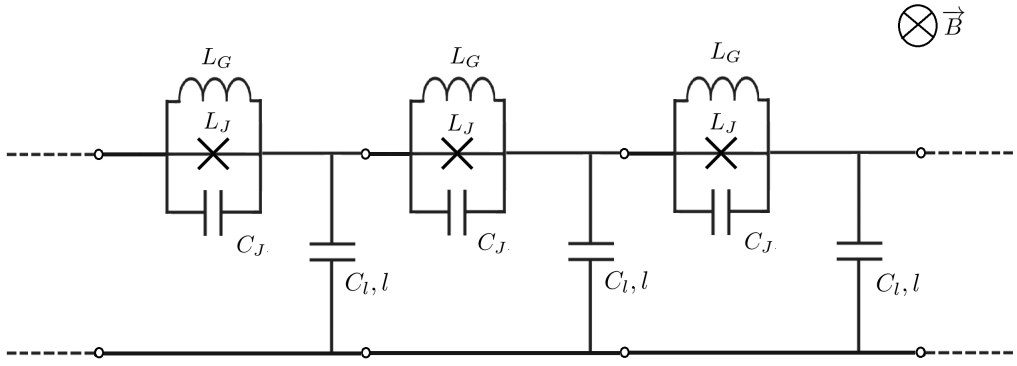

Figure 2.27: RF SQUID transmission line, where the junctions have been modified with a geometric inductance to allow there current-phase relation to be controlled by an external flux bias.

Kinetic inductance

So far we have considered imparting non-linearity to a transmission line medium via discrete Josephson elements. However, as discussed in Section 2.1.2.2, the large relaxation times of Cooper pairs in superconductor materials can result in a significant kinetic contribution to the total inductance. The magnitude of the contribution is related to the London penetration depth λ of the superconductor used. As such this needs to be taken into consideration when calculating the total inductance of a CPW TL/resonator. Another consequence of this kinetic inductance is its non-linear dependence on current I,

$$L_k(I) = L_0\Big[1 + \frac{I^2}{I_*^2}\Big] \tag{2.2.22}$$

where I_* is a scaling parameter which is of order the critical current of the superconducting material and $L_0 \approx \hbar R_n/\pi\Delta$ [48]. As such SCPW's are innately a non-linear medium regardless of the addition of a discrete non-linear element, where the magnitude of the non-linearity is dependent on the superconductor. Devices employing materials such as NbTiN, characterised by a high normal state resistance have been developed to manifest a relatively large non-linear response. Devices employing these materials have found applications as kinetic inductance detectors [49], and parametric amplifiers [50] exploiting non-linear phenomena, that will be discussed in the next section.

Generally the non-linearity is weak in comparison with Josephson junctions, such that a significantly higher current (corresponding to higher power signals propagating through the TL) must be used to achieve a sufficient non-linear response. The discrete nature of Josephson junctions also allows their implementation to be better defined and controllable. As such we will remain focused on the Josephson junction as our default non-linear circuit element. However, when measuring and analysing the response of non-linear SCPW's, detailed in Chapter 6 and 7, the non-linearity owing to kinetic inductance must be considered when working at higher drive powers.

2.3 Wave mixing and associated phenomena in non-linear media

Over the next few sections we will discuss wave mixing via a non-linear media in the context of non-linear optics in order to develop an intuitive understanding of what governs the processes and stipulates the mixed products. Parametric interactions between electromagnetic waves propagating in a non-linear medium are commonly exploited for practical applications in both the microwave and optical frequency range and underpin the operation of JPA's and TWJPA's. Non-linear optics is a wide field, subsequently we will only cover what is necessary to understand the most prominent and relevant parametric interactions, primarily three- and four-wave mixing (TWM and FWM). I refer the reader to [51], [52] for a wider comprehensive account of this fascinating field.

In the case of non-linear optics, parametric interactions originate from a non-linear relationship between an applied field, $\mathcal{E}$, and the medium's dipole moment, p, per unit volume, the polarisation density, $P = Np$, where N is the number density of dipole moments. Considering a non-dispersive, homogeneous and isotropic dielectric medium, given the applied electric field strength is much smaller than the electric field bounding electrons to the constituent atoms/molecules, then the polarisation density, P, can be expanded as a Taylor series around $\mathcal{E} = 0$ as follows

$$P = a_1\mathcal{E} + \frac{1}{2}a_2\mathcal{E}^2 + \frac{1}{6}a_3\mathcal{E}^3 \tag{2.3.1}$$

where the coefficients a_1, a_2 and a_3 are the first, second and third derivatives of P at $\mathcal{E} = 0$. Adopting the convention set out in [53], this is recast as

$$P = \epsilon_0\chi^{(1)}\mathcal{E} + 2d\mathcal{E}^2 + 4\chi^{(3)}\mathcal{E}^3 + ... \tag{2.3.2}$$

where $\chi^{(1)}$ is the linear susceptibility, $d = \frac{1}{4}P^{(2)}$ represents the strength of the quadratic non-linearity and $\chi^{(3)} = \frac{1}{24}P^{(3)}$ the cubic. The first term of the expansion is representative of linear optics in which the polarisation density can be regarded as linear function of the applied field. In the case of a small applied field, such that the higher terms can be neglected, the polarisation density is described by the linear dipole approximation. In this case if we consider a sinusoidal applied field, the polarisation density oscillates at the same frequency as the incident light.

However, if the applied field is large enough to strongly displace the electrons from their equilibrium positions, but not strong enough to ionize the molecule, a non-linear response can be observed corresponding to the higher terms in the series expansion, constituting a non-linear restoring force. The non-linear relationship will allow terms in the polarisation density to oscillate at frequencies other than the applied field. This suggests a coupling and thus mixing of the modes via the non-linear medium, where the nature of the interaction

will depend on the order of the non-linearity and the satisfaction of frequency and phase (energy and momentum) conditions applying to the mixed waves and their products. These non-linear terms are responsible for a number of phenomena, for example the $\chi^{(2)}$ (quadratic) term is responsible for second harmonic generation, optical rectification, the electro-optic effect and three-wave mixing. Whereas the $\chi^{(3)}$ (cubic) term is responsible for third harmonic generation, the optical Kerr effect, self phase modulation, self focusing, cross phase modulation and four-wave mixing.

2.3.1 Non-linear wave equation

The propagation of light in a homogeneous and isotropic dielectric medium can be described by the following wave equation derived from Maxwell's equations

$$\bigtriangledown^2 \mathcal{E} - \frac{1}{{c_0}^2}\frac{\partial^2 \mathcal{E}}{\partial t^2} = \mu_0 \frac{\partial^2 P}{\partial t^2} \tag{2.3.3}$$

The isotropy results in the vectors P and $\mathcal{E}$ always being parallel to each other such that they can be compared on a component-by-component basis. The polarisation density can be expressed as the sum of the linear and non-linear terms

$$P = \epsilon\chi\mathcal{E} + P_{NL} \tag{2.3.4}$$

where

$$P_{NL} = 2d\mathcal{E}^2 + 4\chi^{(3)}\mathcal{E}^3 + ... \tag{2.3.5}$$

Differentiating Equation 2.3.4 and substituting into Equation (2.3.3) gives

$$\bigtriangledown^2 \mathcal{E} - \frac{1}{c}\frac{\partial^2 \mathcal{E}}{\partial t^2} = -S \tag{2.3.6}$$

where

$$\mathcal{S}(\mathcal{E}) = -\mu_0 \frac{\partial^2 P_{NL}}{\partial t^2} \tag{2.3.7}$$

$\mathcal{S}(\mathcal{E})$ represents a source radiating in a linear medium related to the non-linear response of the polarisation density as a function of the applied field. Coupled wave theory can be employed to derive linear coupled partial differential equations using Equation 2.3.6 which govern the interaction of waves propagating through a non-linear medium. This will be discussed further in Section 2.3.5. Before doing so it is instructive to use another approach, know as the Born approximation, to qualitatively describe and define a few relevant phenomena originating from the non-linear interaction between the applied field and the medium.

2.3.2 The Born approximation

Considering a simplistic case where an applied field $\mathcal{E}_0$ interacts with a non-linear medium, as shown in Fig. 2.28. The applied field can consist of a single wave or several monochromatic waves of different frequencies. The source term $S(\mathcal{E}_0)$ given in Equation 2.3.7 is a function of the applied field and as it oscillates will subsequently radiate an optical field $\mathcal{E}_1$, where the non-linear relation in the polarisation density will lead to generation of components in $\mathcal{E}_1$ at frequencies not present in the incident field $\mathcal{E}_0$. This description is known as the first Born approximation where light propagating in a non-linear medium is described by a scattering process in which the incident field is scattered by the medium. It should be noted that this is an iterative process, $\mathcal{E}_1$ will also have a corresponding source $S(\mathcal{E}_1)$ as it continues to propagate through the medium, radiating a field $\mathcal{E}_2$ (the second Born approximation).

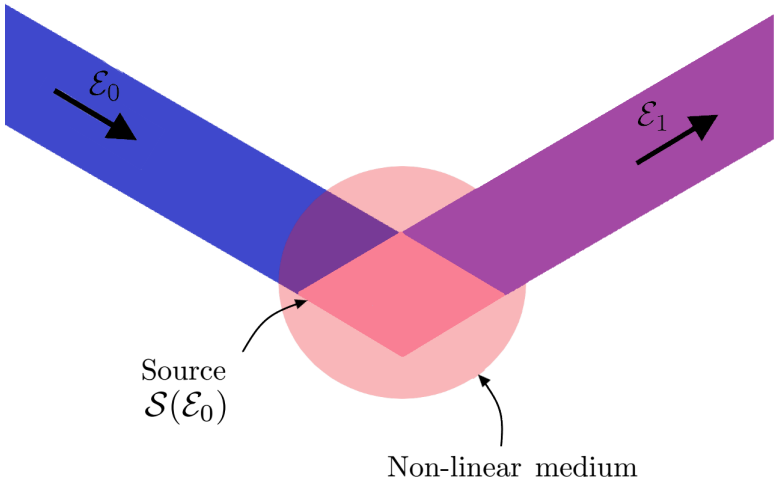

Figure 2.28: Incident field $\mathcal{E}_0$, scatters off the non-linear medium, which radiates a field $\mathcal{E}_1$ containing components of frequency not present in the original field $\mathcal{E}_0$. Adapted from [52].

The first Born approximation holds in the limit of a weak non-linearity. This approximation allows wave mixing to be conveniently characterised. In the following sections we will consider a specific applied field $\mathcal{E}_0$ and calculate the corresponding P_{NL} and source term $S(\mathcal{E}_0)$. Inspection of the oscillating components of the source term will allow for the identification of the conditions (frequency and phase) associated with different mixing regimes, dependent on the incident field and order of the non-linearity being considered.

2.3.3 Second order non-linear media

For the time being we will completely neglect the odd (cubic) terms in P_{NL} and consider only a quadratic term truncating the higher even orders given we are assuming a weakly

non-linear medium.

$$P_{NL} = 2d\mathcal{E}^2 \tag{2.3.8}$$

Considering a harmonic electric field of angular frequency ω and complex amplitude $E(\omega)$

$$\mathcal{E}(t) = Re\{E(\omega)exp(i\omega t)\} = \frac{1}{2}[E(\omega)exp(i\omega t) + E^*(\omega)exp(-i\omega t)] \tag{2.3.9}$$

$$P_{NL} = d[E(\omega)^2 exp(i2\omega t) + 2E(\omega)E^*(\omega) + E^*(\omega)^2 exp(i2\omega t)] \tag{2.3.10}$$

which can be rewriten as

$$P_{NL} = P_{NL}(0) + Re\{P_{NL}(2\omega)exp(i2\omega t)\} \tag{2.3.11}$$

The resulting non-linear polarisation density has a steady state (DC) term and a term oscillating at twice the frequency of the incident field 2ω. The steady state component corresponds to a phenomenon know as the electro-optic effect, exploited in optical rectifiers. If we inspect the corresponding source $\mathcal{S}$ given by Equation 2.3.7 we find a component oscillating with frequency 2ω corresponding to a source radiating at a frequency 2ω with a complex amplitude $S(2\omega) = 4\mu_0\omega^2 dE(\omega)^2$. This effect is commonly referred to as second harmonic generation.

2.3.3.1 Three-wave mixing

Considering the case where the applied field has two harmonic components of frequencies ω_1 and ω_2, such that

$$\mathcal{E}(t) = Re\{E(\omega_1)exp(i\omega_1 t) + E(\omega_2)exp(i\omega_2 t)\} \tag{2.3.12}$$

P_{NL} and the corresponding source $S(\mathcal{E})$ now contains terms oscillating at frequencies: 0, $2\omega_1$, $2\omega_2$, $\omega_1 + \omega_2$ and $\omega_1 - \omega_2$. Once again we have a DC component and components corresponding to the generation of second harmonics $2\omega_1$ and $2\omega_2$, however, we also now have components in P_{NL} oscillating at sum and difference frequency of the respective harmonic components of $\mathcal{E}$, with amplitudes

$$P_{NL}(\omega_1 + \omega_2) = 2dE(\omega_1)E(\omega_2) \tag{2.3.13}$$

$$P_{NL}(\omega_1 - \omega_2) = 2dE(\omega_1)E^*(\omega_2) \tag{2.3.14}$$

This can be interpreted as the second order non-linear medium mixing two waves of different frequencies and generating a third wave at a difference or sum frequency, referred to as a sum or difference frequency conversion. Although there are several possible

harmonic components in the source term, not all will be present in the scattered field as the generated waves are required to satisfy additional frequencies and phase matching conditions. Consider the component of the polarisation density oscillating at the sum frequency of the incident waves, with complex amplitude given in Equation 2.3.13. Given waves 1 and 2 are plane waves with frequencies ω_1 and ω_2 and wave vectors $\overrightarrow{k_1}$ and $\overrightarrow{k_2}$, respectively, such that

$$E(\omega_1) = A_1 exp(-i\overrightarrow{k_1} \cdot \overrightarrow{r}) \tag{2.3.15}$$

$$E(\omega_2) = A_2 exp(-i\overrightarrow{k_2} \cdot \overrightarrow{r}) \tag{2.3.16}$$

then the complex amplitude of the component of P_{NL} oscillating at $\omega_1+\omega_2$ can be rewritten as

$$P_{NL}(\omega_3) = 2dA_1A_2 exp(-i\overrightarrow{k_3} \cdot \overrightarrow{r}) \tag{2.3.17}$$

where

$$\omega_1 + \omega_2 = \omega_3 \tag{2.3.18}$$

defines the frequency matching condition, and

$$\overrightarrow{k_1} + \overrightarrow{k_2} = \overrightarrow{k_3} \tag{2.3.19}$$

defines the phase matching condition. The medium acts as a source at frequency ω_3 (wave 3) with a complex amplitude proportional to $exp(-i\overrightarrow{k_3} \cdot \overrightarrow{r})$, where the frequency and phase conditions ensure both temporal and spatial matching of the three waves for sustained interaction. Products of mixing that do not satisfy these conditions will not be sustained by the medium. This also means that the process does not stop at the generation of the 3rd wave of frequency ω_3. Given wave 3 and wave 1 satisfy the condition $\omega_3 - \omega_1 = \omega_2$ they can combine to radiate at their difference frequency ω_2. Similar $\omega_3 - \omega_2 = \omega_1$ such that wave 3 and wave 2 can interact to generate wave 1. Thus, there is a mutual coupling between each pair of waves interacting resulting in a response at the third frequency determined by the frequency and phase matching conditions. This process is referred to as non-degenerate three-wave mixing (TWM), illustrated in Fig. 2.29. We have already encountered the degenerate situation in the form of second harmonic generation where $\omega_2 = 2\omega_1$ in this case the condition $\omega_2 - \omega_1 = \omega_1$ is also fulfilled such that the difference frequency is also reinforcing ω_1. TWM has obvious application in the context of amplification where a "signal" wave can be reinforced with a "pump" wave.

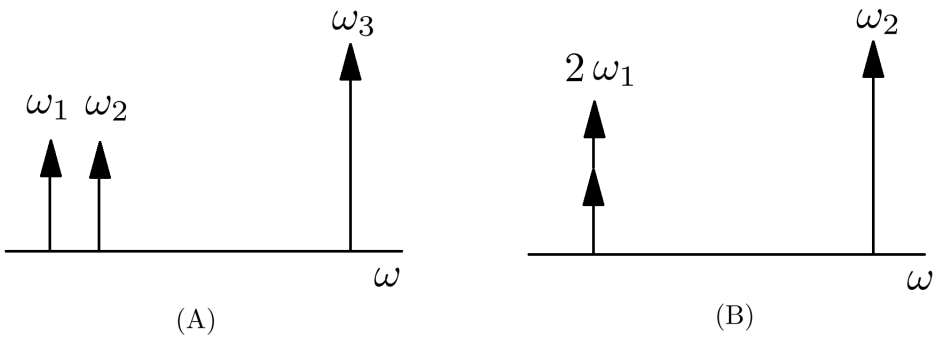

Figure 2.29: (A) non-degenerate TWM (B) degenerate TWM (second harmonic generation)

Wave mixing as a photon interaction process

TWM can be regarded as a photon interaction process. The aforementioned example where two waves (ω_1 and ω_2) generate a third wave (ω_3) can be thought of as two photons of frequencies ω_1 and ω_2 being annihilated and photon of higher frequency ω_3 being created, illustrated in Fig. 2.30.

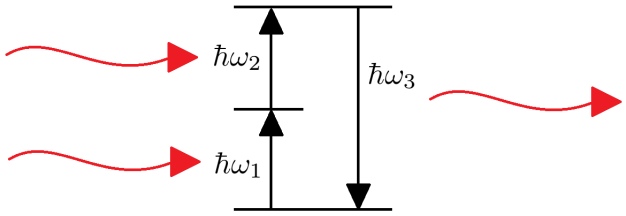

Figure 2.30: Degenerate TWM as a photon interaction process. Two photons are "up converted" to a photon of twice the frequency via the non-linear medium.

Regardless of the specific waves being mixed conservation of energy and momentum is required, in this case

$$\hbar\omega_1 + \hbar\omega_2 = \hbar\omega_3 \tag{2.3.20}$$

$$\hbar\overrightarrow{k_1} + \hbar\overrightarrow{k_2} = \hbar\overrightarrow{k_3} \tag{2.3.21}$$

equivalent to what we have already seen. The photon number must also be conserved. This invariant relation is often expressed in terms of the photon flux densities of the three interacting waves ϕ_1, ϕ_2 and ϕ_3 ($[\frac{photons}{m^2 s}]$). Considering a cylindrical interaction volume of unit area and incremental length Δz then

$$\frac{d\phi_1}{dz} = \frac{d\phi_2}{dz} = -\frac{d\phi_3}{dz} \tag{2.3.22}$$

Recasting this relation in terms of the respective intensities of the waves ($I_i = \hbar\omega_i\phi_i$) gives the Manley-Rowe relation,

$$\frac{d}{dz}\frac{I_1}{\omega_1} = \frac{d}{dz}\frac{I_2}{\omega_2} = -\frac{d}{dz}\frac{I_3}{\omega_3} \tag{2.3.23}$$

Phase mismatch

In order to illustrate the importance of maintaining the phase matching conditions in a practical device, we will consider a slight phase mismatch such that

$$\overrightarrow{\Delta k} = \overrightarrow{k_3} - \overrightarrow{k_2} - \overrightarrow{k_1} \neq 0 \tag{2.3.24}$$

In this case the complex amplitude of the source at the sum frequency $\omega_3 = \omega_1 + \omega_2$ is modified as follows

$$P_{NL}(\omega_3) = 2dA_1A_2exp(-i\overrightarrow{k_3}\cdot\overrightarrow{r})exp(-i\overrightarrow{\Delta k}\cdot\overrightarrow{r}) \tag{2.3.25}$$

The intensity of the third wave, I_3, is proportional to the squared integral of the source amplitude over the length of the interaction with the non-linear medium. Considering the one dimensional case within an interaction length L

$$I_3 \propto |\int_0^L exp(i\overrightarrow{\Delta k}\cdot\overrightarrow{r})dz|^2 = L^2\mathrm{sinc}^2(\frac{\Delta kL}{2\pi}) \tag{2.3.26}$$

This constitutes a reduction factor, where for a non-zero phase mismatch I_3 is reduced depending on the magnitude of the phase mismatch and also the interaction length. For a long interaction length, such as the case of a practical device, strict phase matching of the coupled waves must be maintained throughout the course of their interaction. Although a phase mismatch suggests a violation of the conservation of momentum such that the wave mixing should instantly stop, it is tolerated thanks to the wave-vector uncertainty principle $\Delta k \propto \frac{1}{L}$ associated with confinement of the waves within the interaction length L corresponding to a momentum uncertainty $\triangle p = \hbar\triangle k \propto \frac{1}{L}$ [52].

2.3.4 Third order non-linear media

We will return to the case of a quadratic non-linearity in the context of coupled wave theory in Section 2.3.5. However, beforehand it is constructive to summarise the phenomena associated with a purely cubic non-linear medium using the Born approximation. Neglecting the even terms and truncating the series for higher orders we will now consider a P_{NL} given as

$$P_{NL} = 4\chi^{(3)}\mathcal{E}^3 \tag{2.3.27}$$

This is practically realised in centrosymmetric material which exhibits inversion symmetry, such that the properties of the medium are not altered by the transformation $\overrightarrow{r} \rightarrow -\overrightarrow{r}$.

In these materials $P(\mathcal{E})$ must have odd symmetry, so the reversal of applied field results in the reversal of polarisation density without any other change. Materials exhibiting this characteristic are often refereed to as Kerr media after J. Kerr, who observed a change in the refractive index of organic liquids and glasses in the presence of an electric field known as the optical Kerr effect. This is one of several interesting and important phenomena associated with the cubic non-linearity, including self and cross phase modulation (SPM and CPM, respectively), where the phase of waves propagating in the Kerr medium is dependent on their power (SPM) or the power of other waves propagating through the medium simultaneously (CPM). Although we will not dwell on these phenomena their effects are a prominent consideration in practical devices.

In the next section we will introduce four-wave mixing (FWM), a commonly used mixing regime for amplification as we saw with the TWM case. A similar phase matching condition will be defined which must be met over the course of the interaction length/volume for a sustained and significant coupling of the waves in the media. SPM and CPM complicate this as the phase relation of the coupled waves become dependent on the power/intensity of the respective harmonic components making up the applied field. These effects often lead to additional engineering of FWM devices to compensate for phase modulation over the course of the interaction length.

2.3.4.1 Four-wave mixing

Just as in the case of three-wave mixing, we will consider an incident field $\mathcal{E}(t)$, in this case comprising three harmonic components at frequencies ω_1, ω_2 and ω_3

$$\mathcal{E}(t) = Re\{E(\omega_1)exp(i\omega_1 t) + E(\omega_2)exp(i\omega_2 t) + E(\omega_3)exp(i\omega_3 t)\} \tag{2.3.28}$$

conveniently expressed as

$$\mathcal{E}(t) = \sum_{q=\pm1,\pm2,\pm3} \frac{1}{2} E_q(\omega_q)exp(i\omega_q t) \tag{2.3.29}$$

where $\omega_{-q} = -\omega_q$ and $E_{-q} = E_q^*$. Substituting into P_{NL}

$$P_{NL}(t) = \frac{1}{8}\chi^{(3)} \sum_{q,r,l=\pm1,\pm2,\pm3} E(\omega_q)E(\omega_r)E(\omega_l)exp[i(\omega_q + \omega_r + \omega_l)t] \tag{2.3.30}$$

The resulting polarisation density contains many terms relating to permutations of the sums and difference frequencies of the harmonic components of the applied field (ω_1, ω_2, ω_2). Considering the component $P_{NL}(\omega_1 + \omega_2 - \omega_3)$ with complex amplitude

$$P_{NL}(\omega_1 + \omega_2 - \omega_3) = 6\chi^{(3)}E(\omega_1)E(\omega_2)E^*(\omega_3) \tag{2.3.31}$$

This term corresponds to three waves mixing to give a fourth wave given the condition $\omega_1 + \omega_2 - \omega_3 = \omega_4$ is met. This relation constitutes the frequency matching condition of non-degenerate four-wave mixing

$$\omega_1 + \omega_2 = \omega_3 + \omega_4. \tag{2.3.32}$$

Similar to the TWM case, a phase matching condition can also be defined

$$\overrightarrow{k_1} + \overrightarrow{k_2} = \overrightarrow{k_3} + \overrightarrow{k_4}. \tag{2.3.33}$$

A commonly encountered regime of FWM is the degenerate case where two of the waves are the same $\omega_3 = \omega_4 = \omega_0$ such that the frequency matching condition is given as

$$\omega_1 + \omega_2 = 2\omega_0 \tag{2.3.34}$$

with corresponding phase matching condition

$$\overrightarrow{k_1} + \overrightarrow{k_2} = 2\overrightarrow{k_0} \tag{2.3.35}$$

Degenerate FWM is often exploited in the context of parametric amplification.

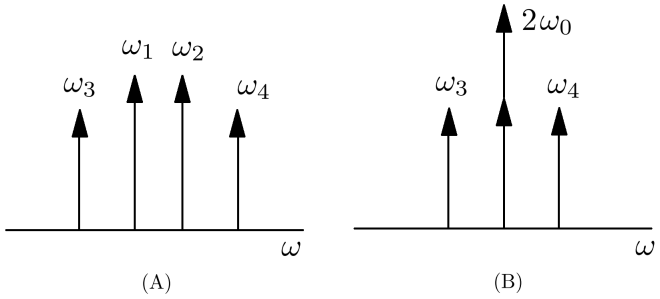

Figure 2.31: (A) Non-degenerate FWM; (B) Degenerate FWM

2.3.5 Coupled wave theory

All of the mixing phenomena discussed so far present a range of possible applications. For current purpose we will mainly focus on amplification. Both the aforementioned TWM and FWM regimes allow for coupling of multiple harmonic components of an applied field, transferring energy between them. In order to understand this further, we will employ coupled wave theory in order to derive the relations that govern energy transfer between waves interacting in a parametric non-linearity. This method can be used to describe TWM and FWM, however, for similarity we will look at the TWM case considering a purely quadratic non-linear polarisation density P_{NL} given by

$$P_{NL} = 2d\mathcal{E}^2. \tag{2.3.36}$$

In this case $\mathcal{E}(t)$ is chosen to be a superposition of three waves of angular frequencies ω_1, ω_2, and ω_3, with complex amplitudes E_1, E_2, and E_3

$$\mathcal{E}(t) = \Sigma_{q=\pm1,\pm2,\pm3}\frac{1}{2}E_1(\omega_q)exp[i\omega_q t] \tag{2.3.37}$$

where once again $\omega_{-q} = -\omega_q$ and $E(\omega_{-q}) = E^*(\omega_q)$. The polarisation density is given by

$$P_{NL}(t) = \frac{1}{2}d\sum_{q,r=\pm1,\pm2,\pm3} E_q E_r exp[i(\omega_q + \omega_r)t] \tag{2.3.38}$$

which corresponds to a radiating source

$$\mathcal{S} = \mu_0\frac{\partial^2 P_{NL}}{\partial t^2} = \frac{1}{2}\mu_0 d\sum_{q,r=\pm1,\pm2,\pm3}(\omega_q + \omega_r)^2 E_q E_r exp[i(\omega_q + \omega_r)t]. \tag{2.3.39}$$

As before, the components of $\mathcal{S}$ contain frequencies of the sums and differences of the original frequencies ω_1, ω_2, and ω_3 in the applied field. The expressions for $\mathcal{E}(t)$ and $\mathcal{S}$ can be substituted into the previously defined wave equation for a non-dispersive, homogeneous and isotropic medium (Equation 2.3.6). What results is a very long differential equation, however, given ω_1, ω_2, and ω_3 are distinct, it is possible to separate the equations into three time-independent differential equations (Helmholtz equations) by equating the terms of equivalent frequencies either side and grouping them with an associated source

$$(\nabla^2 + k_1^2)E_1 = -\mathcal{S}_1, \tag{2.3.40}$$

$$(\nabla^2 + k_2^2)E_2 = -\mathcal{S}_2, \tag{2.3.41}$$

$$(\nabla^2 + k_3^2)E_3 = -\mathcal{S}_3. \tag{2.3.42}$$

The associated sources $\mathcal{S}_i$ $(i = 1, 2, 3)$ each represent a component of $\mathcal{S}$ oscillating with frequency ω_i. Considering the case where the frequency of the three waves in the medium is commensurate such that $\omega_1 + \omega_2 = \omega_3$ then inspecting the components of the radiating source $\mathcal{S}$ given by Equation 2.3.39 allows the associated sources to be determined as

$$\mathcal{S}_1 = 2\mu_0 d\omega_1^2 E_3 E_2^*, \tag{2.3.43}$$

$$\mathcal{S}_2 = 2\mu_0 d\omega_2^2 E_3 E_1^*, \tag{2.3.44}$$

$$\mathcal{S}_3 = 2\mu_0 d\omega_3^2 E_1 E_2. \tag{2.3.45}$$

Substituting into the Helmholtz equations results in the following coupled equations

$$(\nabla^2 + k_1^2)E_1 = -2\mu_0 d\omega_1^2 E_3 E_2^*, \tag{2.3.46}$$

$$(\nabla^2 + k_2^2)E_2 = -2\mu_0 d\omega_2^2 E_3 E_1^*, \tag{2.3.47}$$

$$(\nabla^2 + k_3^2)E_3 = -2\mu_0 d\omega_3^2 E_1 E_2. \tag{2.3.48}$$

These equations and the corresponding source terms illustrate the entwined nature of the waves propagating in the non-linear medium, where the source of one wave is dependent on the electric field of the two other waves. Once again photon number must be conserved. As such is it convenient to redefine the equations in terms of photon flux densities. In this case we will assume the three waves are plane waves travelling in the z direction with complex amplitudes

$$E_i = A_i exp(-ik_i z) \tag{2.3.49}$$

where A_i is a complex envelope and wave-number $k_i = \omega_i/c$. It is common to normalise the complex envelopes for convenience using a variable $a_i = A_i(2\eta\hbar\omega_i)^{-1/2}$ where $\eta = \dfrac{(\mu_0/\epsilon_0)^{1/2}}{n}$ is the impedance of the medium, giving

$$E_i = a_i\sqrt{2\eta\hbar\omega_i}exp(-ik_i z) \tag{2.3.50}$$

The respective intensities of the three waves can be given as $I_i = \dfrac{|E_i|^2}{2\eta}$ which can be used to find the corresponding photon flux densities

$$\phi_i = \frac{I_i}{\hbar\omega_i} = |a_i|^2 \tag{2.3.51}$$

Over the course of the interaction length the coupling results in changes in the waves and the corresponding complex envelopes a_i and thus is a function of the position in the interaction length $a_i(z)$. If the interaction is weak the slowly varying envelope approximation can be used. In this case $\dfrac{d^2a_i}{dz^2}$ is neglected relative to $k_i\dfrac{da_i}{dz}$ and given that

$$(\nabla^2 + k_i^2)[a_i exp(-ik_i z)] \approx -i2k_i\frac{da_i}{dz}exp(-ik_i z) \tag{2.3.52}$$

the previous Helmholtzs equations can be reduced to a much simpler and convenient form, in this case generalised for a finite phase mismatch Δk in the respective wave vectors

$$\frac{da_1}{dz} = -iga_2 a_3^* exp(-i\Delta k z) \tag{2.3.53}$$

$$\frac{da_2}{dz} = -iga_3 a_1^* exp(-i\Delta k z) \tag{2.3.54}$$

$$\frac{da_3}{dz} = -iga_1a_2exp(i\Delta kz) \tag{2.3.55}$$

where $g = \sqrt{2\hbar\omega_1\omega_2\omega_3\eta^3d^2}$. These equations are commonly referred to as the three-wave mixing coupled equations. Solving these equations with the appropriate boundary conditions allows several mixing phenomena to be described. To illustrate this we will briefly cover a few relevant examples.

Example 1: Degenerate parametric amplification

As previously discussed, the degenerate case of three-wave mixing results in second harmonic generation. In this case the frequencies of the mixed waves are given as $\omega_1 = \omega_2 = \omega$ and $\omega_3 = 2\omega$, where momentum is conserved such the wave-vectors obey $2\overrightarrow{k}_1 = \overrightarrow{k}_3$. In the absence of a phase mismatch ($\Delta k = 0$), the coupled wave equations (Equations 2.3.53, 2.3.54, 2.3.55), reduce to

$$\frac{da_1}{dz} = -iga_3a_1^* \tag{2.3.56}$$

$$\frac{da_3}{dz} = -i\frac{g}{2}a_1a_1^* \tag{2.3.57}$$

with solutions

$$a_1(z) = a_1(0)\text{sech}(\frac{1}{\sqrt{2}}ga_1(0)z) \tag{2.3.58}$$

$$a_3(z) = -\frac{i}{\sqrt{2}}a_1(0)\tanh(\frac{1}{\sqrt{2}}ga_1(0)z) \tag{2.3.59}$$

which can be recast in terms of the photon flux densities of the waves ($\phi_1(z) = |a_1(z)|^2$), giving

$$\phi_1(z) = \phi_1(0)\text{sech}^2\frac{\gamma z}{2} \tag{2.3.60}$$

$$\phi_3(z) = \frac{1}{2}\phi_1(0)\tanh^2\frac{\gamma z}{2} \tag{2.3.61}$$

Where $\gamma/2 = ga_1(0)/\sqrt{2}$. The solutions are plotted in Fig. 2.32. At the start of the interaction length the amplitude of the second harmonic is zero, over the course of the interaction length the photon flux density of wave 1 reduces as photons are up converted to the frequency of the second harmonic (wave 2).

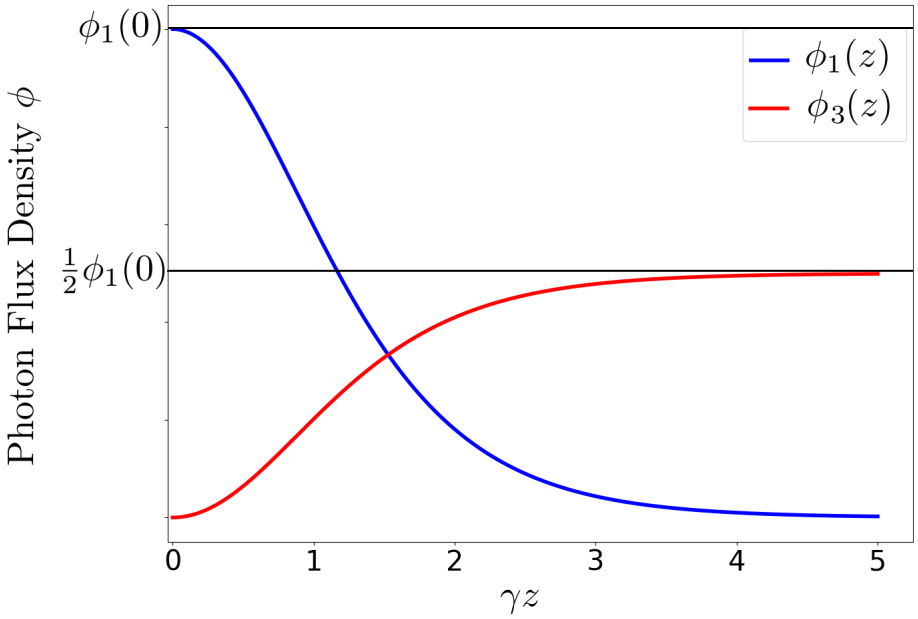

Figure 2.32: Conservation of the total photon number dictates that the sum $\phi_1(z)+\phi_3(z)$ is constant over the interaction length.

Example 2: Non-degenerate parametric amplification

When considering non-degenerate parametric amplification we will conform to a particular terminology for the three waves being mixed. In this situation Wave 1 is the **signal** to be amplified. Wave 2, called the **idler**, is an auxiliary wave created by the interaction process, satisfying the aforementioned frequency and phase matching conditions. Wave 3 will be the **pump** which will supply power to the signal and idler. For simplicity we will assume that the pump is intense enough that it is not significantly depleted over the course of the interaction length, i.e., $a_3(0) \approx a_3(z)$. Once again assuming perfect phase matching ($\Delta k = 0$) the coupled wave equations reduce to

$$\frac{da_1}{dz} = -iga_3(0)a_2^* \tag{2.3.62}$$

$$\frac{da_2}{dz} = -iga_3(0)a_1^* \tag{2.3.63}$$

Given that only the signal is supplied at the input of the interaction length and the initial idler field is zero ($a_2(0) = 0$), solutions can be obtained and recast into the corresponding photon flux densities

$$\phi_1(z) = \phi_1(0)\cosh^2\left(\frac{\gamma}{2}z\right) \tag{2.3.64}$$

$$\phi_2(z) = \phi_1(0)\sinh^2\left(\frac{\gamma}{2}z\right) \tag{2.3.65}$$

where $\gamma = 2ga_3(0)$ is the gain coefficient. The solutions are plotted in Fig. 2.33. As the waves propagate through the medium their respective photon flux density ϕ_1 and ϕ_2 increases, resulting in amplification of the input signal. At some point sufficient power is drawn from the pump and the undepleted pump approximation is no longer valid.

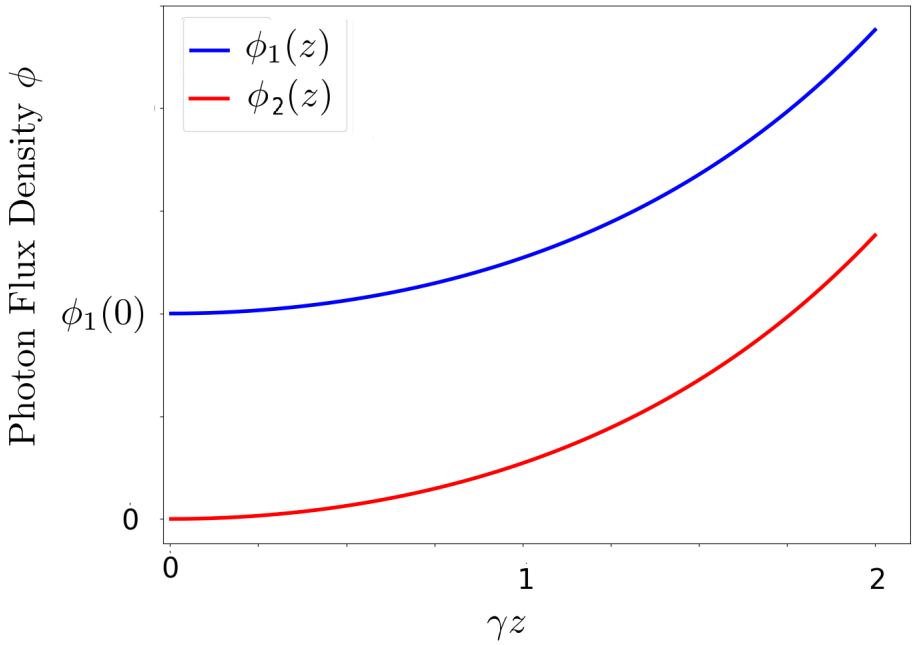

Figure 2.33: Non-degenerate parametric amplification. A signal and pump are incident at the input of the interaction length z, resulting in the generation of an idler over the course of the interaction.

The overall gain G of the parametric amplifier is determined by its length L, given by

$$G = \frac{\phi_1(L)}{\phi_1(0)} = \cosh^2(\frac{\gamma L}{2}) = \frac{(e^{\gamma L/2} + e^{-\gamma L/2})^2}{4} \tag{2.3.66}$$

In the limit of $\gamma L \gg 1$, the gain of the amplifier increases exponentially with γL.

2.3.6 Microwave parametric media

Josephson junction embedded transmission line

The most relevant analogue for a superconducting non-linear microwave medium is the Josephson junction embedded transmission line, depicted in Fig. 2.26. This transmission line configuration has been studied extensively and I refer the reader to [54] for a full treatment of such a transmission line. In its simplest form, neglecting a shunt capacitance on the junction, the wave equation for the medium can be defined by [8]

$$\frac{\partial^2 I}{\partial z^2} - LC\frac{\partial^2}{\partial t^2}\Big(I + \frac{1}{6}\frac{I^3}{I_c^2}\Big) = 0 \tag{2.3.67}$$

where L and C are the total inductance and capacitance to ground of the transmission line, I_c is the critical current of the Josephson junction. This situation is analogous to the case previously studied of light propagating through a non-linear Kerr medium. In this case we will consider the degenerate case of FWM, where $\omega_1 + \omega_2 = 2\omega_0$. Since we will look at this in the context of amplification, it is worth once again defining ω_1 as the signal, frequency ω_s, ω_2 as the idler, frequency ω_i and ω_0 as the pump, frequency ω_p, such that $\omega_s + \omega_i = 2\omega_p$. Similar to previous examples, I can be written as superposition of the three waves propagating with amplitudes A_s,A_i and A_p such that

$$I(t) = \Sigma_{q=\pm s,\pm i,\pm p}\frac{1}{2}A_q exp[i(k_q z - \omega_q t)] \tag{2.3.68}$$

where $\omega_{-q} = -\omega_q$, $k_{-q} = -k_q$ and $A_{-q} = A_q^*$. Using same methods outlined in Section 2.3.5, coupled equations can be derived to describe the change in the amplitudes of the respective waves as they propagate through the medium. Employing the slowly varying envelope approximation and assuming the pump amplitude is much larger than the signal and idler amplitudes, so that we can neglect any upconversion from the signal and idler, the coupled equations in the degenerate FWM case are given as

$$\frac{dA_p}{dz} = \frac{ik_p}{16I_c^2}A_p|A_p^2| \tag{2.3.69}$$

$$\frac{dA_s}{dz} = \frac{ik_p}{16I_c^2}(2A_s|A_p^2|+A_i^*A_p^2e^{-i\Delta kz}) \tag{2.3.70}$$

$$\frac{dA_i}{dz} = \frac{ik_p}{16I_c^2}(2A_i|A_p^2|+A_s^*A_p^2e^{-i\Delta kz}) \tag{2.3.71}$$

The equations are functionally very similar to those derived earlier in the TWM case for a purely quadratic non-linearity (Equations 2.3.53, 2.3.54, 2.3.55), they also contain extra terms related to the phenomena of cross and self phase modulation noted in Section 2.3.4. These terms account for self modulation of the pump with itself ($\propto A_p|A_p^2|$) and the cross phase modulation of the signal and idler with the strong pump ($\propto 2A_{i,s}|A_p^2|$). In the case of a perfect phase match $\Delta k = 0$, similar to the case of TWM discussed in Section 2.3.5, the gain in the limit of a long interaction length scales exponential with the length of the device.

Up to now we have been assuming a continuous transmission line medium (travelling-wave amplifiers), where the length of the line (and strength of the non-linear embedded elements) determine interaction length. SCPW resonators can also be used. In this case a resonator is embedded with Josephson junctions, to constituent a non-linear medium. The interaction length in this case is determined by the quality factor of the resonant mode interacting with the non-linearity. The higher the quality factor the longer the photons in the resonant mode interact with the non-linear medium, increasing the effective

non-linearity. The disadvantage of the resonant architecture is the bandwidth constraint imposed by the cavity, which is a limiting factor in a practical amplifiers and mixers. If bandwidth is not of concern, the resonant approach can yield an extremely reactive non-linear media. Degenerate FWM using a non-linear Josephson medium has been demonstrated both with the use of resonant cavities [55] and continuous transmission lines [8].

RF SQUID embedded transmission line

Although the most predominant Josephson parametric amplifiers make use of the degenerate FWM it does come with its disadvantages. Most glaring is self/cross phase modulation phenomena owing to the cubic order (Kerr) non-linearity. Although not a concern for a resonant geometry, this can have a large impact on a TWPA and often periodic phase matching of the waves propagating in the interaction length must be employed to ensure a significant phase mismatch does not occur. A simpler but ultimately just as important detraction of the degenerate FWM case is the frequency matching condition itself. Fig. 2.31 illustrates this. In the case of FWM the pump is centred around the idler and the signal whereas in the case of TWM the pump is far shifted from the signal. In practical devices this can make a big difference, where using a TWM regime allows the pump to be easily filtered from the output in contrast to the FWM case. This is especially relevant in resonant structure where in the FWM case all components must have frequencies centred around the resonant frequency of the resonator and thus, depending on the quality factor of the mode, the components may require to be closely spaced. Lastly, given TWM relates to the quadratic non-linearity, it presents an innately stronger interaction than achievable with the cubic term due to the quadratic term being a lower order in the expansion with a subsequently larger coefficient.

In order to practically realise TWM an even (quadratic non-linearity) must be employed. As previously mentioned in Section 2.2.5 the Josephson current-phase relation can be modified to include even terms by the use of an RF SQUID geometry where the phase difference over the junction is biased ϕ_{DC} such that a small AC expansion gives,

$$\frac{I}{I_c} = (\beta_L^{-1} + cos\phi_{dc})\phi - \frac{1}{2}\sin\phi_{DC}\phi^2 - \frac{1}{6}\sin\phi_{DC}\phi^3 \tag{2.3.72}$$

This results in both a quadratic and cubic term appearing in the non-linear wave equation for a transmission line embedded with RF SQUIDs. Such a transmission line is proposed by A. Zorin [56], where the magnitude of the non-linear coefficients of the respective quadratic (β) and cubic (γ) terms is a function of the DC phase difference over the junction proportional to the SQUID screening parameter β_L.

$$\beta = \frac{\beta_L}{2}\sin\phi_{DC} \tag{2.3.73}$$

$$\gamma = \frac{\beta_L}{6}\cos\phi_{DC} \tag{2.3.74}$$

The implications of this modification are far reaching, in this case the order of non-linearity exhibited by the medium can be changed by the DC phase drop over the junction ϕ_{DC} typically controlled by an external DC magnetic flux bias threading the RF SQUID loop. The magnitude of the quadratic and cubic component can be tuned to promote the desired mixing regime (TWM, FWM or both simultaneously), this is illustrated in Fig. 2.34.

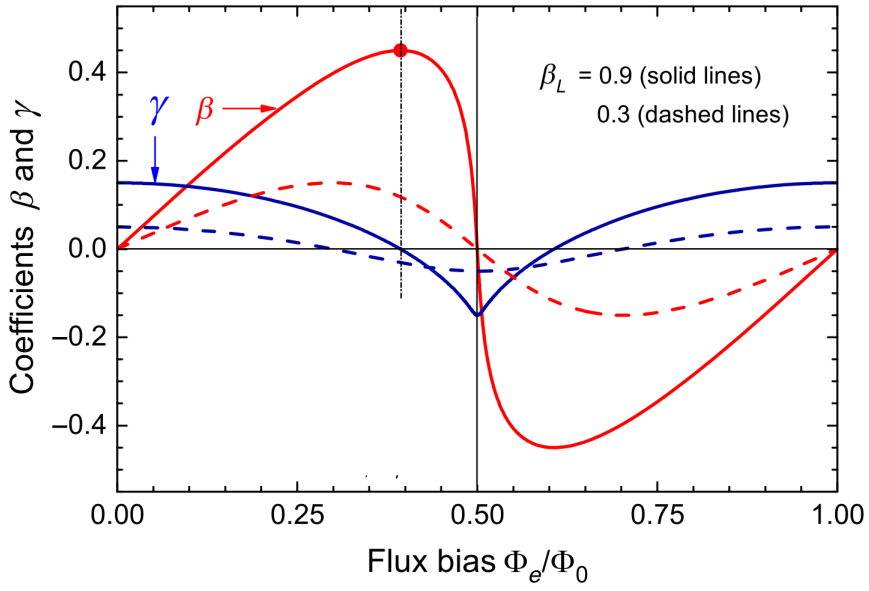

Figure 2.34: Taken from [56]. The flux bias Φ_e/Φ_0 modulates the phase difference over the junction modifying the current-phase relation allowing the magnitude of the non-linear coefficients to be controlled.

Considering the case of non-degenerate TWM where $\omega_1 + \omega_2 = \omega_3$, once again given we are discussing amplification such that it is convenient to rewrite ω_1 as the signal ω_s, ω_2 as the idler ω_i and ω_0 as the pump ω_p such that $\omega_s + \omega_i = \omega_p$. Solving the non-linear wave equation for an RF SQUID transmission line using the slowly varying envelope approximation the coupled wave equations can be defined as

$$\frac{dA_p}{dz} = i\frac{3}{8}\gamma k_p^3 A_p|A_p^2| - \frac{\beta}{2}k_s k_i A_s A_i e^{-i\Delta kz} \tag{2.3.75}$$

$$\frac{dA_s}{dz} = i\frac{3}{4}\gamma k_s k_p^2 A_s|A_p^2| + \frac{\beta}{2}k_i k_p A_i^* A_p e^{i\Delta kz} \tag{2.3.76}$$

$$\frac{dA_i}{dz} = i\frac{3}{4}\gamma k_s k_p^2 A_i|A_p^2| + \frac{\beta}{2}k_s k_p A_s^* A_p e^{i\Delta kz} \tag{2.3.77}$$

These coupled wave equations are in a generalised form not assuming anything about the magnitude of the pump compared to the signal and idler. As seen previously, the

terms originating from the cubic term in the wave equation (terms on RHS $\propto \gamma$) related to cross and self phase modulation of the waves propagating in the medium. The terms originating from the quadratic non-linearity (RHS $\propto \beta$) are representative of the coupled wave equation found in Section 2.3.5. By adjusting the flux threading the SQUID to maximise β and minimise γ effective TWM can be achieved.

The period doubling sample

The concept of the RF SQUID embedded transmission line has a great similarity with a device that will be referred to as the period doubling (PD) sample, shown in Fig. 2.35. This sample was designed by A. Zorin and fabricated in Physikalisch-Technische Bundesanstalt (PTB), with a proposed operation detailed in [57].

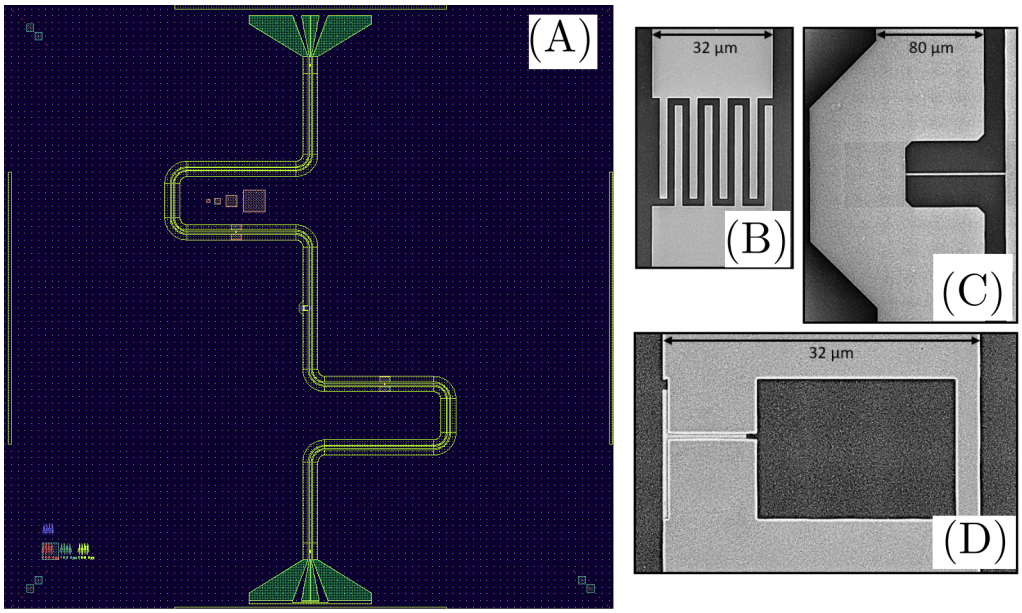

Figure 2.35: Images taken and adapted from [58]. (A) $\frac{\lambda}{2}$ niobium resonator with a single RF SQUID (D) embedded at $1/3^{\text{rd}}$ and $2/3^{\text{rd}}$ the total length of the resonator fabricated by PTB. The sample has a fundamental frequency of approximately 4.3025 GHz, and symmetric interdigitated coupling capacitors (B). The RF SQUID itself features an $I_c = 3$ μA, Nb tri-layer Josephson junction and a L_G such as to define $\beta_L \approx 0.7$. The PTB junction also includes a resistor to ground around the $1/2^{\text{th}}$ the total length (C) primarily to dampen the third mode to prevent third harmonic generation.

The device is a niobium $\lambda/2$ CPW resonator embedded with an single RF at both the $1/3^{\text{rd}}$ and $2/3^{\text{rd}}$ the total length of the resonator. The position of the RF SQUIDs is chosen such that the SQUIDs are coupled to the fundamental (approximately 4.3 GHz) and second mode of the resonator, however, they are uncoupled from the third mode which has a node in its current distribution at this position. The device was designed to exploit the quadratic component produced by biasing the RF SQUIDs with an external flux, two SQUIDs are used to increase the effective strength of the non-linear response.

When operated in its intended mode of operation, only one wave is supplied at the input, a strong pump tone at a frequency corresponding to the second mode of resonator. At a critical pump power, a spontaneous down-conversion of the pump frequency to the signal frequency ($2\omega_s = \omega_p$) occurs resulting in a signal appearing in the output at half the pump frequency, i.e. period doubling, shown Fig. 2.36(A). The devices operation as a period doubling bifurcation detector was reported by my colleague K. Porsch in her PhD thesis [58].

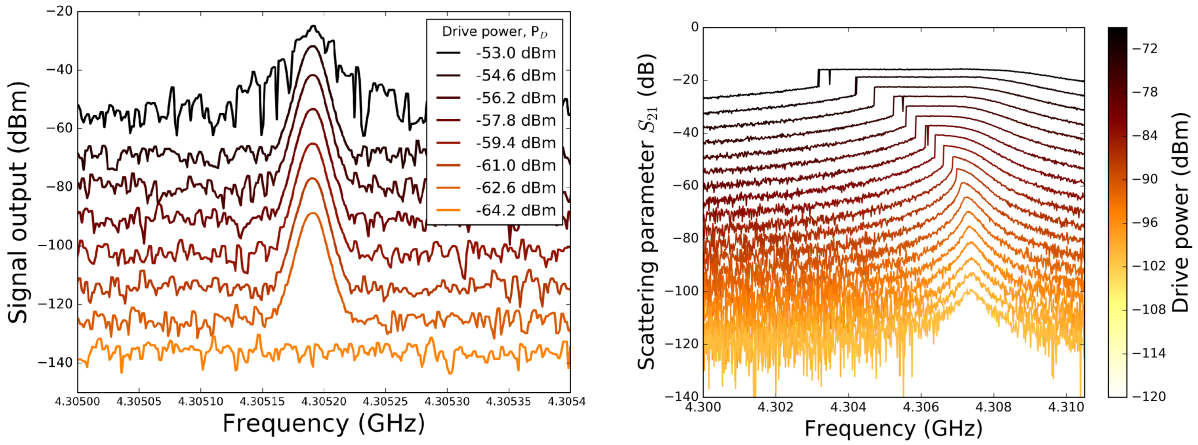

(A) (B)

Figure 2.36: Taken from [58]. (A) Spectrum analyser output in the region of the fundamental mode for multiple pump powers, where the pump frequency is approximately 8.6 GHz. The spectra for each individual pump power is offset for clarity. At lower pump powers, no down-conversion takes place. At a critical pump power ($-$ 62.6 dBm) a period doubling bifurcation occurs and a signal can be seen in the output around the fundamental frequency of the Nb CPW resonator. (B) The PD sample also allows the cubic non-linearity to be employed. In this situation the only input to the devices is provided by a VNA sweeping the frequency around the fundamental mode. Once again the data is offset for clarity. At a critical power (≈ -90 dBm) "bending" of the resonant mode can observed. At higher powers the mode bifurcates. This phenomena, owing to the cubic non-linearity, will be discussed in the next section.

Although the PD sample was intended to exhibit a period doubling bifurcation the sample also provides an arbitrary tunable non-linear media and as such can exhibit a number of the different phenomena noted throughout this section. Therefore I have performed measurements in the context of exploring the possible mixing regimes available and their functionality over the parameter space. These measurements will be detailed in Chapter 4.

2.3.7 Amplitude bifurcation

To conclude this chapter I would like to introduce the concept of amplitude bifurcation, a non-linear phenomenon which will be encountered Chapter 6 and Chapter 7. In this

section we will consider a dynamics approach to describe the behaviour of a non-linear oscillator analogous to a Josephson junction embedded in a resonator. Recalling Section 2.2.3 and the RCSJ model representation of a Josephson junction, show in Fig. 2.23 in this case driven with a current source $I(t) = I_{RF}\sin(\omega t)$ the equation describing its dynamics is given as

$$C_S\phi_0\frac{d^2\delta(t)}{dt^2} + \frac{\phi_0}{R}\frac{d\delta(t)}{dt} + I_c\sin(\delta(t)) = I(t) \tag{2.3.78}$$

expanding $\sin(\delta)$ and truncating at higher orders,

$$C_S\phi_0\frac{d^2\delta(t)}{dt^2} + \frac{\phi_0}{R}\frac{d\delta(t)}{dt} + I_c(\delta(t) - \frac{\delta(t)^3}{3!}) = I(t) \tag{2.3.79}$$

This equation has been explored thoroughly in the context of the Duffing oscillator, a common model employed to understand the behaviour of a driven non-linear oscillator. The Duffing oscillator describes the motion of a mass subject to a non-linear restoring force of the form $F_{restoring}(x) = -x-\rho x^3$, where ρ is a non-linear coefficient of the restoring force. This situation is often represented as a mass attached to a non-linear spring, if we consider the case of a linear spring the $F_{restoring}$ is given as

$$F(x) = -kx \tag{2.3.80}$$

where k is the spring constant, representative of its stiffness. This is analogous with a non-linear spring where the spring constant is dependent on the displacement,

$$F(x) = -k(x)x = -(1 + \rho x^2)x \tag{2.3.81}$$

For $\rho > 0$ the spring gets stiffer with increasing displacement, for $\rho < 0$ the spring gets softer. In the case of a system subject to damping and an external driving force ($F\cos\omega t$), the equation of motion is given as

$$\ddot{x} + 2\Gamma\dot{x} + \omega_0 x + \rho x^3 = \frac{F}{M}\cos(\omega t) \tag{2.3.82}$$

where Γ is the damping parameter, M is the mass and ω_0 is the resonant frequency of the oscillator in the absence of non-linearity. Using the methods outlined in [59] an approximate description of the behaviour of the system can be yielded when the driving frequency is close to the resonant frequency ($\omega \approx \omega_0$). The resonant frequency of the oscillator is modified due to the amplitude dependence incurred by the non-linearity, $\omega_0 \rightarrow \omega_0 + \kappa b^2$, where κ is a definite function of the non-linear coefficients (proportional to ρ) and b is the amplitude of oscillation. Following this methodology allows the amplitude b to calculated for a given driving force as a function of detuning $\epsilon = \omega - \omega_0$, given as

$$b^2[(\epsilon - \kappa b^2)^2 + \Gamma^2] = \frac{F^2}{4M^2\omega_0^2} \tag{2.3.83}$$

The real roots of Equation 2.3.83 give the amplitude of the forced oscillator. Fig. 2.37, shows $b(\epsilon)$ for several different values of driving force amplitude.

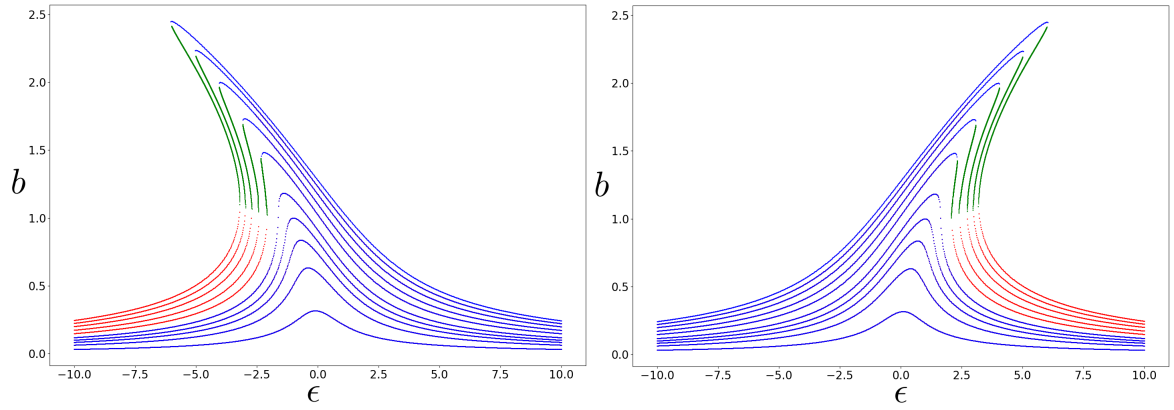

Figure 2.37: Numerical evaluation of $b(\epsilon)$ for increasing amplitude of the driving for (A) $\kappa < 0$ a "hardening" spring (B) $\kappa > 0$ a "softening" spring. Blue and red correspond to stable solutions and green corresponds to unstable solutions to Equation 2.3.83.

For a small driving force the amplitude of oscillation b is also small such that terms of higher order than b^2 can be effectively neglected. In this case the amplitude response of the oscillator follows very closely the linear approximation with a symmetric line-shape over the resonant frequency. At higher drive powers the shape around resonance becomes asymmetric, there is still only a single maximum, however, it has now started to shift away from the natural resonant frequency of the oscillator. The direction it leans is dependent on κ, related to the non-linear coefficients, for $\kappa > 0$ the shift is to positive ϵ and if $\kappa < 0$ the shift is towards negative ϵ. At a certain threshold of the drive power, F_c the behaviour of the oscillator changes dramatically. The gradient of the curve approaches its maximum, $db/d\epsilon \to \infty$, and a bifurcation occurs as the system evolves from a state with only one stable solution to a state of oscillation with two stable solutions and one unstable solution, relating to three real roots to equation above the critical power of bifurcation. Differentiating Equation 2.3.83 and using the condition of $db/d\epsilon \to \infty$ an expression can be derived for the value of ϵ at the points of bifurcation

$$\frac{db}{d\epsilon} = \frac{-\epsilon b + \kappa b^3}{\epsilon^2 - 4\kappa\epsilon b^2 + 3\kappa^2 b^4 + \Gamma^2} \tag{2.3.84}$$

in the limit $\frac{db}{d\epsilon} \to \infty$

$$\epsilon^2 - 4\kappa b^2 \epsilon + 3\kappa^2 b^4 + \Gamma^2 = 0 \tag{2.3.85}$$

in the limit of $\frac{db}{d\epsilon} \to 0$ the maximum amplitude can found to be

$$b_{max} = \frac{F}{2M\omega_0\Gamma} \tag{2.3.86}$$

The amplitude b as a function of detuning is shown in Fig. 2.38 for $F > F_c$ with annotated points of interest. Referring to Fig. 2.38, the unstable solution (D-C branch) corresponds to a state of oscillation such that any action, no matter how small, results in the state of oscillation changing to either the upper or lower stable solution, placing you on the red BC or blue DE curve. The consequence of this system is that there now exists a range of driving frequency that correspond to two states of oscillation with differing amplitudes, depending on the history of the system. Consider sweeping the frequency of the driving force from A to F. As the frequency is increased the amplitude response of the oscillator grows over the path ABC, at the C the amplitude drops discontinuously to E with the amplitude further decreasing to point F. If we now consider reversing the direction of the frequency sweep, this time going from F to A, the amplitude steadily rises along the path FED, at D the amplitude discontinuously increases to B and then steadily decreases from B to A. This is a demonstration of the frequency hysteresis of the Duffing oscillator.

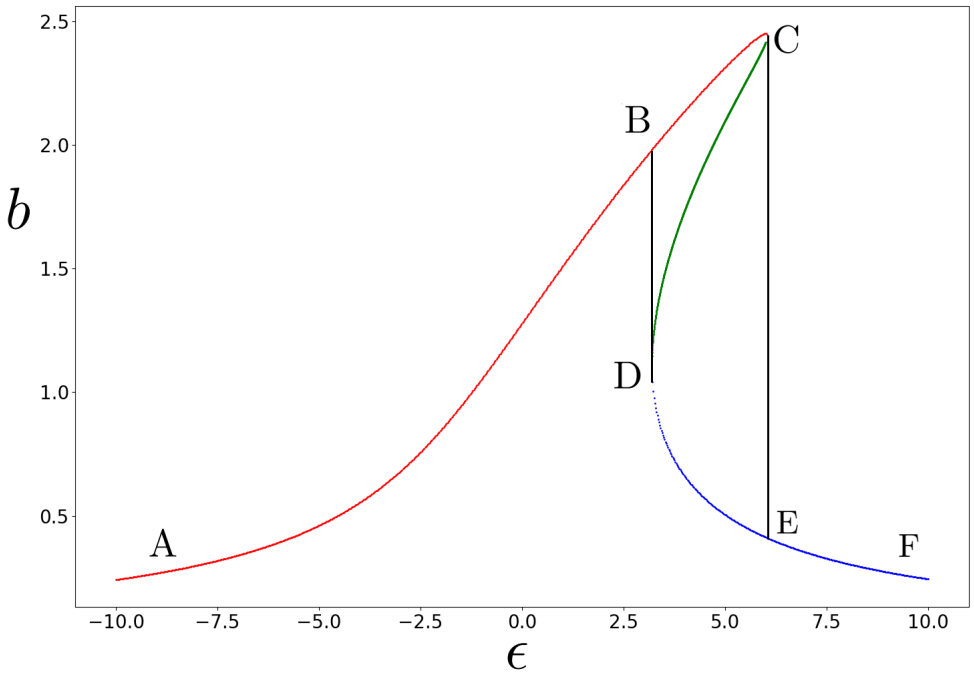

Figure 2.38: Amplitude $b(\epsilon)$ for $F > F_c$. The unstable solutions are given by the green points and the stable solutions are given by the red and blue points.

When driving at $F = F_c$, C-D reduces to a point of inflection such that the two solutions coincide, as shown in Fig. 2.39, where Equation 2.3.83 has been numerically evaluated for the case shown in Fig. 2.38.

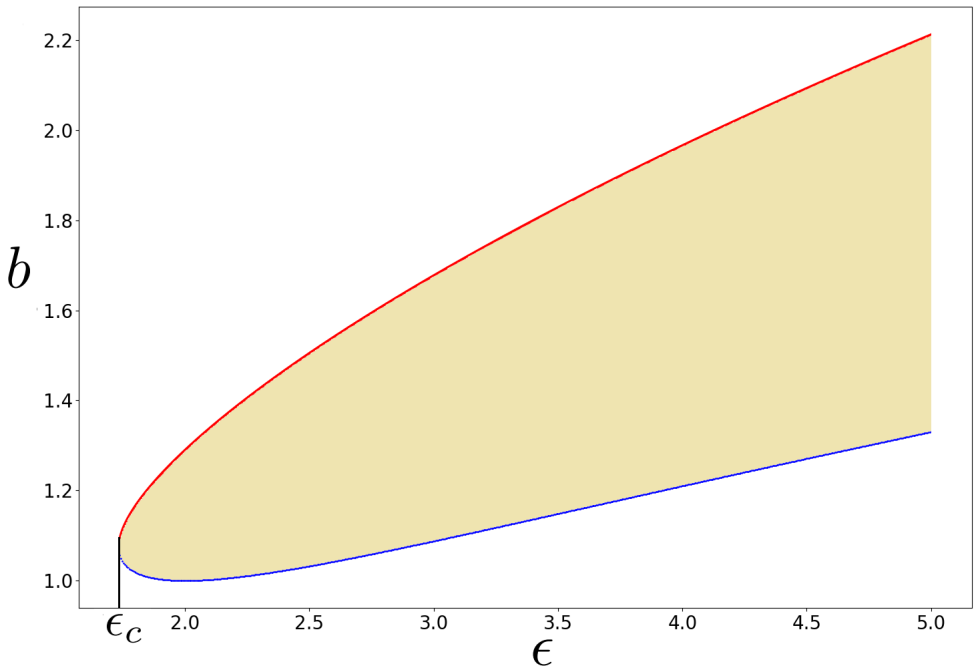

Figure 2.39: Solutions to the amplitude of the Duffing oscillator when $F = F_c$. Red (upper): high amplitude state; Blue (lower): low amplitude state, shaded region corresponds to the region of unstable solutions.

Referring to Fig. 2.39, the red points (upper curve) correspond to the high amplitude state and the blue points (lower curve) correspond to the low amplitude state, the area enclosed corresponds to the region of unstable oscillation. The upper and lower states have the same amplitude at the point of critical detuning ϵ_c, in this case Equation 2.3.83 can be solved to give the F_c and ϵ_c

$$F_c = \frac{32M^2\omega_0^2\Gamma^3}{3\sqrt{3}|\kappa|} \tag{2.3.87}$$

where

$$\epsilon_c^2 = 3\Gamma^2 \tag{2.3.88}$$

The Josephson bifurcation amplifier (JBA) makes use of the extreme sensitivity of the amplitude state to perturbation in the vicinity of bifurcation points, where a small change in the parameters of the oscillator (such as a small increment in the driving power, or a change in the Josephson inductance) can result in a large change in the amplitude/state of oscillation of the system. This can be practically achieved by biasing the oscillator in the low amplitude state near a critical point such that a small change in the drive power results in a switch to the higher amplitude state [60]. In this mode of operation the oscillator acts as a threshold detector (a two-state amplifier). Due to the extreme sensitivity of these amplifiers, unintended fluctuations/noise must be minimised to avoid unwanted transitions between states. Often the dominant source of noise is Johnson noise relating

to the resistive shunting in the model. Johnson noise is related to the thermal motion of charge carriers, associated to their kinetic energy. As such, low temperature operation of these devices is essential to avoid fluctuations. Johnson noise will be revisited in Chapter 3 in the context of noise thermometry. The performance of a JBA is often summarised by so called S-curves (switching probability). The JBA is biased close to a point of bifurcation with the oscillation in the low amplitude state. The bias is then increased and the amplitude of oscillation is remeasured to see if it is still in the low amplitude state or if it has made the transition to the high amplitude state. The measurement is repeated for the same change in bias sufficiently to give an accurate value of the probability of a transition for that particular bias. The bias is then incremented and the process repeated. Fluctuations manifest themselves as a broadening of the S curves width. We will observe bifurcation phenomena in Chapter 7, manifested in a non-linear oscillator created by a Nb CPW $\lambda/2$ resonator with etched nanobridge constrictions.

Chapter 3

Experimental Method

In this chapter I will detail the cryogenic platform, a *Cryoconcept* dilution refrigerator, and equipment used for measurements of the devices reported in this thesis. A primary focus of this chapter is the implementation of current sensing Johnson noise thermometry on this dilution refrigerator. We will also discuss the RF circuit used to measure the samples discussed in Chapter 6. During my PhD I was awarded the qualifications of certified *LabView* associate developer (CLAD) and certified *LabView* developer (CLD) by National Instruments. *LabView* offers a versatile platform for instrument control, measurement and automation. For this reason several program where created for the instrumentation detailed in this chapter. As such I will highlight the most relevant programs, primarily focusing on any novel functionality.

3.1 The cryostat

A photograph of the *Cryoconcept* dilution refrigerator insert, annotating the respective temperature stages and the RF measurement circuit shown in Fig. 3.1. Dilution refrigeration is capable of achieving continuous cooling down to temperatures below 0.01 K using an admixture of Helium-3 and Helium-4. The mixture is circulated in a closed cycle with an intermediate cooling mechanism, generally known as a 1 K pot. Regardless of the mechanism employed, at temperatures below 0.86 K the mixture separates into two distinct phases, a diluted ^{3}He phase (bottom) and a concentrated ^{3}He phase (top), with a phase boundary established in a position dictated by the engineering/design, connected to an isolated thermal conductor (mixing chamber plate). ^{3}He is continuously removed from the bottom dilute phase via pumping, this action results in ^{3}He from the concentrate phase crossing the phase boundary to maintain the finite solubility limit. The process of the ^{3}He crossing the phase boundary is endothermic resulting in a cooling of any thermally connected material. The close cycle operation replenishes the ^{3}He in the concentrate phase with the what has been pumped out of the dilute phase providing continuous cooling power via heat exchangers.

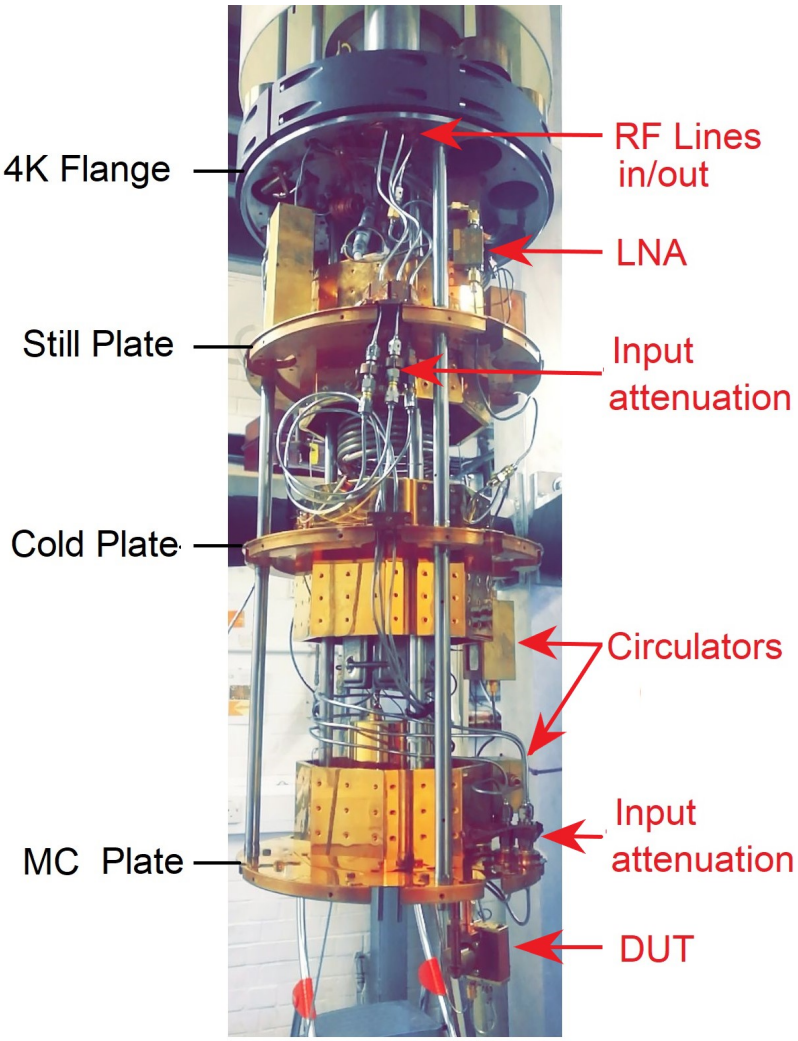

Figure 3.1: Photograph of the *Cryoconcept* dilution refrigerator insert from the 4 K flange down. Black text labels respective temperature stages. Red text labels the components of the RF circuit which will be detailed in Section 3.3.

The *Cryoconcept* dilution refrigerator is novel in the fact that it uses a Joule Thompson expansion process (forced expansion of the mixture through an impedance) as an intermediate cooling mechanism as opposed to a more traditional "1 K pot" which exploits the evaporative cooling of ^{4}He. When initially commissioned the *Cryoconcept* dilution refrigerator was reported to have a cooling power of 400 μW at 0.1 K and a base temperature of approximately 0.012 K without any experimental wiring [61].

The dilution refrigerator's operation is controlled via a WAGO modbus which allows for manipulation the pneumatic values and pumps, communicating their respective state indicators and reporting the value of pressure gauges around the circuit. The modbus is connected to a lab computer via an LAN/Ethernet connection. The "fridge control" program is show in Fig. 3.2. I created and developed the program to allow for manual control of the dilution refrigerator with the inclusion of automated functionality and safeguards to protect the system in the case of equipment failure. The program is a

event-driven queued message handler, a preferred architecture for instrument control used in most of the programs mentioned in chapter. It's primary automated feature is its dynamic "Auto-Start" state, which allows for the system to be cooled from 4.18 K to base temperature without user intervention.

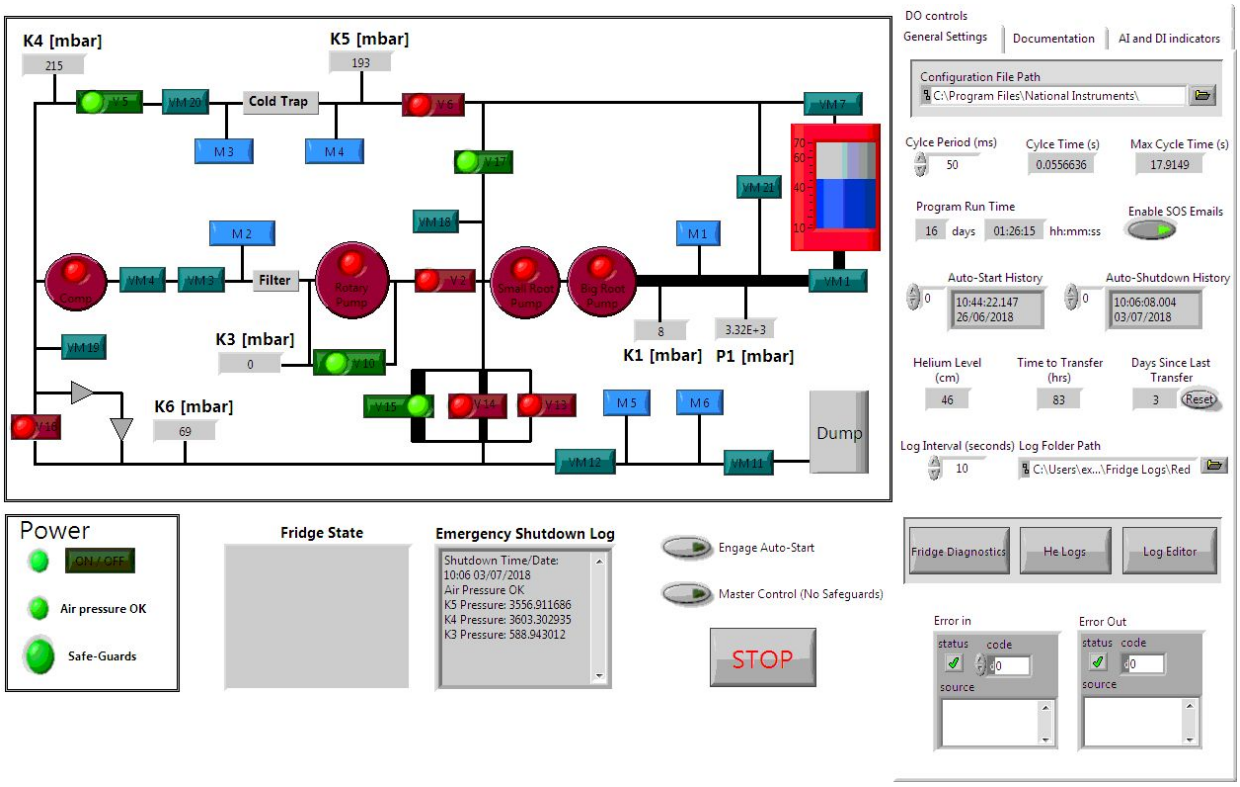

Figure 3.2: Dilution refrigerator control program. Custom software developed over the course of my PhD. This particular image was emailed to all users on the 03/07/2018, such as to inform of an automated shut-down of the circulation system due to high pressures detected around the circulation circuit. The image shows the system in a safe state with the dilution insert open to a large "dump" volume preventing in the system pressurising.

The program features various safeguards, which primarily serve to monitor the most significant pressures around the circulation circuit. If a pressure threshold is exceeded at any part of the circuit, the program automatically carries out a sequenced shut-down of all pumps, opening valves accordingly to alleviate pressures and put the system in a safe state. Upon completion an email is sent to the user with a screen-shot attachment of the front panel of the program indicating the state of the dilution refrigerator. The pneumatic pressure used to switch the values is also monitored to ensure it maintains pressure ($\approx$ 5 bar). If the air compressor supplying the system fails, a non-return value on the input stops any loss of pressure. A buffer volume allows for continued operation of the valves for several hours after the failure of the compressor. A threshold gauge is used to monitor the pressure of the pneumatics, below the 4.5 bar the program sends an email to the users to notify them of the problem. The user is given a set amount of time to fix

the problem, i.e. restart the supply compressor (or turn off the safeguards which is not recommended). If no action is taken and automatic shut-down is performed to make the system safe before a failure of the valves air supply occurs, once again the user is notified via email. A diagnostic program was also made to conveniently monitor all the systems parameters in real time and to review the large volume of data logs of the refrigerators operation and thermometry, shown in Fig. 3.3.

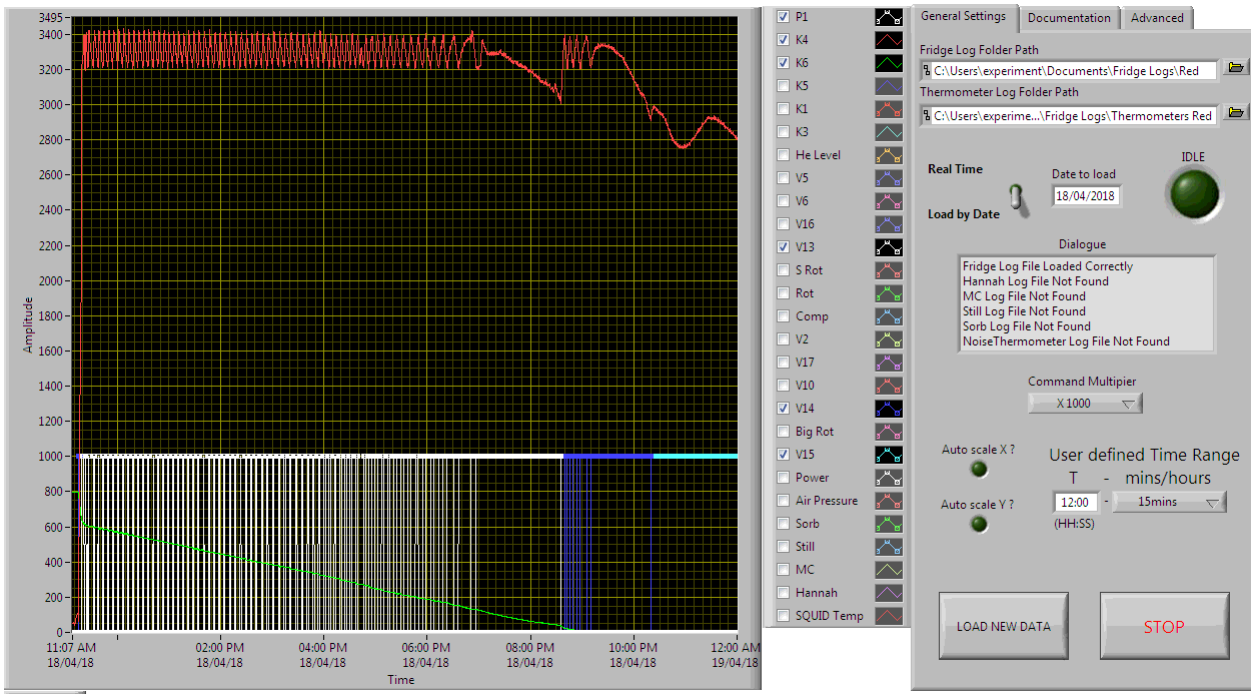

Figure 3.3: Screenshot of "fridge diagnostics" program. In this case an automated Auto-Start sequence is shown. The refrigerator is "fed" the mixture from the dump volume (green line) via a small input impedance. As the mixture is injected the circulation pressure (red) rises. At 3400 mbar the valve of the impedance (white) closes until the circulation pressure reduces to 3200 mbar at which point it opens again. This continues until the dump is empty. The program monitors the condenser pressure and the time between the individual valve switches to decided when to move to a larger input impedance (blue and turquoise). If the time between switches is too short it will switch to a higher impedance input. On this occasion the fridge took approximately 13 hours to reach base temperature.

3.2 Current sensing Johnson noise thermometry

3.2.1 Resistive thermometry

The dilution refrigerator utilities four resistive thermometers, located on the various temperature stages of the system. Four point measurements of the resistance of the respective thermometers are performed by two separate *Stanford Research Systems* (SRS) AC resistance bridge modules housed in a SRS mainframe. One of the resistance bridges is connected to an RuO_2 thermometer on the mixing chamber plate. The second resistance

bridge is connected to a multiplexer in turn connected to the other three thermometers. The multiplexer selects/switches between the separate circuits of the connected thermometers. This configuration is chosen such that one module gives a continuously well-defined measurement of the most important thermometer and the other can be switched between the other respective thermometers at a user defined read out rate with accordingly faster (and correspondingly nosier) acquisition parameters.

The "thermometry control" program is shown in Fig. 3.4. The program allows for control of the acquisition parameters for the respective SRS AC resistance bridge modules and also control of the multiplexer determining the thermometer that the second resistance bridge measures. The user can choose to automatically cycle between any combination of the three thermometers connected to the multiplexer, taking measurements at a desired readout rate which are plotted and logged to a file.

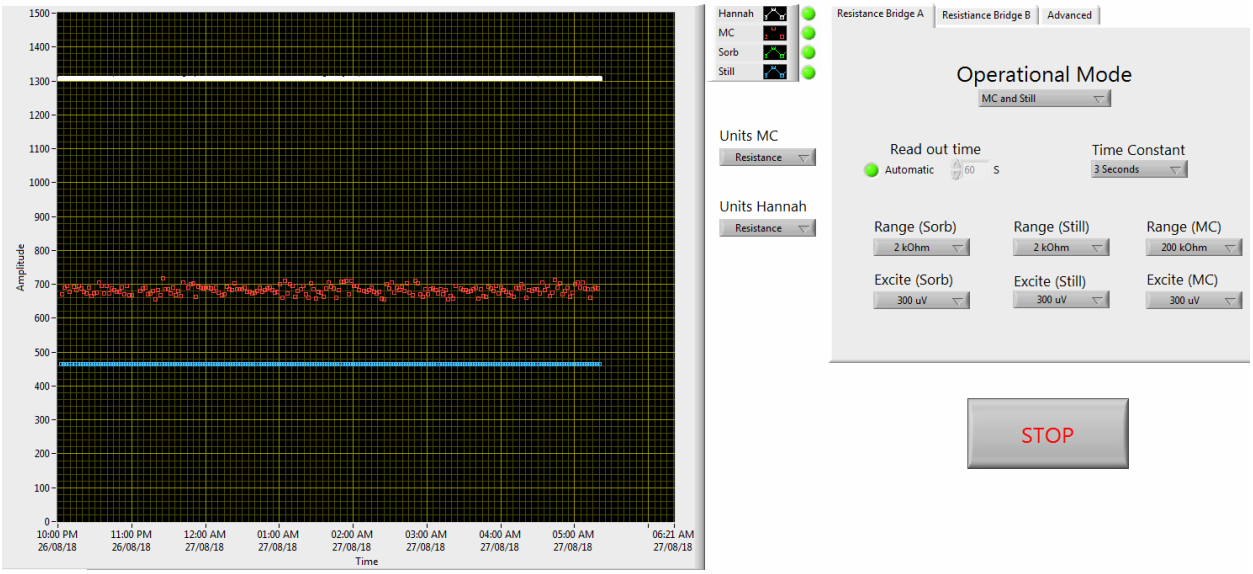

Figure 3.4: Screenshot of thermometry control program. A consequence of the mechanical multiplexer is that it can stick and not switch when requested. For this reason as the program cycles the respective thermometer it queries the multiplexer each time to check it is in expected state. If the multiplexer sticks, the program repeats the command to switch to the multiplexer until it responds or a time-out condition is met.

The accuracy of these resistance thermometers is reliant on their calibration, the quality of the measurement and the temperature range over which measurement is made. When the primary RuO_2 thermometer located on the mixing chamber was installed it was reported to be a reliable, well calibrated thermometer at the base temperature of the dilution refrigerator. However, it was found that below 0.05 K the $Ru0_2$ thermometers did not accurately report the temperature of the mixing chamber. Below 0.05 K the thermometer was shown to be thermally disconnected from the mixing chamber and insensitive to any fluctuations in the mixing chamber temperature such as a small but

known heat load on the mixing chamber temperature stage. Furthermore, at low temperatures the resistance measurement of the thermometer was influenced by acquisition conditions of the measurement circuit.

Several efforts were made to investigate this further with particular attention paid to the experimental wiring of the thermometers and noise characteristics, for evidence of ground loops or a heat leak down the lines. Ultimately the solution was the implementation of current sensing Johnson noise thermometry, replacing the RuO_2 thermometer on the mixing chamber plate as the primary method of thermometry at low temperatures.

3.2.2 Johnson noise

Johnson noise (also know as Johnson-Nyquist noise) is a type of electronic noise intrinsic to all electrical conductors, produced by the random thermal motion of charge carriers within them. This results in a root-mean-squared voltage, V_{RMS}, over a conductor in the absence of any applied voltage/current at non-zero temperatures, given by

$$V_{RMS} = \sqrt{4k_B RdfT}, \tag{3.2.1}$$

where df is the measurement bandwidth, R is the resistance and T is the temperature in Kelvin, assuming thermal equilibrium.

Johnson noise is a form of "white" noise due to its random nature, characterised by a constant power spectral density in the frequency domain. In the case that the resistance is constant, the Johnson noise is solely proportional to the electronic temperature forming its basis as a methodology for thermometry. Given the resistance of the conductor being measured is known, the electronic temperature of the conductor can be determined. However, in general at low temperatures the Johnson noise voltage is generally small, in order to accurately measure these thermal fluctuations novel ways to amplify this noise voltage must be employed, in this case a number of 1996 *Conductus* model niobium DC SQUID sensors and a corresponding control unit.

3.2.3 DC SQUID

In Chapter 2.2 we reviewed the Josephson junction and the RF SQUID geometry in the context of non-linear microwave circuit elements. In this section the operating principle of the DC SQUID, shown in schematically in Fig. 3.5(A), will be discussed in the context of a flux to voltage detector employed to detect the small voltage associated with the Johnson noise current. A DC SQUID is comprised of two Josephson junctions connected in parallel interrupting a superconducting loop. These junctions are typically resistively shunted to eliminate hysteresis in their current-voltage characteristics, as discussed in Chapter 2.2.3. As previously noted, these resistive shunts are also sources of Johnson

noise resulting in a voltage noise across the junctions. This is one of the few intrinsic noise consideration in these sensitive devices.

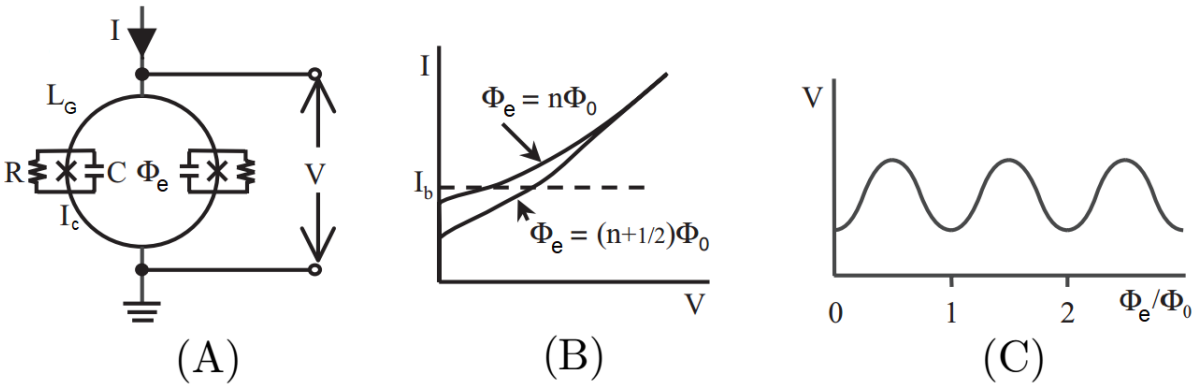

Figure 3.5: Adapted from [44]. (A) Schematic diagram of two RCSJ junctions interrupting a superconducting loop of geometric inductance L_G, threaded by an applied flux Φ_e. (B) I/V characteristics of the DC SQUID at integer and half-integer values of applied flux. (C) Voltage over DC SQUID as a function of applied flux.

Consider biasing the DC SQUID shown in Fig. 3.5(A) with a current, I. In the absence of any external magnetic field, I is split equally between the two branches. Now suppose a small magnetic field is applied, such that a small fraction of a flux quantum ($\Phi_e << \Phi_0$) threads the loop. Flux quantisation dictates that the flux threading a superconducting loop must be integer number of flux quanta. Thus in this case a screening current, I_s, circulates around the loop, generating a magnetic field cancelling the applied flux threading the loop. The current flowing in the respective branches is now $I/2 + I_s$ and $I/2 - I_s$. When the current in either branch exceeds the critical current, I_c, of the junction a voltage is generated over the SQUID. Now consider the situation where the external field is increased such that a flux just greater that $\Phi_0/2$ threads the loop. Now it is energetically favourable for the screening current to increase the flux threading the loop to Φ_0 by reversing the direction of the screening current. With increasing flux the direction of the screening current alternates. This means that changes in the applied magnetic flux causes the voltage over the SQUID to swing between two extrema (Fig. 3.5(B)), producing oscillations with a period of Φ_0 as shown in Fig. 3.5(C), commonly referred to as the V/Φ_e curve.

The maximum response to an applied field occurs when $\Phi_e = (2n+1)\Phi_0/4$ where the $\frac{dV}{d\Phi_e}$ (the voltage transfer coefficient) is maximum. This is the typical "working point" (W) chosen when operating a SQUID as a flux to voltage converter giving maximum sensitivity too applied fields, this is illustrated in Fig. 3.6(A). In order to fix the working point an electronic feedback circuit is used, shown in Fig. 3.6(B). The SQUID is biased at the appropriate point, W, on the V/Φ_e curve to ensure maximum sensitivity. The

deviation of the SQUID voltage V from that working point V_b is amplified, integrated and fed back into the SQUID via a feedback resistor and a modulation coil in close proximity to the superconducting loop keeping the SQUID "locked" at the working point of the V/Φ_e curve. Typically when operated in this "Flux-locked loop" (FLL) mode the SQUID acts as a null detector. When a flux $\delta\Phi_e$ is incident on the SQUID an opposing flux $-\delta\Phi_e$ is applied from the feedback circuit to keep the flux through the SQUID constant. This produces an output voltage over the feedback resistor proportional to $\delta\Phi_e$, linked by the voltage transfer coefficient which can be thought of as the gain of the system.

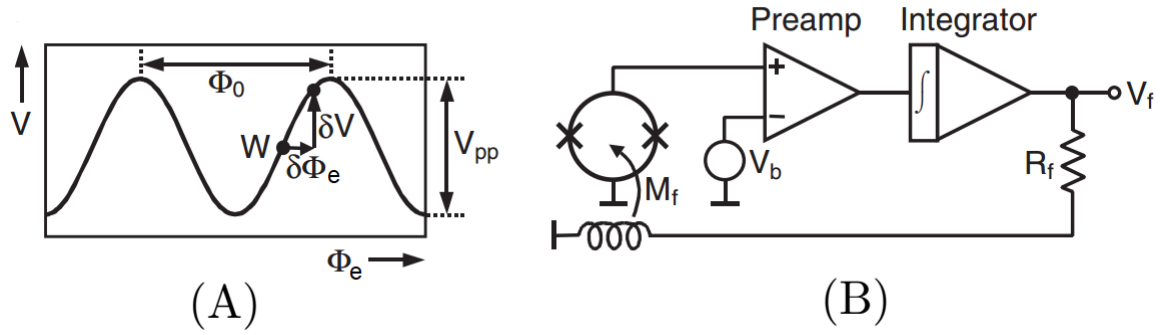

Figure 3.6: Adapted from [44]. (A) V/Φ_e relationship showing the typical working point W. (B) Generic direct-coupled flux-locked loop circuit diagram.

The *Conductus* DC SQUID features an input coil inductively coupled to the SQUID, similar to the modulation coil used to fix the working point. This allows the SQUID to be operated as a current to voltage converter. Thus a Johnson noise source can be wired to the terminals of the input coil such that the noise current produced flows through the input coil producing a measurable flux through the SQUID loop proportional to electronic temperature of the noise source.

3.2.4 DC SQUID sensor characterisation

Preliminary measurements where performed at 4.18 K in a liquid Helium transport Dewar. The first step was to ascertain the performance of the *Conductus* DC SQUID sensors provided. For these measurements the input coil was left open to access the noise characteristics of the DC SQUID sensors without any external circuity. The sensors have an integrated Nb outer casing to provide shielding from ambient electromagnetic fields capable of inducing noise in the system. For several of these measurements the sensor was also suspended at the centre of continuous Nb open ended tube to provide addition shielding. The Nb tube length is approximately 10 times larger than the inner diameter. Below the Nb transition temperature the Meissner effect screens ambient field penetrating either

ends of the Nb tube. The ratio of the diameter and length of the tube define the attenuation of the incident magnetic field, in this case the ratio is such that the incident field is completely attenuated at the centre of the Nb where the SQUID is positioned. Similar shielding is used for the RF measurement of SCPW samples, which will be discussed near the end of this chapter.

The SQUID is operated by a *Conductus* SQUID controller box supplied with the sensors, capable of automatically tuning the V/Φ_e curve to maximise the sensitive of the SQUID to external flux (i.e. maximising the transfer coefficient). The analogue output of the feedback circuit (V_s) was filtered by a 80 kHz *Stanford* low pass filter and connected to an analogue to digital converter connected to a computer. The voltage signal was sampled at typically 100-200 kHz. Using a fast-Fourier Transform (FFT) allows the spectral composition of the signal to be observed. Multiple SQUID sensors where cooled such as to inspect their V/Φ_e curve and noise characteristics. A FFT showing the noise floor of an open circuit *Conductus* SQUID sensor is shown in Fig. 3.7

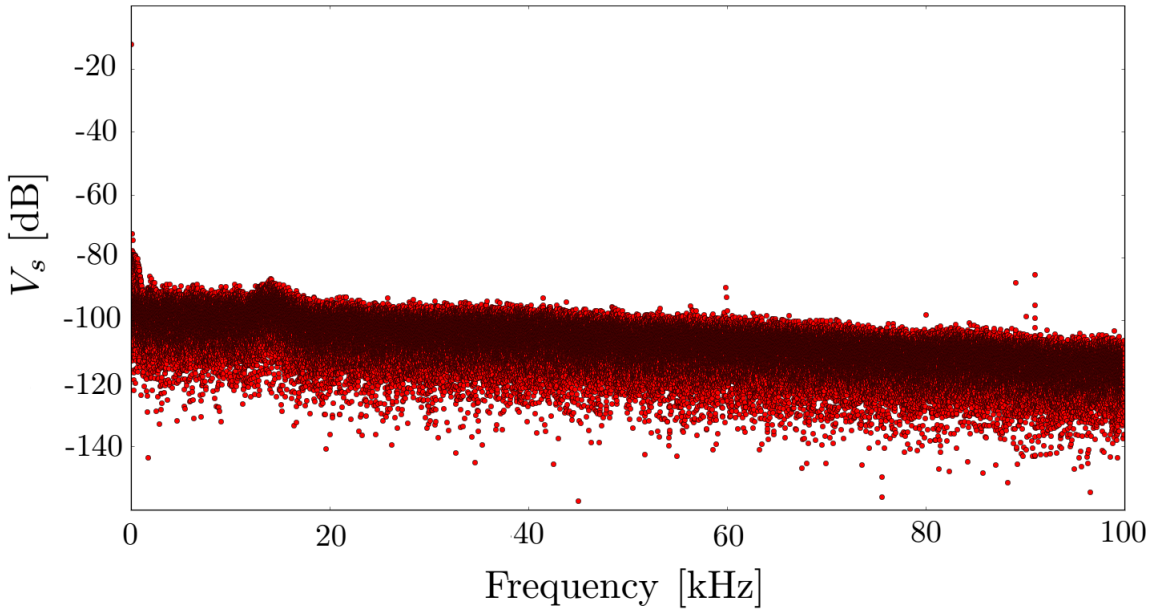

Figure 3.7: Log-linear plot of a FFT of the open circuit SQUIDs voltage V_s. A small amount of 1/f noise is present at the lower frequency end, a common feature of these devices. Otherwise the signal is very "clean" and the intrinsic noise floor of the SQUID, approximately 2×10^{-5} V$/\sqrt{Hz}$ up to 20 kHz, is low enough for the white noise of an appropriate Johnson noise current to be observed.

Conductus provided a specification sheet for each sensor, giving the originally measured voltage transfer coefficient [V/Φ_0] and the current input coupling [Φ_0/A], together defining the gain G [V/A] of the SQUID when operated as a current to voltage converter. It was decided to re-measure this parameter given the age of the SQUID sensors and the

possibility of degradation. This was achieved by measuring a known input current, provided by a signal generator. The current was applied to the input coil via a set of twisted pairs with a surface mounted resistor soldered in series prior to the connection to the input coil, such as to limit excessive current being fed into the sensor. A sinusoidal signal of known magnitude was supplied to the input coil via the measurement wires and the SQUIDs voltage response measured for multiple frequencies of the applied input signal. This allowed the gain of the SQUID as a function of frequency to be measured, shown in Fig. 3.8. The gain was measured to be approximately 1.32 $\times 10^6$ VA^{-1} at low frequencies and was approximately constant up to 20 kHz. In comparison the gain quoted on the specification sheet was 1.4 $\times 10^6$ VA^{-1} at 1 kHz.

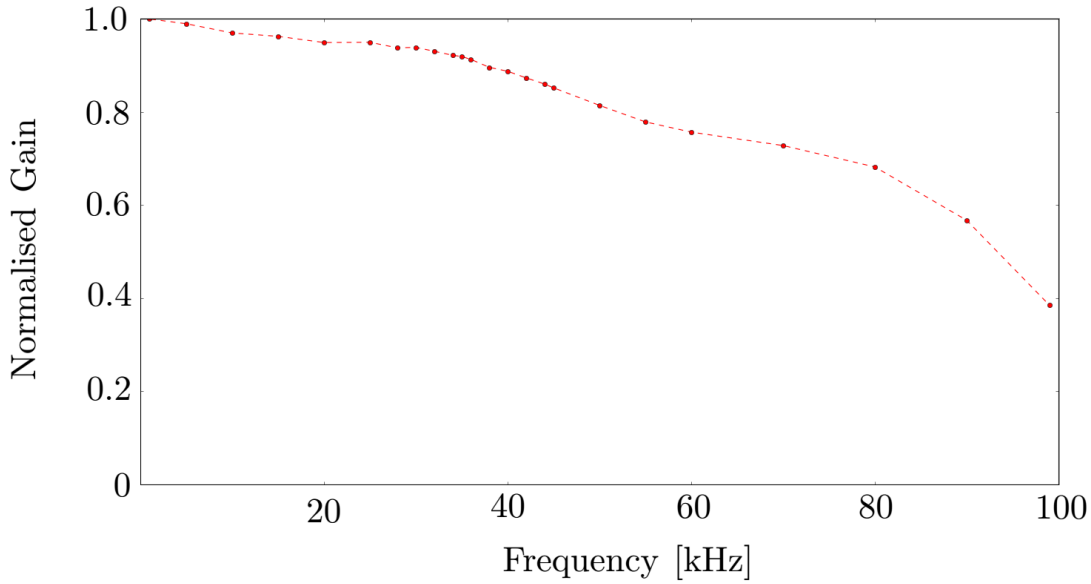

Figure 3.8: Gain response function. The Y-axis represents the measured current divided by the input current, normalised by the measured gain at low frequencies. The gain is approximately level up to 30 kHz, however, shows a significant drop by 50 kHz, corresponding to the end of the operating bandwidth of the SQUIDs FLL circuit quoted by *Condutus*.

3.2.5 Noise resistor

Once a selection of SQUID sensors has been tested and characterised the Johnson noise source (noise resistor) to be used must be considered. As previously discussed any electrical conductor will produce a noise current however there are a few considerations to be made. Firstly, the resistance should be constant throughout the temperature range of operation for the thermometer. Secondly, the magnitude of the resistance will determine the magnitude of the noise current. A small noise current will produce a signal below the noise of the SQUID and be unmeasurable. Conversely a large noise current could potentially produce a big enough flux incident on the SQUID to overwhelm the feedback system, "unlocking" it from the working point. Finally, the cut off frequency of the signal

must be also be addressed $f_{cut} = \frac{1}{2\pi}\frac{R}{L}$, where the inductance L is introduced from the input coil coupled to the SQUID, also including any the contribution from any wiring present in the input circuit. If the resistance is too low the cut off will be in the low frequency end of the spectrum complicating measurement requiring a larger number of samples/integration time to improve the resolution of the FFT of the signal around the lower frequency end of the spectra.

For initial tests a 2 mm long piece of 0.5 mm diameter phosphor bronze wire coupled to a copper heat sink was used. Superconducting CuNi clad NbTi twisted pairs were connected to define a segment of the wire using superconducting Sn/Pb solder. This allows the noise resistor to be connected to the SQUID input terminals without contributing to resistance to the circuit. In order to determine the resistance of the sensor a 4-point measurement, using a *Perkin-Elmer* 7465 lock-in amplifier, was made at 4.18 K in a transport Dewar. The measured resistance of the phosphor bronze wire was approximately 400 $\mu\Omega$. The phosphor bronze noise sensor was then connected to the input circuit of the SQUID and measured at 4.18 K. An FFT of the resulting voltage signal from the SQUID sensor, is shown in Fig. 3.9.

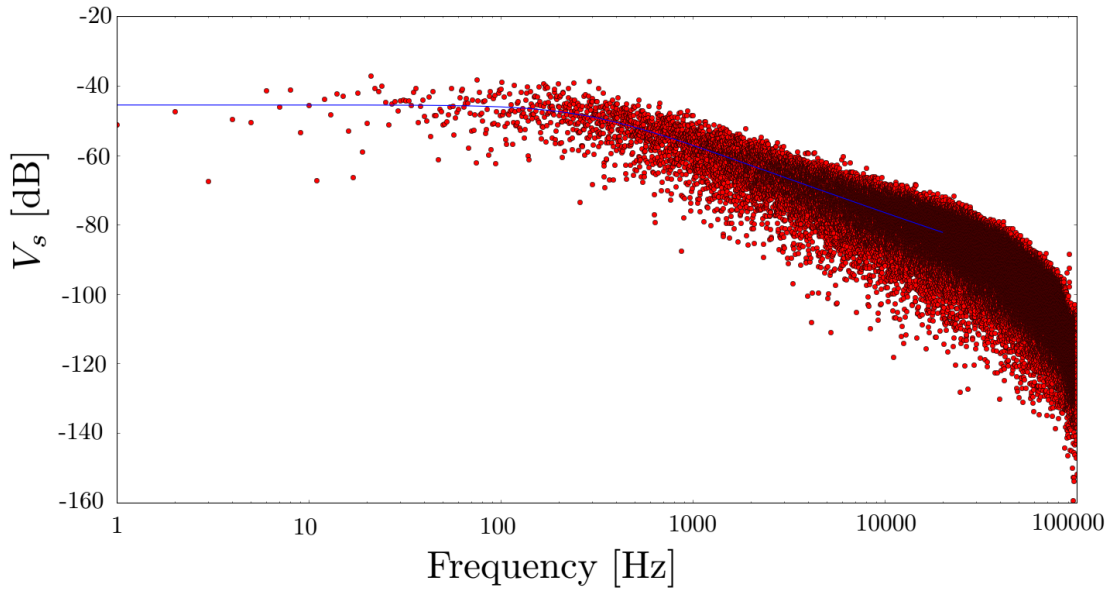

Figure 3.9: Log-Log plot - FFT of 1 second of voltage data acquired at 200 kHz sampling rate of V_s (sensor output) with the noise resistor connected. The (white) Johnson noise extends out to approximately 400 Hz, followed by a linear (log-log) drop due to the inductance of the input circuit effectively filtering the circuit. The effect of the *Standford* low pass filter can be observed at 80 kHz. Blue shows the fit to Equation 3.2.2. The fitting range is 20 kHz given this is the region the gain response curve is known to be reasonably flat.

The FFT of the voltage data was fit with the following function

$$V_s = G\sqrt{\frac{4k_B RdfT}{R^2 + (\omega L)^2}} \tag{3.2.2}$$

where G is the current to voltage gain of the SQUID previously measured, with the temperature constrained to 4.18 K. The fitted data yielded a resistance value of 359 ± 9 $\mu\Omega$ and an inductance of 220 ± 5 nH. The resistance value is very close to that measured previously using a lock-in amplifier, however, at first the measured inductance appeared erroneous due to a discrepancy with that quoted on the specification sheet of 600 nH. Several further measurements were carried out, incrementally increasing the inductive contribution of the input circuit. The increased inductive contribution was observed by shifting of the cut off frequency of the Johnson noise. The resistance of the input circuit was measured consistently regardless of the increased inductive contribution. Given that the SQUID correctly responded to the input circuit in a controlled way it was assumed that the quoted inductance of the input coil was measured in the specification sheet was erroneous.

Regardless of the inductance of the circuit, for the purpose of thermometry only determination of the white noise level of the Johnson noise source (V_{RMS}) is required. This system could be operated as an absolute thermometer if all the circuit parameters were known. However, with the temperature control of the dilution refrigerator, an easier methodology can be employed. The *Cryoconcept* dilution refrigerator is a "wet" system, the dilution insert is enclosed in a chamber under vacuum (IVC) and then immersed in a liquid ^{4}He bath for thermal isolation from the room temperature environment. As such the insert can be thermalised with the bath by injecting a small amount of gaseous ^{4}He into the IVC providing a strong thermal conduction pathway between the bath and the insert. This allows for a fixed temperature point for calibration such that the resistance of the circuit can be measured. Once the thermometer is calibrated, given that the resistance of the Johnson noise source is independent of temperature, the relative change in the magnitude of the Johnson noise voltage, communicated via the feedback circuit of the SQUID sensor, gives the change in the electronic temperature of the noise resistor.

3.2.6 Input circuit construction

In order to implement this method of thermometry on the dilution refrigerator a suitable input circuit must be constructed, such that a noise resistor can thermally linked to the mixing chamber with shielded measurement line connecting the noise resistor to the SQUIDs Nb input terminals. The first consideration is the material of the noise resistor. Although several other materials are considered including platinum tungsten, phosphor

bronze is chosen due to the familiarity with the test noise resistor discussed in the previous section. The most important characteristic of the material is that its resistance is independent of temperature past the calibration point of the system at 4.18 K. In order to ensure this, resistivity measurements are made of appropriate length of the phosphor bronze wire at different temperatures to determine its temperature dependence. The room temperature resistivity is found to be $\rho_{300K} = 1.59 \times 10^{-6}\ \Omega m$. The wire segment is then immersed in liquid N_2 and ^{4}He and remeasured such as to calculate the residual resistivity at approximately 77 K and 4 K, respectively. It was found that $\rho_{77K} = 0.875\ \rho_{300K}$ and $\rho_{4K} = 0.856\ \rho_{300K}$. Given that the relationship between the temperature and resistance of a metal is linear, saturating at a residual resistivity defined by impurities, the residual resistivity ratios observed infer that the resistance of phosphor bronze becomes independent of temperature before 4.18 K.

In order to thermally link the noise resistor to the mixing chamber of the dilution refrigerator a phosphor bronze wire segment of diameter 0.5 μm and appropriate length was hard soldered to a copper heat sink. Once again CuNi clad NbTi measurement wires were then soldered on to the phosphor bronze wire segment, where the spacing of the two soldered measurement wires define the length and thus the resistance of the noise resistor. This length was chosen to be 1.5 mm to 2.5 mm defining a 250 $\mu\Omega$ to 340 $\mu\Omega$ resistor at 4.18 K given the prior characterisation data.

Although the noise resistor is mounted to the mixing chamber, the SQUID sensors themselves are installed at higher temperature stages of the refrigerator. This is due to the potential of the SQUID sensors placing a significant thermal load on the mixing chamber. The same consideration must be made for the noise resistors themselves. Although the circuit is passive (not current biased in a traditional sense) the measurement lines connecting the noise resistor on the mixing chamber to the SQUID on a higher temperature plate provides a heat link between the respective temperature stages through the measurement lines. The superconducting NbTi centre is not of concern however the CuNi metal cladding is a normal metal and constitutes a channel of conduction down to the mixing chamber. The heat load can be estimated given the thermal conductivity of the cladding, its dimensions and the temperature difference between the stages. Although not significant in this situation this is a real concern when employing Johnson noise thermometry to ultra low temperature (μK) where a heat load from the measurement lines can cause the thermometer to report higher temperatures, or heat the cold stage.

The measurement wires are threaded through superconducting Nb capillary to provide shielding from ambient noise as they are taken up from the mixing chamber to the SQUID Nb input terminal. To ensure a minimal contact resistance in the joint between the measurement wires and the SQUIDs input terminal, the CuNi cladding is etched with nitric acid such that a superconducting contact can be made between the Nb input terminals of the sensors and the NbTi core of the measurement lines. Two noise resistors where

constructed and connected to two SQUID sensors located on the cold plate and still plate respectively, shown in Fig. 3.10.

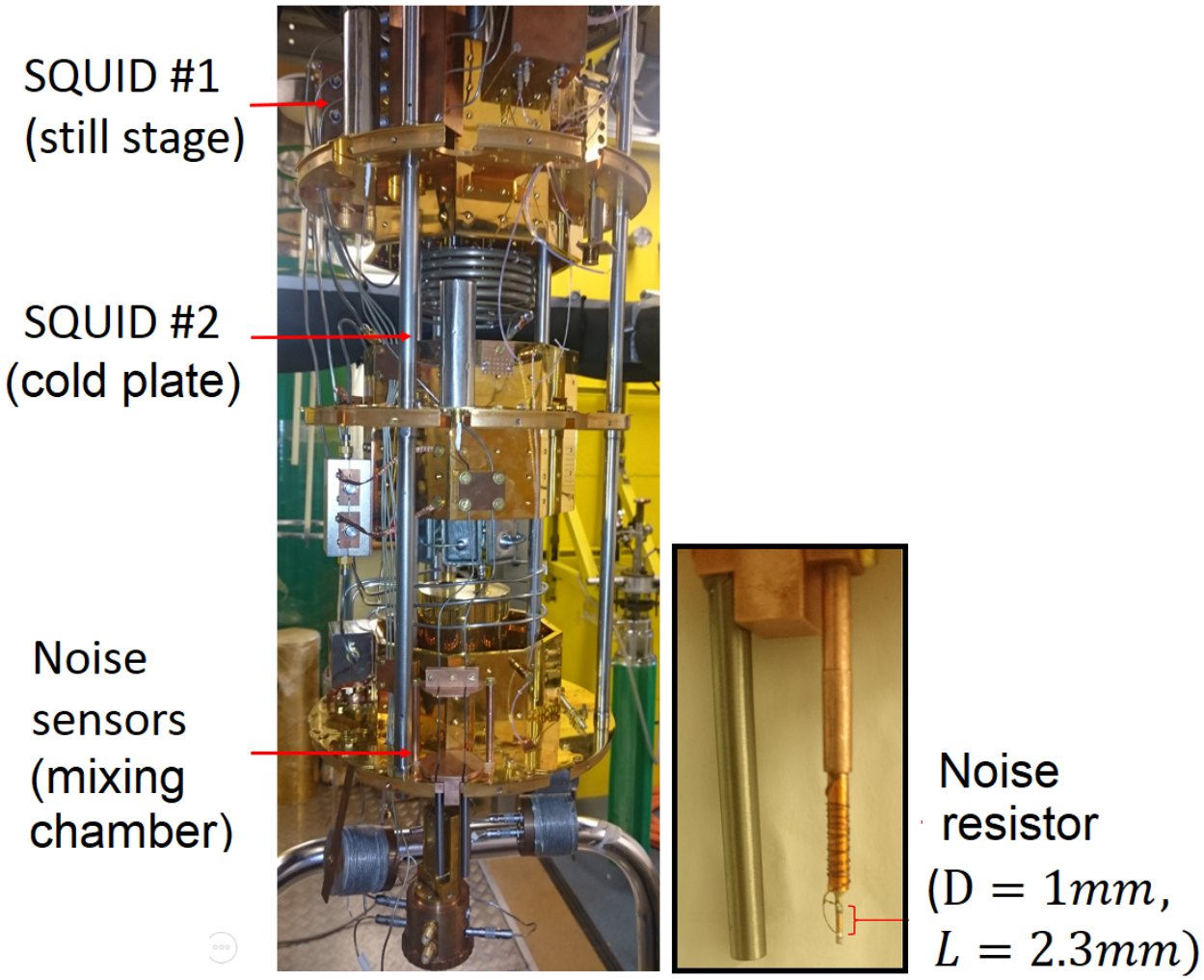

Figure 3.10: Pictures of the two noise thermometers installed on the dilution refrigerator. The SQUIDs are wrapped in an additional layer of μ-metal to enhance shielding.

3.2.7 Low temperature thermometry

The dilution refrigerator was thermalised at 4.18 K and the noise thermometers were calibrated. With the temperature constrained, the respective sensors were measured and fitted for the resistance of each noise resistor at the calibration temperature. The individual sensors resistances where $R_{coldplate} = 222.5 \pm 8\ \mu\Omega$ and $R_{still} = 266.5 \pm 9\ \mu\Omega$. The fridge was then cooled to its base temperature with the resistance constrained, fitting the Johnson noise signal V_s for the temperature of the phosphor bronze noise resistor thermally coupled to the mixing chamber. The fitted temperature estimation for the cold plate SQUID is shown in Fig. 3.11, in comparison with the aforementioned RuO_2 (MC) thermometer also located on the mixing chamber plate.

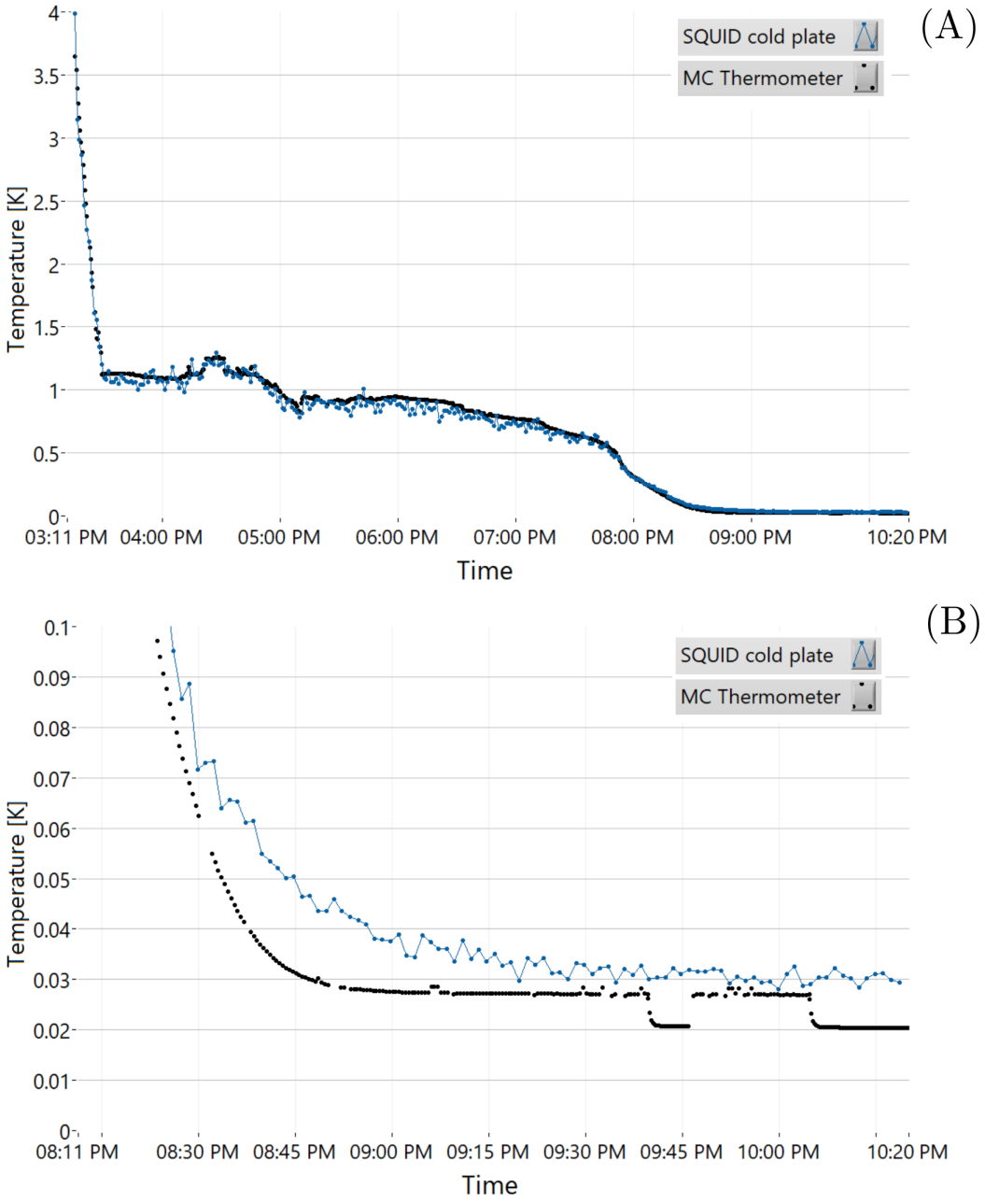

Figure 3.11: Blue points: Cold plate SQUID temperature estimation using 4.18 K calibration. Black points: RuO_2 (MC) thermometer measured using SRS AC resistance bridge. (A) Full temperature range. (B) Below 0.1 K.

The MC thermometer and cold plate SQUIDs estimation of the temperature is in agreement over the range of 4 K to 0.1 K. However at lower temperatures the mixing chamber thermometer bottoms out to 0.027 K while the SQUID thermometer still shows cooling. It was long suspected that the MC thermometer was thermally disconnected below 0.05 K however with the noise thermometer for comparison this became very apparent. Even slight variations in the dilution refrigerator heat load were detected in the Johnson noise signal while the MC thermometer showed no significant response until the

SQUID temperature was above ≈ 0.045 K.

The still plate sensor however was less successful, this is illustrated in Fig. 3.12. The still plate sensor is in agreement with the cold plate sensor around 3 K to 4 K, however past 3 K it over estimates the temperature of the mixing chamber. As the mixing chamber cools further the still plate sensors estimation saturates around 0.75 K while the cold plate sensor shows continued cooling. Unfortunately after closer inspection it was found that the still sensor was following the temperature of the still stage as well as the mixing chamber. This is highlighted in Fig. 3.12 when comparing the still plate SQUID sensor's temperature estimation with the temperature of the still plate given by an uncalibrated resistance thermometer, which has been scaled in Fig. 3.12 for clarity.

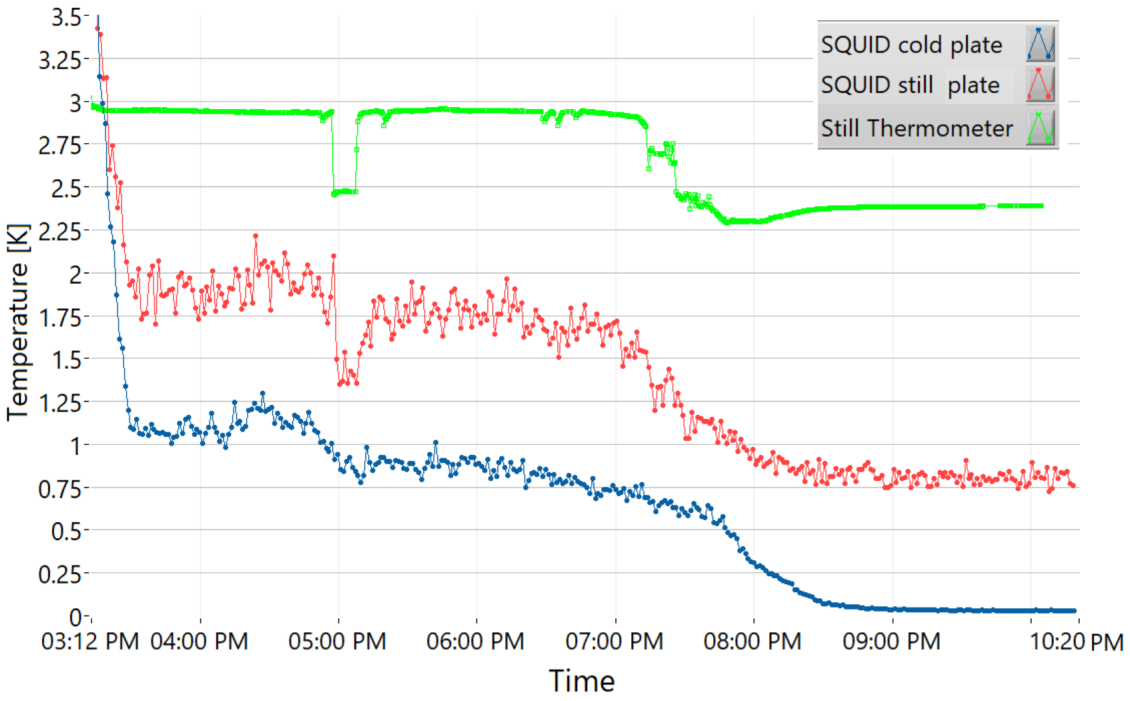

Figure 3.12: Blue points - cold plate SQUID temperature estimation. Red points - still SQUID temperature estimation. Green points - scaled resistance value of the still plate thermometer. Around 5pm a sharp drop in the still resistance can be observed corresponding to a cooling event, which is also seen on the still SQUID but not the cold plate SQUID. These events are characteristic of instabilities in the still temperature due to the ^{3}He/^{4}He mixture condensing and evaporating as the fridge is cooled to base temperature.

It was assumed that a second Johnson noise source has been introduced to the input circuit of the still plate SQUID, thermally coupled to the still plate, modifying the overall Johnson noise current I_T in the input circuit. This results in the V_s being related to both the noise source coupled to the still plate of resistance R_s at temperature T_s and the intended noise source owing to the phosphor bronze of resistance R_{mc} at temperature T_{mc}.

$$V_s = \frac{G}{\sqrt{R_T^2 + (\omega L)^2}} \left(\sqrt{4k_B T_s R_s df} + \sqrt{4k_B T_{mc} R_{mc} df} \right) \tag{3.2.3}$$

where $R_T = R_s + R_{mc} = 266.5 \pm 9\ \mu\Omega$. Although the temperature estimation of the still is approximate, fitting to the measured data of the still sensor with T_s and T_{mc} constrained gives $R_s = 75\ \mu\Omega$. It was suspected that this originated from a contact resistance at the Nb input terminals of the SQUID. Subsequently, the Nb terminals where well scrubbed to ensure no surface oxide was present and the NbTi measurement wire re-etched, however the issue persisted.

3.2.8 Vibrational noise

Moving back to the functional cold plate SQUID. An FFT of the V_s at $T = 4.18$ K and $T = 0.035$ K is shown in Fig. 3.13.

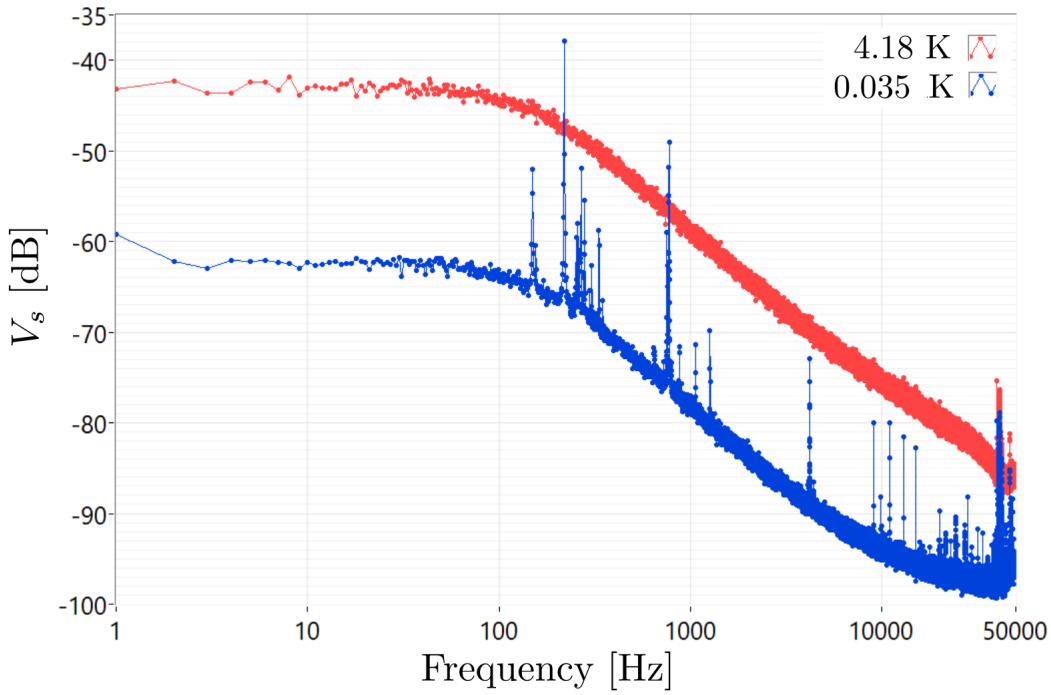

Figure 3.13: FFT of V_s for 4.18 K point (red) and 0.035 K (blue) Both dataset have acquisition parameters: 100 averages, 100 kHz sampling rate, 100k samples.

At low temperatures the Johnson noise current diminishes and the noise floor is reduced revealing pick-up above 100 Hz. However, there is no pick up at 50 Hz or 100 Hz which would be expected if the pickup was due to ambient field in the case of insufficient electromagnetic shielding. The noise is in fact mechanical in nature generated when the dilution refrigerator is subject to mechanical vibrations. In the case of Fig. 3.13 the noise appears in the spectra not because the sensor is cold, but because the pumps circulating

the dilution mixture are transmitting vibrations through the pumping lines of the circulation system. Once the pumps are switched off the noise disappears. It was found that the cold pate sensor was sensitive even to small mechanical perturbations. Vibrational pickup can be generated in absence of the pumps at 4.18 K simply by rhythmical tapping on the support frame of the dilution refrigerator, shown in Fig. 3.15. The vibrational noise is detrimental to the accurate fitting of the Johnson noise signal (Fig. 3.14 (A)) and if unaccounted for leads to a overestimation of the mixing chamber's temperature.

3.2.9 The noise thermometer program

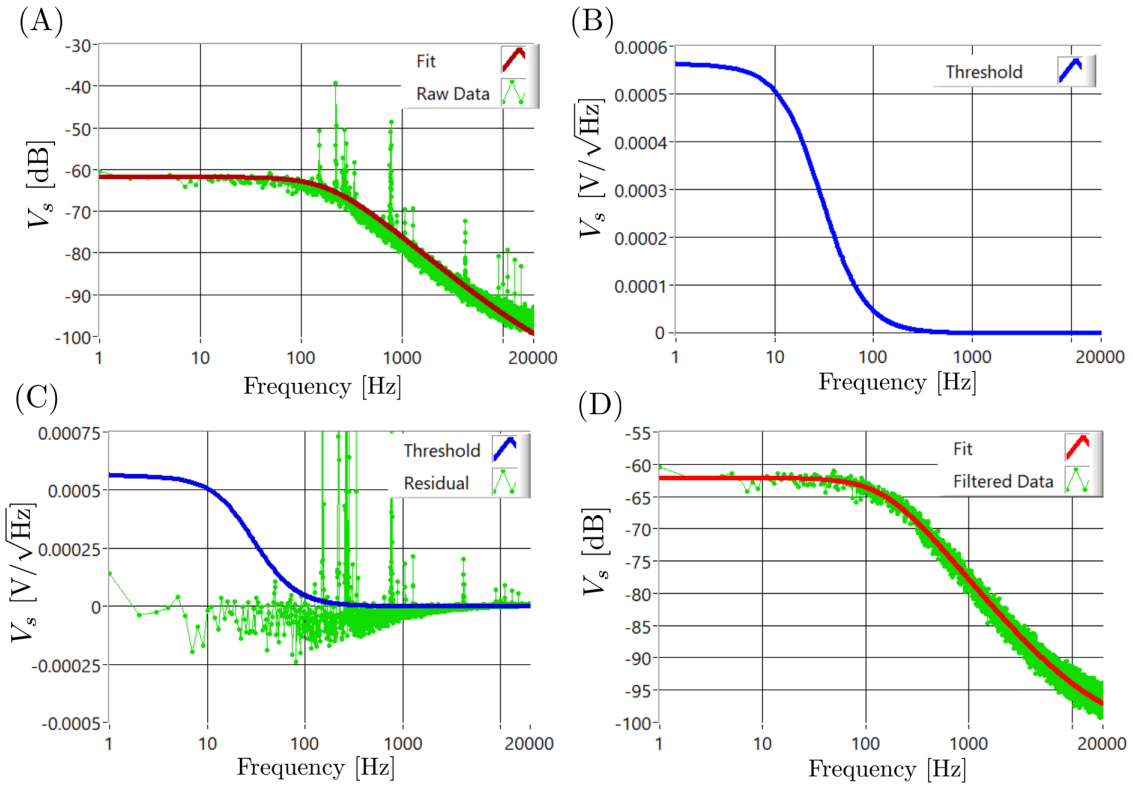

Figure 3.14: Peak removal routine. (A) Initial fit of the data. (B) A threshold for the peak removed is generated using the initial fit. (C) The threshold is compared with the residual of the initial fit to the data to determine pick up. (D) Data with peaks removed is again fit to determine the temperature in the absence of the pick up.

In order to realise a practical thermometry system a program was developed to provide continuous temperature estimations via fitting the SQUID sensors voltage for user defined arbitrary acquisition conditions. Depending on the temperature state the main acquisition parameter of merit is the number of averages. Typically, 30 averages are sufficient to give the temperature estimation to a few % (variance between repeated measurements at a constant temperature). Prior to the temperature estimation a peak removal method is employed to remove ("filter") pick-up above a certain threshold from the dataset. The filtered data is then fitted to give the temperature of the sensor in the absence of the

influence of the vibrational induced noise. There are many ways of implementing peak removal. The main obstacle in this case is the inductive filtering of the spectra, which must be accounted for when considering the threshold level of the pick-up. The peak removal method employed is shown in Fig. 3.14 and the "noise thermometry" program is shown in Fig. 3.15. Referring to Fig. 3.14, (A) shows the unfiltered data being loosely fitted with the standard fitting function. In this case the temperature estimation would be skewed by the presence of the pickup. The initial fit serves several purposes. Firstly a residual is calculated (data minus fitted function). The initial fit also gives an estimate of the cut-off frequency due to the inductance of the input circuit. The first 50 Hz, prior to the inductive cut off, are inspected to give the mean white noise level and the variance. (B) The inductive cut off and the white noise level are used to define a filter function which will act as the peak detection threshold. In this case a 1^{st} order Butterworth filter function is used. (C) The filter function and the residual for the initial fit are compared and any data above the threshold level is considered pick up and removed, "filtering" the dataset. (D) The filtered data is refitted in the absence of the pick up to give an accurate estimation of the white noise level and thus the temperature. The peak removal process takes approximately 2 seconds. Although quicker methods were considered ultimately time is not a constraint when using parallel processing, such that acquisition and peak removal/temperature estimation run in tandem.

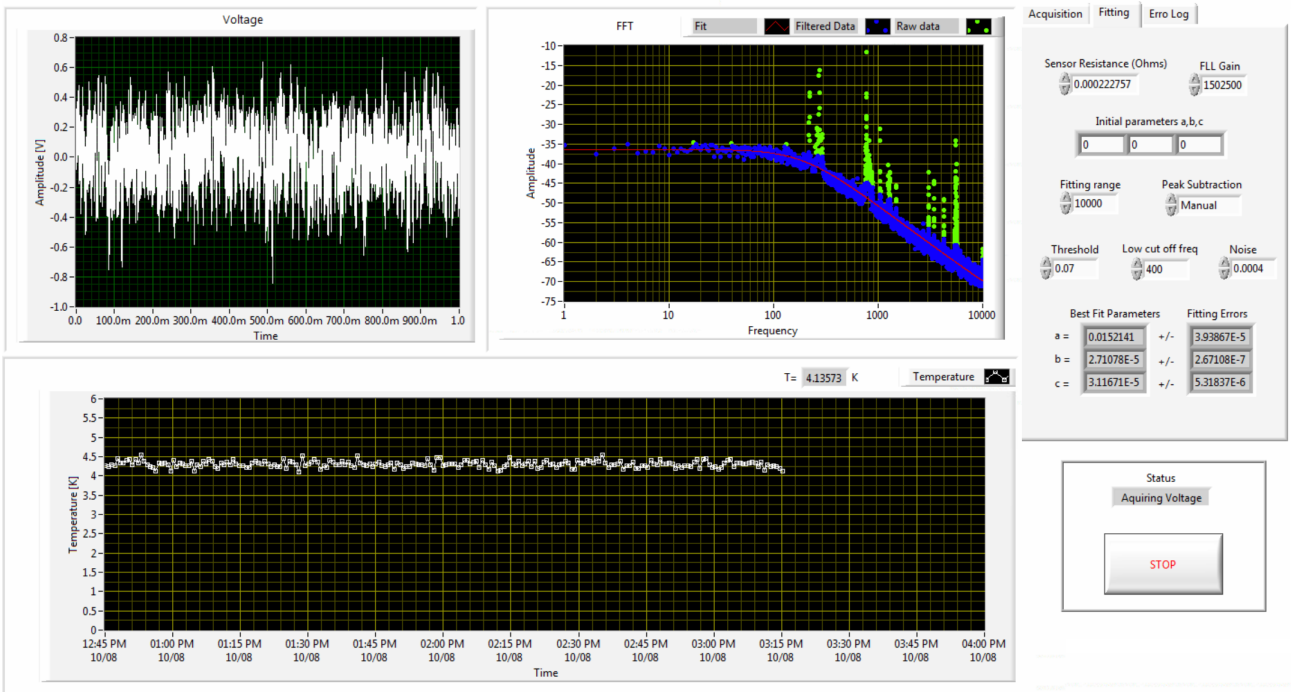

Figure 3.15: Front panel of the noise thermometry program. In this case the temperature is approximately 4.2 K. The FFT of the voltage signal shows pick up, produced by rhythmically tapping the frame of the dilution refrigerator. The pick up is removed via the peak removal method detailed in Fig. 3.14.

Summary

Although issues with the still plate SQUID were never fully resolved, the cold plate SQUID immediately established itself as the primary thermometer for the mixing chamber stage. Its sensitivity and accuracy were beneficial for both experimental temperature control as well as providing diagnostic insight into the behaviour of the dilution refrigerator. This is especially relevant to RF measurements, which can put a considerable heat load on the system. Without responsive thermometry on the mixing chamber stage this cannot be accounted for.

3.3 Experimental wiring

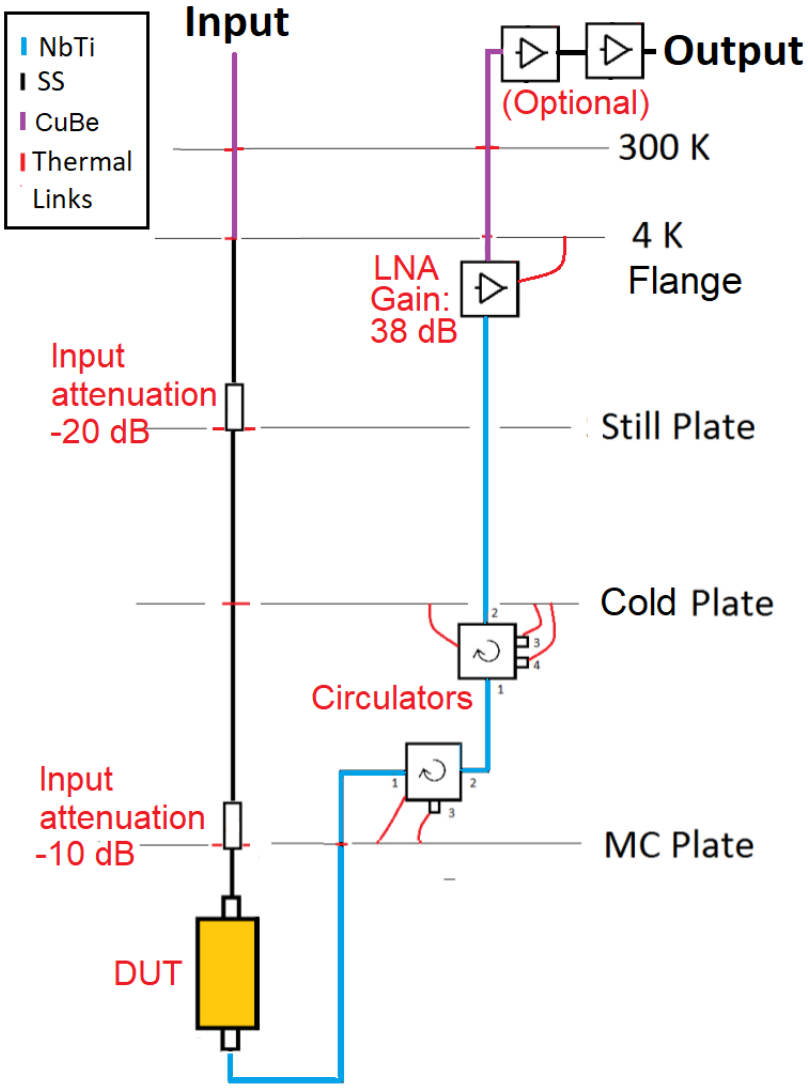

Figure 3.16: Schematic representation of the RF circuit installed on the dilution refrigerator for low temperature measurement. Annotated components of the circuit will be discussed individually. LNA refers to the low noise amplifier, two additional amplifiers are often used at the 300 K output prior to measurement.

The low temperature RF circuit installed on the dilution refrigerator is shown in Fig. 3.16. $|S_{21}|$ transmission measurements where the DUT has been replaced with a "straight through" connection is shown in Fig. 3.17. Several different materials are employed for the coaxial (co-ax) transmission lines in the circuit shown in Fig. 3.16. Copper Beryllium (CuBe) is used between the 300 K and 4 K flange, characterised by a high attenuation to increase thermal isolate the respective temperature stages. Stainless steel (SS) co-ax is used on the input line between the 4 K stage and the input of the DUT, again used for increased thermal isolation. The output line however uses superconducting NbTi co-ax to reduce any attenuation of the output signal of the DUT prior to amplification via the LNA located at the 4 K flange.

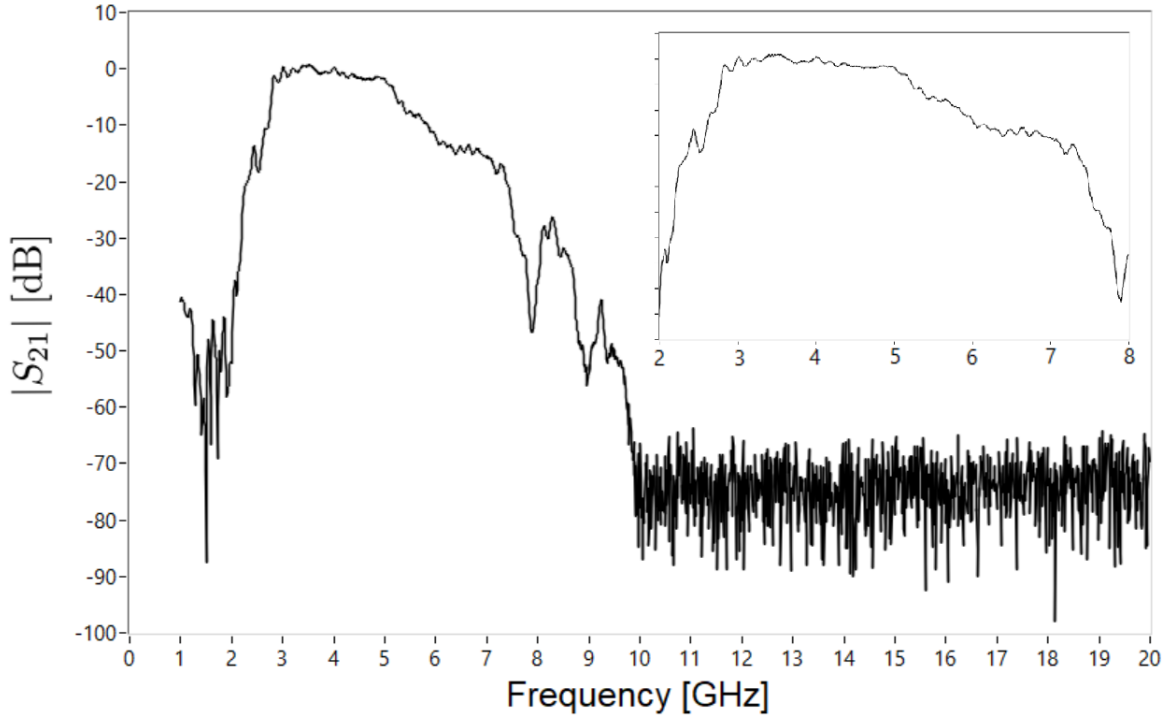

Figure 3.17: The DUT shown in Fig. 3.16 is replaced by a SMA short such as to measure transmission through the circuit in absence of the sample. The bandwidth constraints on the output are primarily imposed by the circulators with a quoted operational range of 3.5 GHz to 7.5 GHz. The data is taken at 300 K and as such is not representative of the transmission at lower temperatures due to the NbTi being in a normal state and adding attenuation to the output. The LNA also has a different gain response at 300 K compared to 5 K. The output around 3 GHz to 5 GHz is relatively flat, however, transmission reduces between 5 GHz and 7.5 GHz. This is due to the attenuation of the CuBe coaxial lines increasing at higher frequencies and must be considered when estimating the input attenuation for low temperature measurements.

Attenuation

The RF input line is interrupted by two *Midwest* microwave attenuators at the still and MC temperature stage of the dilution refrigerator, with the attenuator outers thermally anchored to the respective temperature stages. The attenuators serve two functions; they conveniently reduce the input signal such that lower power RF measurements can be made of the DUT but most importantly they prevent the flow of thermal radiation down the measurements lines. Thermal photons could stimulate the DUT, especially relevant given the sensitivity of a non-linear oscillator, such as discussed in Chapter 2.3.7. Similarly, the thermal radiation could lead to sample heating and a high heat load on the mixing chamber temperature stage of the refrigerator, both detrimental scenarios for experimental measurements. For this reason generally a 20 dB attenuator is used at the still stage and a 10 dB attenuator is used at the MC stage to reduce the effective temperature.

Circulators

Although attenuation is used on the input lines to block the transmission of thermal radiation from the higher temperature stages to the DUT, this method cannot be applied to the output line as any attenuation between the 4 K flange and the MC stage would similarly attenuate the output signal of the DUT prior to amplification via the LNA. *Pamtec* 3.5 to 7.5 GHz bandwidth 4-port circulators are employed to constrain the directionality of the RF signals transmitted through them to a single direction. Two circulators are used successively at the MC chamber stage and cold plate stage respectively to reinforce the isolation ($\approx$ 45 dB). This effectively blocks the propagation of thermal noise down the output line isolating the DUT.

Amplifier chain

A cryogenic low noise amplifier is used at 4 K to amplify the output signal such that it is not completely attenuated as it travels up the CuBe output line to the top of the dilution refrigerator. For the majority of measurements the low temperature amplifier used is a *Low Noise Factory* 4-8 GHz cryogenic low noise amplifier (LNF-LNC4.8C), with noise and gain characteristics shown in Fig. 3.18. The LNA was installed on the dilution refrigeration and thermally anchored to the 4 K flange. Thermalised DC lines connect the 300 K constant current power supply to the LNA on the 4 K plate. Two room temperature amplifiers were also employed for the numerous measurements. A *Miteq* AFS3 amplifier is placed on the port of the 300 K output, with a gain of approximately 31 dB and noise temperature of 66 K between 4-8 GHz. This was followed by a broadband 0.4-20 GHz *Microsemi AML* amplifier with gain 35 dB and a correspondingly higher noise temperature of 290 K, if required.

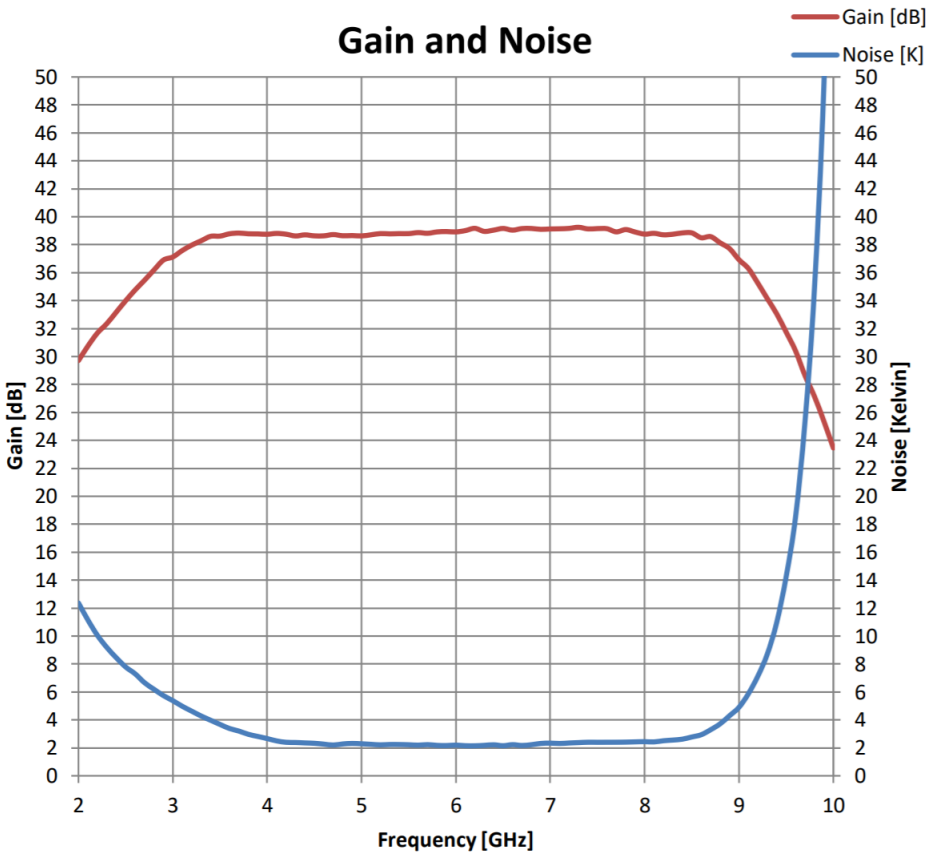

Figure 3.18: Taken from [62]. Gain and noise performance of LNF-LNC4.8C 4-8 GHz Cryogenic LNA at 5 K provided with purchase. The LNA has a fairly flat gain of approximately 39 dB and noise temperature of 2 K.

3.3.1 Sample holders

The two sample holders used to connect fabricated SCPW resonators for measurement are shown in Fig. 3.19. The copper PCB sample box, shown in Fig. 3.19 (A), houses a 3×3 cm^2 PCB. The PCB defines a 50 Ω CPW transmission line to the sample with vias holes to damping spurious resonances supported inside the sample box itself (box modes). SMA ports connect to the PCB via *Anritsu* K-connectors. The sample is secured to the bottom of the PCB via GE-Vanish and connected to the central conductor and ground plane of the PCB CPW with multiple Al wire bonds. The number and density of wire bonding is maximised to reduce the capacitance of the connections and to act as redundancy given their fragility. This was the primary sample box used on the dilution refrigerator RF circuit. Electromagnetic shielding was provided by enclosing the sample in a superconducting tinned (60%Sn/40%Pb) copper cylinder with an additional layers of μ-metal surrounding the outer circumference.

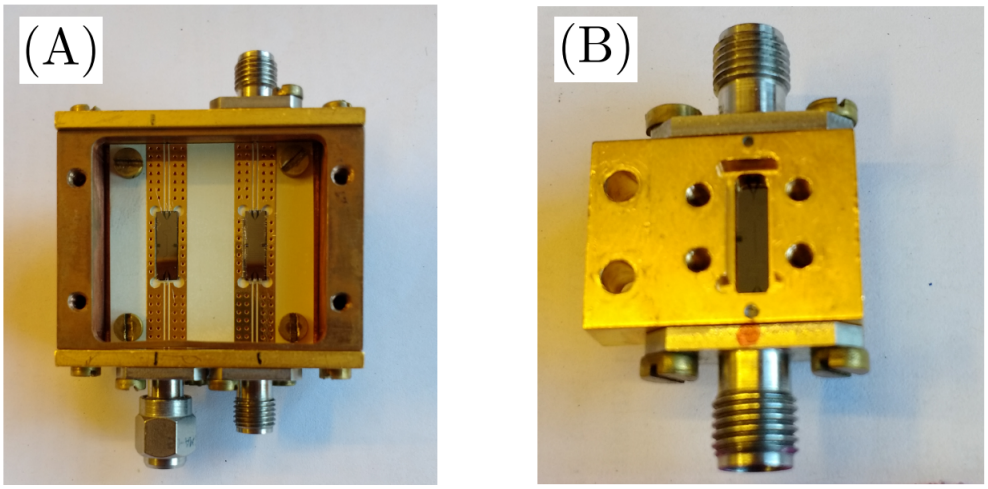

Figure 3.19: Photographs of sample boxes with top plates removed. (A) "PCB sample box" used for primarily for dilution refrigerator measurements. (B) "Contact sample box" primarily used for RF probe measurements conducted at 4.18 K in a transport Dewar.

The gold-plated copper contact sample box, shown in Fig. 3.19 (B), houses a single 3 mm × 7 mm CPW resonator. Instead of a PCB, mechanical contact is used to electrically connect the ground plane and central conductor. A lip of the edge of the sample box is mechanically put into contact with the outer ground plane of the sample. *Anritsu* K-connectors are similarly brought into mechanical contact with the central conductor either side of the sample, connecting it the inner conductor of the SMA ports. The sample box is designed for the precise dimensions of the CPW resonator such that the need for alignment is minimised. A light contact pressure is applied via screw fastenings pushing the sample up into contract with the ground plane and the K-connectors. In practice sample installation is straightforward, but mishandling of samples during installation is more probable in comparison with the PCB sample box, which can lead to defect generation. The pressure applied to form the connection must also be constrained so as not to damage the sample or the K-connectors. An advantage to this sample holder is its smaller dimensions in comparison with the PCB sample box, corresponding to higher frequency box modes in comparison to the PCB sample box. This sample box was primarily used for measurement of samples at 4.18 K using an RF measurement probe immersed in liquid He (provided by a transport Dewar). The probe simply consists of stainless steel SMA terminated coaxial lines (in/out), with a copper heat sink to which the sample is anchored to. Shielding is provided by a Nb cylinder to attenuate penetrating magnetic fields either end.

Chapter 4

PTB Period Doubling sample

The period doubling (PD) sample was discussed in Chapter 2.3.6. The sample consists of a $\frac{\lambda}{2}$ Nb CPW resonator with a single Nb tri-layer RF SQUID embedded at $1/3^{\text{rd}}$ and $2/3^{\text{rd}}$ the total length of the resonator. The sample was fabricated at PTB, designed by A. Zorin et. al [57] primarily to exhibit a period doubling bifurcation. This effect was studied by my colleague K. Porsch and I refer the reader to her PhD thesis [58] for a comprehensive review of the sample and its operation as a period doubling bifurcation detector. I studied this sample in the context of wave mixing, as such the PD sample influenced the design of RHUL fabricated samples that will be discussed in Chapter 6 and 7.

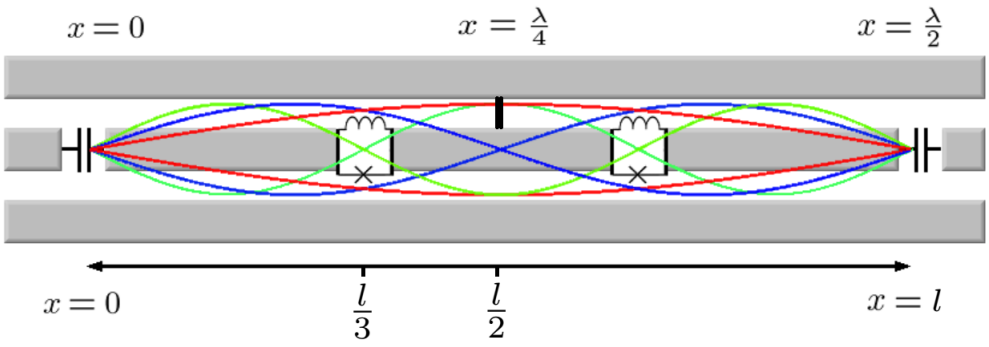

Figure 4.1: Representation of the period doubling sample. The RF SQUIDs are located at the current node of the third mode such as to minimise third harmonic generation. Two SQUIDs were used to increase the effective non-linearity. There is also a resistor to ground around the $l/2$ position such as to dampen the third mode, at the expense of also dampening the fundamental mode.

The period doubling bifurcation is a manifestation of the quadratic non-linearity imparted to the Nb resonator. The magnitude of the quadratic non-linearity can be tuned via the DC phase drop (ϕ_{DC}) over the junctions, which is controlled by an external magnetic flux, as discussed in Chapter 2.3.6 and shown in Fig. 2.34. In this mode of operation the sample constitutes a non-linear medium which can support TWM, with the resonant

geometry increasing the interaction time of the photons with the non-linearity. The position of the non-linearity in the resonator determines the magnitude of the interaction between the non-linear media (the RF SQUID) and the individual modes. The location of the RF SQUIDs in this device were chosen to couple the first two modes of the resonator. The third mode has a node in its current distribution at the insertion point of the non-linear elements. This was chosen to prevent the flow of power into the third mode of the resonator via third harmonic generation, as discussed in Chapter 2.3.4.

With an appropriate change in the external flux bias threading the RF SQUID loop the sample can also behave as a cubic media supporting FWM. This allows a number of different mixing regimes to be realised using this sample. In order to illustrate this I would like to highlight a particular measurement taken of the PD sample performed at 4.18 K using the dilution refrigerator RF circuit detailed in Chapter 3.3. The measurement set-up is shown in Fig. 4.2, consisting of an input provided by two *Anritsu* CW microwave sources, where the output is captured by an *Anritsu* spectrum analyser.

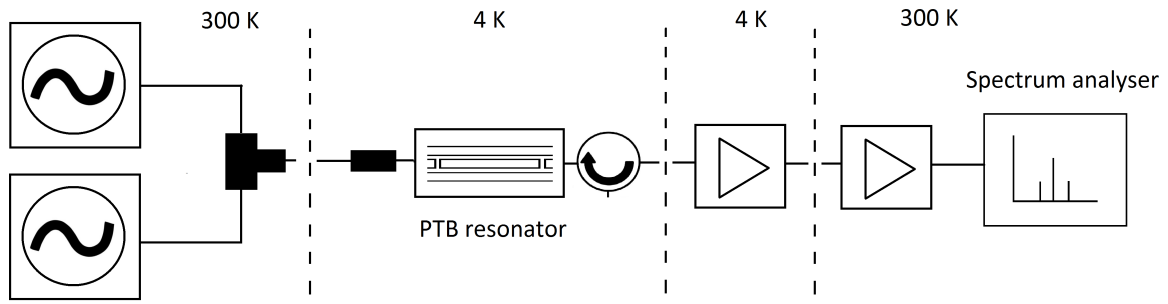

Figure 4.2: Two continuous wave (CW) sources are used to provide the input signal sent to the sample input via the measurement circuit detailed in Chapter 3.3 (Fig. 3.16). The output is amplified and measured using a spectrum analyser. A magnetic field is used to control the external flux, tuning the order of the non-linearity.

The CW sources provide two waves to be mixed via the non-linear media with other modes meeting the frequency and phase conditions for a sustained interaction. For the purpose of this measurement we will refer to the frequencies of these sources as ω_s and ω_p, representing the signal and the pump respectively. The signal $\omega_s = 4.3020$ GHz is close to the resonant mode (4.3025 GHz) at a constant power of approximately -90 dBm, its frequency and power will remain constant throughout this measurement. The pump is set to a frequency of 8.6050 GHz corresponding to the second mode of the resonator. The pump frequency is constant throughout the measurement, however, its power will be swept. The spectrum analyser acquisition window is positioned around the signal such as to measure the signal amplitude and any mixed products appearing around the signal frequency. An external flux is manipulated via a DC voltage over a superconducting NbTi

coil in close proximity to the sample, threading a DC flux through the RF SQUID loop allowing the phase over the junction, ϕ_{DC}, to be adjusted.

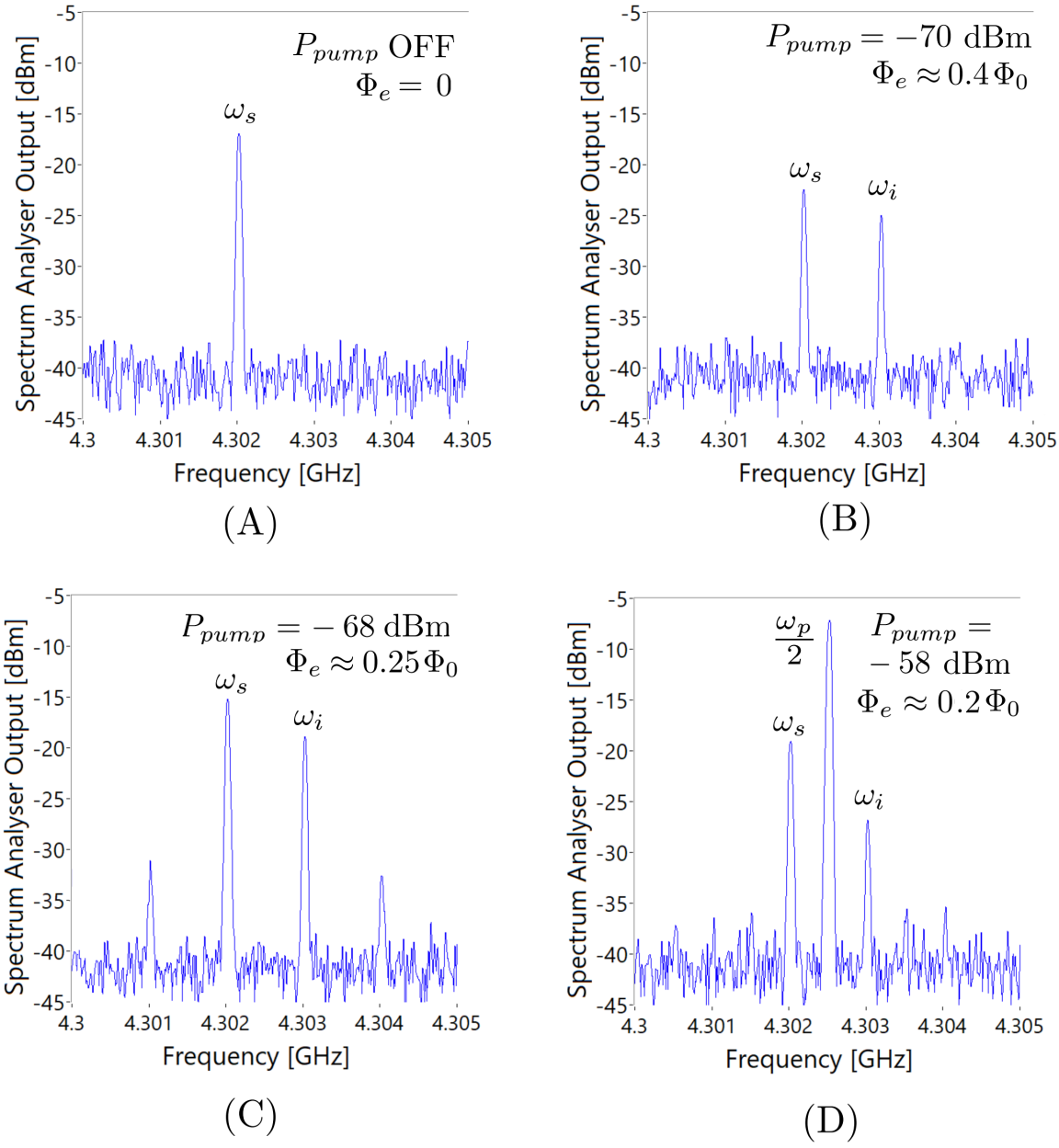

Figure 4.3: PD sample - A selection of spectrum analyser outputs at different positions of flux, demonstrating observable mixing regimes. The signal frequency is $\omega_s = 4.3020$ GHz and the pump frequency is $\omega_p = 8.6050$ GHz. When the pump is off (A) no mixing is observed. When the pump output is on, mixed products can be seen in the output around the fundamental mode (4.3025 GHz), where the mixing regime corresponds to order (and relative magnitude) of the non-linearity at that point in flux. The following mixing regimes can be observed: (B) non-degenerate TWM (C) non-degenerate TWM and non-degenerate FWM (D) non-degenerate TWM and a period doubling bifurcation (PD) ($\omega_p = 2\omega_s$).

The measurement procedure is as follows. An arbitrary external flux is set, the signal

output is turned on while the pump output remains off. The amplitude of the signal is measured via the spectrum analyser and fitted for the peak amplitude in the absence of the pump tone for that position of flux. Given the resonant frequency of the resonator can also change with flux as the inductance of the RF SQUID is changed, it is important to repeat this measurement in the absence of the pump at every new point in flux. Once a reference has been made of the signal amplitude, the pump is output at a fixed frequency, with the spectrum analyser capturing a suitable window around the resonance. The pump power is incremented from -80 dBm to -46 dBm, with the spectrum analyser capturing the response around the resonance at each step. Once the power sweep of the pump is complete, the flux bias is incremented, changing the flux threading the SQUID, modulating the phase ϕ_{DC} over the junctions. The process is repeated until the flux has been incremented through 1 Φ_0. A selection of spectrum analyser outputs are shown in Fig. 4.3.

Analysis is performed primarily with a peak detection algorithm employing a least squares fit. The output of the spectrum analyser for a certain pump power and external flux bias is scanned for peaks in the spectra of a specified width and threshold amplitude. The amplitude and location of significant peaks in the spectra can be compiled. Given the frequency of the pump and signal are known the frequency matching conditions of TWM and FWM can be used to attribute the locations of the peaks in the output spectra with the corresponding mixed products/components. Depending on the observed components the mixing regime can be categorised. For example, if a peak is detected at $\omega = \omega_p - \omega_s$ (Fig. 4.3(B)) then this would be attributed to an "idler" ω_i and the mixing regime would be categorised as TWM.

In this measurement the manifestation of the cubic component of the non-linearity is observed via the mixing of components generated via non-degenerate TWM. An example is shown in the Fig. 4.3(C). When a significant cubic non-linearity is present in the conjunction with a quadratic non-linearity the signal and idler generate sidebands, corresponding to FWM with relation $\omega_i + \omega_s = \omega_3 + \omega_4$.

Fig. 4.4(A) shows the relative change in the signal tone's amplitude as a function of the external flux and the pump power. Fig. 4.4(B) shows the change in the amplitude of the idler $\omega_i = \omega_p - \omega_s$ which was not supplied at the input. The relative change in the idler and signal as a function of external flux can be used understand the non-linearity mediating the parametric interactions. However, given the output of the spectrum analyser can be categorised (TWM, FWM, PD or a combination) by the mixed products appearing in the spectra around the fundamental, a map of the mixing regimes encountered as a function of flux and power can be plotted, shown in Fig. 4.5.

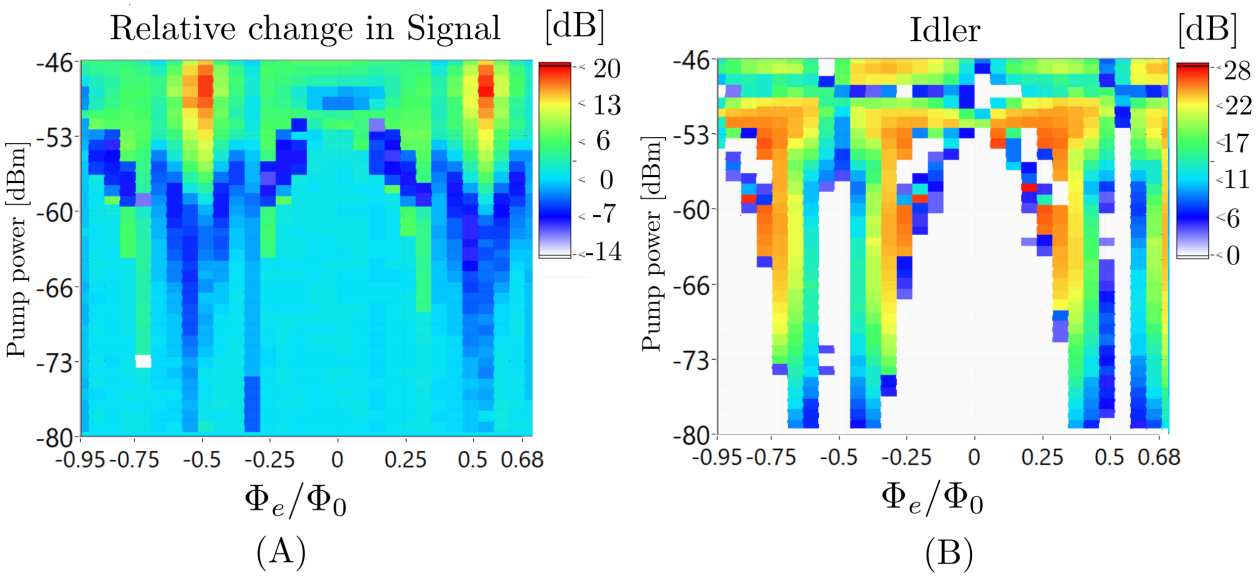

Figure 4.4: Relative change in amplitude as a function of power pump and flux bias for (A) Signal tone (B) Idler tone. A modest 20 dB gain in the signal amplitude can be observed at high pump powers, including the generation of a sizeable idler for a wide range of pump power and flux bias.

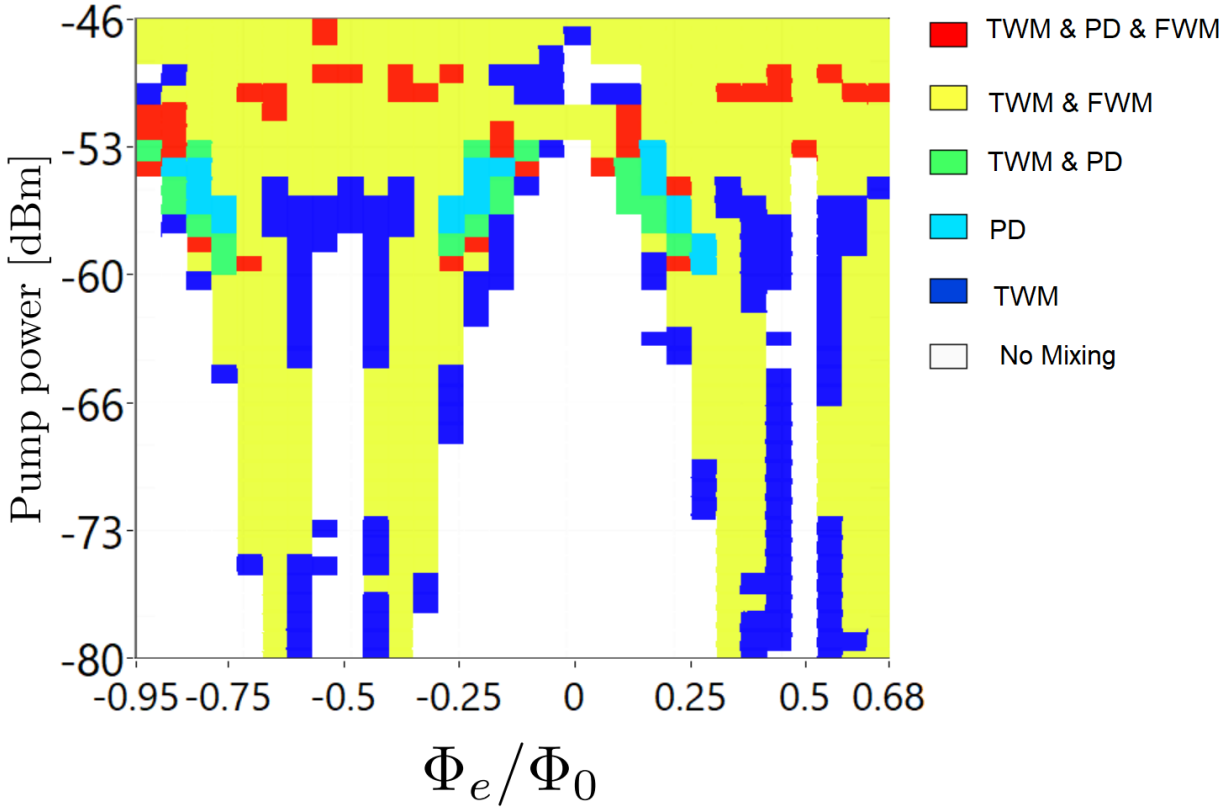

Figure 4.5: Mixing regimes as a function of applied flux and pump power. Legend: TWM - Three-wave mixing, PD - Period doubling bifurcation, FWM - Four-wave mixing. No mixing - only the signal can be distinguished from the noise.

Firstly, addressing the observed mixing at low pump powers (-80 dBm to -60 dBm). In this case the mixing observed is in good agreement with magnitude of the non-linear coefficients as a function of the external flux bias of the RF SQUID, shown in Fig. 2.34. Starting at the position $\Phi_e/\Phi_0 = \pm 0.5$, no mixing is observed, this is expected as the quadratic non-linearity is zero at this point, such that TWM cannot be supported by the media. Around $\Phi_e/\Phi_0 = \pm 0.5$ the magnitude of the quadratic non-linearity increases and TWM is observed even at the lowest powers due to the maximised quadratic non-linear coefficient in this region. Moving toward integer flux FWM is encountered as the cubic non-linear coefficient becomes larger. As the flux gets closer to integer flux (Φ_e/Φ_0) mixing is restricted to higher powers, corresponding to the reduced strength of the quadratic non-linearity. No mixing is observed in the region of integer flux.

At higher pump powers, -60 dBm to -46 dBm mixing can be observed at almost every position of flux even at the points corresponding to an external flux of $\Phi_e/\Phi_0 = \pm 0.5$ and integer flux. At higher pump powers the pump tone itself can significantly modify the phase difference over the junction resulting in a perturbation of the non-linear response. Around integer flux this is less noticeable as the gradient of β as a function of the phase difference over the junction is low, however, around $\Phi_e/\Phi_0 = \pm 0.5$ the gradient of β as a function of the phase difference over the junction is much higher, with a small deviation in the phase resulting in a large change in β.

The PD sample design presents a versatile parametric non-linearity. The main advantage of the sample is the ability to promote a significant quadratic non-linearity which allows for a TWM regime and non-degenerate parametric amplification to be manifested with the aforementioned advantages over the more tradition degenerate FWM available with a solely cubic non-linearity. The cubic component can similarly be promoted via the changing of the external flux threading the loop, such that if desired FWM could be manifested around the fundamental mode.

Chapter 5

Fabrication

The primary focus of my PhD project was the fabrication of superconducting CPW resonators with integrated Al Josephson junctions, using the facilities available to me at RHUL. Of great interest is the development of low critical current $Al/AlO_x/Al$ tunnel junctions, in order to realise non-linear microwave Josephson circuit elements. In this chapter the methodology and procedures for the fabrication of Nb CPW resonators, small area Al Josephson junctions and the subsequent integration of these technologies will be discussed. These techniques were used to fabricate the samples detailed and measured in Chapter 6. The fabrication of Nb nanobridges was also explored and will be discussed in final section of this chapter. Measurement of fabricated Nb CPW resonators with etched nanobridge constrictions is reported in Chapter 7. This chapter will focus on the methodology and techniques developed over the course of my fabrication efforts. Example step-by-step recipes detailing the main fabrication processes discussed in this chapter can be found in Appendix A.1, A.2 and A.3.

5.1 Niobium CPW resonators

5.1.1 Resonator design

The quartz-chrome optical mask used to define the CPW resonators which will be used for this project is shown in Fig. 5.1, designed by a previous PhD student, I. Alfaleh, and fabricated by *Compugraphics Jena GmbH*. The mask features several different geometries of $\lambda/2$ CPW resonators among other patterns. The three most relevant designs, which will be referred to as R1, R3 and R5, are shown in Fig. 5.2 and Fig. 5.3.

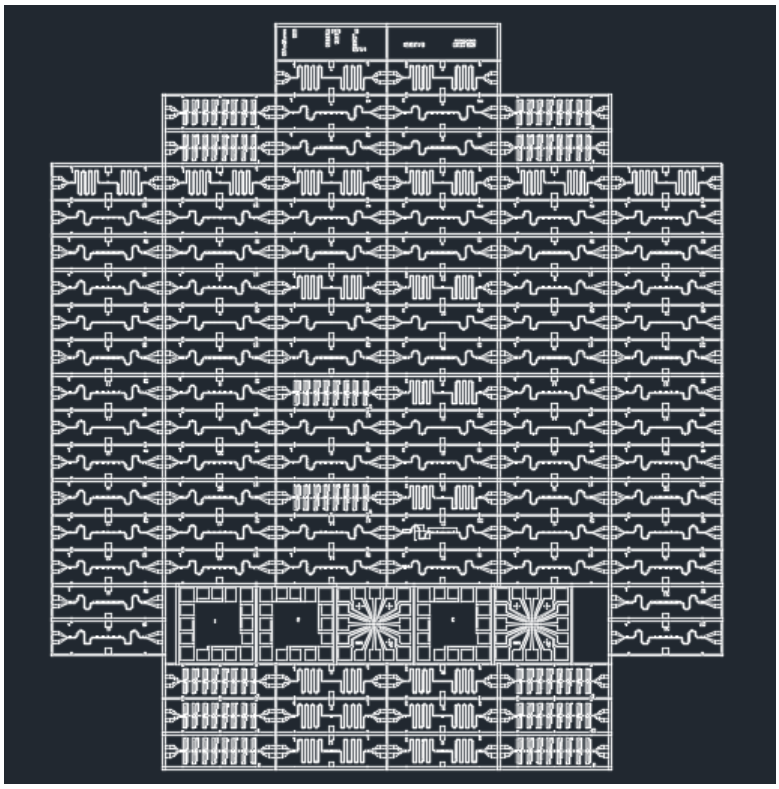

Figure 5.1: Design of 2 inch quartz chrome optical mask used for optical lithography.

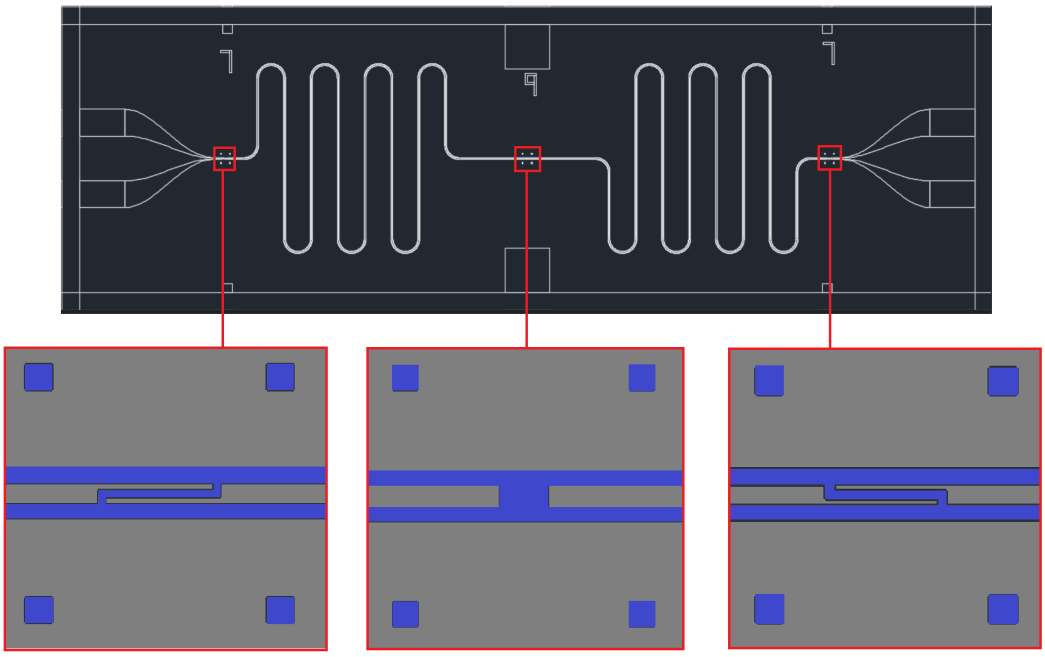

Figure 5.2: R1 design CPW resonator (overall dimensions 3 mm $\times$ 10 mm). Intended resonant frequency is 1.85 GHz, chosen such as to have numerous harmonics over a 1-10 GHz bandwidth. A gap in the central conductor is located at the $l/2$ point of the fundamental mode, where l is the length of the resonator. The gap is 10 μm in width. The square geometries surrounding the central gap and the capacitors are intended to be used as electron beam lithography markers.

The CPW geometry employed in the R1 design has a central conductor width of $W = 10$ μm, the ratio of the width to the ground plane separation is $\frac{S}{W} \approx 0.52$, with a typical $\epsilon_{eff} = 6.4$, corresponding to an approximate 50 Ω impedance. Two symmetric coupling capacitors defining the cavity have capacitance $C_{in} = C_{out} \approx 1$ fF . The resonator has an intended resonant frequency of 1.85 GHz. A defining feature is the gap in the central conductor at the middle of the resonator ($l/2$ point). The gap is intended to be filled by a discrete element bridging the central conductor. Although a convenient feature when insertion of an element at $l/2$ is required, this feature does limit the applications for this design.

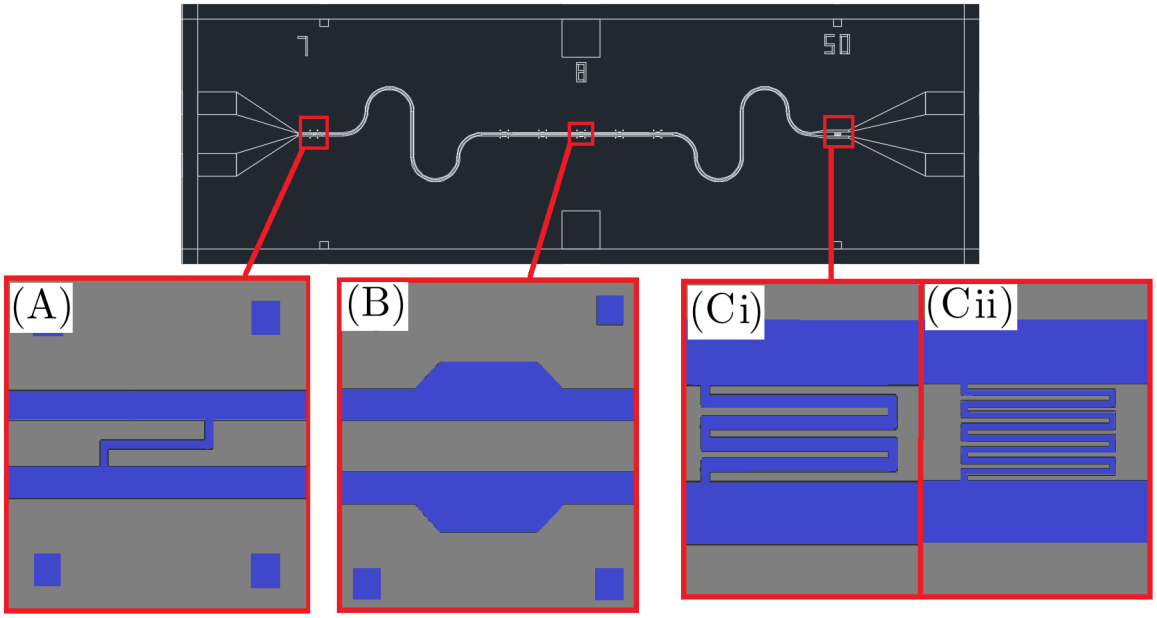

Figure 5.3: R3 and R5 design $\lambda/2$ CPW resonator, both have an approximate resonant frequency of 6 GHz. The R3 and R5 resonator designs have the same C_{in} (A), however differing C_{out}. The R3 design has a "3 finger" interdigitated capacitor (Ci), whereas the R5 design has a "5 finger" interdigitated capacitor coupling to the output of the transmission line (Cii). The central conductor has five sites for intended EBL integration such as that shown in (B).

R3 and R5 design have a higher resonant frequencies; R3 $\approx$ 5.96 GHz and R5 $\approx$ 5.91 GHz. The CPW geometry employed in R3 and R5 is identical, with W= 20 μm and $\frac{S}{W} = 0.52$ once again defining a 50 Ω impedance given $\epsilon_{eff} = 6.4$. In contrast to the R1 design, R3 and R5 feature an asymmetric coupling capacitance. Where $C_{out} \approx 10$ fF for the R3 design and $C_{out} \approx 30$ fF for the R5 design.

Each of the three designs has positives and negatives. The R1 design has the highest loaded quality factors of all three of resonators due to the lower capacitive coupling, however, the gap in the central conductor at the $l/2$ point constrains its functionality unless the device design requires a discrete element in the middle of the central conductor. The

R3 an R5 designs are more versatile. The "bare" resonators (no modification/insertion of additional elements) can be easily studied without introducing ambiguity such as a superconducting short required to measure the "bare" R1 design. Although a gap is not featured in the optical mask of the R3 and R5 design a gap can be manually engineered via electron beam lithography (EBL) and reactive ion etching (RIE), which will be discussed in Section 5.3.

A main detraction of the R3 and R5 design is the design of the CPW geometry around the points of intended discrete element integration. Shown in Fig. 5.3(B) the ground plane can be seen to widen, increasing the central conductor ground plan spacing from approximately 10 μm to 20 μm around these positions, altering the capacitance to ground. As discussed in Chapter 2.1.1 the characteristic impedance of a CPW is determined by its geometry). The widening of the ground plane separation defines an impedance mismatch around these points of integration, lowering the quality factor of the resonant modes. This also has potential implications regarding integration of nano-fabricated components which will be discussed in Chapter 6.2.1. Although this is a disadvantage in comparison to the R1 design which does not feature these widenings, the R3 and R5 design are still favoured due to their continuous central conductor. Allowing them to be easily characterised at 4.18 K prior to modification as well as not being constrained by having to bridge the central conductor at $l/2$ as in the R1 design.

5.1.2 Fabrication of Nb CPW resonators

Optical Lithography

The resonators were fabricated using a 200 nm thick sputtered niobium film deposited on a high resistivity thermally oxidised silicon 2 inch wafer. Although the entire Nb wafer could be patterned with the entirety of the optical mask, shown in Fig. 5.1, this mask features several undesired resonator designs. In order to limit waste the wafers were diced using a "dicing saw" into individual 3 mm $\times$ 10 mm rectangular "chips". This allows for individual resonators to be patterned with the desired design featured on the optical mask.

The resonators are fabricated using optical lithography, illustrated in Fig. 5.4, which begins with the application of positive *Microposit* S1800 series photoresist to the chips surface. Speaking generally resist are comprised of three components, a resin or base material, a photo-active compound and a solvent controlling the viscosity of the resin. In a positive resist patterning process the photo-active compound in its unexposed state acts as an inhibitor to solution in a chemical bath called the developer. When the photo-active compound is exposed to radiation of a specific frequency a chemical reaction occurs in which it becomes more sensitive, increasing the dissolution rate of the resist. Modern resists intended for micro/nano-fabrication (e.g. diazoquinones) employ a myriad of other

chemical reactions to produce the best results such as the inclusion of amide functional groups which undergo chemical reactions, out-gassing N_2 to assist dissolution in the developing agent (agitator).

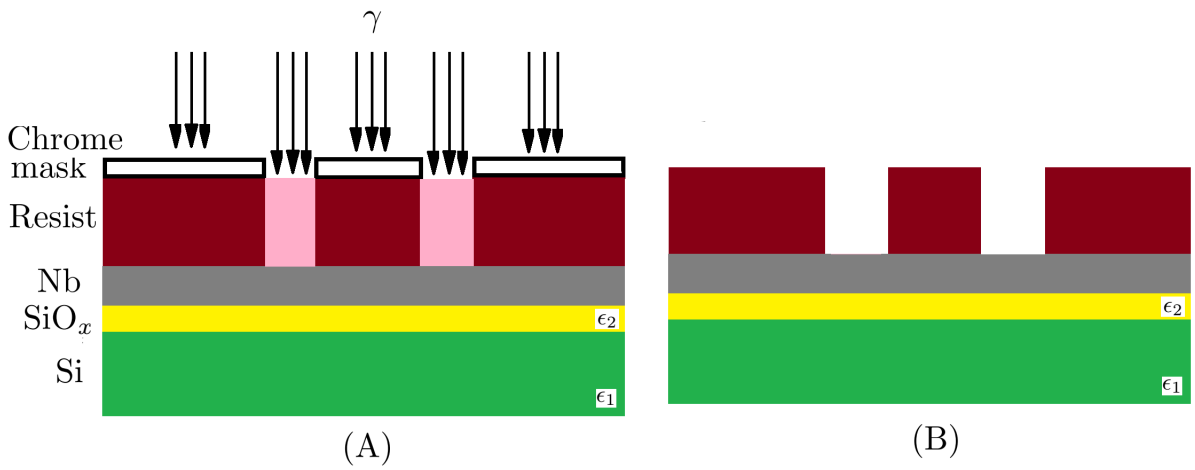

Figure 5.4: Optical lithography process, red - unexposed resist, pink - exposed resist. (A) Optical exposure results in chemical reactions changing the solubility of the exposed resist in the developer. (B) Development. Exposed resist dissolves in the developer resulting in the formation of a patterned mask.

A resist spinner is used to evenly distribute the resist over the surface of the sample with the angular velocity determining the thickness of the resist layer. A hot plate is then used to reduce the content of the solvent in the resist, solidifying and hardening it. The temperature and duration of the baking will also influence the solubility of the resist in the developer. The resist can then be exposed using a *Karl Suss* mask aligner. The optical mask (Fig. 5.1), consists of a plated chrome surface with gaps defining the spacing between the central conductor and the ground plane of the CPW resonator and the capacitors at either end. The mask is placed in front of the radiation source and the sample is brought into contact with the surface of the mask. By its nature contact mask aligner exposure is a defect generating process as in order to produce a high pattern contrast the surface of the resist must be as close as possible to the quartz chrome mask, which acts as a diffraction grating. Exposed resist is then removed via the immersion in the developing agent (MF319), leaving a hard resist mask defining the resonator.

Reactive Ion Etching

Etching of the niobium is performed by the *Oxford Instruments* Plasmalab 80 Plus. Etching commonly refers to a process of removing material via a chemical reaction with an etchant. Reactive ion etching was developed primarily due to the need for highly anisotropic etch. If we consider the example of etching silicon with chlorine, silicon etches slowly in ambient Cl_2 where atomic Cl undergoes chemical absorption on the surface of the

Si but does not break the underlying Si-Si bonds in order to penetrate into the Si leaving the silicon chlorides coating the surface impeding further etching of the Si. Bombarding of the surface with ions using a DC field allows the surface volatiles to be removed freeing more absorption sites allowing chlorine atoms to penetrate deeper into the Si. A DC field in the reaction chamber directs the ions vertically towards the surface to be etched to promote anisotropy of the etch profile. A RF field is also employed to remove secondary electrons generated on the surface of the sample by the ion bombardment. Using the correct combination of process gases and controlling the species present in the plasma allow for selectivity of what you etch and the isotropy. Including the etching of materials such as Nb, the Plasmalab RIE can also perform several other process which are used for surface treatment of chips at various states of fabrication. For example an O_2 plasma can be used to remove (de-scumming/ashing) organic resist residue remaining after the resist masks removal. Ion milling using an Ar plasma can also be used to remove surface oxides on metals.

In order to etch the Nb resonators different process gas recipes are experimented with over the course of fabrication. The two primary etchants considered are SF_6 and CF_4. The CF_4 process is adapted from [63], the etching process was characterised by using off cuts of Nb/Si chips. In order to calculate the etch rates of the S1813 photoresist and the Nb, multiple segments of Nb chips are coated with a known thickness of photoresist, exposed and etched for a varying time, profiling the surface at each time interval with an *KLA-Tencor* Alpha-step profilometer. The surface is profiled firstly with the mask intact and secondly with the mask removed to infer the thickness of the respective layers. The adapted CF_4 recipe was 46 SCCM CF_4 with 5 SCCM O_2, a chamber pressure of 100 mTorr and forward power of 100 W. The addition of the O_2 was added primarily to control the species in the plasma but subsequently decreased the anisotropy of the etch. The etch rates for Nb and S1813 using the aforementioned recipe where both approximately 10 nm min^{-1}.

The process was repeated using a more traditional SF_6 process gas. In this case the etch recipes used were shipped with the Plasmalab RIE system for the intention of etching Nb. The first recipe employed is the Nb etch (20 SCCM SF_6, 10 SCCM Ar), this results in an anisotropic etch were the Ar provides surface aggravation to prevent the build-up of the etchant products during the process. The second plasmalabs Nb etch recipe employed is SF_6 with O_2 (40 SCCM SF_6, 50 SCCM O_2). O_2 is added to specifically to change the anisotropy of the etch, recessing the resist side in order to promote a gradual sloped etch profile. The smooth profile is preferred for deposition as a vertical step profile can result in a discontinuity at the interface of two surfaces, we will discuss this further in Section 5.3 when we consider the integration of an etched Nb resonator with an Al component. Regarding etch rates, the SF_6/Ar process etches Nb 20 nm min^{-1} with a negligible etching of the S1813 photomask. The SF_6/O_2 process was approximately similar in the rate of

etching Nb however the thickness of the S1813 was also reduced (etched) at appropriately 10 nm min^{-1} due to the addition of the O_2.

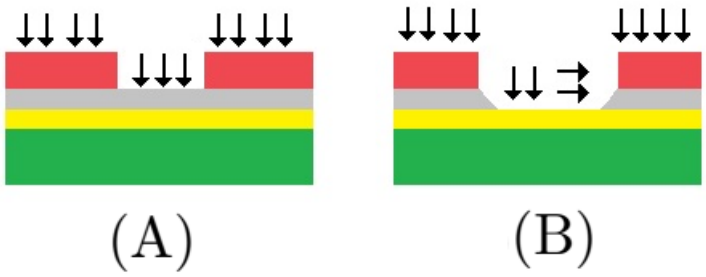

Figure 5.5: Etching processes. (A) Anisotropic etch. (B) Isotropic etch.

Complications

The process of patterning and etching Nb CPW resonators is straightforward in principle, however, problems arise given small rectangular dimensions of the chips (3 mm × 10 mm). As discussed, the resist is thinned to the desired thickness using a resist spinner. Spun resist will "bead" around the edges of small square and rectangular geometry samples as shown in Fig. 5.6, forming globules of thick resist impeding further fabrication. The mechanism for this is air turbulences at the edges and above the corners of the substrate causing the resist at the edge of the chip to dry during the spinning. The hardened resist acts as a barrier preventing the resist being properly spun off from the centre of the sample and a side-wall builds up around the edges.

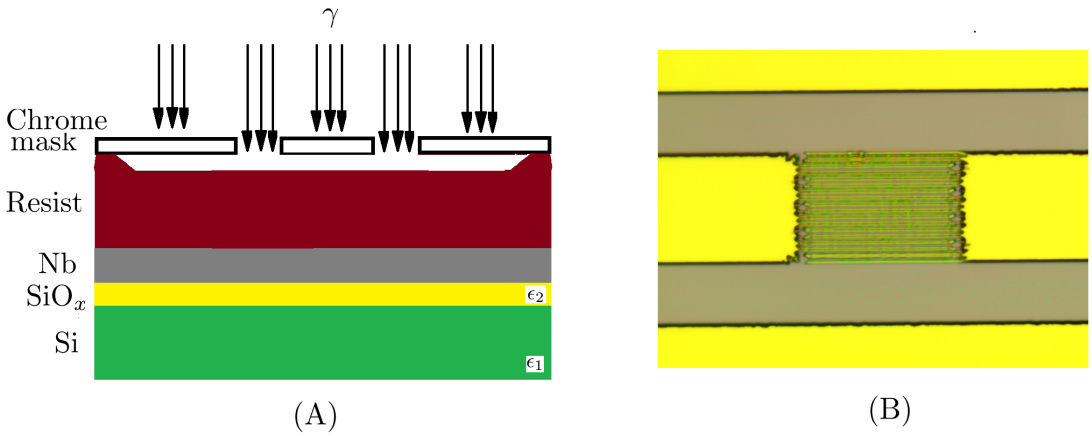

Figure 5.6: (A) Sample with resist mask (red). Beading prevents contact of the chrome mask with the entirety of the surface of the sample. (B) Optical image of the resist mask defining the coupling capacitor of an R5 resonator. In this case resist beading around the edges has lead to a poorly defined pattern in the mask. Resist beading is especially detrimental in the case of the optical contact mask aligner process. Luckily in the case of EBL beading is often irrelevant as the exposure is a non contact process.

The resist beading on the edge of the sample greatly impedes the mask aligners performance and thus the resonator pattern quality. The beading around the edges prevents the chrome mask from making contact with the surface of the resist, promoting diffraction and reducing pattern resolution. The hardened resist bead can also crack and fracture under the pressure of the mask aligner, degrading the fabricated sample. Bead removal is a concern to industrial micro-fabrication and bead removal solvent is available, however it is found that reducing the thickness of the resist by increasing the spin speed results in reduced beading while maintaining a thick enough resist mask layer to withstand the required etching time for the 200 nm of Nb to be removed. Results can be improved further by saturating the sample surface with resist prior to spinning. Optical checks are performed at every step and if imperfections are noted the chip can be cleaned via a hot solvent bath and surface treatment using the RIE, if required. Once cleaned, the resist can be reapplied and the process repeated until the optical resist pattern is deemed acceptable for etching.

5.1.3 4.18 K measurements of fabricated CPW resonators

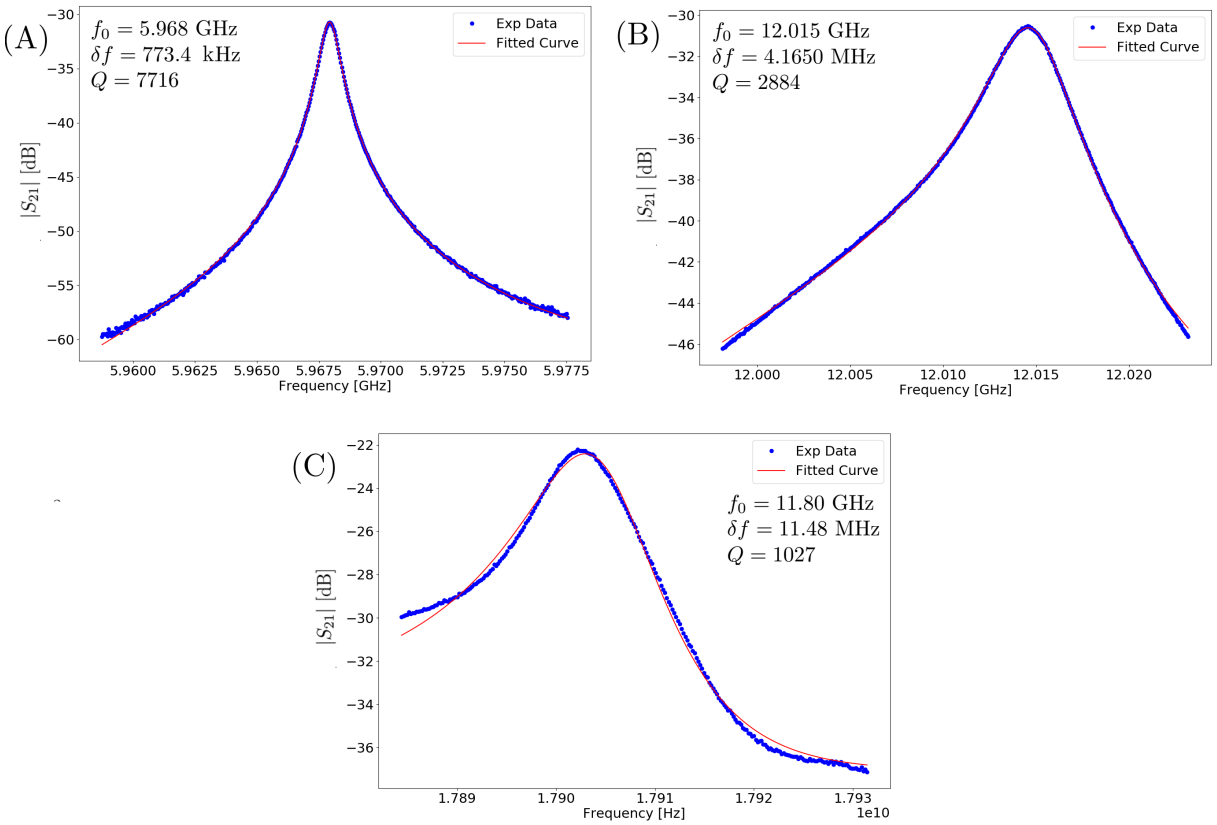

Figure 5.7: $|S_{21}|$ data as a function of frequency for (A) fundamental (B) second mode (C) third mode, of a typical R3 resonator. The data is fitted with a Lorentzian function to determine the quality factor of the modes.

Before integration of additional components, a number of the R3 and R5 resonators were fabricated and measured at 4.18 K using an RF measurement probe immersed in liquid ^{4}He to access their resonant characteristics prior to modification. Fig. 5.7 show the first three modes of a R3 design Nb CPW resonator at 4.18 K, fitted to obtain the respective quality factors of the modes. Although in general all test resonators were in good agreement regarding their fundamental frequency and loaded quality factor there were instances where a highly asymmetric line-shape of the resonant modes was observed. A typical example is shown in Fig. 5.8. As discussed in Chapter 2.1.4 the Fano line-shape is often used to describe such resonant features. In order to manifest a Fano resonance the discrete state, in this case the resonant modes, must be coupled to a broad continuum of states. As discussed in Chapter 3.3.1 two sample boxes were used for the majority of measurements, the contact and the PCB sample box. The PCB mounted samples use Al wire bonds to link the ground plane of the sample to the circuit. It was reported that by removing the wire bonds anchoring the CPW ground plane an asymmetric line-shape can be induced due to the varying of the ground potential over the length of the resonator. Fano resonances are also observed when testing CPW resonators using the contact sample box, such as shown in Fig. 5.8. In this case surface imperfections (non-planar features) could be preventing good electrical contact over the entirety of the length of the ground plane of the CPW and the ground plane of the contract sample box. The asymmetry could also be caused by defects in the sample, allowing a pathway for interference with the resonant modes. However this is speculative and ultimately the exact nature of the asymmetry is not well understood. We will encounter asymmetric line-shapes again in Chapter 6 and Chapter 7.

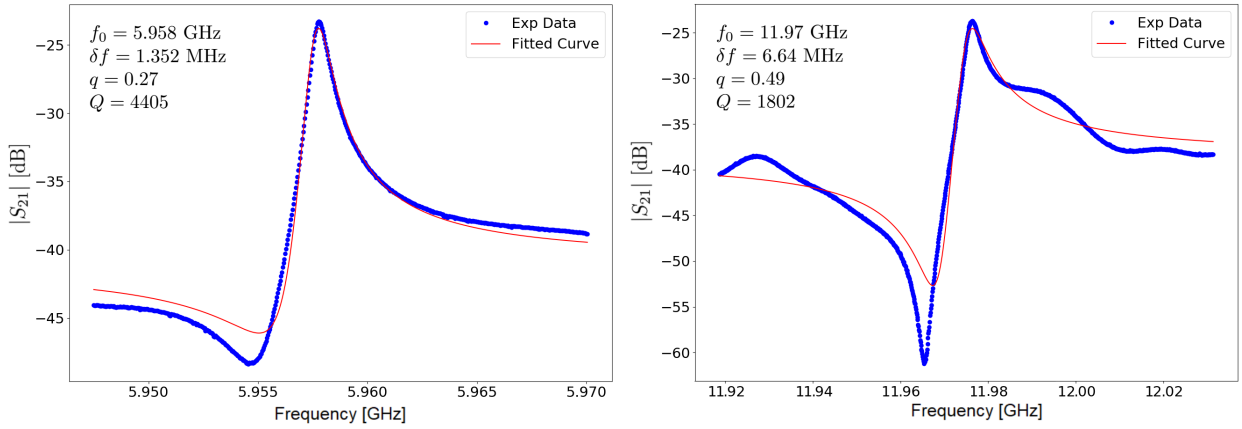

Figure 5.8: $|S_{21}|$ data as a function of frequency for the fundamental and second mode of a R3 resonator measured using the contact sample box. The data is fit using the Fano function (Chapter 2.1.4; Equation 2.1.55). q is the fitted asymmetry parameter, related to the phase shift between the discrete state and the continuum band of states.

5.1.4 Power dependence

At 4.18 K no power dependent behaviour is noted. Fig. 5.9 shows the $|S_{21}|$ measurement as a function of frequency centred around the fundamental mode of R3 design Nb CPW resonator, measured at 4.18 K, for a range of power levels from −40 dBm to −20 dBm in 1 dBm steps.

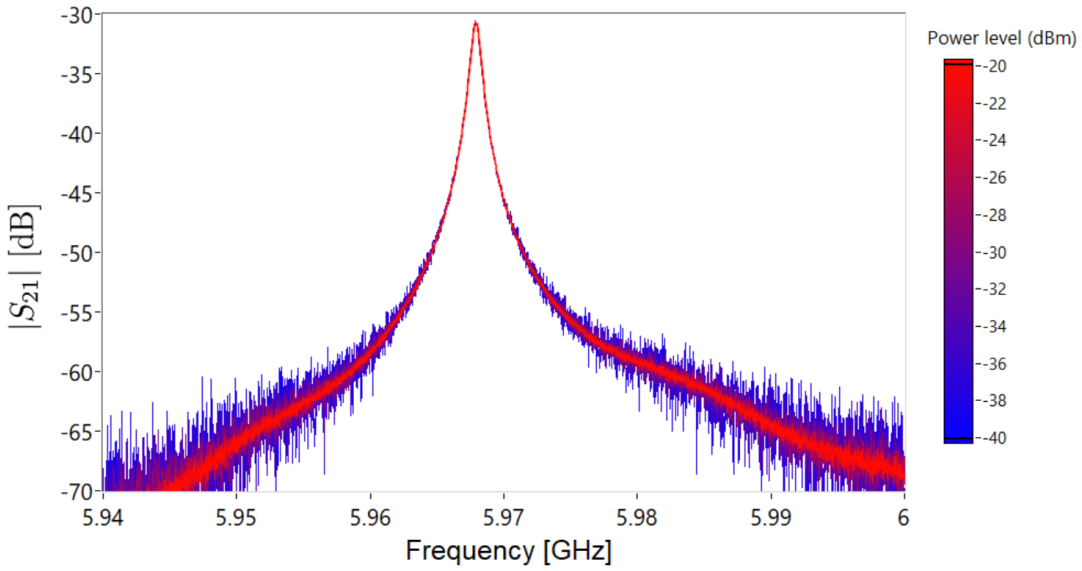

Figure 5.9: $|S_{21}|$ as a function of frequency measurements of the fundamental mode of an R3 resonator for multiple power levels from −40 dBm to −20 dBm in 1 dBm steps. The individual measurements at each power level have been overlaid to show that there is no change in the position or quality factor of the mode with increasing power.

At lower temperatures SCPW's are known to exhibit power dependence due to their intrinsic kinetic inductance, discussed in Chapter 2.2.5. A similar resonator design using an approximately identical sputtered Nb wafer, and measured at RHUL at low temperatures by G. Tancredi [64]. Below 0.1 K anomalous power dependence was noticed at power levels higher than −60 dBm. This behaviour was attributed to the kinetic inductance of the Nb film. Although these resonator samples will be operated below 0.1 K in Chapter 6, as discussed in Chapter 3.3 the low temperature RF circuit on the dilution refrigerator is characterised by a highly attenuated input line, such that this power range will be generally inaccessible. However this will be kept as a consideration throughout measurements.

5.2 Aluminium Josephson junctions

The fabrication of an Al Josephson junction via a shadow angle evaporation process using an EBL mask employing a bilayer resist with a patterned Dolan bridge is shown in Fig.

5.10. The profile of the bilayer resist can be controlled via the use of two resists with differing development and exposure characteristics. The dimensions of the Dolan bridge and the respective angle of deposition of the metallic layers define the dimensions of the junction. The insulating barrier in this case is an oxide grown between the depositions. The material, dimensions of the junction and the thickness of the insulating barrier define the fabricated junctions behaviour.

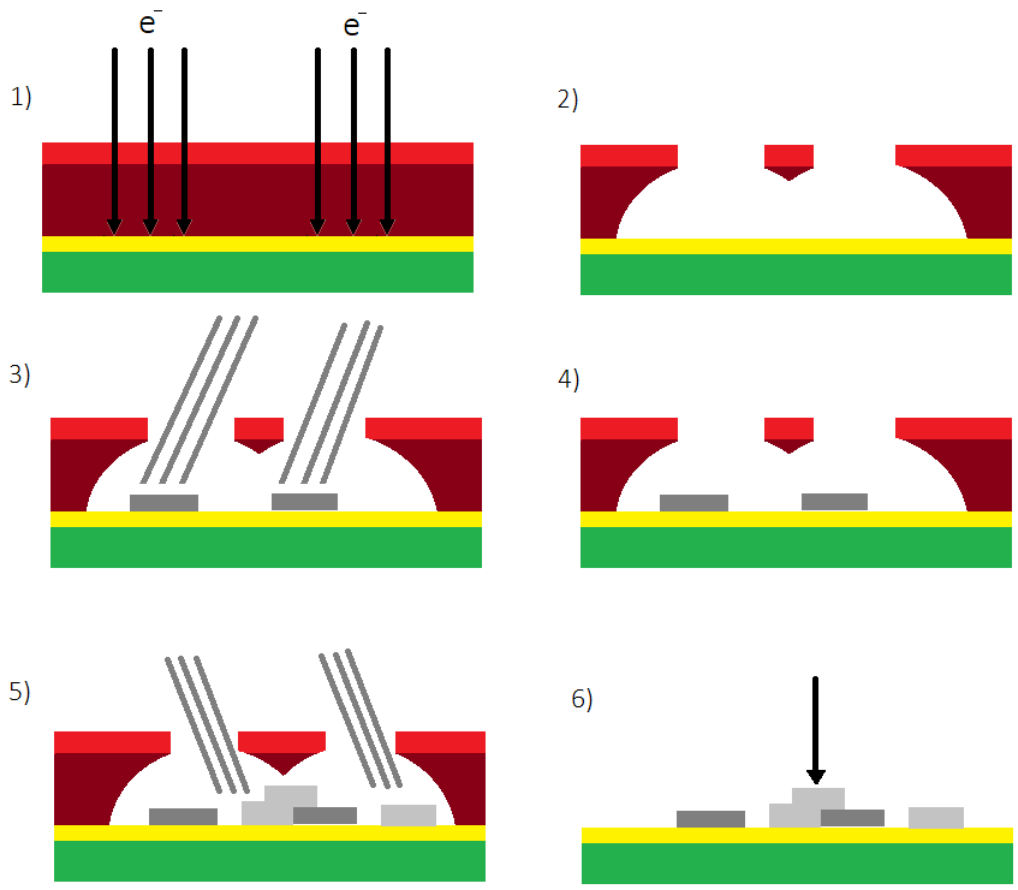

Figure 5.10: Double angle shadow evaporation using a Dolan bridge to form an $Al/AlO_x/Al$ tunnel junction. (1) Bilayer resist stack is exposed via EBL. (2) The exposed resist is removed using an appropriate developer. Resulting in the formation of the Dolan bridge. (3) First angle deposition of the electrode material. (4) The first layer is oxidised. (5) Deposition of second layer forming the overlapping electrodes separated by the oxide barrier. (6) Removal of resist mask.

The fabrication of high quality Josephson junctions is a widely studied subject given their aforementioned importance to cQED. Development of qubit technologies especially have driven the material science behind junction fabrication in order to understand and ultimately overcome the defects and non-idealities in these structures. Fabrication technology is also continuously improving with advances in EBL and deposition allowing for unprecedented levels of control over nano-fabricated geometries. A primary focus of this

work was the development of small (low I_c) Al Josephson junctions for the purpose of integrating with the Nb SCPW resonators discussed in the previous section. In this section we will discuss the design choices and the fabrication methods involved in the fabrication of these Al junctions characterised by a high normal state barrier resistance.

5.2.1 Design considerations

Before discussing the design and fabrication it is worth outlining the desired Josephson junction. A primary focus is on low $I_c \approx 100$ nA structures such as to manifest a non-linear response for even small changes in the current through the junction (approximately -120 dBm assuming a 50 Ω impedance). Aluminium Josephson junctions are routinely realised with overlap areas of the order 20000 nm^2, with a normal state barrier resistance of order several kΩ depending on the barrier thickness and junction area. Although low I_c junctions are of primary interest, larger junctions are also desirable. An optimal junction process would be able to produce scalable junctions ranging from lateral dimensions of 100 nm to several μm.

A design constraint is that the Al junction design and fabrication methods must be compatible and allow for integration with the Nb CPW resonators. Ideally the junctions should be able to be deposited directly into gaps arbitrarily placed along the Nb CPW's central conductor. A primary concern in this regard is the material interface between the Nb and Al. Nb readily oxidises, as such if the oxide is not removed prior to the deposition of the Al a large contact resistance can be incurred at the interface. In the case of a CPW resonator integrated with an Al component, a contact resistance at the Nb/Al interface would lead to loss and dissipation into the environment and would be significantly detrimental to the performance of the device. The surface oxide NbO_x can be removed via an Ar plasma mill performed under vacuum, directly prior to the deposition of the Al. The Ar mill must be substantial enough to clear all NbO_x from the surface of the intended Nb/Al interface however it must not damage or deform the EBL patterned resist mask which defines the geometry formed via the double angle Al deposition.

A brief Ar mill is commonly performed to clean surfaces/interfaces prior to deposition. In this case the milling is generally light (several seconds) and has little effect on the EBL mask. However in order to ensure the Nb surface oxide is completely removed the Ar mill must be extended. As such there is the possibility of damage to the EBL mask defining the junction, structural failure of the Dolan bridge being a primary concern. Furthermore, EBL resist (specifically thin layers ≈100 nm or less of PMMA) can become cross-linked when subjected to an extended Ar milling, which makes them effectively irremovable from the samples surface, this is a further constraint on the design. Subsequently, the necessity for an extended Ar mill requires a robust Dolan bridge, generally requiring the use of a thick resist mask for increased structural integrity and removing the likelihood of cross-linking becoming an issue.

The final stipulation on the junction design is that it must be achievable with the equipment available, that being the RHUL EBL and the Edwards thermal evaporator. As mentioned previously there are several reports of high quality junction fabrication, some of their accounts employ techniques or equipment that are not available to me. This sounds like a mundane design choice but recognising and overcoming constraints of equipments or process method was one of the most challenging aspects of producing a reliable consistent junction fabrication process.

5.2.2 The "T" design

The method shown in Fig. 5.10 details a fairly traditional approach to Josephson junction fabrication, which we will refer to as the overlay design. To fabricate small area junctions using this method generally requires a narrow (100/150 nm) Dolan bridge to space two 100/150 nm wide electrodes. The angle of deposition can be varied, however, typically small angles are employed (15-20°) to overlay the two Al electrodes. Excess Al lands on the surface of the substrate and the resist side wall, how the excess lays is highly dependent on the profile of the bilayer resist and the undercut recess. An advantage of this design is its prominence, it is a proven method to produce consistent Josephson junctions. The disadvantage is although the dimensions are not unreasonable and a 100 nm Dolan bridge is possible to pattern reliably, it can still be regarded as working at the limit of the RHUL EBL's operating range, at least when using thick resist masks. Typically, when attempting to define this order of geometry thin resist bilayers are employed. The narrow Dolan bridge and the possibility of being required to use a thin resist bilayer to fabricate junctions using the overlap design are not ideal when considering the extended Ar etch that must be employed when integrating with Nb. Although some experimentation with this design was carried out, ultimately, another design is chosen with characteristics suited to integration with Nb.

The "T" design Josephson junction is outlined in [65] and a similar design is reported in J. S. Kelly's PhD thesis [66], shown in Fig. 5.11. A MAA/PMMA resist stack on a sapphire substrate is used where the two resists can be selectively patterned with EBL, a 350 μC/cm^2 dose is used to expose the MMA and a 1500 μC/cm^2 dose is used to expose both the PMMA and underlying MMA. A quoted advantage of this recipe was the reported structural integrity of the Dolan bridge and its ability to withstand an extended Ar mill which was used to remove surface oxide for integration with larger Al structures. Deposition and oxidation are all performed in a Plassys system where the layer thickness was 60 nm/100 nm for the respective Al electrodes.

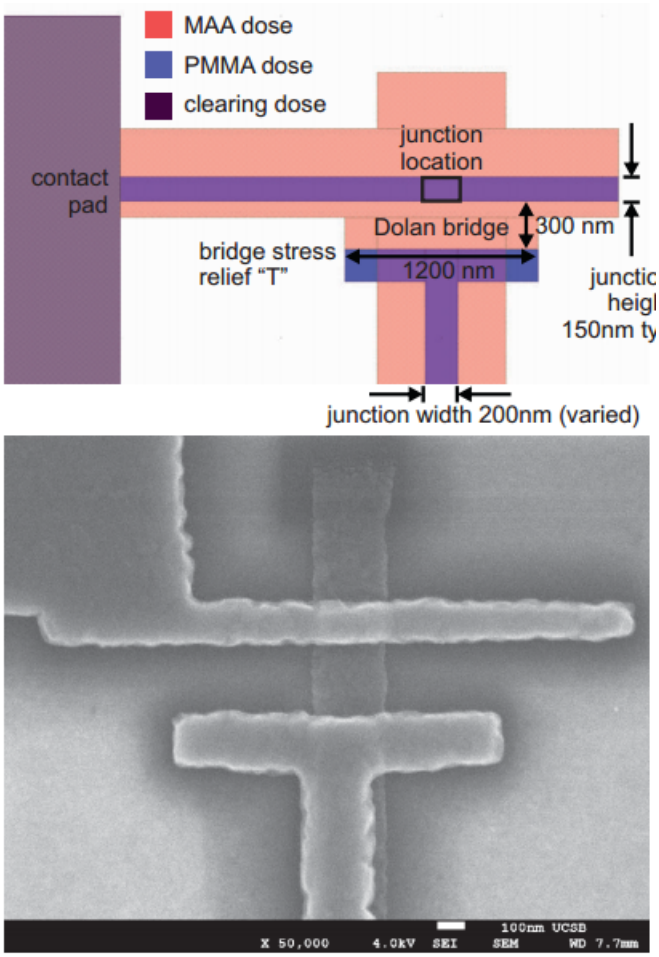

Figure 5.11: Image taken from [66]. T design - The junction is formed much like the overlap design however the two electrodes are now perpendicular. The first layer is deposited at an extreme angle such that the majority of the excess Al is deposited on the resist side wall past the horizontal electrode. Following an intermediary oxidation step. The second layer is deposited at the normal to the surface. The excess which landed on the side wall from the first evaporation is removed when the resist is removed by an appropriate solvent bath.

The reported robustness of the Dolan bridge and the ability to withstand an extended Ar mill was attributed to the stabilising effect the T shaped head on the Dolan bridge. These features were the main motivation to develop the T design using the RHUL fabrication facilities. A secondary advantage related to the large angle of the deposition, the first layer being deposited at an extreme angle of approximately 60° and the secondary evaporation at the normal to the sample surface (0°). The larger angle is necessary given the wider Dolan bridge however it also means almost all of the excess from the angled evaporation is deposited on the side wall. Controlling the excess in the double angled evaporation is very important. In the case of small angles the excess Al can land on the Si and be underpinned by the subsequent deposition, this can result in Al in unwanted places (flag formation). However there is a caveat, the more extreme angle means that less of the deposition material will land on the angled surface of the substrate, as such

the deposition thickness will be reduced unless compensated for by increasing the overall deposition thickness for the respective layer.

One of the main obstacles of adapting the design to work with the RHUL equipment was resist patterning. Instead of having a resist stack and EBL allowing for selective exposure, a more traditional copolymer/PMMA stack was employed. Using the magnitude of the exposure dose, baking conditions, layer thickness and development to promote a sufficient undercut and proximity exposure of the copolymer underlying the PMMA bridge. The majority of the problems encountered while attempting to implement this design were caused by an insufficient clearing of the copolymer under the Dolan bridge, blocking the path of the initial evaporation at the extreme angle. The next section discusses the main considerations regarding EBL and thermal evaporation, in the context of this design of Josephson junction, the problems encountered and how they were overcome.

5.2.3 Fabrication

5.2.3.1 Electron-beam lithography

The resist mask which defines the geometry of the Al electrodes and the Dolan bridge is fabricated via EBL. The methodology is similar to that discussed regarding photolithography, with exposed resist becoming more soluble in the developing agent. In this case the radiation source is electrons accelerated towards the surface of the resist. The resist absorbs energy resulting in chemical changes promoting solubility in the developer. Once the resist has been exposed it is said to be bleached, such that it is transparent to the incident radiation, allowing the electrons to expose the underlying resist. The situation is complicated by the scattering mechanisms available to the electrons. Forward scattering of incident electrons leads to slight pattern broadening however the backscattering off the sample substrate leads to a much broader large area exposure. This can lead to significant exposure of resist in the vicinity extending past the primary exposure dose. This phenomena is often referred to as the proximity effect and is generally modelled with a double Gaussian beam accounting for the effect of the scattering mechanisms. These effects are reduced for thinner resist layers, resulting in the ability to pattern small structures with less concern for these scattering mechanisms. Although proximity effects can be problematic, they also allow for an extra layer of control such that the area of resist can be exposed indirectly if the proximity effect dosing is employed correctly.

Deposition masks often use bilayer resist stacks to form undercuts, such as the resist stack featured in Fig. 5.10. This primarily helps with lift off, the process of removing the mask and the excess deposition material from the sample surface via a hot solvent bath. In the case of a material deposition the undercut ensures separation of the deposition material and the excess landed on the surface of the resist such that discontinuities or tears do not appear when it is removed. In the case of the junction fabrication the

regression of the bottom lying lift off resist layer is going to be essential to clearing the area under the Dolan bridge, such that the initial deposition is able to pass under the Dolan bridge forming the underlying layer of the junction. For a narrower Dolan bridge ($\approx$ 100 nm) such as the overlap design junction this is less concerning, with a 50 nm uncut expected without much effort using standard lift off resists and recipes. However in order to clear out the area under the nominally 300 nm Dolan bridge in the T design (for increased structural integrity) a more extreme undercut is required.

Although a range of resists are available, a copolymer/PMMA bilayer resist stack is used for the majority of my fabrication work. The copolymer/PMMA resist stack can be exposed using the RHUL *Jeol* 6460 EBL system, typically using the maximum accelerating voltage of 30 keV. The bilayer is generally exposed single dose of approximately 100-250 $\mu C/cm^2$ depending on the dimensions of the exposure, resist thickness and the proximity to other exposures. Both the copolymer and the PMMA are exposed with the same radiation dose and developed in the same developing agent. The extremity of the undercut depends on several factors:

- The magnitude of the dose and the proximity considerations due to scattering
- The molecular weight of the respective layers, which can be controlled by solution in an appropriate solvent, (typically anisol)
- The thickness of the respective layers
- Individual resist baking conditions
- Development time and conditions

In this resist stack the PMMA can be thought of a high resolution mask that will be patterned to define the junction electrodes and the Dolan bridge. The copolymer allows for the suspension of the Dolan bridge above the samples surface with the underlying copolymer cleared out such as to allow the deposition material to pass through unimpeded.

5.2.3.2 Thermal evaporation

Deposition of Al is performed using an *Edwards* thermal evaporator. The sample holder allows for a rotation of the sample 360° around a fixed axis which is used to perform the angled evaporations. Two process gases can be fed into the chamber including Ar which is used to perform an Ar mill to clean surfaces prior to the deposition. The second process gas is O_2 which is used to form the insulating barrier between deposited layers of Al using a typical oxidation pressure of 950 mtorr for 2.5 mins.

Thermally evaporating Al is a relatively routine procedure however thicker depositions can be quite difficult to consistently achieve using a thermal evaporator. Although the deposition thickness can be relatively low to form a suitable junction (some recipes use

as little as 20 nm to 40 nm per layer), in this case a thicker deposition is required due to the extreme angle of the deposition. Thicker layers also offer more structural integrity and help to ensure the film is continuous and well-defined. The design shown in Fig. 5.11 calls for a 60 nm Al layer to form the bottom electrode and a 100 nm Al layer to form the top electrode, deposited at a rate of 1 $\text{nm}s^{-1}$. This is an aspect of the design I also favoured, under the principle of promoting a more robust junction. However this was achieved with a *Plassys* electron beam deposition system. Practically achieving the desired layer thickness using a thermal evaporator was non-trivial. Thermal evaporation is achieved by Joule heating of a resistive "boat" in good thermal contact with the deposition material under vacuum. In this work the boats used for evaporations are made of tungsten, favoured for its high melting point, resistivity and general inertness. The thickness of the boat is approximately 0.005 inches. The tungsten has a pressed divet in the centre in which the deposition material is placed. The boat bridges two electrodes. The user can control the voltage across the electrodes and thus the rate of evaporation of the source material. A deposition thickness monitor allows the user to adjust the voltage for the desired rate of deposition.

These particular boats are used as they behave as a well-defined point source for thermal evaporation of materials. Although it was previously stated that tungsten is used for its inert properties, in the case of an Al evaporation an alloying reaction occurs between the tungsten boat and the "molten" Al evaporation source. For low deposition thickness this is not overly concerning and the quality of the evaporated film is unaffected. After the process finishes the used boat however is noticeably brittle and can easily shatter or break in two simply from removal from the electrodes. Generally the boats cannot be reused after any substantial Al deposition. In evaporations which go past a 50 nm deposition thickness using a single boat, the effects of this alloying reaction become much more pronounced. The weakest area of the boat is around the wall of the pressed divet, where the thickness of the boat is reduced due to the curvature. The alloying typically first manifests itself by forming a hole in the Tungsten in the region of this area. This will be immediately noticeable to the user as the current is channelled around the defect caused by the alloying resulting in an increase of the resistance of the circuit, reducing the rate of evaporation. The glow discharge becomes notably more intense as the voltage across the boat is increased to compensate for the increased resistance of the boat. At this point the rate of evaporation can change rapidly with the need for constant compensation by the user. As the boat degrades further intense hots spots can be observed in the mirrored evaporation shield with the intensity of the light increasing over time. The point at which the boat fails, an unideal end to a deposition, is highly dependent on a number of factors and although the user is an important part of controlling the process I could never consistently deposit over 120 nm from a single boat of these dimensions, furthermore the maximum rate of deposition achievable was only 0.5 nms^{-1} and achieving a constant rate

over the course of the evaporation while having to apply feedback to compensate for the degradation of the boat was very difficult. Two solutions were considered, silica coated tungsten boats in order to prevent any alloying action, or thicker tungsten boat that would at least be more resilient to degradation over the course of the evaporation. The latter was explored to minimise the variation of the process by introducing another component (silica) to the problem. Thicker 0.01 inch tungsten boat where sourced with increased lateral dimension also allowing for the accommodation of more deposition material. These boats made a massive difference to process of evaporating Al, completely abating the alloying degradation which had previously constrained the layer thickness that could be reliably deposited. Using the larger boats it is possible to deposit well over 500 nm from a single boat spread over multiple evaporations at stable rates of 1 nms^{-1}.

5.2.4 Fabrication and design development

Test junctions were fabricated on what will be referred to as DC chips, comprised of an oxidised Si substrate with gold leads and contact pads that allow for electrical contact to be made with fabricated devices. These DC chips are patterned using optical lithography and the gold is deposited using thermal evaporation. Due to the poor surface adhesion of gold to the Si substrate a thin (5 nm) NiCr adhesion layer is deposited prior to the evaporation of the gold (80 nm). Each DC chip has 9 sample spaces, Fig. 5.12 shows one individual sample space on a DC chip in a typical configuration used for test junctions. The DC chips allow for a large number of junctions to be produced with leads attached to the gold contacts such that measurements can be made of their IV characteristics. The primary tool for measuring the normal state resistance of the junctions (R_n) is a four point measurement DC probe station with a *Kiethley* 2602 source meter. The probe needles make contact to the gold contact pads connected to the junctions. The voltage is swept between $\pm$ 100 μV and the current is recorded. A linear fit is used to give the resistance of the junction R_n.

As previously stated the most important feature is the formation of a Dolan bridge defined in the PMMA with a clearing of the underlying copolymer to allow the angular evaporation of the underlying layer of Al forming one electrode of the junction. The desired exposure cross-section of the Dolan bridge is illustrated in Fig. 5.13(A). This is the ideal situation with all of the underlying copolymer resist exposed resulting in its complete solution in the developer. However achieving an undercut of this extremity proved difficult.

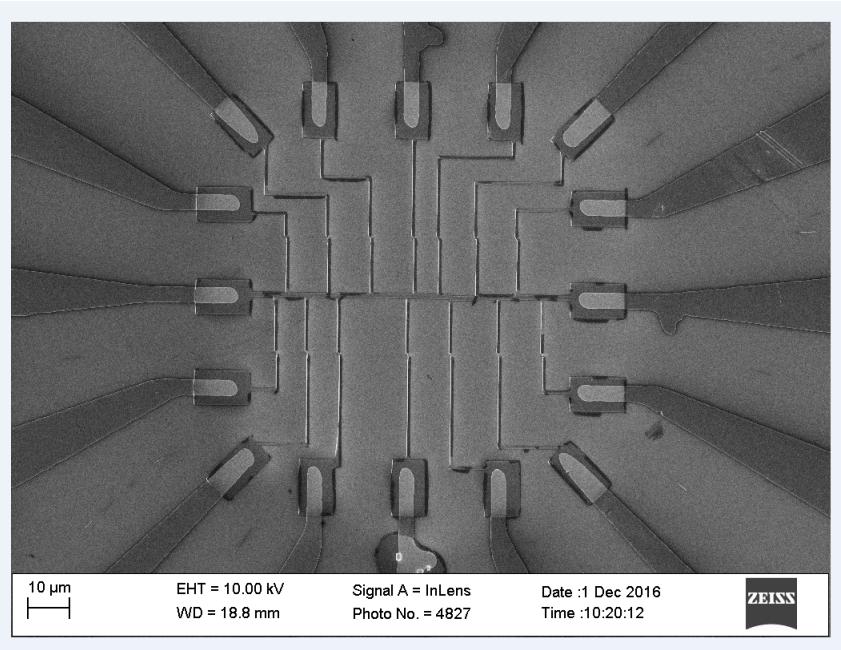

Figure 5.12: SEM image of the configuration used for testing Al junctions. A central conductor runs left to right which acts as a shared ground to individual junctions either side connected to the other gold pads around the perimeter of the sample space. In this case two point measurements of the junction's resistance can be measured with the measurement of solely the shared ground inferring the order of the lead resistance (typically 60 Ω). A four point measurement configuration can also be adopted however the 2 point configuration allows for a larger number of junctions to be characterised.

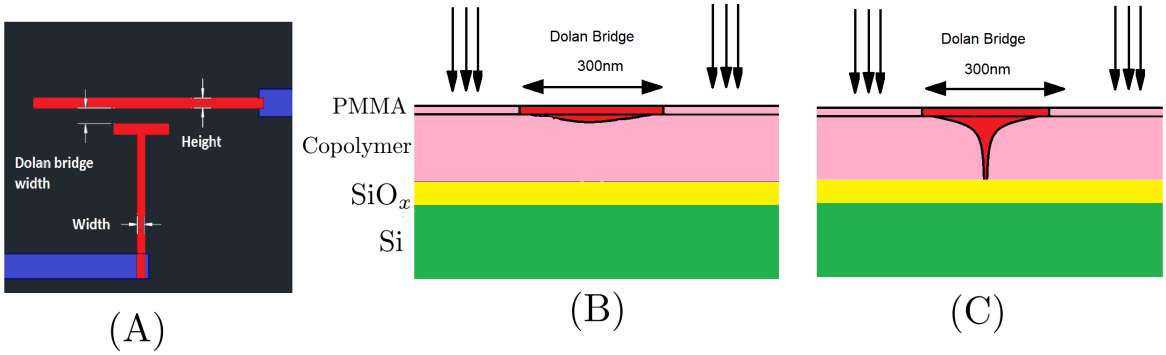

Figure 5.13: (A) The T design exposure pattern, red corresponds to high dose (typically 200-250 μC/cm^2) used to define the junction electrodes and the Dolan bridge separating them. The leads connecting to the junction to the measurement wires are usually larger geometries typically 0.3-0.5 μm and as such require a reduced dose of approximately 150 μC/cm^2. (B) and (C) show possible exposure cross-sections, in this case pink represents exposed resist which will be removed via the developer and red shows unexposed resist which will form the mask. (B) The desired profile, where the copolymer underlying the Dolan bridge is cleared out such that the first electrode can be deposited. (C) A much less ideal situation commonly encountered where the copolymer underlying the PMMA is not fully removed, blocking the angled evaporation forming the electrode.

In many cases fabricated test chips were unsuccessful due to the failure to form a large enough undercut/exposure of the copolymer underlying the PMMA resist bridge, resulting in an exposure cross-section shown in Fig. 5.13(B). In this case fabricated junctions failed to form as the initial extreme angle evaporation hits the unexposed side wall of copolymer under the Dolan bridge, this is illustrated in Fig. 5.14.

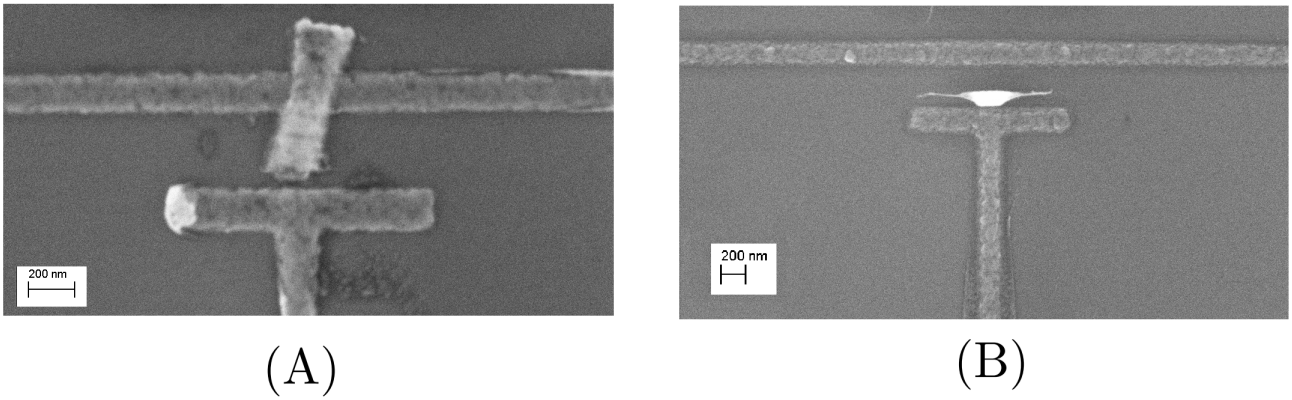

Figure 5.14: SEM images of test junctions. (A) The first layer (60 °) indented to form the underlying electrode at the junction interface can be seen sitting on top of the secondary (normal) deposition, indicating that it was impeded from penetrating under the Dolan bridge. (B) Once again a side wall of copolymer due to insufficient clearing under the Dolan bridge has resulted in the first layer not making it under the Dolan bridge to form the junction. In this image the profile of the first layer's characteristic T shape can be seen vertically standing off from the samples surface (flag).

In order to try to promote a better clearing of the copolymer almost every parameter associated with the resist bilayer properties, its exposure and development was iterated with. The only exception to variation was the molecular weight/solution of the resist and also the width of the Dolan bridge. Although these constraints makes the problem harder it is important the developed recipe be as robust as possible for consistent results when integrating with Nb. An obvious starting point was experimentation with the magnitude of the exposure dose. Primarily higher doses up to 250 μC/cm^2 were trialled. Although some samples seemed promising overall the results were inconsistent with some samples showing a clearing under the Dolan bridges and others losing the Dolan bridge completely due to over exposure. Selective dosing was also attempted using a low dose (50 μC/cm^2) in the hope of exposing the copolymer over the PMMA however this was unsurprisingly unsuccessful given they are so similar in exposure profile. The baking temperature of the individual resist layers was also iterated with. The baking temperatures were varied from 110 °C to 150 °C for the respective layer given PMMA flows around 125 °C. However no discernible change was noted. Extending the development time was more successful with a notable increase in the size of the undercut when development was brought to saturation (approximately 3 mins in a H_2O:IPA developing agent). Ultimately even with these efforts the junctions were still extremely inconsistent due to improper clearing of the

copolymer under the Dolan bridge. Resistance measurements of a typical sample space are shown in Fig. 5.15 illustrating these inconsistencies.

Sample space	Junction number	Design	Width [nm]	Height [nm]	Area [nm^2]	Dolan bridge width [nm]	Resistance [Ω]
S1_1	1	Standard	150	150	22500	300	o/c
	2	Standard	150	150	22500	300	o/c
	3	Standard	150	150	22500	300	o/c
	4	Standard	150	150	22500	300	o/c
	5	Standard	200	150	30000	300	o/c
	6	Standard	200	150	30000	300	o/c
	7	Standard	200	150	30000	300	o/c
	8	Standard	150	150	22500	200	o/c
	9	Standard	150	150	22500	200	2650
	10	Standard	150	150	22500	200	2590
	11	Standard	200	200	40000	200	1210
	12	Standard	150	200	30000	300	3260
	13	Standard	150	200	30000	300	19500

Figure 5.15: Normal state resistance measurement of "standard" T design. The width, height and area are defined as shown in Fig. 5.13 (A). In this sample space all of the junctions with a patterned Dolan bridge width of 300 nm failed to form (open circuit o/c) due to copolymer underlying the Dolan bridge blocking the angled evaporation. Reducing the bridge width to 200 nm yields better results however the robustness of the bridge has now been reduced and even still results are inconsistent (junction 8).

Although the problem of insufficient clearing of the copolymer remained, looking at each part of the process individually allowed for a greater understanding and ultimately control of the resist stack, its exposure characteristics and its development. After being confident that I was producing the most favourable resist stack for an exaggerated undercut to form the bridge I decided to revisit exposure conditions. Previously it has been observed that increasing the overall magnitude of the dose of the electrodes (250 μC/cm^2) although successful at exposing all of the copolymer underlying the bridge also resulted in the over exposure of the PMMA layer thus the dolan bridge was either removed via the developer or the PMMA pattern was substantially rounded from the increased exposure such that the bridge had narrowed significantly.

As such, a new tactic was adopted. In this case the dose of the electrodes is reduced to 200 μC/cm^2 resulting in a well-defined pattern in the PMMA defining the junctions electrodes and Dolan bridge. In order to also expose the underlying copolymer a small area targeted secondary dose of the same magnitude (200 μC/cm^2) in the vicinity of the Dolan bridge was used, illustrated in Fig. 5.16. Given the resist in this region had already been exposed and bleached the incident energy of the secondary does can travel to the substrate with minimum adoption, where it backscatters. Once again the resist

in the immediate vicinity should be bleached from the initial dose such that the broad backscattered exposure reaches the copolymer underlying the Dolan bridge which was not fully exposed by the initial dose. The secondary additional exposure does slightly narrow the Dolan bridge and broaden the electrodes of the junction in this vicinity, however this is barely noticeable with imaging and is only really inferred from normal state resistance of the different designs. Depending on the location and number of secondary exposures small but consistent differences in the normal state resistance of fabricated junctions can be observed corresponding to larger junction overlaps (thus larger electrodes) in the case of additional targeted secondary exposures.

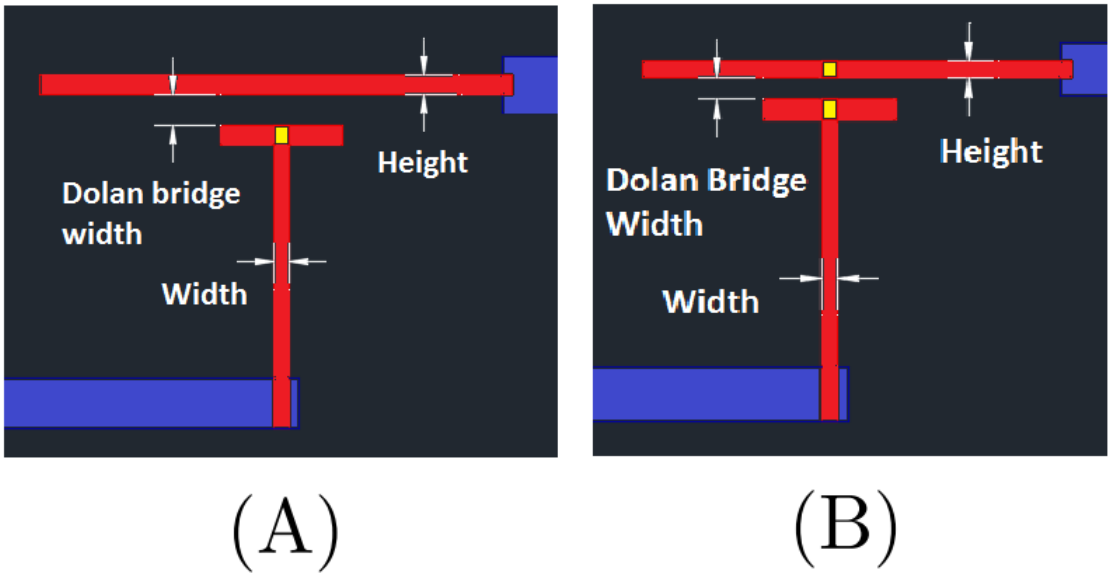

Figure 5.16: T design employing secondary exposures. Blue - 150 μC/cm^2, Red and Yellow - 200 μC/cm^2. (A) Overlap design; (B) Double overlap design. The exposure is much the same as shown in Fig. 5.14 however in this case a secondary exposure dose (yellow) is performed directly after the initial dose (red). The secondary dose leads to a slight broadening of the electrodes due to additional exposure of the PMMA layer, however in general this is subtle and as such the Dolan bridge width is still approximately 300 nm

This methodology was applied to several designs where a secondary targeted exposure demonstrated a consistent ability to clear out the copolymer underlying the Dolan bridge. As such the yield of successful junctions per sample space was dramatically increased to near 100%. Of course there were still some defect junctions noted over wider fabrication batches, however in most instances this was attributed to substrate condition or mishandling rather than a problem with the Dolan bridge. Fig. 5.17 shows a typical junction formed using the overlap design.

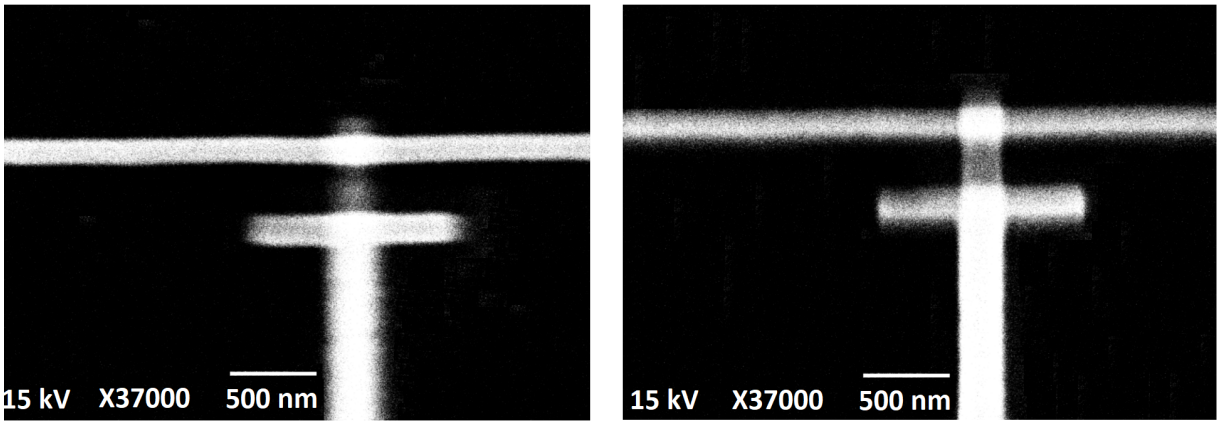

Figure 5.17: RHUL SEM images (A) and (B) show the same single overlap design junction. Imaging on the RHUL *Joel* SEM can be limited, so in general focusing on the top layer (A) and bottom layer (B) individually allows for the best inference of the successfulness of the junction formation.

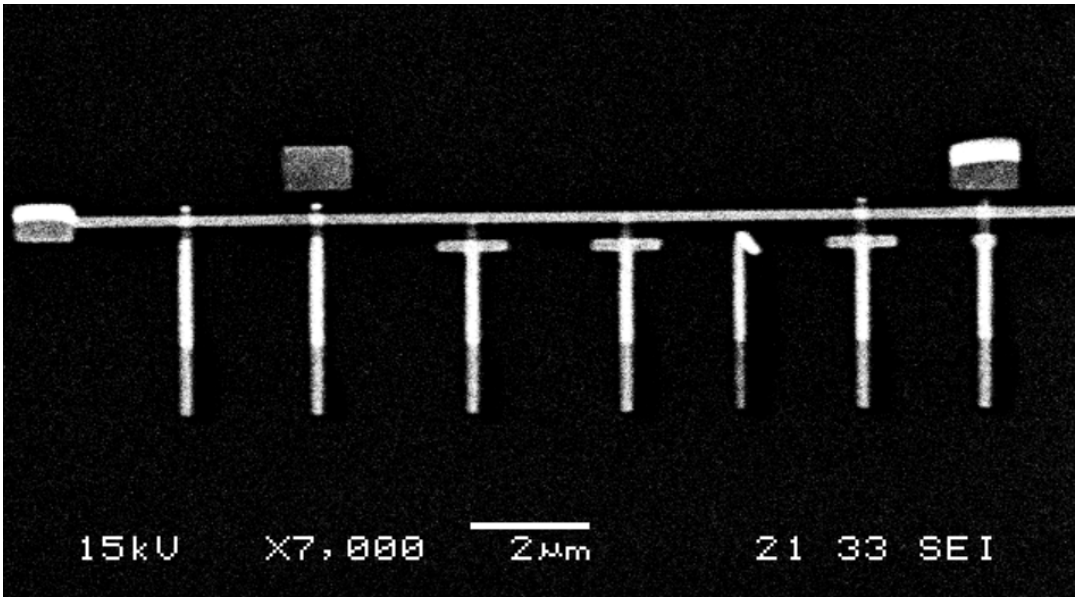

Figure 5.18: SEM image of multiple junction designs employing the secondary exposure method. Several differing designs can be seen in a "free standing" geometry. This was often used when working on test iterations for imaging as well as measurement such as to maximise the total number of junctions fabricated per sample space. Designs from left to right, two headless, two single overlap, one long headless, one double overlap, one double overlap with a reduced T head width.

Several other variants of the T design employing a secondary target exposure were also iterated with over the course of fabrication, as shown in Fig. 5.18. In some designs the

head of the T was completely removed ("headless") design. Although the characteristic T shape was quoted to provide stability to the Dolan bridge there was concern that excess of the first layer of Al deposited on the far sidewall would inconstantly break off from Al forming the bottom layer of the junction. The headless T design was trialled with the idea of reducing the excess landing on the side wall and limiting the effect of it being lifted off (tearing away) from the layer forming the junction. Another notable design choice was the addition of a secondary exposure/deposition above the junction, this was often referred to as a "brute force" method. This additional component does not contribute to the junction formation. Instead, similar to the "headless" design its inclusion was to constrain the excess landing on the far side wall from the angled evaporation. Ultimately it was found that the excess consistently broke away from the Al forming the bottom layer making the headless and brute force approach redundant. As such the overlap and double overlap design were carried forward, a selection of normal state resistance measurement for Al junctions fabricated using these designs is shown in Fig. 5.19.

5.2.5 Inconsistency in oxidation

Over 150 small area Al junctions were fabricated and measured to ensure consistency and reproducibility of the developed designs. Although yield remained high ($\approx 100\%$), a notable variance of the normal state resistance was noted between identically patterned but separately evaporated junctions. This was most notable in the smallest junctions which exhibited an approximately 15% variance in the measured resistance values when looking over several separate evaporations. Junctions fabricated in the same evaporation did not show this variance. It was inferred that the variance was associated with an inconsistent oxidation of the bottom layer of Al prior to the deposition of the top layer. This has been noted by previous users of the system [61] when attempting to fabricate Al tunnel junctions. In order to mitigate this the oxidation time and pressure was increased to try to bring the oxidation process to saturation. However, this did not remove the variance noted between individual evaporations. As such the variance must be remembered when quoting the intended normal state resistance value of a fabricated junction that cannot be directly measured.

Sample space	Junction number	Design	Width [nm]	Height [nm]	Area [nm^2]	Dolan bridge width [nm]	Resistance [Ω]
S2_2	1	T overlap	150	150	22500	300	14300
	2	T overlap	150	150	22500	300	14800
	3	T overlap	150	150	22500	300	13700
	4	T overlap	150	150	22500	300	14400
	5	T overlap	200	150	30000	300	10600
	6	T overlap	200	150	30000	300	10500
	7	T overlap	200	150	30000	300	9980
	8	T overlap	150	150	22500	200	11700
	9	T overlap	150	150	22500	200	13100
	10	T overlap	150	150	22500	200	13100
	11	T overlap	200	200	40000	200	7820
	12	T overlap	150	200	30000	300	11100
	13	T overlap	150	200	30000	300	11300
S2_3	1	Headless	150	150	22500	200	14100
	2	Headless	150	150	22500	200	14000
	3	Headless	150	150	22500	200	13200
	4	Headless	150	150	22500	200	14500
	5	Headless	200	150	30000	200	10200
	6	Headless	200	150	30000	200	10100
	7	Headless	200	150	30000	200	10500
	8	Headless	150	150	22500	150	12400
	9	Headless	150	150	22500	150	13100
	10	Headless	150	150	22500	150	13300
	11	Headless	200	200	40000	200	8240
	12	Headless	200	200	40000	200	8740
	13	Headless	150	200	30000	200	11300
S2_4	1	T overlap	150	150	22500	300	13300
	2	T double overlap	150	150	22500	300	13100
	3	T double overlap	150	150	22500	300	11800
	4	T double overlap	150	150	22500	300	12800
	5	T double overlap	200	150	30000	300	11600
	6	T double overlap	200	150	30000	300	9700
	7	T double overlap	200	150	30000	300	9710
	8	T double overlap	150	150	22500	200	11600
	9	T double overlap	150	150	22500	200	14100
	10	T double overlap	150	150	22500	200	12100
	11	T double overlap	150	200	30000	200	9750
	12	Headless	150	150	22500	200	12100
	13	Headless	150	150	22500	200	11700

Figure 5.19: Normal state resistance measurements of different junction designs focused on small area junctions. The Headless design and the T overlap design result in similar values of R_N, unsurprising given the only difference in these designs is the head of the T which only serves the purpose of making the Dolan bridge more robust. The double overlap design has slightly smaller R_N for the same patterned geometries compared with the single overlap design. This is due to the extra secondary dose which widens the electrode in this area, forming a slightly larger junction.

5.2.6 Critical current

The Al test junction iterations primarily focused on three different dimensions of junction, 150 nm × 150 nm, 200 nm × 150 nm and 200 nm × 200 nm, patterned using the single and double overlap method. The highest normal state resistances were observed in the 150 nm × 150 nm single overlap design junction which ranged from 13-15 kΩ, the variance assumed due to inconsistency in oxidation pressure. The double overlap 200 nm × 200 nm junctions had normal state resistances of approximately 6-7 kΩ. Given this range of normal state resistances R_n, the Ambegaokar Baratoff [67] relation can be used to estimate the critical current at T= 0 K in the absence of fluctuations.

$$I_c^0 \approx \frac{1.764\pi k_B T_c}{2eR_n} \tag{5.2.1}$$

For Al, T_c= 1.2 K, this gives the junctions I_c^0's a range from 60 nA to 20 nA. A small number of larger junctions 250 nm × 200 nm were also fabricated using the double overlap method with increased exposure dosing. The normal state resistance measurements of junctions produced using this geometry and design gave an estimated critical current of $I_c \approx 100$ nA. In the ideal case low temperature measurements of the DC IV behaviour of the fabricated test junctions would be carried out before further device integration in order to determine I_c experimentally. However in practice this measurement is non-trivial. To measure the IV characteristics of a low I_c junction ($\approx$ 100 nA) below 100 mK, effective filtering of the bias and voltage measurement lines is essential and although achievable on our dilution refrigerator, there is a real possibility of the junction being damaged as it is vulnerable to electrostatic discharge. Although DC characterisation prior to integration with the Nb CPW resonator is desired, the RF cavity has several practical benefits in regards to reducing the risk associated with DC measurements. Removing complications regarding measurement line filtering, with the coupling capacitors offering protection from DC discharge. For this reason the decision was made to move ahead with the integration of the fabricated Nb CPW resonators and Al Josephson junctions.

5.2.7 Resist residue

Organic residue left behind by the EBL mask after its removal is often observed on the surface of fabricated devices, as shown in Fig. 5.20. A similar residue was noted by I. M. Pop et al. [65] when fabricating Al tunnel junctions. As suggested this residue can be removed via a light oxygen etch without degradation to the junction.

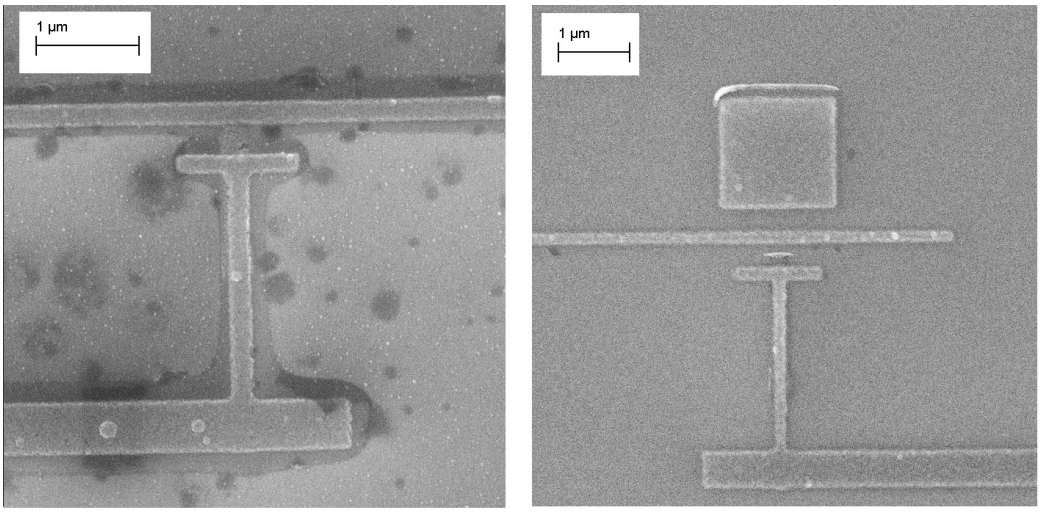

Figure 5.20: NPL SEM images of early (failed) junctions. (A) Mask removed via a hot solvent bath (*Microposit* 1165 at 60 °C) (B) Mask removed via hot solvent bath, followed by 2 minute PlasmaLab recipe O_2 plasma surface treatment.

5.2.8 Large area junctions

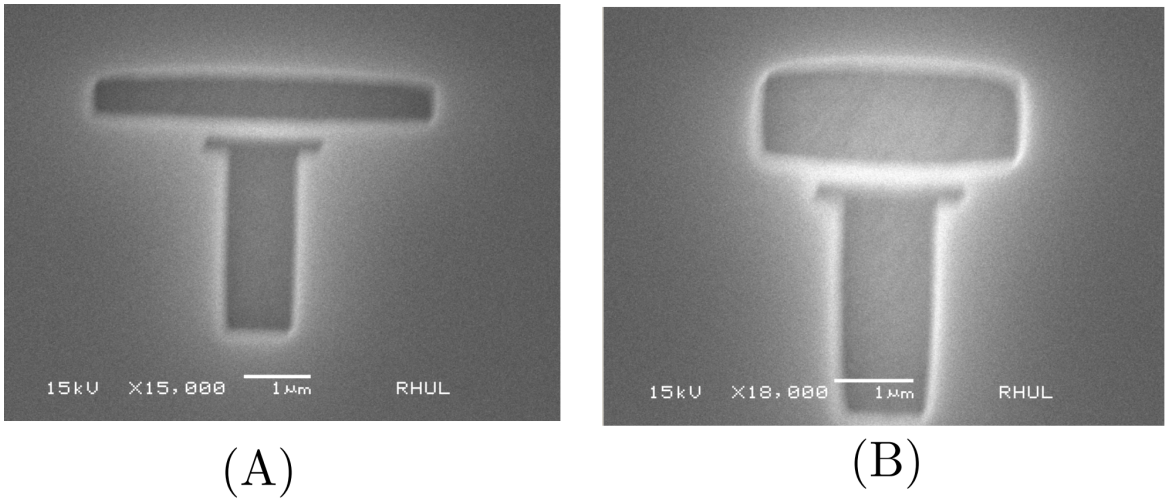

Figure 5.21: SEM imaging of exposed and developed resist bilayer defining large area variants of the T junctions. SEM imaging of the resist offers a convenient way to optimise the exposure dose when trialling new patterns without requiring repeated evaporations.

Although larger area junctions were experimented with, they were not fully characterised. In principle this design is simple to scale up to larger cross-sectional areas, as the Dolan bridge width and geometry is the same as in the small area junction design. The only parameter to increase is the junction electrode area. Fig. 5.21 shows some of the initial experimentation to correct the exposure dose for these larger geometries.

5.3 Integration of Nb CPW resonators with Al Josephson junctions

As discussed in Section 5.1.1, there are three differing resonator designs (R1, R3 and R5) on the optical mask, each with differing considerations relating to integration with the Al Josephson junctions. The R1 design features an approximately 10 μm gap in the central conductor at the $\lambda/4$ point of the fundamental mode, defined by the optical mask. In this case a junction can be easily deposited in the gap in the central conductor. The R3 and R5 designs have a continuous central conductor with no gaps. For these resonators a gap in the central conductor for insertion of an Al element can be manually engineered. This is achieved with EBL and RIE similar to the method used to etch the resonator using optical lithography, however in this case EBL is used to define the area of Nb to be removed rather that a quartz chrome mask.

In order to etch the gap in the central conductor an appropriate EBL mask must be chosen capable of defining an area approximately 20 μm $\times$ 20 μm, reliably positioned on the central conductor. The mask must be able to withstand the 10-12 minutes SF_6/O_2 etching process. The addition of the O_2 increases the etch rate of the EBL resist however an isotropic etch is required to add a smooth slope on the etch profile of the edge of the gap formed in the Nb. If an anisotropic etch was used the edge of the gap would be defined by a step profile between the 200 nm thick Nb and the Si substrate. A deposition of Al bridging the gap could thus suffer from a discontinuity at these points. The addition of the O_2 results in a regressing of the resist side wall throughout the etching process. This results in a gradual sloped edge such that the thickness of the Nb reduces from 200 nm to the Si substrate over approximately 1.5-2 μm. The slope removes the chance of a discontinuity occurring at the Nb/Al interface, ensuring a good electrical and mechanical contact between the respective layers.

The addition of the O_2 in the etching process rules out the use of a thin high resolution PMMA layer to define the pattern given that PMMA and copolymer etch at roughly the same rate as the Nb in the SF_6/O_2 plasma (20 nm min^{-1}). Thicker single layers of PMMA were trialled, however, when this was attempted a secondary issue was found. In several instances the thicker PMMA layer had become cross-linked and was not removable from the Nb sample surface. Cross-linking refers to polymerisation of the resist resulting in hardening, which is most likely caused by secondary electrons and ions produced during the etching process. As such a thicker (≈ 0.8 μm) single layer copolymer resist mask was adopted. As discussed, the copolymer is primarily a lift off resist and as such produces a broader pattern when exposed via EBL in comparison to PMMA. However, given the large geometric order of the exposure 20 μm $\times$ 20 μm this is perfectly acceptable. A gap etched in the central conductor of a Nb resonator using this method is shown in Fig. 5.22.

It should be noted that any exposed SiO_2 not covered with the resist mask will also be etched at a rate of 3 nm min^{-1} in the SF_6/O_2 plasma.

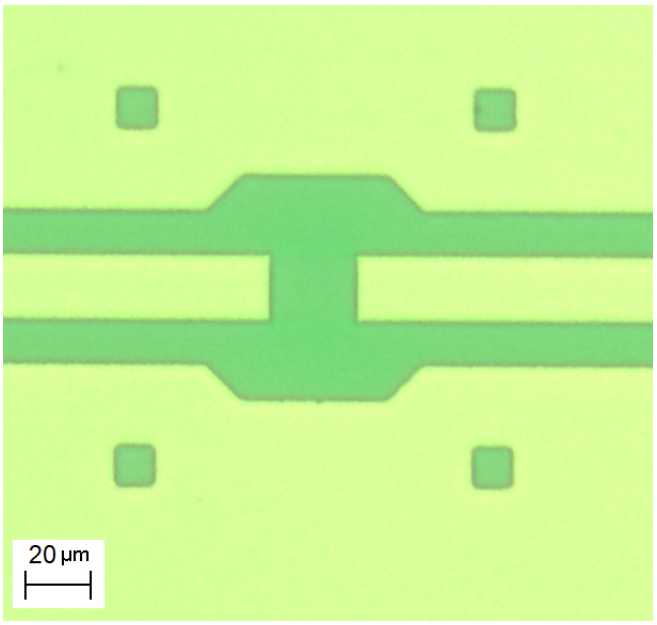

Figure 5.22: Optical image of a gap etched in the central conductor of an R3 Nb CPW resonator using a copolymer mask. The mask is patterned via EBL, in order to correctly position the pattern defining the gap the four squares seen in the image are used as EBL markers. The R3 and R5 resonator have five others sites with EBL markers along the central conductor of the resonator. If it was desired to do lithography on a point elsewhere on the central conductor this can be achieved by using the width of central conductor itself as a marker, either side of the intended area of exposure.

The primary concern regarding the deposition of an Al Josephson junction to bridge the gap formed in the central conductor is the quality of the Nb/Al interface. The surface NbO_x must be thoroughly removed prior to the deposition of the Al otherwise the interface could define a significant contact resistance. The method of removing the NbO_x is an extended Ar mill prior to deposition. In order to ensure that a sufficient mill is performed to remove all of the surface oxide several test resonators are prepared and their central conductors etched with several gaps. The same PMMA/copolymer mask used to fabricate the junctions was used to define a bridge over the centre of a gap in the central conductor of a test resonator. Approximately 50 nm of Al was then deposited via thermal evaporation after a Ar mill of a set time. This results in a Al bridge over the gap in the central conductor show in Fig. 5.23. The resistance of the Al bridge is then measured using the 4 point probe station. The process is then repeated extending the time of the Ar mill prior to the deposition in 1 minute intervals. It is found that for Ar milling in excess of 2.5 minutes there is no significant difference in the resistance of the Al bridge.

This indicates that the NbO_x has been removed and further etching does not change the quality of the Nb/Al interface.

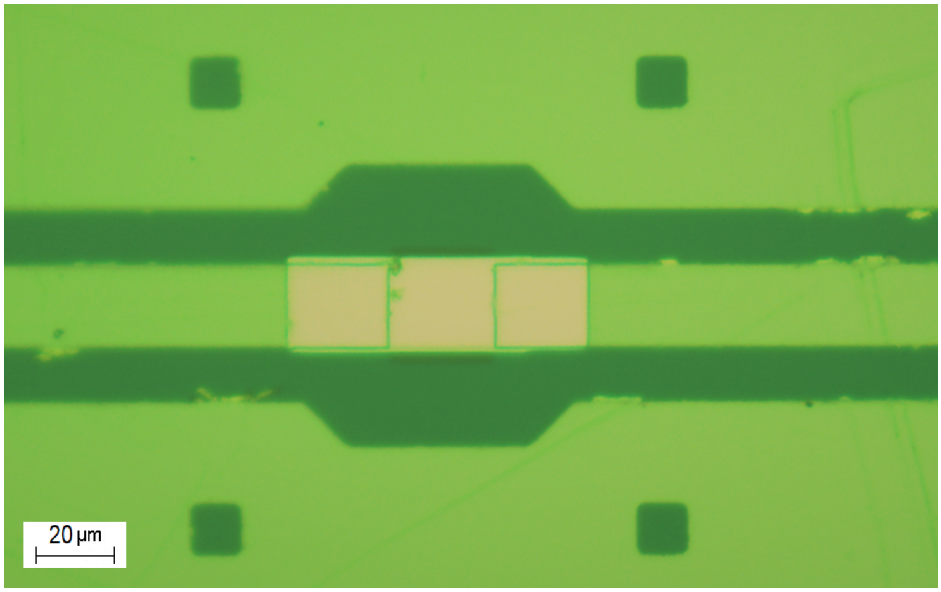

Figure 5.23: Optical image of a thermally evaporated 50 nm thick Al bridge over a gap etched in the Nb CPW resonators central conductor. The surface imperfections, are caused by the measurement probe needles landing on and tarnishing the Nb film in order to measure the resistance over the gap. Given the destructive nature of the measurement, each Al link is measured several times, changing where the probe makes contact to the central conductor such as to ensure measurement is representative of the conduction across the gap and not how the probe needles are landing on the Nb.

Ideally a resonator with an Al link bridging the gap would be measured below the T_c of Al. In this situation the quality factor of the resonator can be used to infer a contact resistance at the interface. However given the measurements of the resistance of Al bridges were consistent with Ar etching time, it was decided to move on to integration of an $Al/AlO_x/Al$ junction embedded in the etched gap of the Nb CPW resonator. As such several Al Josephson junctions fabricated as detailed in Section 5.2 were deposited directly into several gaps along the central conductor, employing a 3.5 minute Ar mill prior to the deposition. The normal state resistance of the Al junctions was then measured using the probe station, making contact with the central conductor either side of Al integration. The measurements were consistent with the DC chip test junctions concluding the development cycle of this iteration of sample design. The techniques detailed in this chapter were used to fabricate the sample known as SA1, a Nb CPW resonator with an embedded Al Josephson junction. SA1 will be discussed in the next chapter including how the results of its measurement influenced subsequent sample design and fabrication.

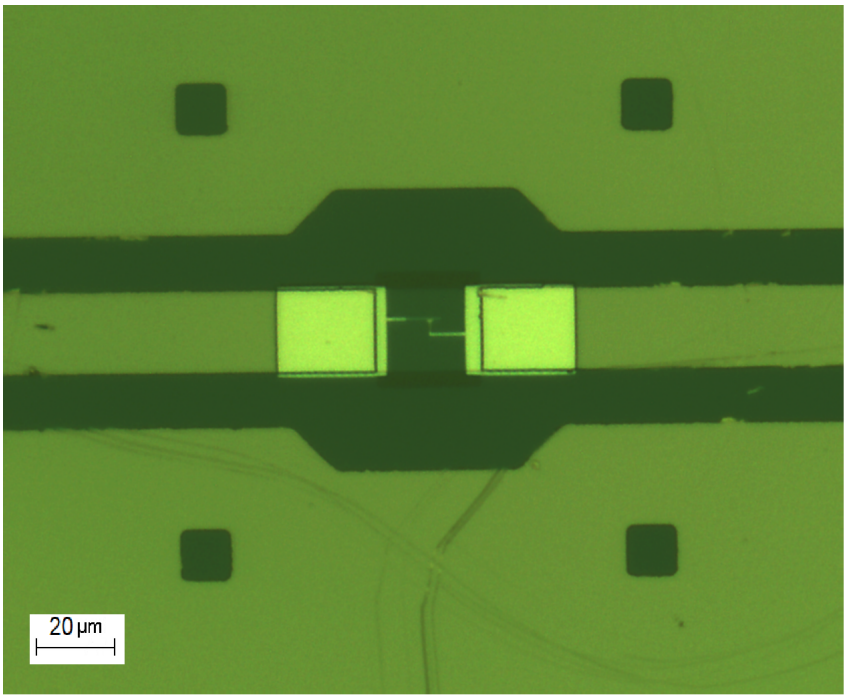

Figure 5.24: Optical images of an Al junction deposited into an etched gap in a Nb CPW resonator. Once again tarnishes are visible from repeated resistance measurement to ensure that R_n is consistent with Al junctions fabricated on DC chips.

5.4 Niobium nanobridges

Nb nanobridges were not originally a primary focus of this project, however this interesting geometric exhibition of the Josephson effect and the potential benefits of having access to another source of non-linearity tempted investigation. Furthermore, the higher T_c of Nb allows for operation of devices at 4.18 K easily achievable with a transport Dewar instead of requiring a dilution refrigerator measurement platform. Although a Nb nanobridge would not be expected to replicate a low I_c Al tunnel junction, they do offer a Josephson element which can operate at a more convenient temperature for device characterisation to aid further sample design and development. Furthermore, due to their extreme geometries resulting in them being hard structures to fabricate and the prevalence of tunnel junction technology they have not received as much attention as their counterparts. This has changed over the last decade with the advent of more precise fabrication technology, especially focused ion beam lithography, however they are still fairly novel structures to explore.

5.4.1 Fabrication

The fabrication of the Nb nanobridges follow on from the work carried out to engineer gaps in the central conductor of the resonator via EBL and RIE. The hope was similar to taking gaps out of the central conductor of the resonator for the insertion of an Al junction,

it would be possible to use an EBL resist patterned mask and RIE to form nanobridges using the Nb central conductor itself. Although the geometrical considerations involved in the understanding of the characteristic behaviour of a nanobridge is complicated, a gauge of the dimensions required for such a structure is the coherence length of the material forming the superconducting electrodes. In the case of Nb the coherence length is approximately 38 nm. Although modern EBL can now pattern with below 10 nm resolution, patterning a structure of geometries of this order with the RHUL EBL is extremely ambitious. Furthermore in order to attempt such a small pattern it is highly recommended to use a thin bilayer resist stack. However, although that may be a suitable mask for a deposition process the requirements of a mask for RIE is very different, as the mask must withstand the etching of the Nb. Although several methods were trialled that involved a "direct write" approach such that the dimensions of the nanobridge are defined by a PMMA resist mask, this was ultimately unsuccessful and a different approach was taken.

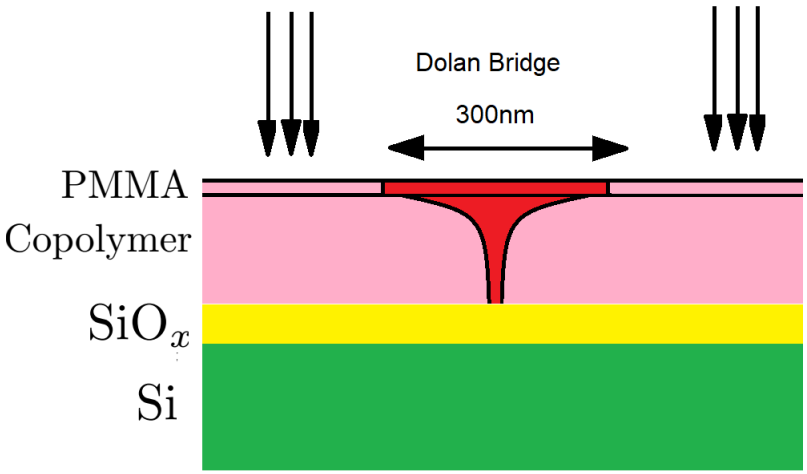

Figure 5.25: Thick PMMA/copolymer resists stack used for the Al junction fabrication. In the case of the junctions this situation was avoided with additional dosing in the proximately of the Dolan bridge. In the case of nanobridge fabrication this problem can be exploited to form a very narrow copolymer mask, thick enough to survive the etching of the excess Nb.

Recalling Section 5.2.4, a primary issue with the realisation of a reliable method of fabricating the Al T design junction was the insufficient clearing of the copolymer layer beneath the Dolan bridge, illustrated in Fig. 5.25. In this case a small unexposed wall of copolymer was impeding the deposition of the first angled Al layer such that the junction was not being formed. As discussed a lot of time was spent trying to mitigate this problem. From inferences of the undercut of the resist it was clear that the wall of copolymer would have to be quite thin (of order 50 nm). It was also quite well-defined/robust enough that it could consistently stop a sample with 100 junctions being formed without exception. Although a problem in the context of the junctions, this presents a way of reliably forming

a thick narrow layer of copolymer over an area of Nb we wish to protect from the RIE. In this way we are not forced to pattern the dimensions of the nanobridge itself but instead using a combination of proximity dosing and the regression of the copolymer resist undercutting the PMMA to form a mask that defines a very small nanobridge. The resist recipe was changed slightly to reduce the thickness of the top lying PMMA layer to approximately 100 nm thick. Although we are relying on the copolymer to form the mask defining the nanobridge the PMMA is still used as this is a familiar resist bilayer such that the uncut features are known and exposure dosing is well understood.

5.4.2 Etching

Once again there are two options available when etching Nb. An anisotropic etch (SF_6/Ar_2) and an isotropic etch (SF_6/O_2) where the later can be used to promote a sloped sidewall of the etched surface as discussed in previous sections. Both of these process gas mixtures were trialled with the nanobridge resist mask outlined in the previous section. Fig. 5.26 shows two examples of constrictions etched in the central conductor of a Nb CPW resonator using the SF_6/O_2 etch. A consequence of the isotropic etch was that the constriction formed appeared to have a reduced thickness compared to the electrodes which could be a desirable feature for a nanobridge geometry.

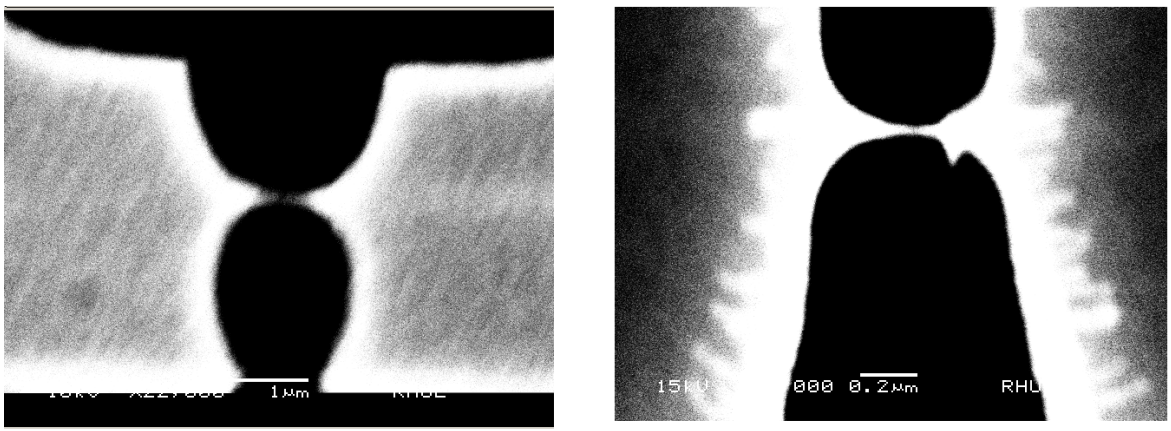

Figure 5.26: SF_6/O_2 etched Nb using a PMMA/copolymer bilayer. (A) Multiple bridges were observed that seem to thin around the centre of the constriction. (B) Although iteration with the design yielded some narrow bridges, there was a concern that the isotropic etch did not promote the best uniformity.

Although several very narrow nanobridge like constrictions were observed, the isotropic etch did have drawbacks, mainly the broadening of the etch profile. There was also a worry of bridges being discontinuous or not well-defined due to the additional thinning of the thickness of the Nb bridging the electrodes. For these reasons the SF_6/Ar etch

was primarily adopted. The resulting constrictions, shown in Fig. 5.27 were scalable, reproducible and generally well-defined.

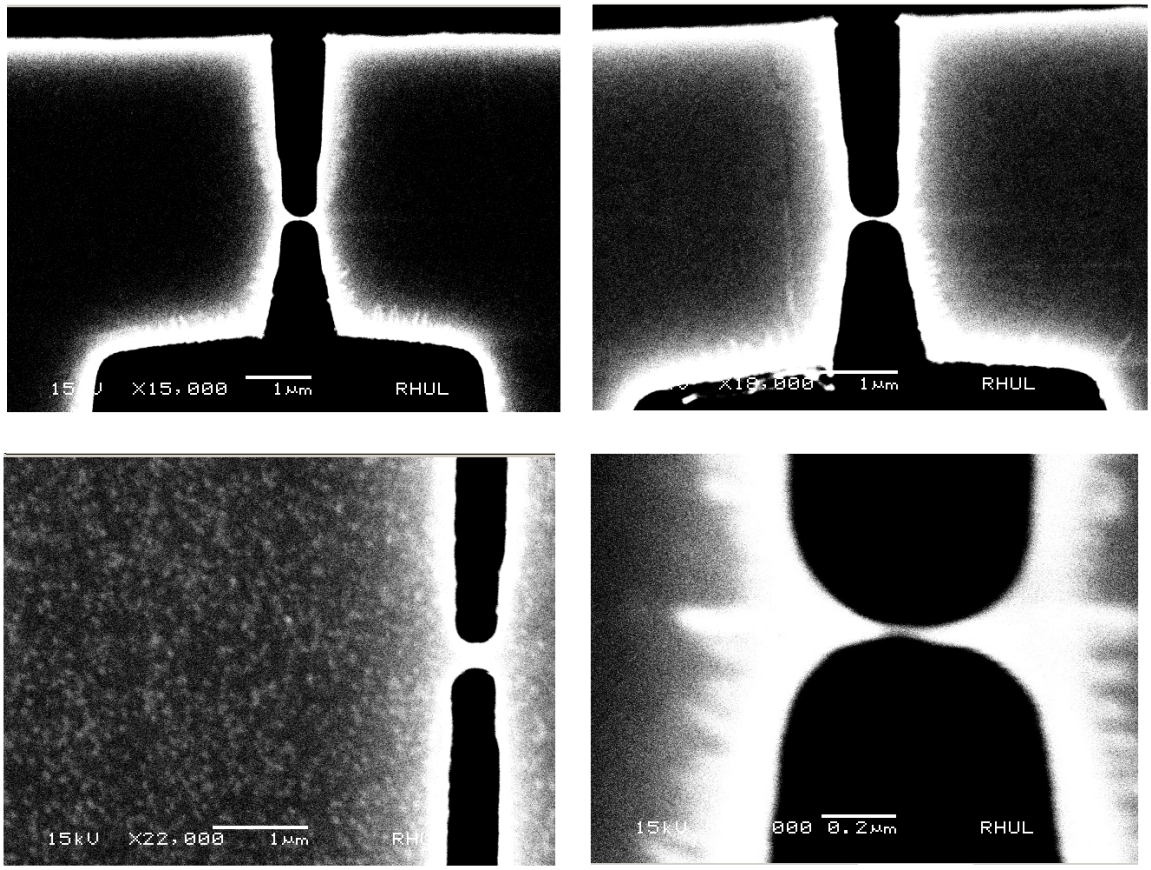

Figure 5.27: A selection of SEM images of Nb etched using SF_6/Ar masked with a PMMA/copolymer bilayer to form narrow constrictions separating two electrodes.

5.4.3 Device design

The resulting constrictions lend themselves well to incorporation with other geometries. Geometric inductance (SQUID loops) can be exposed and etched at the same time as the constrictions allowing for a single step process. Such geometries can be seen in Fig. 5.28 and Fig. 5.29. Once the recipe was defined several samples based around these constrictions were fabricated for measurement in order to access the behaviour of these potential nanobridges. The measurement and behaviour observed relating to these devices is detailed in Chapter 7.

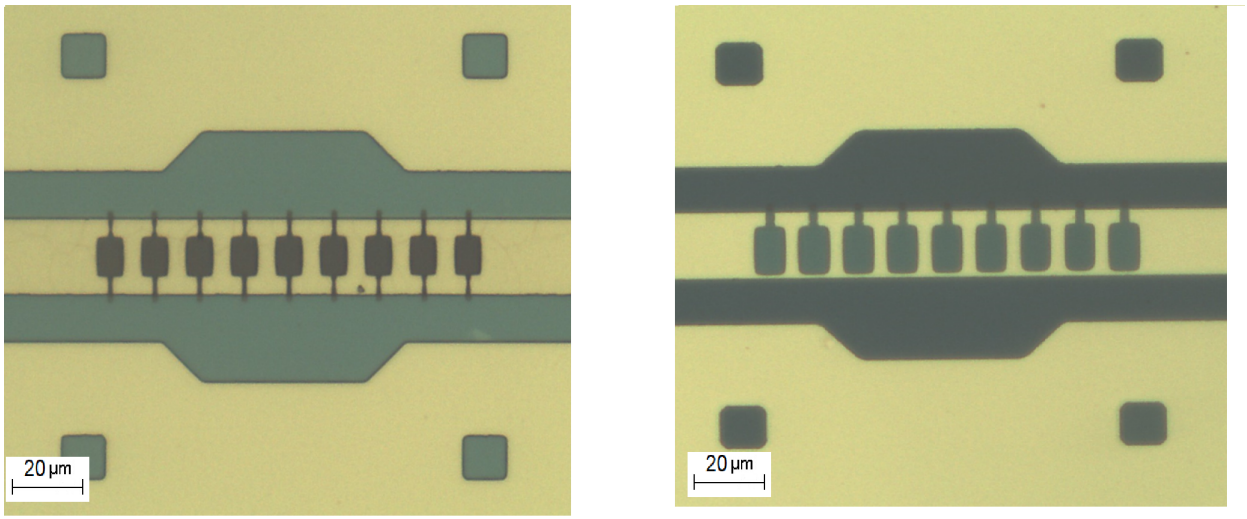

Figure 5.28: Optical images of a Nb CPW resonator with SQUID array employing etched constrictions in (A) DC SQUID configuration and (B) RF SQUID configuration. The constriction separating the larger electrodes are essentially invisible to optical inspection.

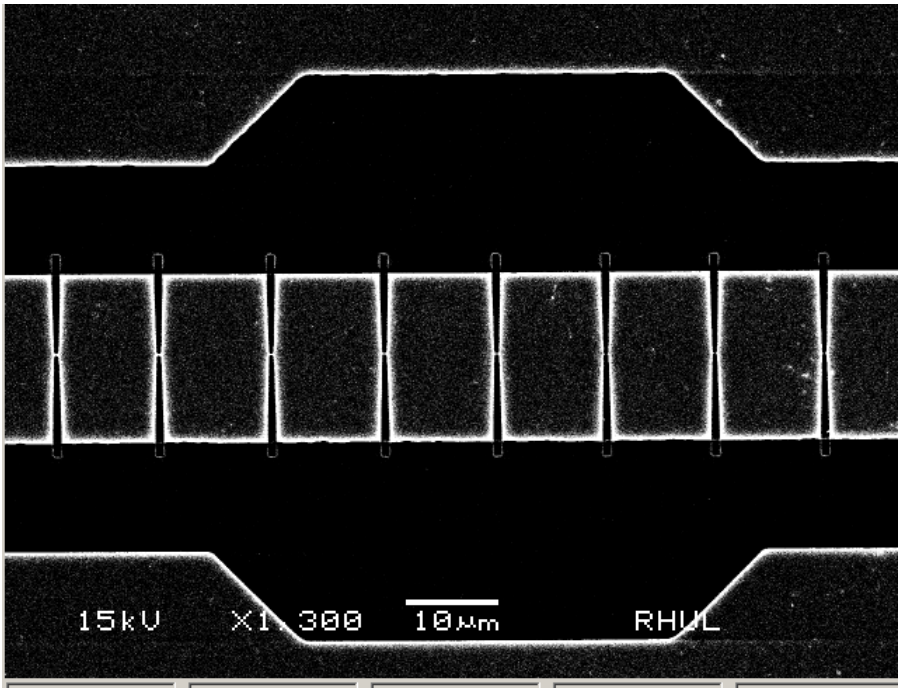

Figure 5.29: SEM image of several constrictions etched in the central conductor of a Nb CPW resonator. A test device where the width of the patterned bridges is reduced left to right.

Chapter 6

Measurements of Al Josephson junction Nb CPW resonators

6.1 Sample design - SA1

This chapter details the low temperature measurement of RHUL fabricated niobium CPW resonators with embedded small area Al/AlO_x/Al tunnel junctions. This chapter will focus on two samples which will be referred to as SA1 and SA2, respectively. The samples were fabricated as discussed in Chapter 5, an example recipe is given in Appendix A.2.

Once fabrication procedures had been established, multiple design possibilities were considered. As discussed in Chapter 5.2.6, the critical currents of the Al/AlO_x/Al test junctions estimated from normal state resistance measurements range from 20 nA to 100 nA, depending on the patterned overlap area and design employed (single or double overlap). The low critical current junctions represent highly non-linear circuit elements. Using the low I_c junctions in combination with a high quality factor Nb CPW resonator allows for a highly reactive non-linear oscillator (media) to be realised, which would exhibit a non-linear response even at very low driving power if the junction technology and integration with the Nb CPW resonator is successful. The nature and magnitude of the non-linear response will depend on the strength and order of the imparted non-linearity (quadratic or cubic) and the position of the non-linear element(s) in the cavity.

Adopting an RF SQUID design, such as that employed in the PTB period doubling (PD) sample discussed in Chapter 4, allows for the dominant order and magnitude of the non-linearity to be controlled via an external flux bias. As demonstrated in Chapter 4, this allows the three-wave mixing (TWM) to be realised, a favourable mixing regime in many cases in comparison to four-wave mixing (FWM). However, in the case of an RF SQUID the figure of merit regarding the strength of the non-linearity is β_L, the RF SQUID screening parameter relating the critical current of the junction I_c to the geometric inductance for SQUID loop L_G. As seen in Chapter 2.2.4, β_L is directly proportional to the magnitude of the non-linear response. The PD sample had a designed $\beta_l \approx 0.7$. This was achieved with RF SQUIDs with a geometric inductance $L_G = 7.6 \times 10^{-11}$ H and a

tri-layer Nb Josephson junction with critical current $I_c = 3$ μA. In order for β_L to be close to 1 for an RF SQUID employing a 100 nA Al junction would require a geometric inductance of 2×10^{-9} H. From a fabrication standpoint adding an Al RF SQUID with such a large geometric inductance to the central conductor of the CPW resonator is impractical at best, requiring significant engineering of the ground plane of the CPW resonator to accommodate it. Although the RF SQUID design is attractive, it does not play to the strength of the low I_c Al junctions. We will revisit this sample design consideration again in Chapter 7. Although higher I_c Al junction designs were investigated (Chapter 5.2.8), the opportunity to study a low I_c (< 100 nA) junction interacting with a small number of photons in a high quality factor resonator remained the primary focus.

For this reason sample design focused around a single junction positioned at the $l/2$ point of the central conductor, where l is the length of the resonator. In this configuration the junction can be driven by the fundamental and the third mode of the resonator. If successful, this would allow for a host of interesting phenomena to be observed at very low drive powers. This includes amplitude bifurcation and FWM regimes such as parametric amplification and up/down-conversion to the third mode (third harmonic generation/period tripling). In order to simplify the design, a single junction is chosen over a DC SQUID geometry. Although this does not allow for flux modulation it simplifies fabrication such as to minimise potential complications and reduce ambiguity regarding the junction's behaviour.

6.2 SA1

SA1, shown in Fig. 6.1, is a $\frac{\lambda}{2}$ Nb CPW resonator with a Al/AlO_x/Al tunnel junction deposited in the central conductor of a R3 Nb resonator. The R3 resonator design is used for its higher loaded quality factor in comparison with the R5 design. The Al Josephson junction is positioned at the middle ($l/2$) of the central conductor corresponding to a current anti-node at the fundamental and odd modes and a current node of the even modes. The fabrication of the sample is a three step process detailed in Chapter 5. To briefly summarise, the resonator pattern is etched from a 200nm thick Nb film sputtered on a Si substrate via optical lithography. A gap is then etched in the central conductor of the cavity using EBL and RIE. Finally, an Al Josephson junction is deposited in the etched gap via a double layer shadow evaporation and oxidation process.

The resist mask defining the junction dimension was patterned to give an overlap area of 150 nm $\times$ 150 nm for the respective Al layers forming the junction, the first layer was oxidised at 950 mtorr for 5 minutes to form the insulating barrier prior to the deposition of the second layer. Unfortunately there is no method of measuring the junction resistance prior to measurement without risking damaging the sample. However the design and geometry corresponds to measured test junctions with a normal state

resistance of approximately 12 kΩ ($I_c^0 \approx 30$ nA). The low I_c design was chosen to maximise the non-linear response at low drive powers. As noted in Chapter 5.2.5, although the test junctions achieved near 100% yield with respect to junction formation there was variance attributed to inconstancy in oxidation, which must be considered when estimating the critical current of the junction inside SA1.

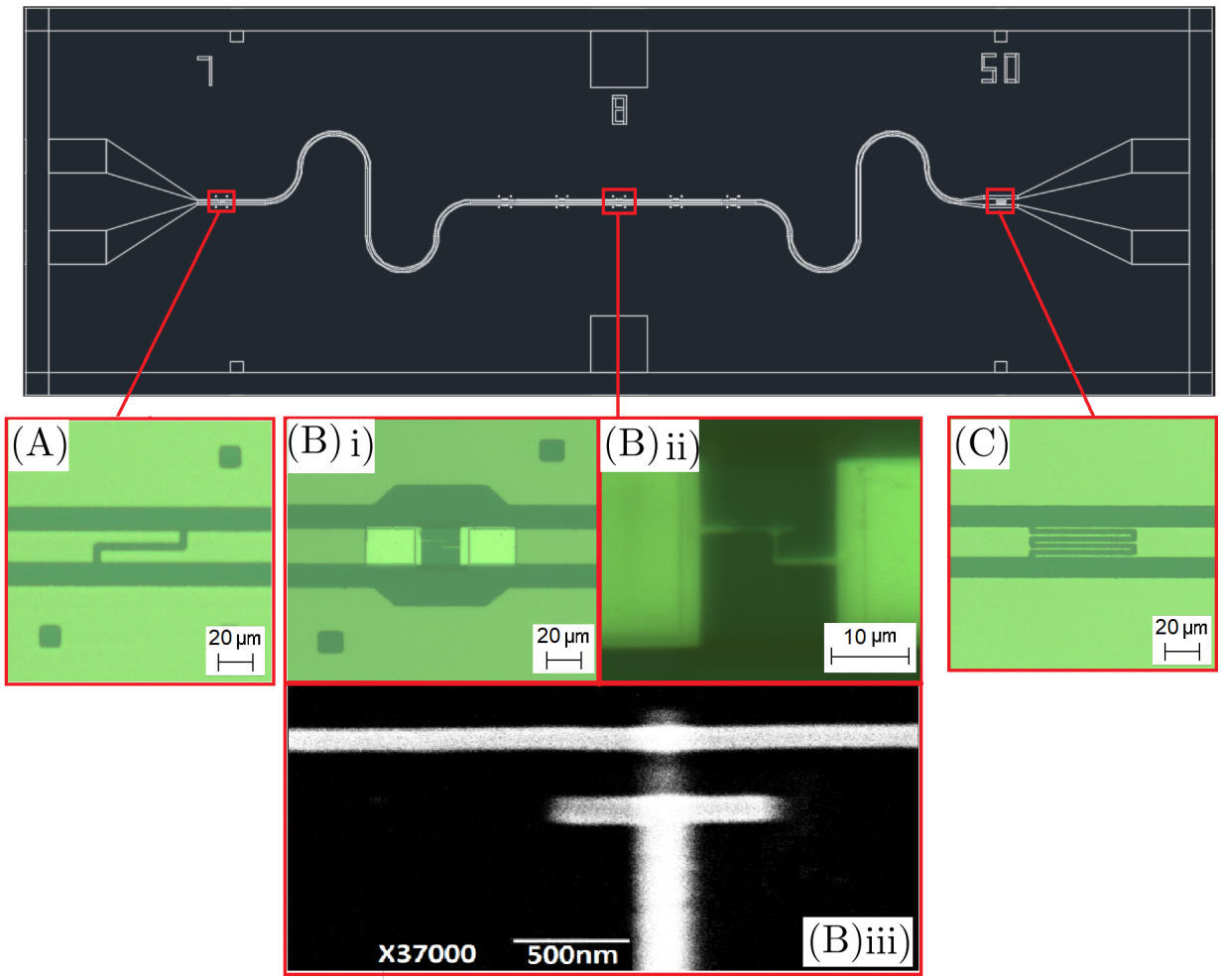

Figure 6.1: SA1, Al Josephson junction embedded $\lambda/2$ Nb CPW resonator. (A) and (C) are optical images of the input and output coupling capacitor respectively. (B)i) and ii) are optical images of the Josephson junction located at the $l/2$ point deposited in an etched gap in the central conductor. (B)iii) is an SEM image of a representative test junction with a geometry correspond to that patterned in SA1.

6.2.1 4.18 K measurements

For initial characterisation SA1 was measured at 4.18 K using an RF measurement probe immersed in a liquid He transport dewar. At this temperature the Al component would be in a normal state and thus a highly dissipative element in the centre of the cavity. Even so a 4 K measurement is important to confirm there is transmission through the sample before it is mounted on the dilution refrigerator. Furthermore, as discussed in Chapter

3.3 the RF circuit installed on the dilution refrigerator has an output bandwidth of 3.5 GHz to 7.5 GHz, thus only the fundamental mode of the resonator (≈ 6 GHz) would be visible in the output window when the sample is installed on the dilution refrigerator circuit and measured at low temperatures. Thus a measurement at 4.18 K temperatures is a convenient way to look at the higher frequency end of the SA1's spectra. Further more, although the central Al component of the resonator is in the normal state, the second mode of the resonator (≈ 12 GHz) should have a current node around the position of the junction, such that the dissipative aluminium should have a reduced effect on this mode compared with the fundamental mode of the resonator. The spectra of the sample at 4.18 K can be seen in Fig. 6.2 over a 1 to 20 GHz range. The sample is also thermal cycled to ensure that observed features relate to the superconducting Nb and not the box modes supported by the geometry of the sample box.

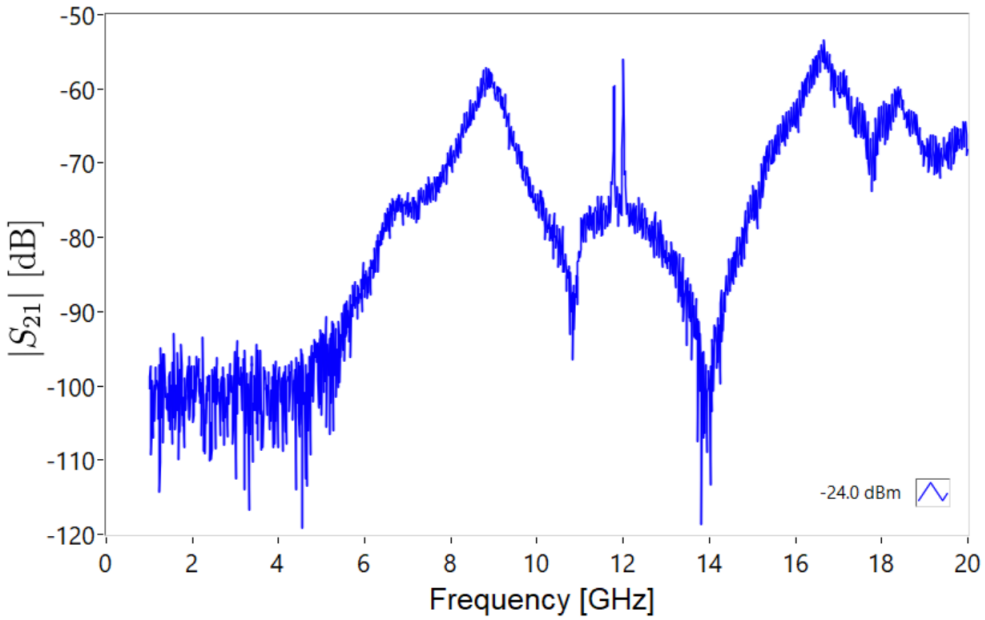

Figure 6.2: $|S_{21}|$ of SA1 over a wide bandwidth at 4.18 K. The fundamental mode, expected around 6 GHz is absent from the spectrum, however there are two clear peaks around where the second mode is expected.

At 4.18 K the fundamental mode is absent from the spectrum, this is assumed to be due to the highly dissipative Al component placed at the current anti-node of the fundamental effectively damping the resonance at this temperature. The region around where the second mode of the resonator is expected, shown in Fig. 6.3(A), is more ambiguous. Instead of a single resonance two well-defined peaks are noted, centred around 11.8 GHz and 12.02 GHz respectively. It is worth comparing these features with an unmodified resonator shown in Fig. 6.3(B) with the 11.8 GHz (LHS) an 12.02 GHz (RHS) mode individually, shown in Fig. 6.3(C) and 6.3(D). The quality factors are obtained by fitting a generalised Lorentzian fitting function to the $|S_{21}|$ transmission data. The centre

frequency of the RHS is very close to the centre frequency of the second mode of an unmodified resonator. The reduction in quality factor is most likely influenced by the presence of the dissipative aluminium.

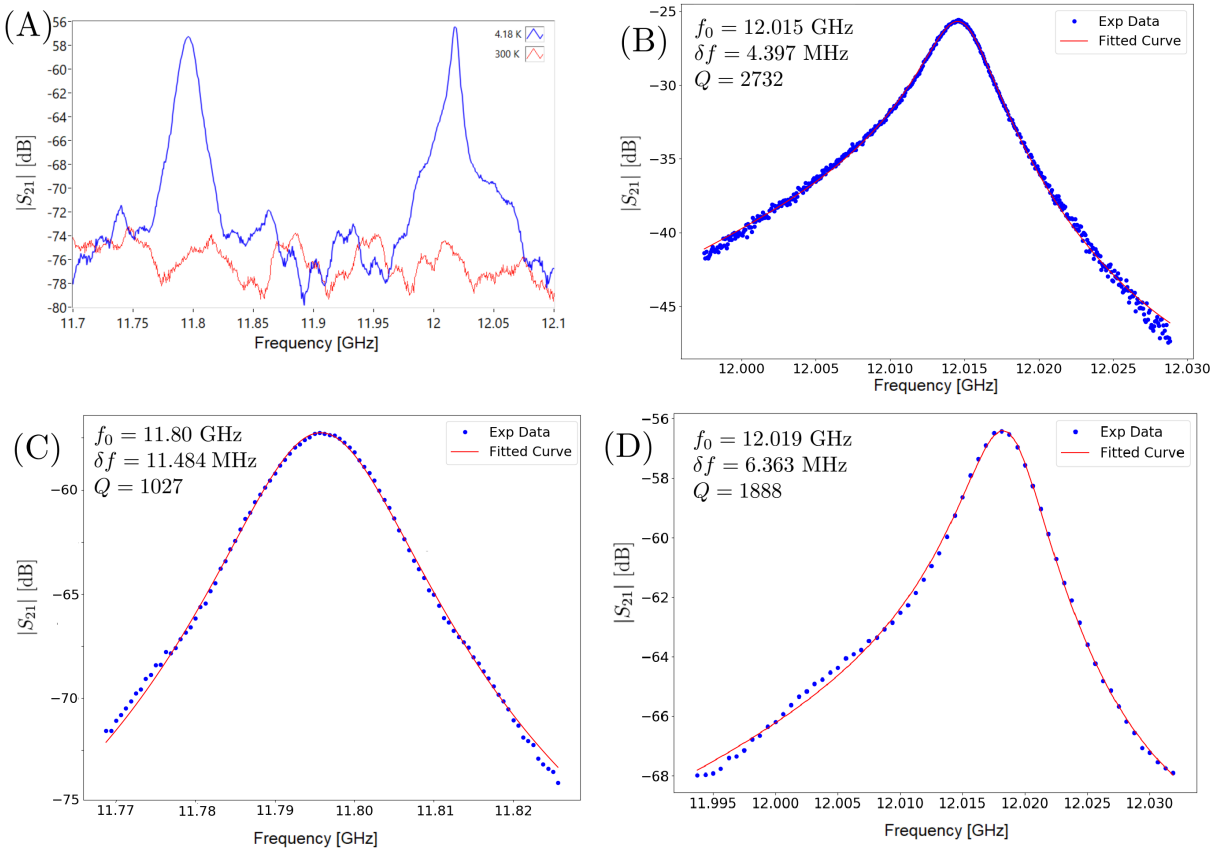

Figure 6.3: $|S_{21}|$ as a function of frequency for (A) SA1 - where the second mode is expected at 4.18 K (blue) and 300 K (red). (B) Second mode of a unmodified R3 resonator (C) SA1 - LHS mode. (D) SA1 - RHS mode.

The mode centred around 11.8 GHz is harder to account for. It has a broader lineshape however its presence could be significant, a narrow feature like this which doesn't owe to the superconducting Nb central conductor has not been observed when measuring unmodified resonators. As such it is possible that the LHS mode is related to the integration of the Al Josephson junction.

One possible explanation for the appearance of this mode is that the Al integration has led to an impedance mismatch around the centre of the cavity. This could be incurred from modification of the width of the central conductor and its spacing from the ground plane where the junction is embedded. This was a noted worry of the single junction sample design. As we have seen in Chapter 2.1.1 the CPW capacitance and inductance per unit length, which defines its characteristic impedance, is primarily defined by its geometry, the width of the central conductor W and the gap between the central conductor and the ground plane S forming the transmission line. By changing the geometry at the

point of the Al integration an impedance mismatch is generated. This is difficult to avoid when the sample design involves narrowing the central conductor to a point to form the Al junction. Ideally the ground plane would be extended to compensate for the narrowing to the point of the junction cross-section such as to maintain the ground plane central conductor spacing S along the entirety of the resonator. However in the R3 design resonator this is actually exacerbated at the $l/2$ point where the ground plane widens (Fig. 6.1(B)). The assumption was made that although an impedance mismatch is almost guaranteed it would not be significant enough to greatly affect the operation of the device, i.e. if the impedance mismatch generated reflection at the point of the junction, this would be tolerable as long as enough power could still be transmitted to drive the mode and thus the junction. However, the appearance of this LHS mode poses the question of whether the impedance mismatch allows the resonator to support another mode of oscillation generated by reflections from a boundary condition originating from the modification of the CPW geometry at the location of the Al junction positioned at the centre of the resonator.

As well as introducing a change in the capacitance to ground via the narrowing of the central conductor the impedance is also modified by the capacitance of the junction itself. The Nb/Al interface is also suspect. As discussed in Chapter 5.3 an extended Ar etch is used to remove native surface NbO_x to ensure a superconducting connection with the Al. If the oxide is not fully removed it could form a channel of dissipation but could also act capacitively. Although removal of the NbO_x was tested using the resistance measurements of the normal state Al/Nb interfaces, if not fully removed it could generate an impedance mismatch at the interfaces located $20 - 40$ μm either side of the junction.

Although an impedance mismatch around the centre of the cavity seems plausible, the separation of the two peaks is approximately 200 MHz. Assuming the same speed of propagation, this would suggest the LHS mode has a half wavelength approximately 200 μm longer than the half-wavelength of the cavity. Given the total length of the Al integration (measured from the extremes of the Nb Al interface either side of the junction) is of order 80 μm it seems implausible that the Al component could support such a wavelength given its location and its relative length compared to the wavelength of the LHS mode. As such it is possible that the LHS mode is unrelated to the Al integration and is a product of another factor. Ultimately to investigate further measurements below the transition temperature of the Al component are required. As such the sample was installed on the dilution refrigerator.

6.2.2 Low temperature measurements

SA1 was installed on the dilution refrigerator circuit, detailed in Chapter 3.3. A wide spectrum of the sample output at temperature 10 K, 4 K and 0.035 K is shown in Fig. 6.4

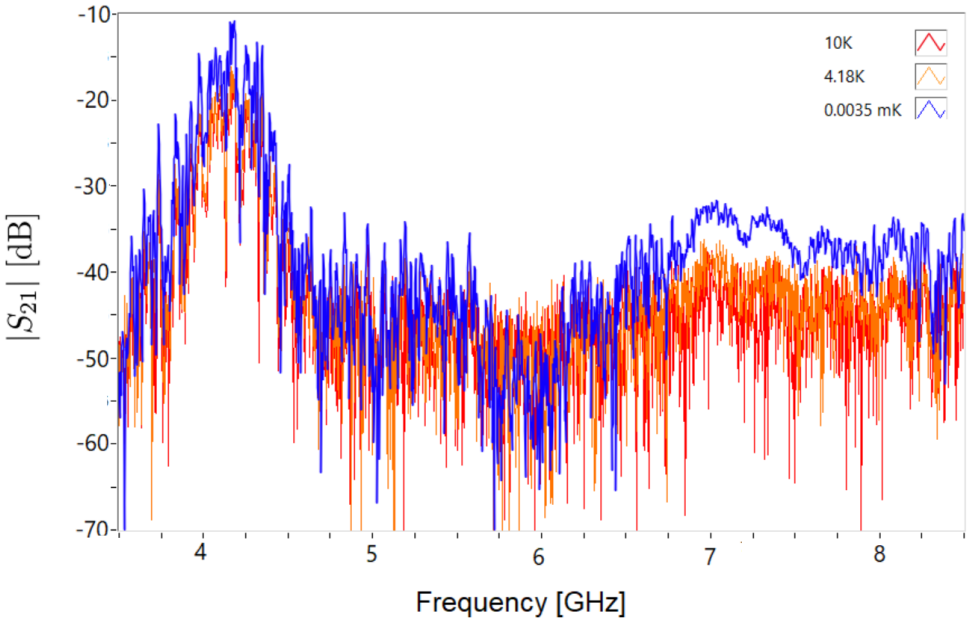

Figure 6.4: $|S_{21}|$ as a function of frequency over the full output bandwidth for 10 K (red), 4.18 K (orange) and 0.035 K (blue). A slight change in the spectrum can be observed around 6.75 to 7.5 GHz a region that bares little relevance as far as the sample is concerned, and thus probably represents a temperature dependent response of the RF circuit itself.

At $T = 0.035$ K no resonance is observed in the region where the fundamental mode is expected (≈ 6 GHz). In the case of the 4 K measurements the fundamental resonance was inferred to be absent due to the presence of the dissipative Al component. Below $T = 1.2$ K the Al component should be superconducting. However assuming a low I_c junction, it would be expected that probing the resonator frequency at even modest drive powers would result in a current bias over the junction capable of driving it normal. The normal dissipative junction would dampen the mode just as it did at 4.18 K. If this assumption is valid then by reducing the probing power of the measurements incrementally at some point the bias over the junction should drop below I_c and a resonance recovered. It should be noted that if the bias is below but close to I_c than the inductive contribution of the Josephson junction would be large, given the Josephson relation. This would lower the frequency of the resonant mode as the inductance increases. When the current is reduced far below I_c the inductive contribution should be negligible and the resonance should be centred around its unmodified resonant frequency dictated by the resonators inductance.

Since I_c is low the sample must be probed with low power levels such as not to significantly bias it. A high number of averages must be taken to ensure the region of interest is being probed effectively at low powers, greatly increasing the measurement time. This is compounded by the fact that the resonance would be shifted away from its expected resonant frequency if L_J is significantly large, increasing the frequency range over which the resonance might be positioned as a function of power. Several differing

measurement methodologies where attempted to probe the response around the region where the fundamental mode was expected. Including using a VNA to probe several areas of interest (Fig. 6.5) and also attempting to drive the fundamental and higher modes of resonator with CW sources and observe the response around the fundamental with a spectrum analyser. Despite this no resonance was observed in the region of the fundamental mode.

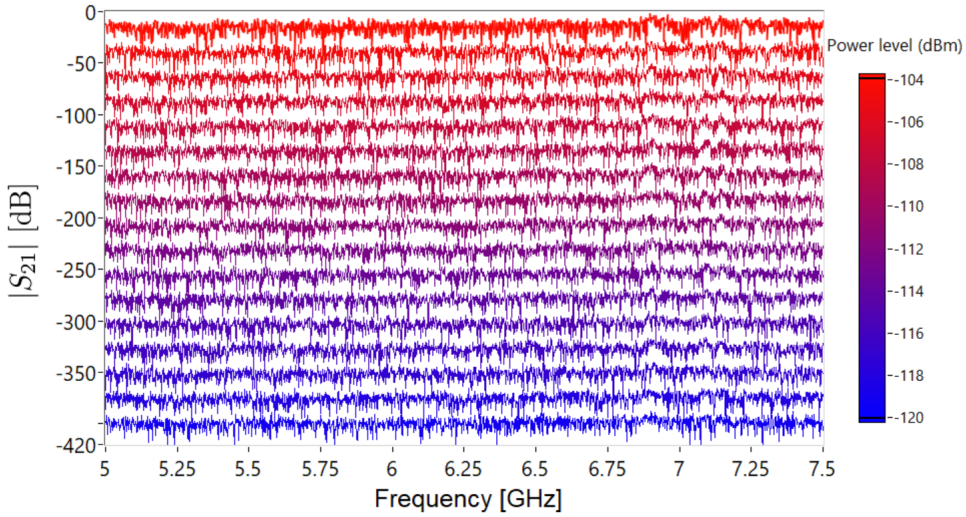

Figure 6.5: $|S_{21}|$ as a function of frequency measurements around the fundamental mode of SA1 for several different power levels, ranging from -104 dBm to -120 dBm in 1 dBm intervals. Each power level is offset $+20$ dB from the previous for clarity. An example sweep is displayed. This region of the spectrum was thoroughly investigated at a variety of power intervals and frequency windows. Ultimately no resonance was observed in the parameter space explored.

Another methodology employed the third mode (≈ 18 GHz). The third mode should have a reduced quality factor with respect to the fundamental, which corresponds to a reduced current density in the region of the junction, therefore the junction should be less sensitive to perturbation. Measurements employing the third mode involve driving the resonator with a CW source at a range of frequencies and powers around the expected frequency of the third mode and looking around the region of the fundament mode (≈ 6 GHz) using a spectrum analyser. Several acquisition windows were used to maximise bandwidth and sensitivity. If the junction is functional we can assume a cubic non-linearity which should mediate third harmonic generation/downconvertion ($\omega_1 = 3\omega_2$). Ultimately these measurements, much like the low power measurements, around 6 GHz amounted to no conclusive result with nothing of significance being observed. Although these measurements were performed with the appropriate rigour the wide parameter space rendered the search infeasible. Another potential problem is loss at low power due to the presence of two level systems (TLS's) or other parasitic effect, often attributed to

dielectrics and material interfaces as discussed in Chapter 2.1.3. Fluctuations in the current distribution of the resonator could also be a concern, owing to the electric or thermal environment and could be responsible for over driving the junction.

It was previously suggested that the LHS mode, observed around 11.8 GHz at 4.18 K, may originate from an impedance mismatch around the junction resulting in reflection at a certain interface in the cavity. It may be possible that this impedance mismatch around the Al component is reflecting a significant proportion of the input power. S_{11} measurements show no significant reflections around 6 GHz. Given the high input line isolation of the RF circuit (approximately -70 dB at 6 GHz) this is hardly an unexpected result as any reflected signal would be attenuated by the input line.

After SA1's measurement on the dilution refrigeration it was remeasured at 4.18 K using the RF probe to inspect the second mode, outside the measurement bandwidth of the dilution refrigerator circuit. The sample was unchanged compared with data taken prior to its installation and measurement on the dilution refrigerator. Transmission through the sample was measured using the DC probe station by making contact to the Nb central conductor either side of the junction. The normal state resistance was approximately 15 kΩ. Although the variance of the oxidation must be considered, this increase from the intended value (13 kΩ) is assumed to be due to ageing of the Al/AlO_x/Al junction. This effect was noted in test iterations where junctions showed a 10-20% increase in their normal state resistance when remeasured after a period of approximately one month in atmospheric conditions.

6.3 SA2

6.3.1 Design considerations

Several design changes were made to the SA1 design for samples subsequently fabricated. From the inferences made from measurements of SA1 the focus of the new sample design was to minimise any potential impedance mismatch imposed by the Al component, utilise a larger area junction with a higher critical current to make measurement less ambiguous and ensure the Nb/Al interface was being consistently cleaned prior to the deposition of the Al.

Increasing the critical current of the embedded junction geometry was straightforward, a larger area design which had been reliably fabricated in test iterations was selected as a replacement. The variance of the oxidation was noted as less extreme for larger area overlaps. The chosen junction geometry corresponded to a 200 nm$\times$ 150 nm overlap, test iterations of the same geometry had a normal state resistance of approximately 8 kΩ corresponding to a critical current estimation of approximately 60 nA. This higher critical current should be harder to perturb in comparison with the junction embedded in SA1,

however, it should still be low enough to manifest a significant non-linear response for low drive powers.

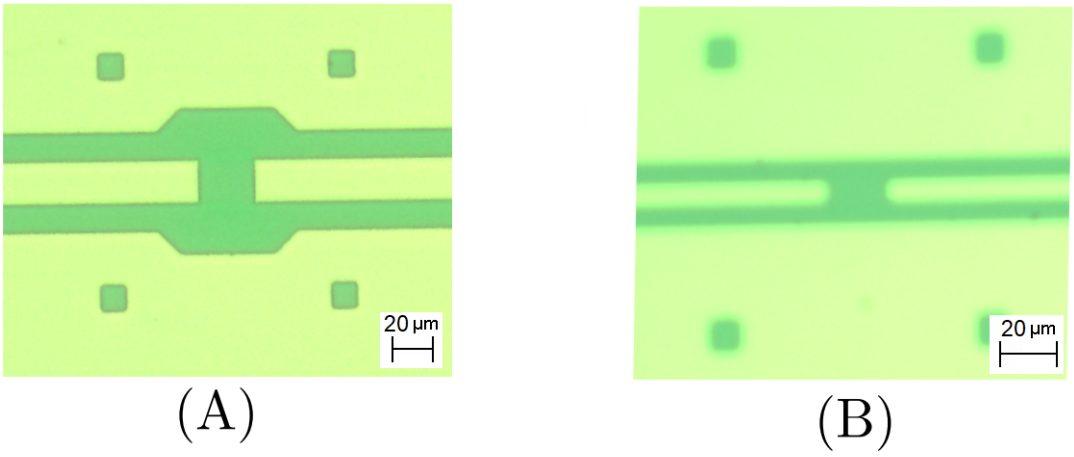

Figure 6.6: Optical image of (A) R3 resonator $l/2$ point. The gap is etched using an EBL and RIE process. (B) R1 $l/2$ point. The gap in this case is defined by the photo-mask.

The most challenging concern was to reduce any impedance mismatch due to the junction's integration. The R3 design resonator had been favoured given their versatility, with the possibility of integration of an aluminium element at arbitrary point in the central conductor. The widening of the ground plane at points of intended EBL (Fig. 6.6(A)) was undesired. Given sample design had focused around a single junction at the $l/2$ point using a R1 design resonator was considered. The $l/2$ point of an R1 resonator is shown in Fig. 6.6(B). As well as having a uniform separation of the central conductor and ground plan over the entire length of the resonator, as noted in Chapter 5.1.1, the R1 design also had a narrower central conductor width and ground plan separation. The R1 design has a width and separation of approximately $W = 10$ μm and $S = 5$ μm, in comparison with the R3 design $W = 20$ μm and $S = 10$ μm. As discussed the junction is essentially a narrowing of the central conductor. This changes the inductance and capacitance to ground at the point of its integration. For this reason the reduced dimensions of the central conductor/ground plane spacing of the R1 resonators is more favourable in comparison to the R3 design.

Another notable advantage of adopting the 1.85 GHz resonator is the relatively low resonant frequency. Given the bandwidth of the dilution refrigeration RF output circuit (3.5 GHz to 7.5 GHz), although the resonant mode would be outside the measurement bandwidth several of the harmonics would be within the output measurement window. The third harmonic (odd mode), around 5.5 GHz with a current antinode at the $l/2$ point would be used to drive the junction just as the fundamental would, albeit requiring higher drive powers to produce a similar non-linear response due to the intrinsic lower

quality factor of the higher harmonic mode. This is not a major disadvantage given prior considerations and a worry of over-driving the junction. The even modes around 3.5 GHz and 7 GHz would have a current node at the $l/2$ point and thus their excitation should not modulate the phase over the junction such that these modes should not exhibit a non-linear response. Although they shouldn't interact with the junction their presence in the output bandwidth is extremely welcome, mainly due to experiences with SA1 where at low temperatures the fundamental was absent and it was hard to infer anything about the sample with the second mode outside of the measurement bandwidth. Although the even modes are not substantially interacting with the Al component their quality factor is still of interest and representative of the environment of the sample at low temperatures. Further-more the mysterious LHS mode (11.8 GHz) observed near SA1's second mode noted in Section 6.2.1, could be potentially related to the junction integration and thus may be dependent on the state of the junction at low temperatures.

6.3.2 Prerequisite measurements

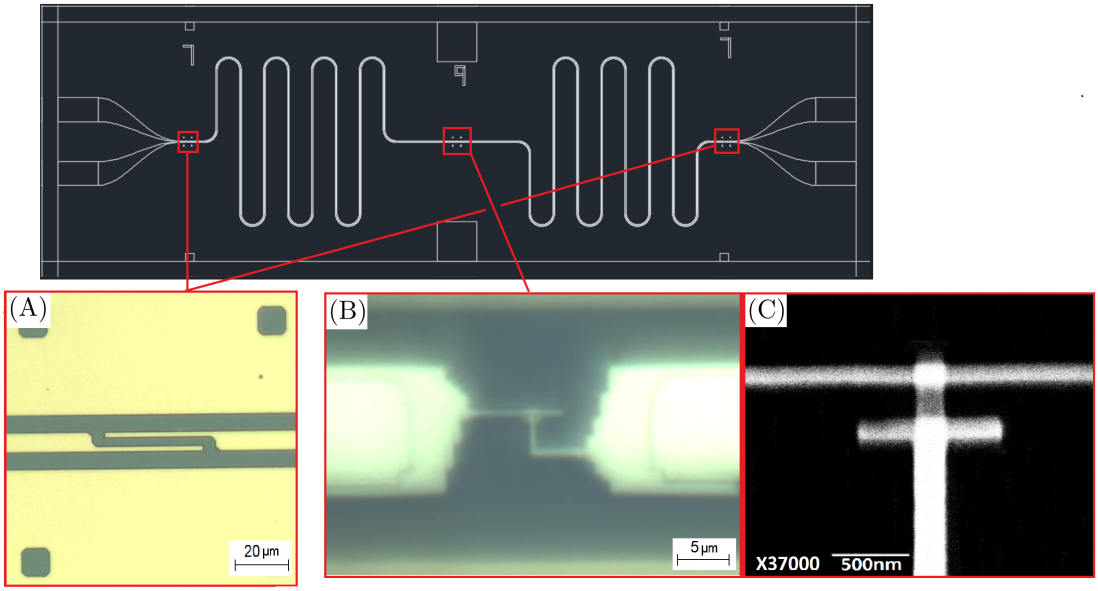

Figure 6.7: SA2, Nb $\lambda/2$ resonator with an embedded Al junction. Theoretical fundamental frequency of 1.85 GHz. (A) Optical image of C_{in}/C_{out}. (B) Optical image of the Al Josephson junction located at the $l/2$ point. (C) SEM image of a representative test junction with a geometry corresponding to that embedded in SA2.

The sample designated SA2 is shown in Fig. 6.7. The fabrication procedure was similar to that outlined for SA1. Given the R1 resonator already features a gap in the central conductor no additional etching was required to deposit the Al junction. A further design change to ease the impedance mismatch was the introduction of a step function as the Al component narrows to the junction. A step function is chosen due to the double angle process in which the Al is deposited. The right angles of the steps reduce the likelihood of

flagging due to the large angle evaporation used to lay down the first layer of Al forming the junction. Given the narrow central conductor width ($W = 10\ \mu$m) of the R1 design the Al/Nb interface cross-section was accordingly enlarged to compensate. An R1 test sample was fabricated with Al shorts over etched gaps in the central conductor, similar to the process outlined in Chapter 5.3. The shorts were measured using the DC probe station to ensure the new geometry did not incur any additional resistance and that the extended Ar etch process was removing the NbO_x prior to the deposition of the Al.

The sample is once again measured in a transport dewar at 4.18 K prior to installation on the dilution refrigerator. The first four modes of SA2 are shown in Fig. 6.8. Similarly to SA1 the fundamental mode is not visible at 4.18 K. The second mode is well-defined and there is no sign of a secondary (LHS) resonance in the vicinity as observed in SA1. As expected the pattern repeats for the higher frequency harmonics.

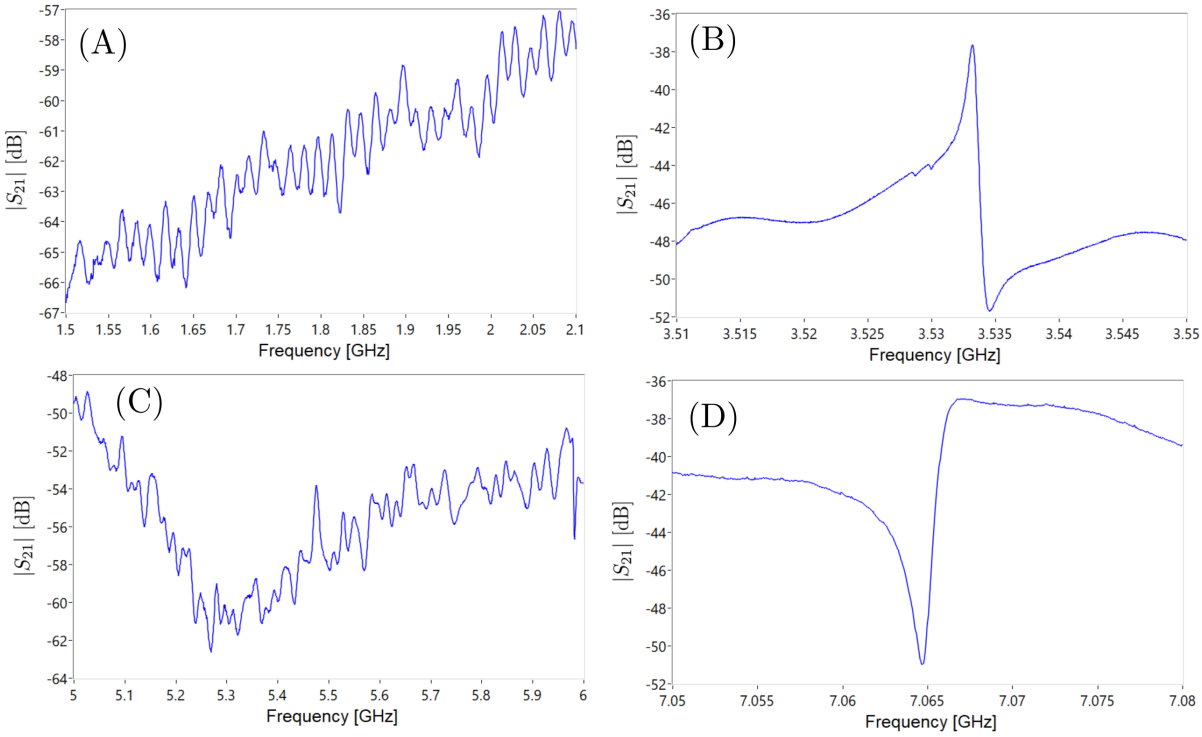

Figure 6.8: $|S_{21}|$ as a function of frequency of first four modes of SA2 at 4.18 K. Measured on an RF probe. (A) Spectrum around the expected position of the fundamental mode. (B) The second mode of the resonator. Note the asymmetrical line-shape. This was observed on several samples. (C) Spectrum around the expected position of the third mode. (D) Fourth mode of the resonator.

The even modes of the resonator (second and fourth mode) exhibit an asymmetrical line-shape indicative of a Fano resonance discussed in Chapter 2.1.4. As previously noted the observation of these features is not unusual. Fano line-shapes were observed in unmodified resonator discussed in Chapter 5.1.3. It was assumed that Fano resonance arises from an asymmetric ground plane potential, attributed to surface imperfections

preventing good electrical contact over the length of the resonator when using the contact sample box (shown in Fig. 3.19). SA2 however is installed in the PCB sample box. As discussed in Chapter 3.3.1, Al wire bonds are used to connect the PCB to the sample. The wires connecting the ground plane are closely spaced. As such any non-uniformity in the ground potential over the length of the resonator should be minimised. Therefore it is not clear where the broad state originates in SA2. A possibility is that the Al integration has induced these spectral features, maybe inadvertently supporting a broad mode with a shifted resonant frequency interfering with the individual harmonic modes of the resonator. Another possibility is parasitic defects have been introduced from the sample fabrication. Ultimately the precise cause of the asymmetric line-shape in this sample is unknown.

After its initial characterisation, SA2 was installed on the dilution refrigerator circuit. Measurements at 4.18 K are repeated for consistency. The second and fourth modes are fitted using the Fano function detailed in Chapter 2.1.4. The quality factors of the second and fourth mode at 4.18 K are approximately 4500 and 3500, respectively.

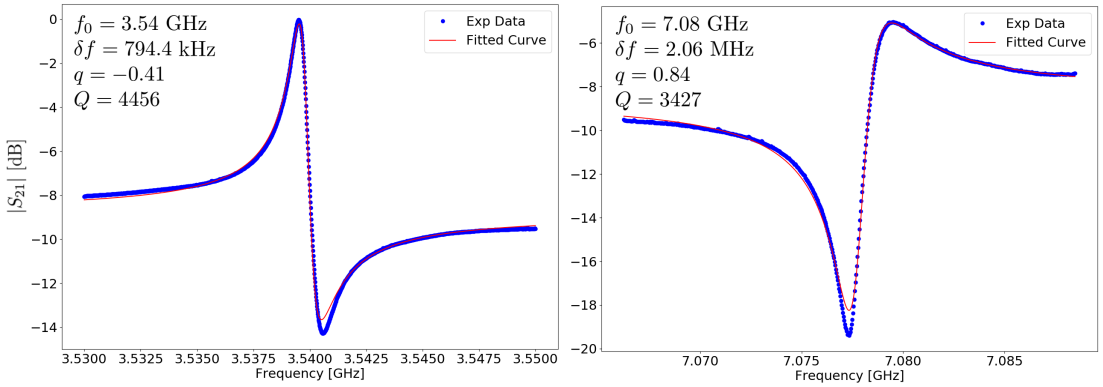

(A) (B)

Figure 6.9: $|S_{21}|$ as a function of frequency of SA2 at 4.18 K. (A) Second mode. (B) Fourth mode. Fitting with a Fano function gives the asymmetry parameter $q = -0.41$ and $q = 0.84$ for the second and fourth mode respectively. Data was taken at 4.18 K on dilution refrigerator RF circuit. A notable feature is that the asymmetry is reversed for the respective modes, indicating a different phase relation for the individual discrete resonances and the broad state they are coupled to.

6.3.3 Initial low temperature measurements

I will briefly summarise the general behaviour of SA2 before expanding on the observed phenomena in more detail in subsequent sections. The sample was cooled to 0.025 K and the modes in the measurement bandwidth were probed at different power levels. Although the third mode was of primary interest, the second and fourth modes were also inspected. Fig. 6.10 and 6.11 show $|S_{21}|$ data for five power levels in 10 dBm intervals, in the region of the second and fourth mode respectively.

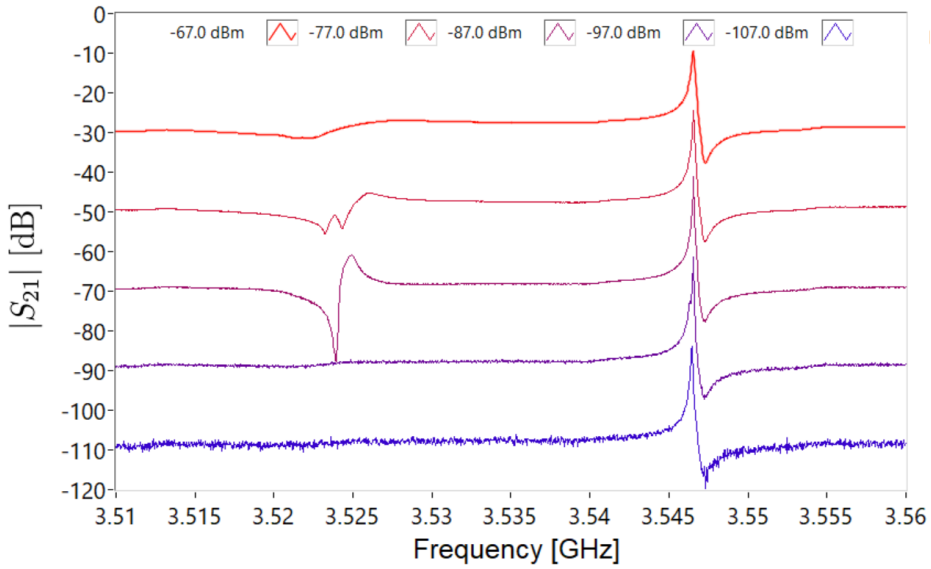

Figure 6.10: $|S_{21}|$ as a function of frequency measurements around the second mode for several different power levels, ranging from -107 dBm to -67 dBm in 10 dBm intervals. Each power level is offset $+20$ dB from the previous for clarity.

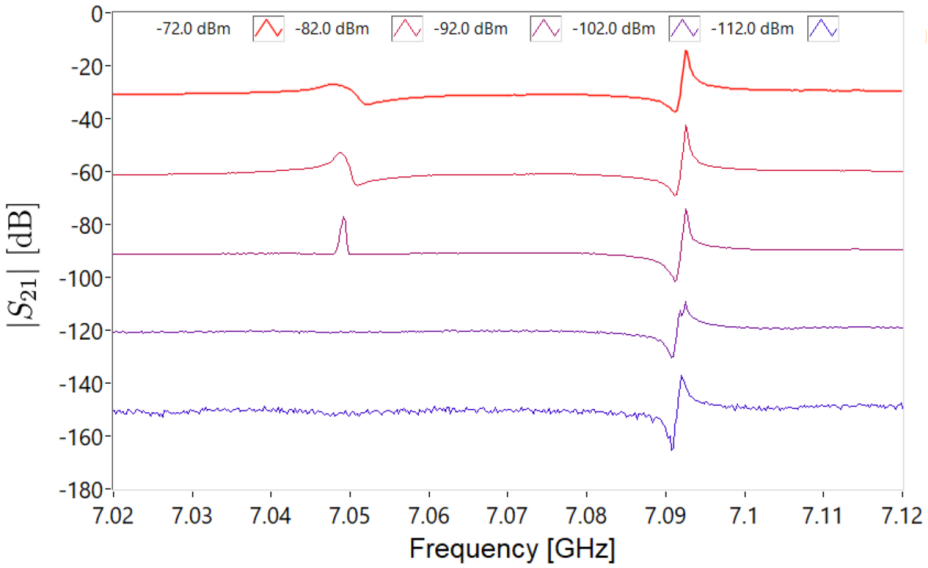

Figure 6.11: $|S_{21}|$ as a function of frequency measurements around the fourth mode for several different power levels, ranging from -112 dBm to -72 dBm in 10 dBm intervals. Each power level is offset $+20$ dB from the previous for clarity.

The most apparent feature present in Fig. 6.10 and 6.11 is the appearance of a lower frequency mode in the transmission spectra, which appears and then subsequently decays. Referring to Fig. 6.10, the separation of two modes is approximately 20 MHz and in Fig. 6.11 the separation is approximately 40 MHz. The S_{21} data centred around the second mode at a input power level of -87 dBm is shown in Fig. 6.12. The mode centred around

3.525 GHz has an asymmetric line-shape, with a positive asymmetry parameter, q, in contrast to the second mode centred around 3.545 GHz with a negative q. The linear progression due to the finite length of the measurement lines has been removed from the phase data via fitting and subtracting an appropriate sawtooth function. There is a phase shift between the two resonances given their respective response to the drive. This would explain why the asymmetry parameter is reversed. If the resonances (discrete states) are out of phase then their respective phase shift with the broad state is similarly out of phase relative to each other, resulting in opposite asymmetry parameters.

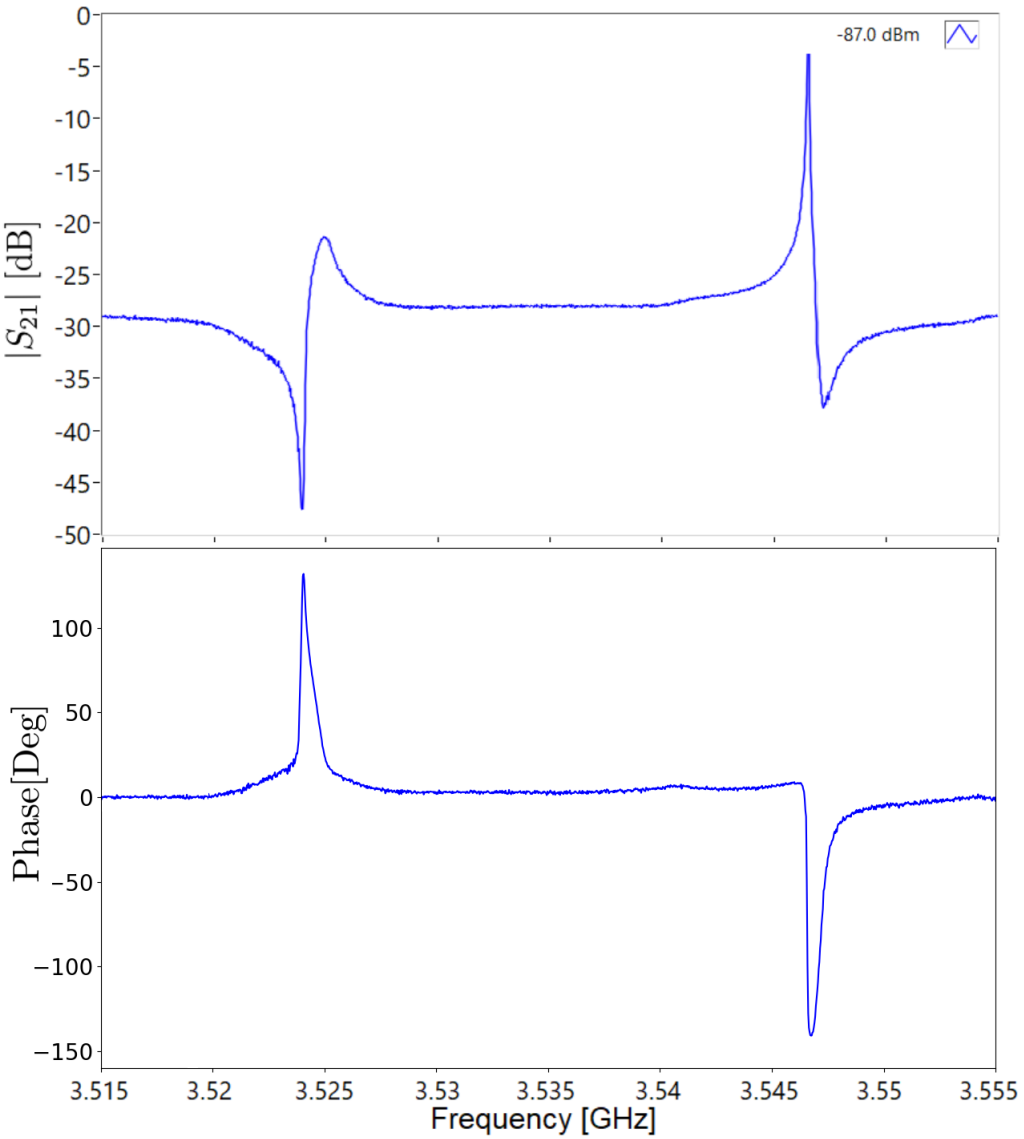

Figure 6.12: S_{21} measurement as a function of frequency around the second mode, for a power level of −87 dBm. Top: $|S_{21}|$. Bottom: Phase, where the linear progression of the phase due to the measurement lines has been removed via fitting and subtracting a sawtooth function to the data.

Fig. 6.13 shows $|S_{21}|$ measurements around the second mode for a power range of −95 dBm to −73 dBm in 1 dBm intervals. The mode centred around 3.525 GHz appearers

at an approximate power level of −92 dBm. Its linewidth starts to broaden as the power level increases further. At approximately −85 dBm the mode appears to split and collapse in on itself. At the higher power levels it is reduced to a bump in the spectrum with no significant phase response. Although we have been focusing on the component centred around 3.525 GHz, variations can also be seen in the second (3.545 GHz) and fourth mode (7.09 GHz) as the power level increases.

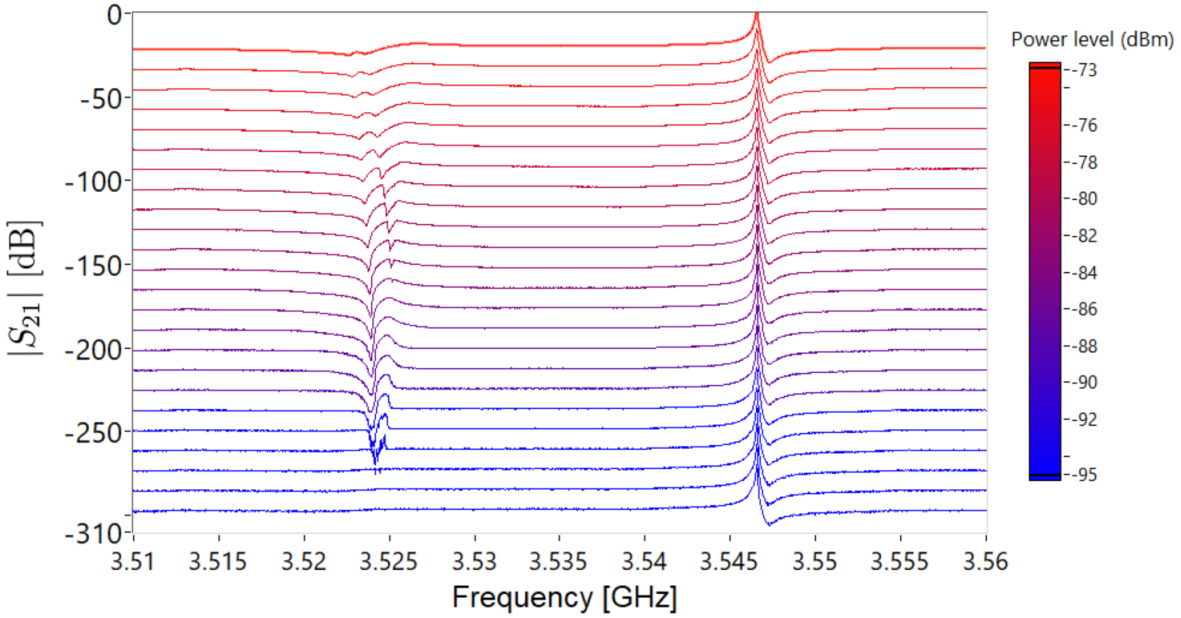

Figure 6.13: $|S_{21}|$ as a function of frequency measurements around the second mode for several different power levels, ranging from −95 dBm to −73 dBm in 1 dBm intervals. Each power level is offset +12 dB from the previous for clarity.

Over the next few sections we will focus on the behaviour of the second mode centred around 3.545 GHz and the power dependent resonant feature centred around 3.525 GHz, which will be referred to as the "sigma" mode for convenience.

6.3.4 Second mode

Fig. 6.14 and Fig. 6.15 show S_{21} measurements at power levels ranging from −107 dBm to −67 dBm in 1 dBm steps now centred around the second mode of the CPW resonator (3.462 GHz to 3.5468 GHz). The second mode shows significant power dependence over this range. At approximately −105 dBm, the resonant mode appears to split with a component moving towards lower frequencies. Around −92 dBm a similar event can be observed, this power level corresponds to the appearance of the sigma mode in the spectrum around 3.525 GHz. As the power increases further the second mode appears to broaden, with the quality factor of the mode reduced. We will first discuss the low power level interval −107 dBm to −93 dBm before looking at the behaviour of the mode

between −96 dBm to −77 dBm, where the sigma mode appears in the spectrum followed by a reduction in the quality factor of the second mode.

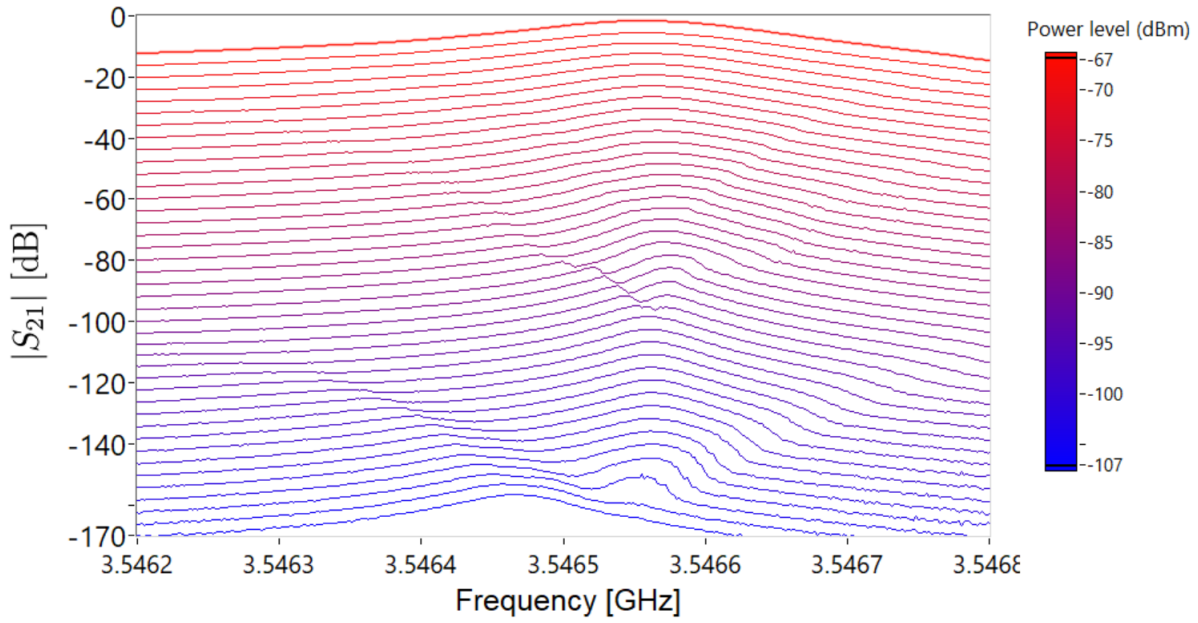

Figure 6.14: $|S_{21}|$ as a function of frequency measurements centred around the second mode for several different power levels, ranging from −107 dBm to −67 dBm in 1 dBm intervals. Each power level is offset +4 dB from the previous for clarity. The resonance shifts over the power range to higher frequencies, broadening at higher powers. Frequency bending can also be observed both towards higher and lower frequencies.

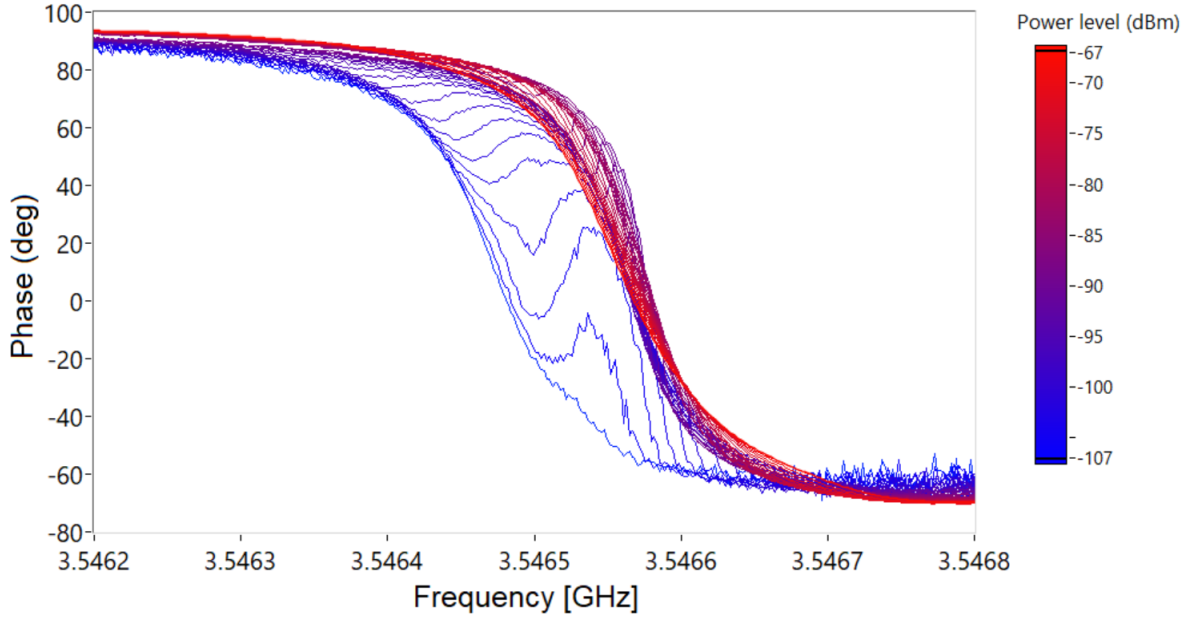

Figure 6.15: S_{21} Phase data corresponding to $|S_{21}|$ shown in Fig. 6.14. Measurements at each individual power level has been overlaid for comparison. Detuning, perturbation and damping of the resonant mode can be observed for increasing power.

6.3.4.1 Second mode: −107 dBm to −93 dBm

Fig. 6.16 shows a fitted $|S_{21}|$ measurement of the second mode at a power level of −107 dBm. The resonance is still asymmetric, the antiresonance is not visible due to the narrower frequency range. The data can be well described by a generalised Lorentzian fit, giving a quality factor of approximately 45000 for this power level.

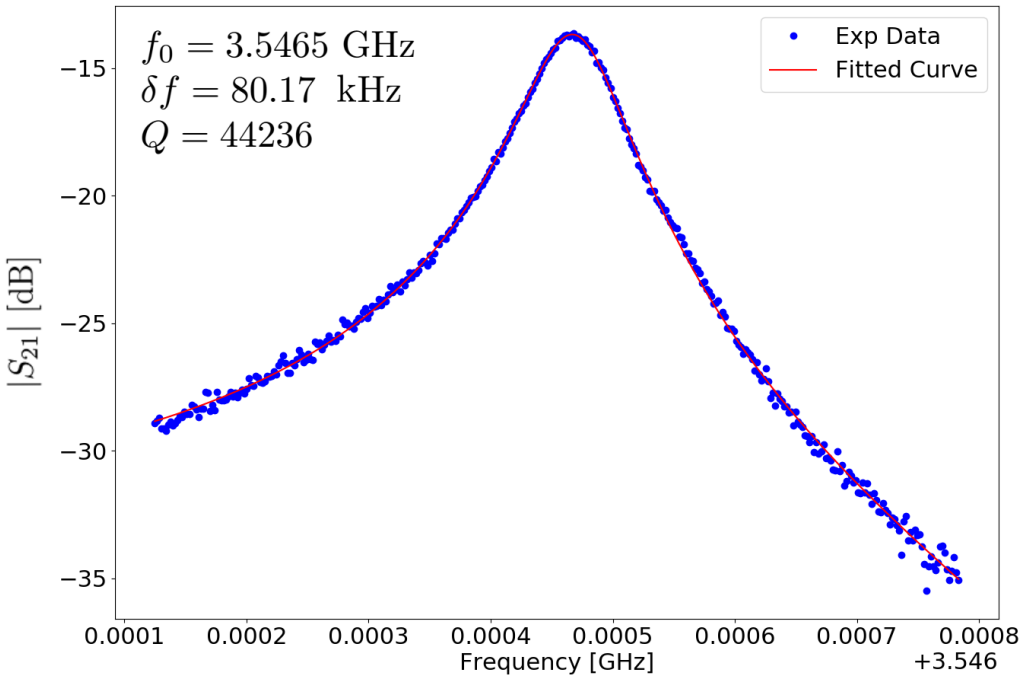

Figure 6.16: $|S_{21}|$ as a function of frequency for a power level of −107 dBm.

Fig. 6.17 shows changes in the frequency and phase response around resonance between the power level interval −107 dBm to −100 dBm. Over this range the mode appears to evolve into two separate components. A LHS component, originating from the location of the centre frequency of the second mode at −107 dBm and a RHS component centred around 3.5466 GHz. Both components show slight but noticeable frequency pulling. The LHS component bends toward lower frequencies as power is increased while the RHS component establishes itself as the dominate peak in the spectrum. A steep gradient in the response can also be seen on the higher frequency side of RHS component. This behaviour can also be observed in the phase response, where the phase change is shifted towards higher frequencies (RHS component) with the phase change due to the LHS component reducing as the power level is increased.

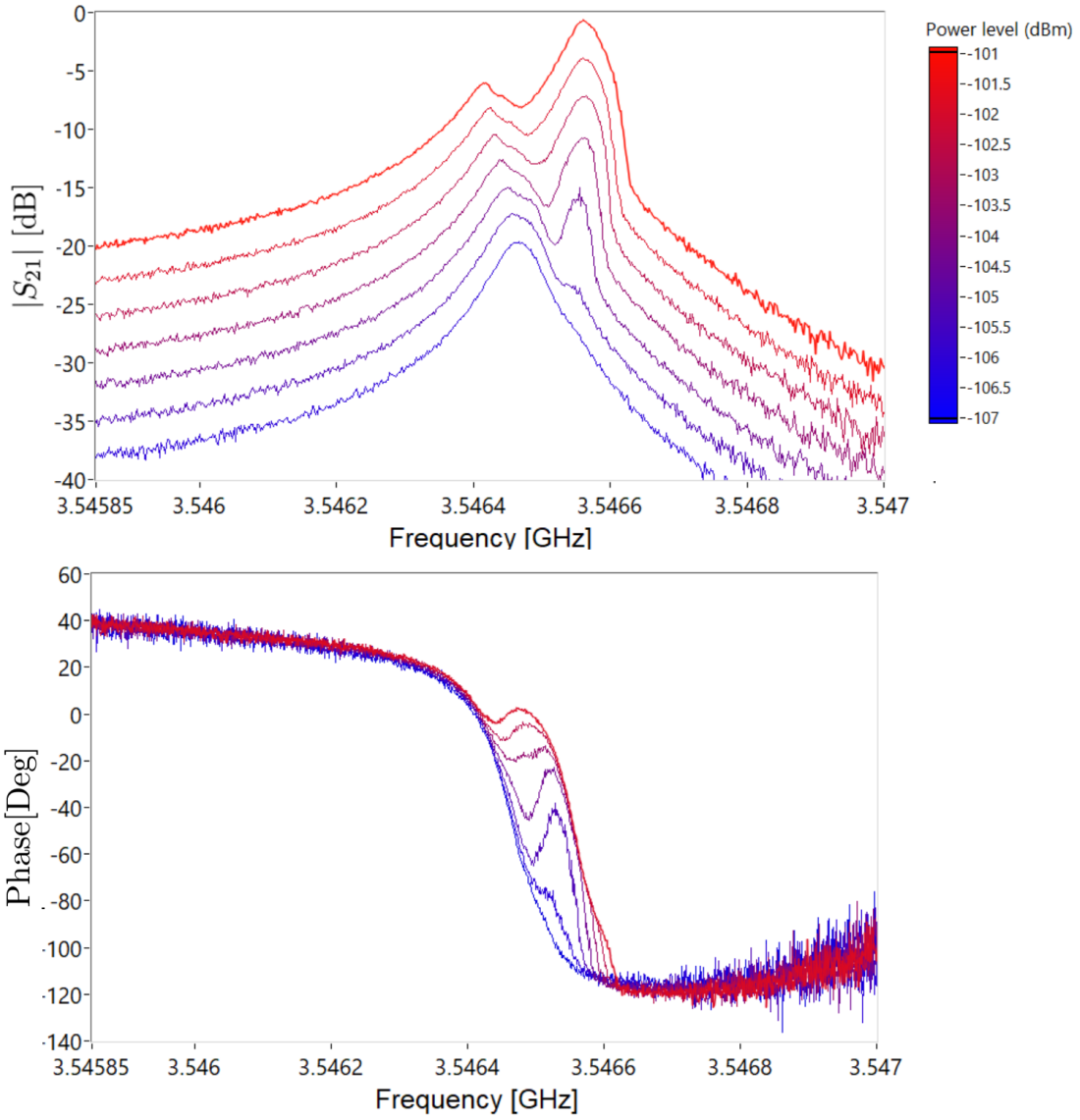

Figure 6.17: S_{21} as a function of frequency for several different power levels, ranging from -107 dBm to -100 dBm in 1 dBm intervals. Top: $|S_{21}|$. Each power level is offset $+3$ dB from the previous for clarity. Bottom: Phase. Measurements at individual power levels have been overlaid for comparison.

As the power is increased further, shown in Fig. 6.18 over the range of -100 dBm to -93 dBm, the LHS component continues to move towards lower frequencies gradually smoothing as the power level is increased. The RHS component which is now effectively the second mode (albeit shifted to a higher frequency), appears well-defined. Frequency bending can also be observed on the higher frequency side, also smoothing as the power level is increased.

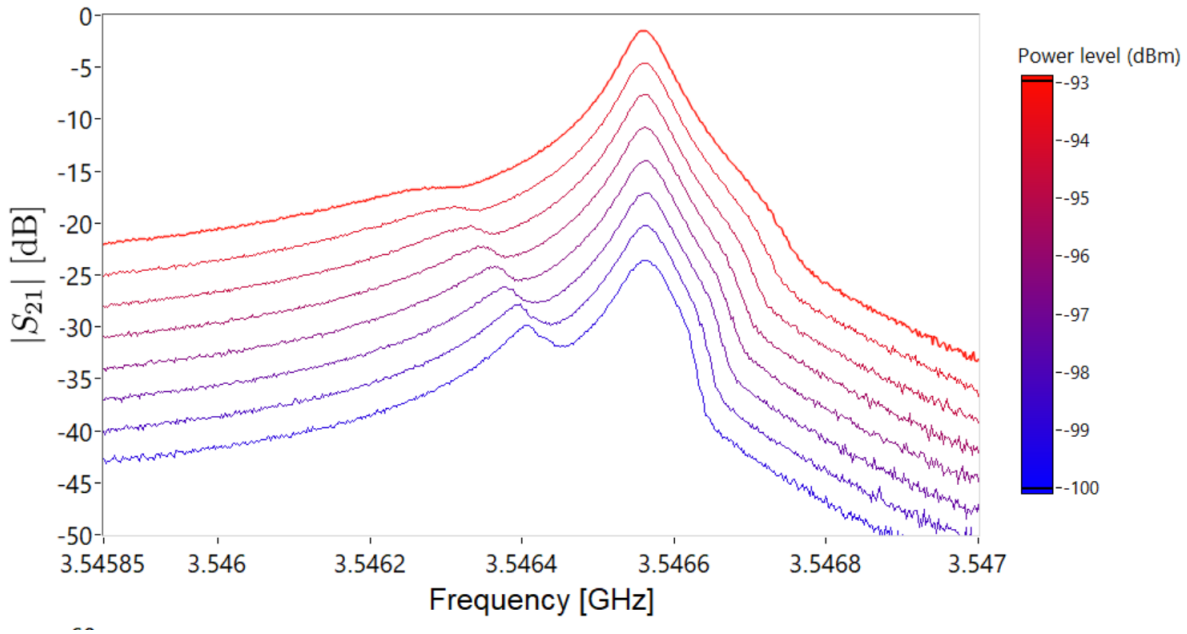

Figure 6.18: $|S_{21}|$ as a function of frequency for several different power levels, ranging from -100 dBm to -93 dBm in 1 dBm intervals. Each power level is offset $+3$ dB from the previous for clarity.

The fitted data at a power level of -93 dBm is shown in Fig. 6.19. The mode is centred at a frequency 3.54656 GHz, corresponding to a detuning of approximately 90 kHz from its position at -107 dBm (3.54647 GHz). The quality factor has increased to approximately 55000.

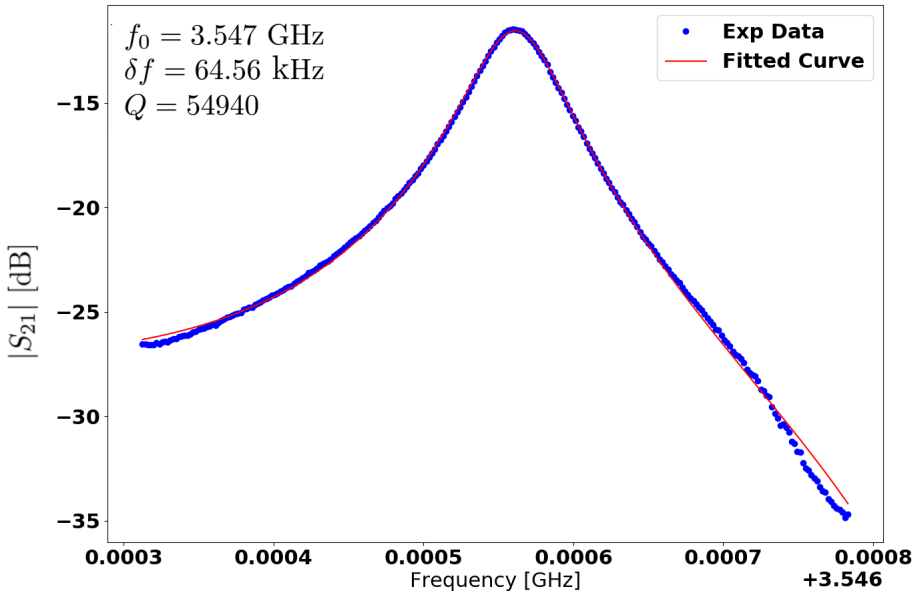

Figure 6.19: $|S_{21}|$ as a function of frequency for a power level of -93 dBm. The data fits well to a generalised Lorentzian however frequency bending can be still be observed at the extremities.

Before moving on to discuss the power level interval corresponding to the appearance of the sigma mode in the spectra it worth making some inferences regarding this behaviour. The shifted resonant frequency is indicative of a change in inductance at this power level. A sensible assumption is that any change of inductance at this low power level (-106 dBm) is related to the embedded Al junction at the $l/2$ point. However this is inconsistent with the assertion that there is a current antinode at the position of the junction. At this frequency we would not expect to be able to drive the junction and L_J should be zero.

This is expected in an ideal case where the junction is defined as a point particle at the centre of idealised $\lambda/2$ resonator. In the case of SA2 we would not expect for the junction to be perfectly positioned on the $l/2$ point. Regardless, for the time being we will assume that the junction is approximately close enough to the $l/2$ point to correspond to a node in the current distribution at its location. In this case driving at the resonant frequency would produce no oscillating current over the junction such that we would not expect an inductive response. However damping and subsequent broadening of the resonance allows for modes slightly detuned from the resonant frequency to also be supported. As such in a realistic situation, generally, there would be a small but finite perturbation of the junction with respect to the excitation of frequencies slightly detuned from the resonant frequency of the second mode. Due to the low critical current ($I_c \approx 60$ nA) a small bias may result in a inductive response. This may be achievable even with a weak junction-mode coupling. As the power increases, L_J increases, pulling the modes its interacting with towards lower frequencies. At a sufficient bias a non-linear response of the resonance would be expected given the cubic restoring force presented by the junction, discussed in Chapter 2.3.7. If the driving force and non-linear restoring force is strong enough bifurcation in the amplitude state of the resonance should result.

These arguments can be applied to the LHS mode observed to bend towards lower frequencies as the power increases. However bifurcation is not observed and as the power increases further the LHS components smooths. This could be a consequence of the resonant condition, as the component detunes further from the resonant frequency of the second mode. However, this does not explain the RHS component. If we interpret the RHS modes as the second mode of the resonator, shifted to a higher centre frequency over this power level, then that would correspond in a reduction in the total inductance. This is harder to relate to the junction.

It is worth considering other possible causes for this behaviour. It worth at this point addressing the kinetic inductance of the Nb CPW resonator. As discussed in Chapter 2.1.2.2, the total inductance of a SCPW resonator relates to its geometry and the characteristic properties of the superconductor used and is given as the sum of the geometric (magnetic) inductances L_M and the kinetic inductance L_k. The geometric and kinetic inductance can be estimated for this geometry of Nb CPW resonator using the R1 design files giving $L_M = 430$ nHm^{-1} and $L_k = 55$ nHm^{-1} resulting in a contribution ratio

$\alpha = \frac{L_k}{L_M} \approx 0.1$. Given L_k has a non-linear dependence on the current I this would also lead to a non-linear inductive response as a function of drive power. However as mentioned in Chapter 2.2.5, the dependence on I is relatively weak (scaled by I_*), as such high currents corresponding to much higher power levels would be required to modulate the kinetic inductance of this Nb CPW resonator. A similar design of resonator without any Al integration using an nominally identical 200 nm thick Nb sputtered film to that used in the SA2 was measured at low temperature by a previous member of the research group, G. Tancredi, and reported in her PhD thesis [64]. In this case frequency bending was observed at a power level of approximately −60 dBm, attributed to the kinetic inductance of the film. Further more, the mode being driven had a quality factor reported as approximately 600,000. This contrasts highly with observation of SA2's second mode power dependence which seems to manifest at power levels of −106 dBm where the quality factor of the mode is substantially lower. As such we will discount kinetic inductance being responsible for this perturbation of the resonance around this power interval.

A further consideration is dielectric loss and TLS's as discussed in Chapter 2.1.3. Although we would expect these non-idealities to become more prominent at low input powers, primarily resulting in a detriment to the quality factor, it is hard to see how their presence would lead to the observed behaviour. As such we will continue to explore the behaviour of the second mode at higher powers, bearing these considerations in mind.

6.3.4.2 Second mode: −96 dBm to −77 dBm

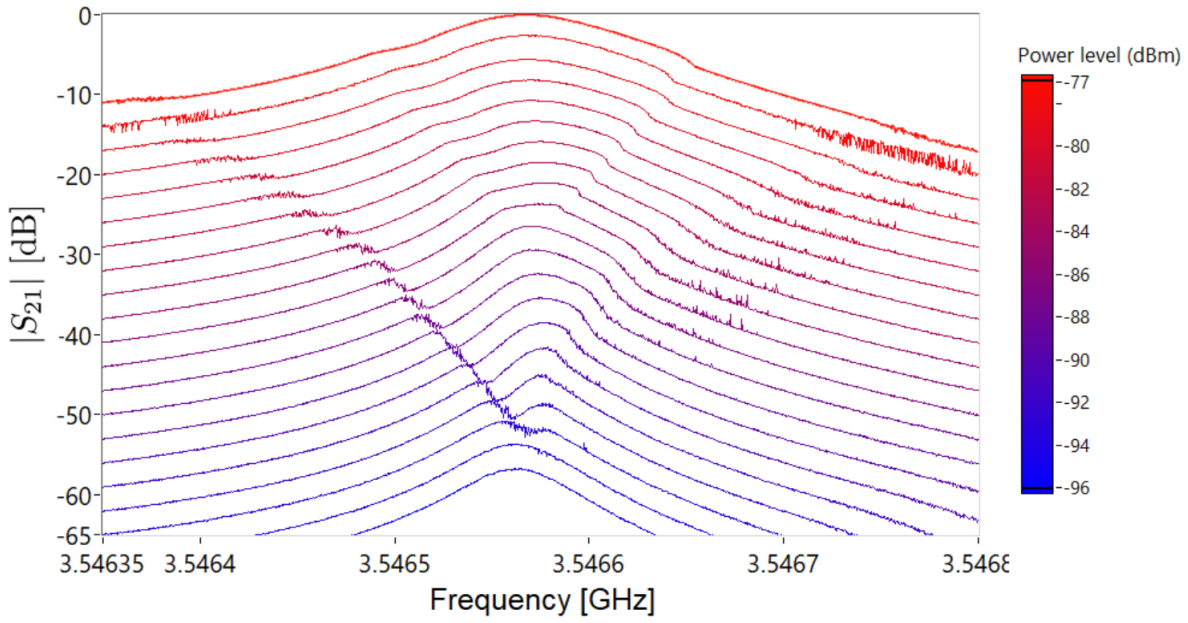

Figure 6.20: $|S_{21}|$ as a function of frequency measurements around the second mode for a power interval −96 dBm to −77 dBm in 1 dBm steps. Each power level is offset +3 dB from the previous for clarity.

We will now look at the power dependence of the second mode over a power range of −96 dBm to −77 dBm, this corresponds to range where the sigma mode appears in the spectra around 3.525 GHz and then subsequently dampens towards higher drive powers. $|S_{21}|$ as a function of frequency for several different power levels, ranging from −96 dBm to −77 dBm in 1 dBm intervals, is shown in Fig. 6.20.

The behaviour of the resonance over this range is similar to that observed in the case of lower powers. The resonance seems to split into two components with frequency bending observed either side, moving towards lower and higher frequencies respectively. Fig. 6.21 shows the initial onset of this event, around a power interval of −97 dBm to −88 dBm, in this case no offset has been applied to the data. Around −93 dBm the mode appears to evolve into two separate components, with the phase shifted towards higher frequencies at higher powers.

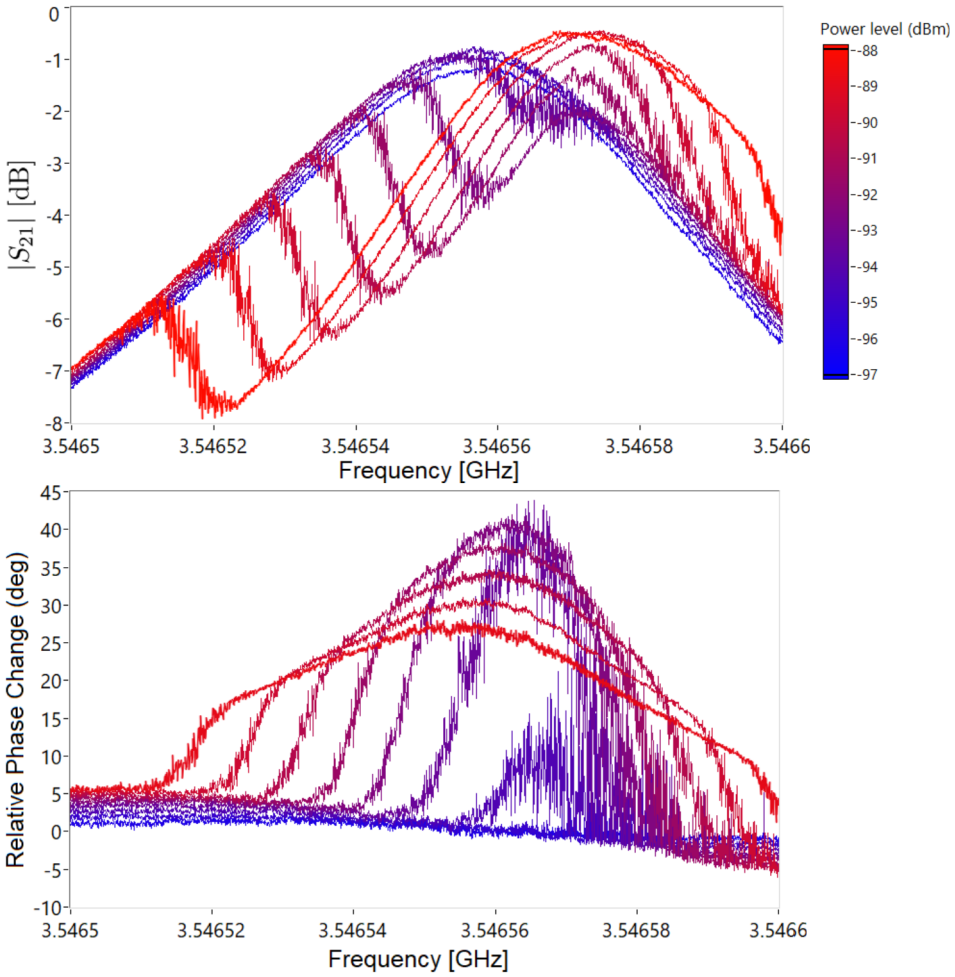

Figure 6.21: S_{21} as a function of frequency measurements for a power interval −96 dBm to −88 dBm in 1 dBm steps. Measurements at each individual power level have been overlaid for comparison. Top: $|S_{21}|$. Bottom: Relative phase change as a function of frequency. The phase at a power level of −96 dBm has been subtracted from the phase at higher power levels such as to give the relative change in phase over the frequency range as the power is increased.

As the frequency bending components move to lower and higher frequencies respectively the resonance appears to re-establish itself at a slightly higher frequency moving from 3.5455 to 3.5457 GHz. Above −85 dBm (Fig. 6.22) the mode begins to dampen as the drive power is further increased. Similar to the previous event around −92 dBm and −106 dBm, frequency pulling either side of the resonance can also be observed.

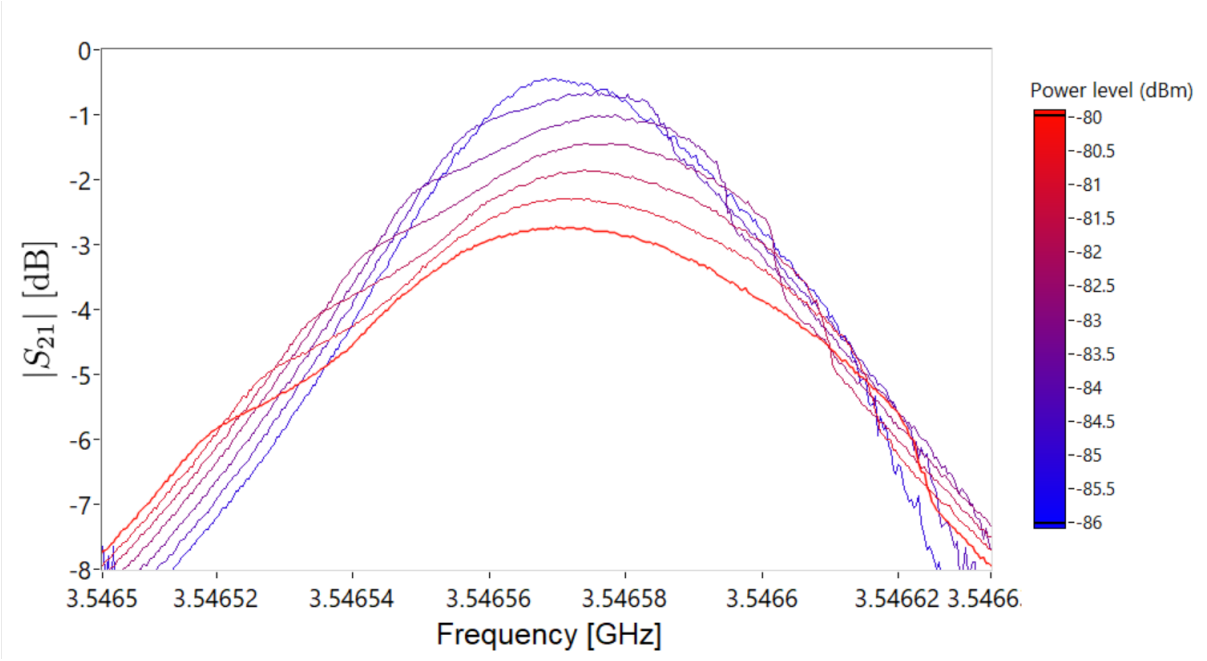

Figure 6.22: $|S_{21}|$ as a function of frequency for a power interval −86 to −80 dBm in 1 dBm steps. Measurements at individual power levels have been overlaid for comparison.

At a power level of approximately −80 dBm an extreme response is observed shown in Fig. 6.23. The components either side of the resonance (A and D) are the two components that originated at −92 dBm which have been gradually moving to lower and higher frequencies respectively with increasing power. Over this range the amplitude state of the respective components can be seen becoming increasingly unstable (Fig. 6.20). In the case of Fig. 6.23 the components A and D appear bifurcated such that there are two states of oscillation in these regions analogous to the amplitude of a Duffing oscillator, discussed in Chapter 2.3.7, when $F > F_c$. It is interesting to observe this behaviour seemingly removed from the resonant mode of the cavity. This could be indicative of driving the Josephson junction using the second mode of the cavity. Since there is a current node at the centre of the resonator the spatial current variation is maximum. This means the uncertainty in the junction current is significant and dependent on the frequency within the resonant band.

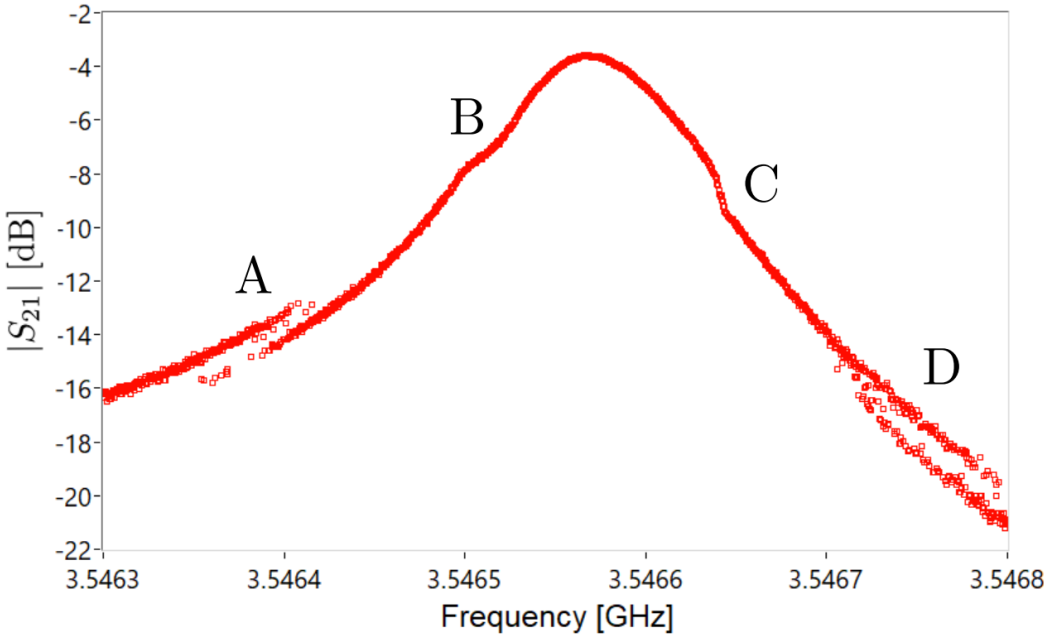

Figure 6.23: $|S_{21}|$ as a function of frequency for a power level of -78 dBm. A, B, C and D represent points of interest (bistability and frequency bending/pulling behaviour) referred to in the text.

6.3.4.3 Quality factor

The presence of a strong non-linearity interacting with the second mode of this sample is quite apparent. Before we interpret the behaviour of SA2 further we will look at how the quality factor of the second mode changes over the power interval of -107 dBm to -66 dBm. Fig. 6.24 shows the change in quality factor of the second mode as a function of drive power. The process of fitting for the quality factor with an appropriate Lorentzian function is complicated due to the frequency pulling and splitting of the second mode. This is especially prominent around -105 dBm and -92 dBm (red points) where the second mode splits into two components. The line-shape around these powers is considerably distorted and no longer accurately described by a Lorentzian function. Further complications arise due to the frequency bending components noted in previous sections. These features can lead to an overestimation of the quality factor, illustrated in Fig. 6.25(A). This was noted in several fits (green point), in this case the quality factor was manually calculated by measuring the width at the half maximum (-3 dB point), an alternative way to calculate the quality factor for high signal-to-noise ratio.

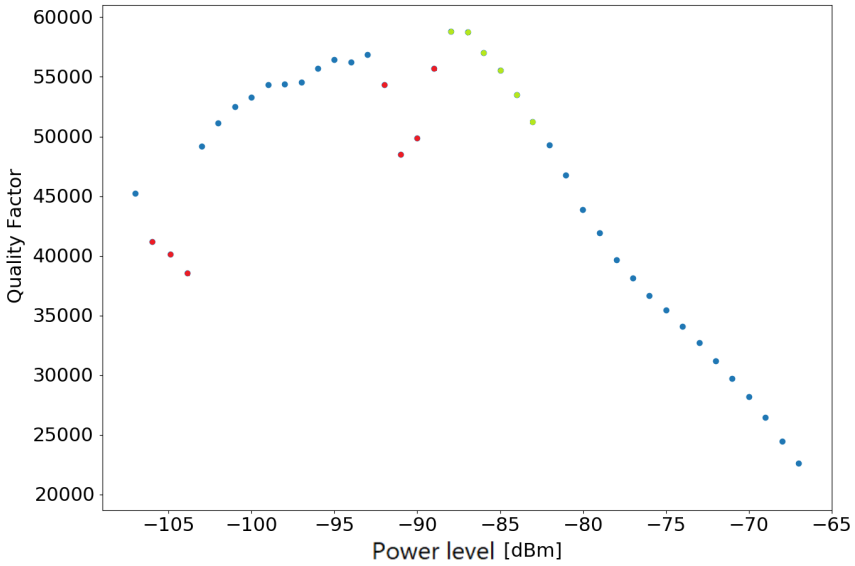

Figure 6.24: Quality factor of second mode as a function of power level. Blue points - fitted with generalised Lorentzian fitting function. Red points - correspond to a underestimation of the quality factor due to the splitting events. Green points - manually calculated.

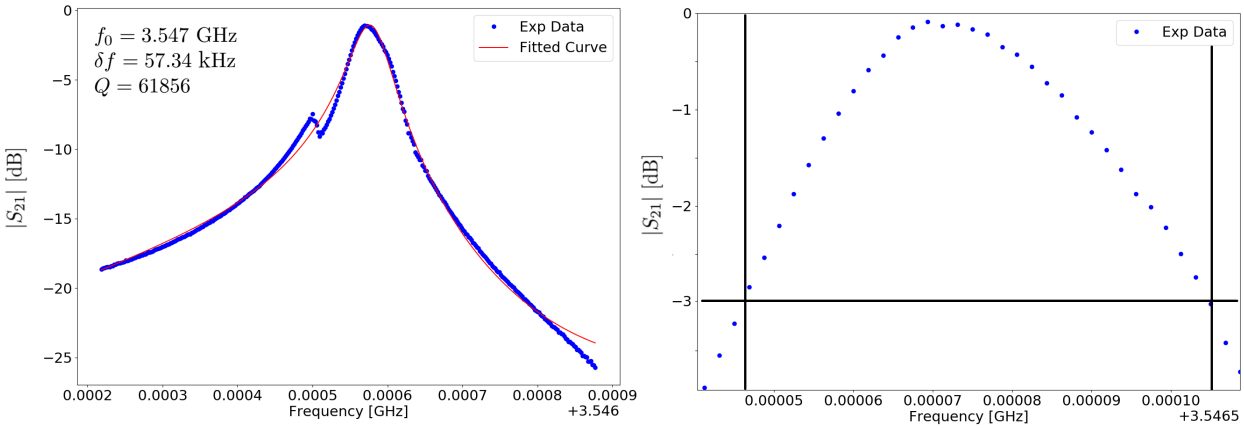

(A) (B)

Figure 6.25: $|S_{21}|$ as a function of frequency for power level of -87 dBm, corresponding to a green point on Fig. 6.24. At this power level the LHS and RHS components obstructed a good fit to the data leading to an overestimation of the quality factor (A). Although several methods were attempted to compensate, manual estimations were used where a goodness of fit test was not met (B).

Given the frequency bending and splitting makes fitting the line-shape for the quality factor of the mode ambiguous, an alternative method of interpreting the behaviour is shown in Fig. 6.26, where the data is just fitted for the centre frequency of the dominant (largest) peak in the spectra. The position of the resonance shifts towards higher frequencies around power levels of -105 dBm (≈ 100 kHz) and -92 dBm (≈ 10 kHz).

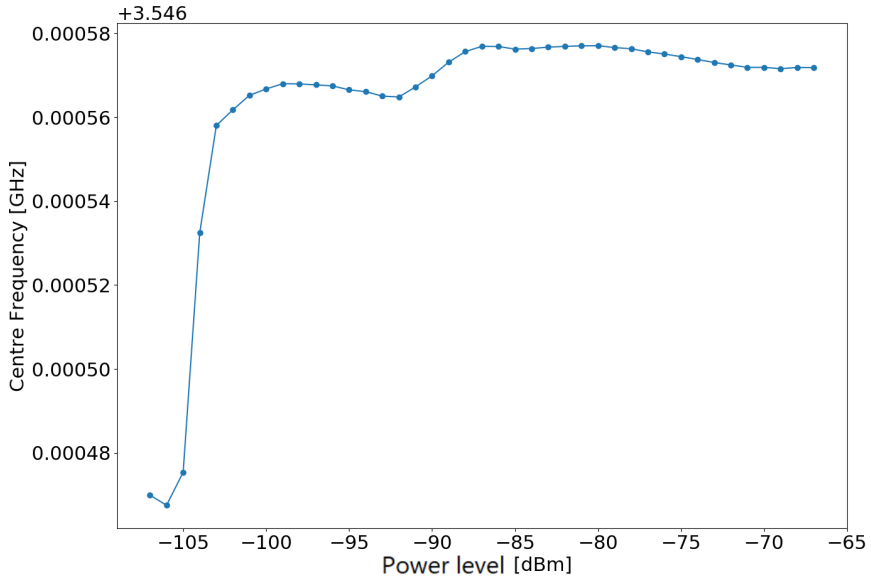

Figure 6.26: Centre frequency as a function of power level - $|S_{21}|$ data is fitted for the centre frequency of the dominant (largest) peak in the measured output spectrum for a given power level. The position of the resonance shifts towards higher frequencies around power levels of -105 dBm and -92 dBm

For power levels above -86 dBm the quality factor begins to reduce while the position of the resonance remains approximately constant. At the highest power levels, shown in Fig. 6.27, the quality factor of the mode is approximately 22000.

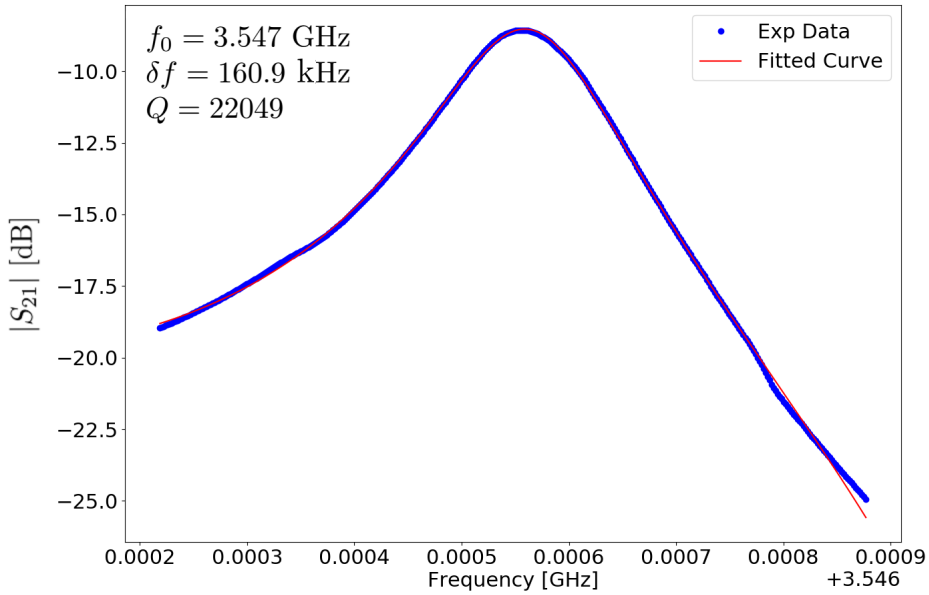

Figure 6.27: $|S_{21}|$ as a function of frequency for power level of -67 dBm. Fitted with a Lorentzian function.

Frequency pulling and bifurcations are a strong indication of a significant non-linear

interacting with the second mode of the CPW resonator. The reduction of the quality factor for power levels above -86 dBm seems indicative of dissipation in the resonator. This could correspond to exceeding the critical current of the junction when driving the second mode around this power level. However, frequency pulling and bifurcation behaviour can still be observed either side of the resonance while the quality factor reduces.

Given the junctions location at the $l/2$ point we expect a node in the current distribution such that driving at the exact resonant frequency of the second mode should result in no current bias over the junction and thus it should not be over-driven. However excitations of frequencies slightly detuned from the resonant frequency with correspondingly shifted current distributions would result in perturbation of the current over the junction and modulate of the L_J. The spread of frequencies capable of interacting with the junction is determined by the quality factor of the mode.

To illustrate this argument it is constructive to refer back to Fig. 6.23, showing $|S_{21}|$ data as a function of frequency for a drive power of -78 dBm. This corresponds to a power level where the quality factor is significantly reduced. Frequency bending (points B and C) and bifurcation like behaviour (points A and D) is also observed at this power centred around the resonant frequency of the second mode. Considering moving from lower to higher frequencies, for frequencies detuned from the resonant frequency the junction's inductance is modulated resulting in bifurcation behaviour observed at point A. As the frequency is increased towards resonance the current bias over the junction reduces, hence decreasing its inductance. This is highlighted by point B where the amplitude response deviates from its upward trajectory, this could indicate a change in inductance, increasing the resonant frequency of the second mode. As the frequency passes through resonance the inductive response of the junction is recovered, potentially at point C. As the frequency is increased further, the current over the junction increases and a significant non-linear response is observed at point D. Although this could explain some of the observed features it does not explain why for higher drive powers the quality factor of the second mode reduces given the current node at its resonant frequency. However it could be possible that the junction is over driven at frequencies below point A (and above point D). Around A and D a significant non-linear response is observed indicating the magnitude of the oscillating current bias around these frequencies, either side of the resonance, is close to I_c. In this manner the over driven junction would dissipate heat into the environment resulting in a reduction of the quality factor as the drive frequency is swept through resonance.

This argument makes several assumptions and although seems applicable in the case of Fig. 6.23 is does not explain the behaviour observed at lower powers around -106 dBm where the second mode initially splits/shifts to higher frequencies. It also doesn't offer any indication to the nature of the sigma mode and its origin.

6.3.5 Sigma mode

Referring to Fig. 6.28, the sigma mode appears in the spectrum at an approximate power level of −92 dBm around 3.525 GHz, approximately 0.02 GHz lower in frequency than second mode. The mode quickly beings to broaden after its appearance as the power level is increased. At a power level of −86 dBm the mode seems to split and collapse in on itself, with the response in that region of the spectrum flattening with increasing power. This corresponds to the power level interval where a reduction of the quality factor of the second mode was observed in the previous section.

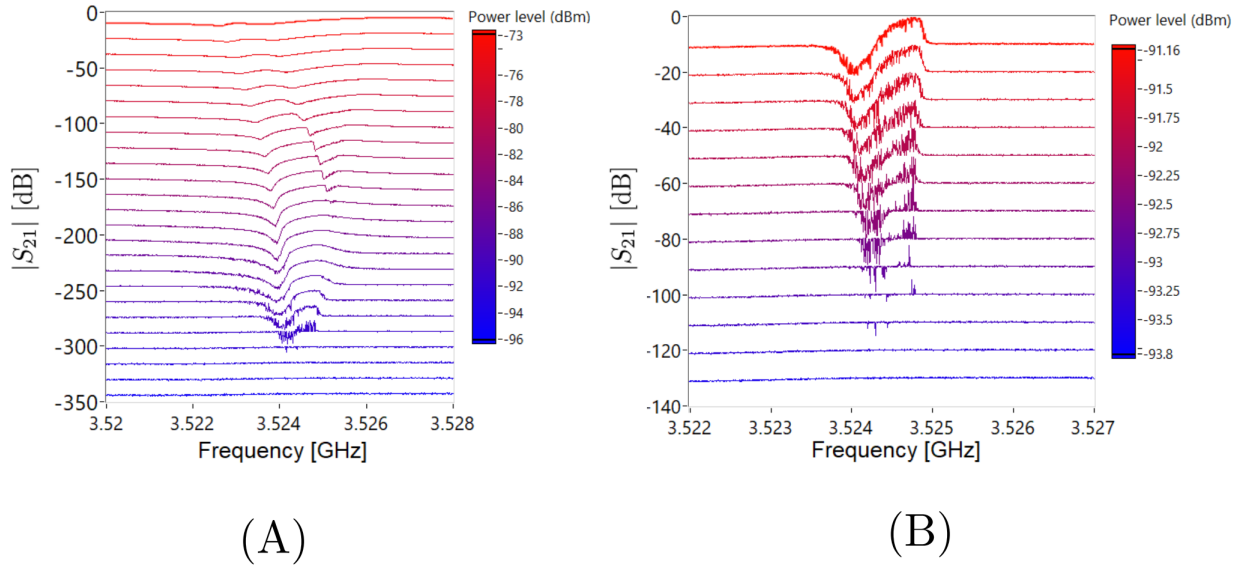

Figure 6.28: $|S_{21}|$ as a function of frequency for a power level interval of (A) −96 dBm to −73 dBm in 1 dBm steps, offset +13 dB. (B) −93.8 dBm to −91.16 dBm in 0.2 dBm steps, offset +13 dB.

This phenomenon is quite unusual. A simplistic interpretation of the behaviour is that when driving above a certain power level, the resonator can support another mode of oscillation with a corresponding frequency of 3.525 GHz, which is out of phase with the second mode. Although their behaviour seems correlated with the sigma mode is observable when driving at a sufficient power in the region of 3.525 GHz regardless of excitation of the second mode. Fig. 6.29 and 6.30 show S_{21} measurements of the region around the sigma mode over a power range of −94 dBm to −91 dBm in 0.02 dBm intervals. The $|S_{21}|$ and phase data is plotted against power level and frequency.

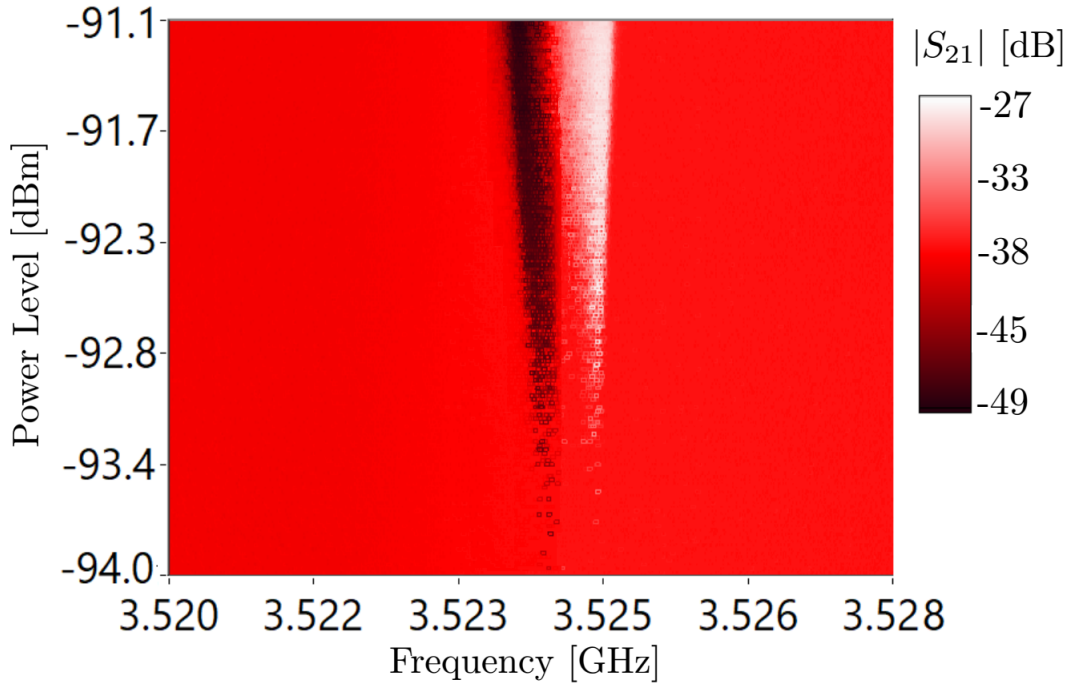

Figure 6.29: $|S_{21}|$ as a function of power level and frequency around the location of the sigma mode.

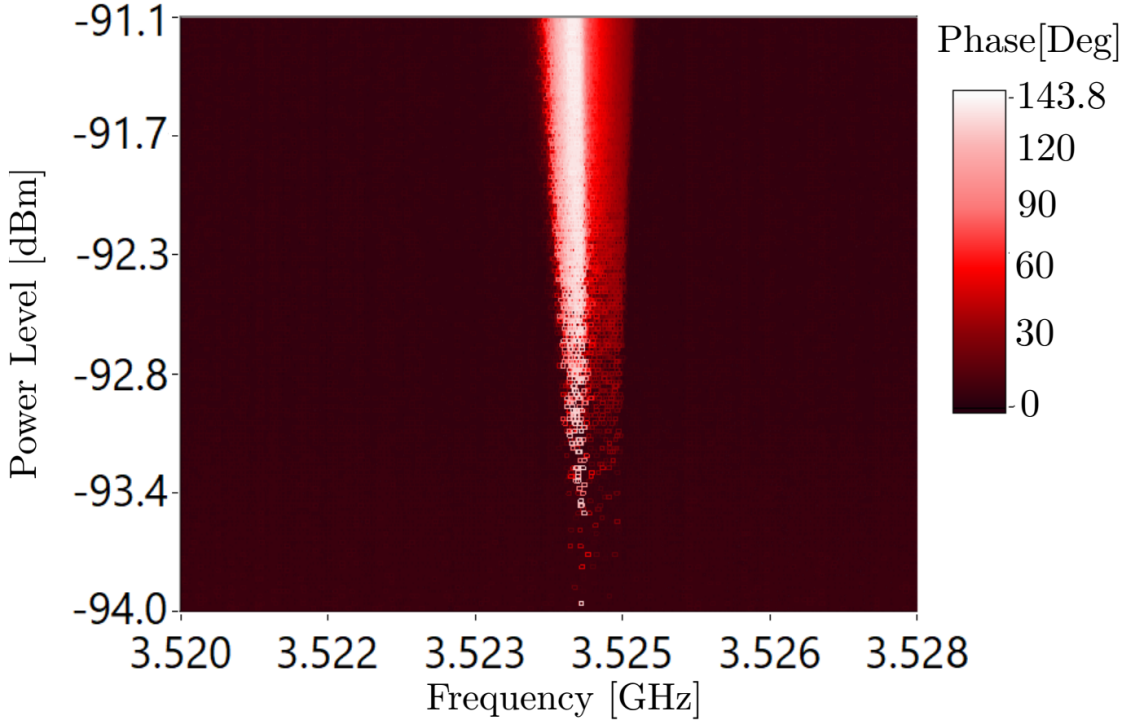

Figure 6.30: S_{21} phase as a function of power level and frequency around the location of the sigma mode. The linear progression of the finite measurement lines has been removed via fitting and subtracting a sawtooth function.

An $|S_{21}|$ measurement of the sigma mode at a power level of -86 dBm is shown in

Fig. 6.31, fitted with a Fano function. The line-shape although asymmetric in appearance only approximately fits to the Fano function for this power level. Although attempts were made to improve the goodness of fit by accounting for skew and other generalisations to the spectral response, it appears slight frequency pulling is distorting the characteristic line-shape of the resonance.

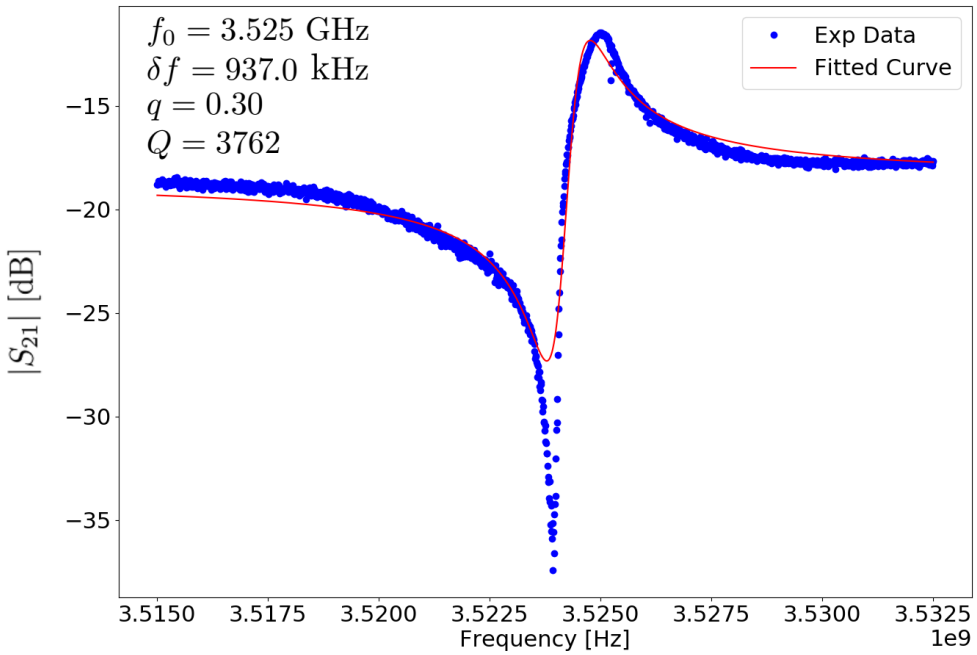

Figure 6.31: $|S_{21}|$ measurement as a function of frequency for a power level of −86 dBm fit with a Fano function. Although the sigma modes line-shape is clearly asymmetric, the Fano function only approximately describes it. This seems to be due to the peak amplitude bending towards higher frequencies.

As the power level increases, shown in Fig. 6.32, the mode appears to broaden. It is hard to tell if there is also frequency pulling towards higher frequencies, regardless at approximately −86 dBm fluctuations in the amplitude are observed around the peak of the sigma mode. At higher power the mode appears to split, with a corresponding perturbation of the phase response, moving towards lower frequencies with increasing power.

This behaviour is difficult to interpret but it is similar to the power dependence and mode splitting events seen on the second mode. At a critical power a second resonance appears at the peak of the sigma mode. The mode also has Fano line-shape with a reversed asymmetry (q). With increasing power the mode moves towards lower frequencies. Using the same argument applied when discussing the second mode this could be interpreted as a modulation of L_J, increasing with power level. As the power level is increased further the component continue to move towards lower frequencies with the sigma mode becoming increasingly damped. Fig. 6.33 shows a S_{21} measurement of the sigma mode at a power of −67 dBm.

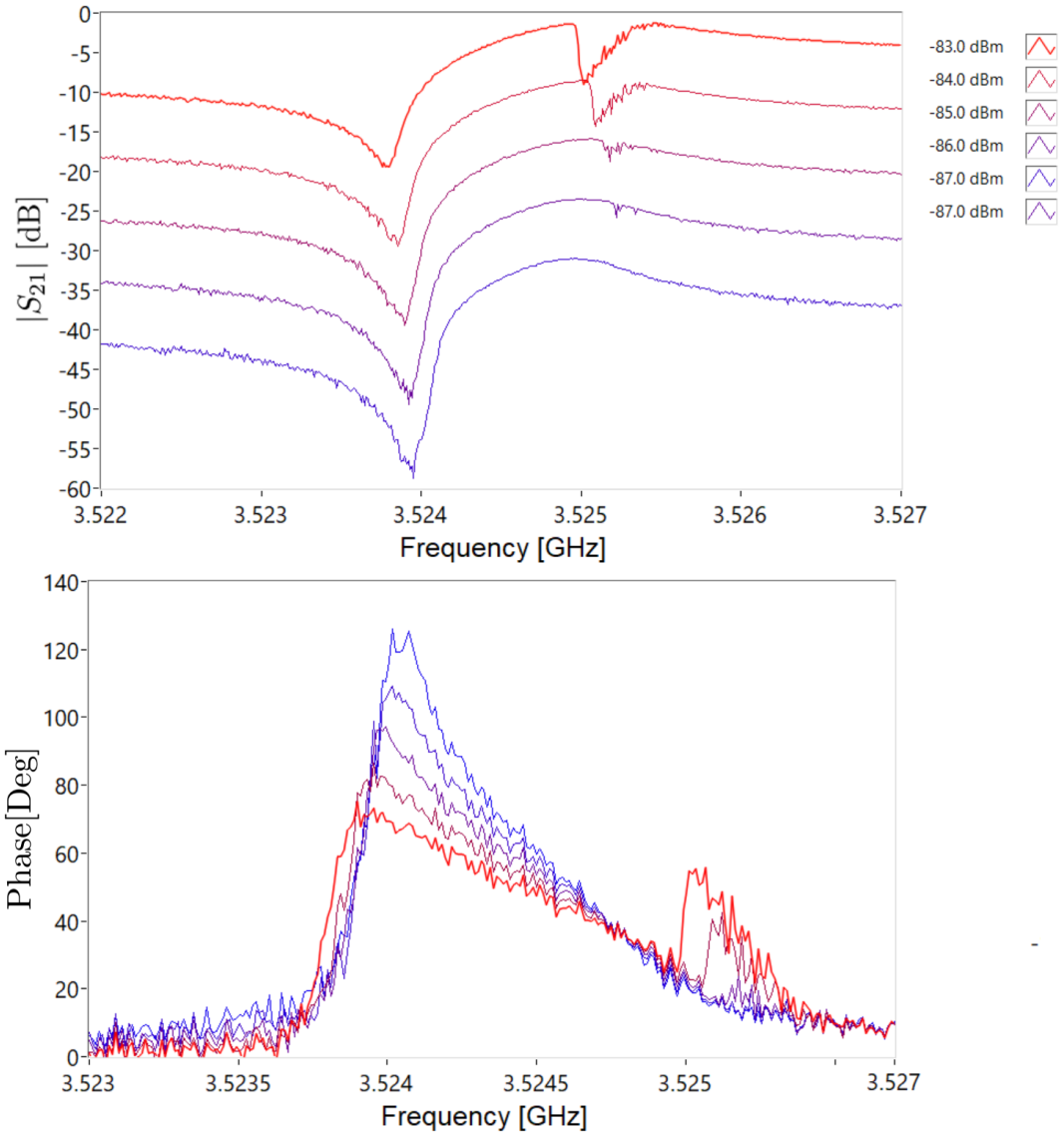

Figure 6.32: S_{21} measurements for a power interval of -87 dBm to -83 dBm in 1 dBm intervals. Top: $|S_{21}|$. Each power level is offset $+8$ dB from the previous for clarity. Bottom: Phase. Measurements at individual power levels are overlaid for comparison. The linear progression has been remove by fitting and subtracting a sawtooth function.

Previously we assumed that the damping of the second mode was due to over driving the Josephson junction resulting in dissipation into the environment. The fact that the sigma mode shows a similar response means that the same arguments can be applied such that at some critical power the junction becomes over-driven. It is still not fully understood how the resonator is able to support the sigma mode.

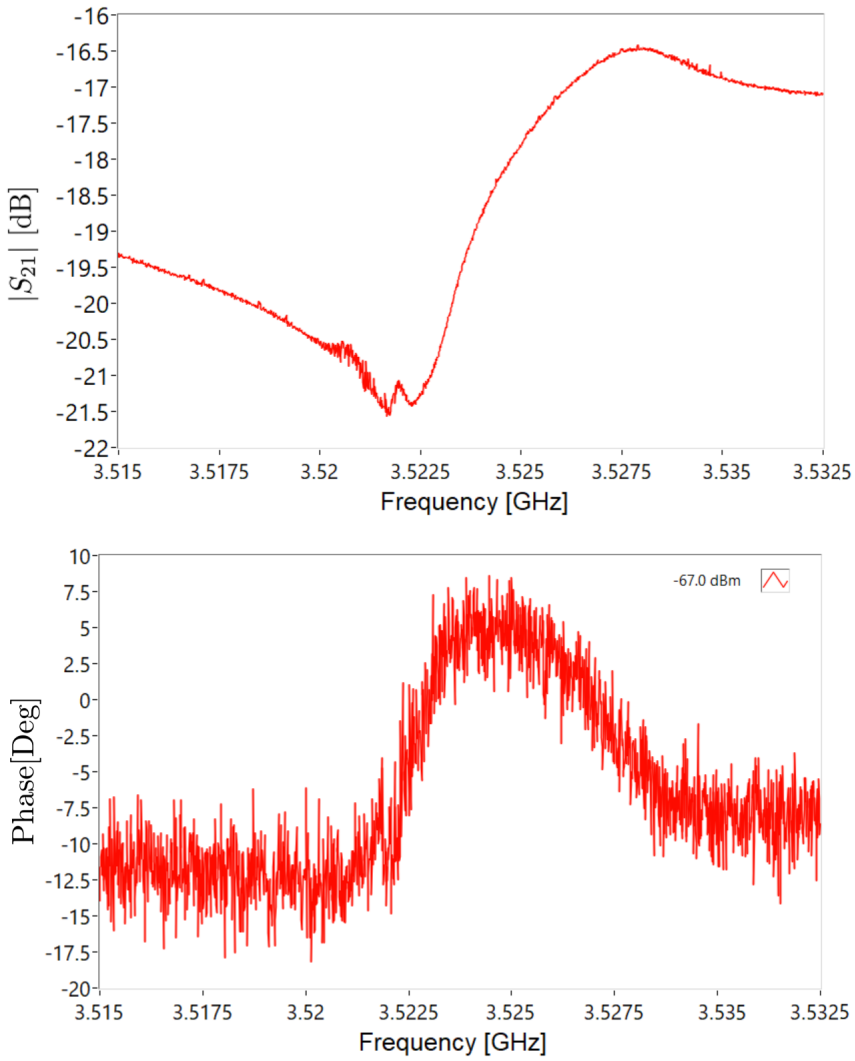

Figure 6.33: S_{21} measurements for a power level of -67 dBm. At this power level the quality factor of the sigma mode is significantly reduced however there is still a small response in amplitude and phase.

6.3.6 Temperature dependence

Given the respective temperature dependence of the superconducting Al and Nb, it is instructive to change the experimental temperature. Fig. 6.34 shows such a measurement, where the second mode and sigma mode are measured as a function of temperature. In this case the power level is -86 dBm and is kept constant as the temperature is increased. This was also repeated for several other power levels.

Referring to Fig. 6.34, the measurement is uneventful below 0.3 K however around 0.35 K noticeable changes can be seen in the line-shape of the sigma mode, with its maximum amplitude reducing. For all drive powers the sigma mode began to decay and subsequently vanish from the S_{21} measurements at a temperature of approximately 0.35

K. Over this temperature range we would not expect any significant changes to the Nb component of the resonator (T_c = 9.3 K). Changes in the Al component (T_c = 1.2 K) would be more relevant, with onset of variations in the superconducting gap and the quasi-particle density around this temperature, as discussed in Chapter 2.1.2.2. The bulk Al should still be superconducting and the changes should be small at a temperature of approximately 0.35 K. However given a low critical current Al junction, small fluctuations may still be significant.

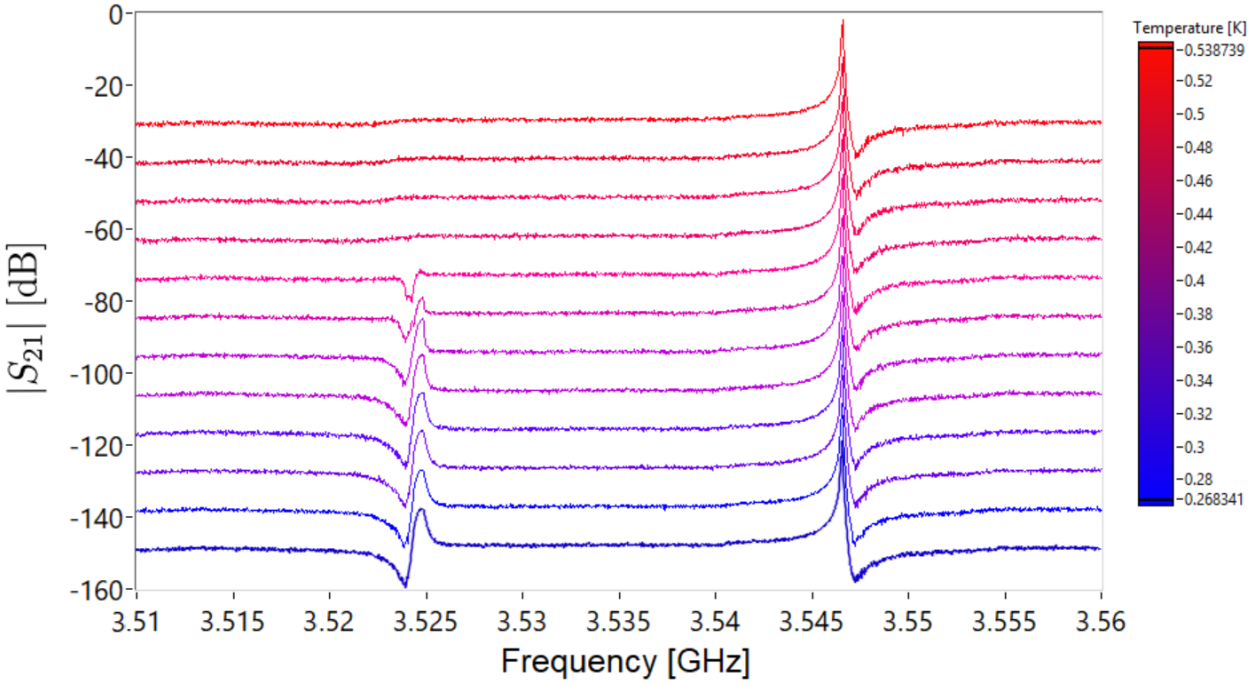

Figure 6.34: $|S_{21}|$ as a function of frequency for a constant power level of −86 dBm at several temperatures ranging from 0.25 K to 0.54 K. Each temperature measurement is offset +10 dB from the previous for clarity. Around 0.45 K the sigma mode vanishes and the oscillation is no longer supported by the resonator.

The quality factor of the second mode is also reduced over this temperature range. For a constant power level of −86 dBm (Fig. 6.34) the quality factor reduces from 45000 at 0.025 K to approximately 30000 at the point the sigma mode disappears from the spectra (0.45 K). The quality factor substantially drops around 1-1.2 K (Fig. 6.35) to below 15000, indicative of the superconducting gap closing and the Al component becoming dissipative. As the temperature is increased further the quality factor decreases due to the increasing quasiparticle density, in this case owing to the Nb component.

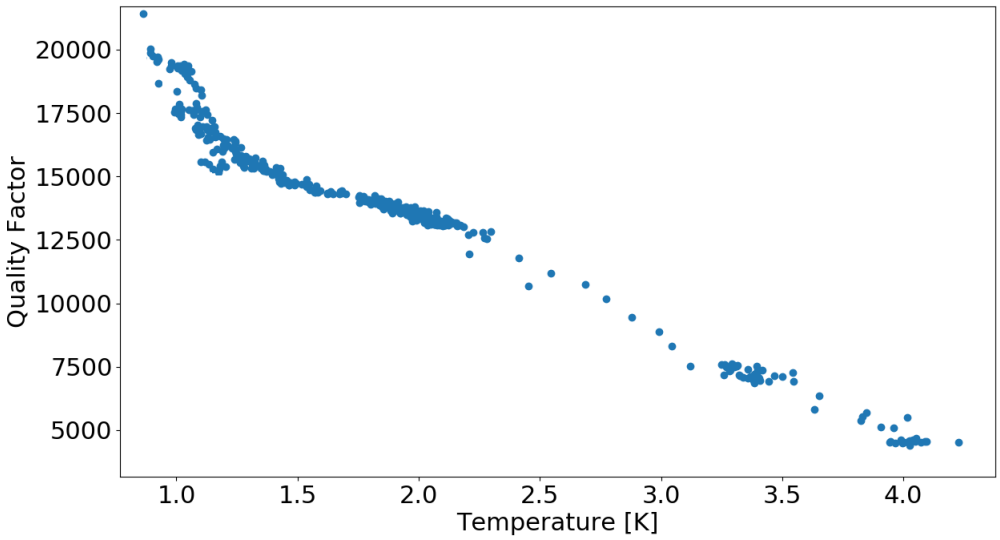

Figure 6.35: SA2 - Quality factor of second mode measured at constant power as a function of temperature.

6.3.7 Coupled modes

There is a strong correlation regarding the behaviour of the sigma mode and the second mode, however their relation is still unclear. So far we have been looking at the behaviour of the second mode and the sigma mode using S_{21} measurements. In this section we will use continuous wave (CW) sources and a spectrum analyser to probe these components independently. The experimental set-up is similar to that discussed in Chapter 4, and is shown in Fig. 6.36.

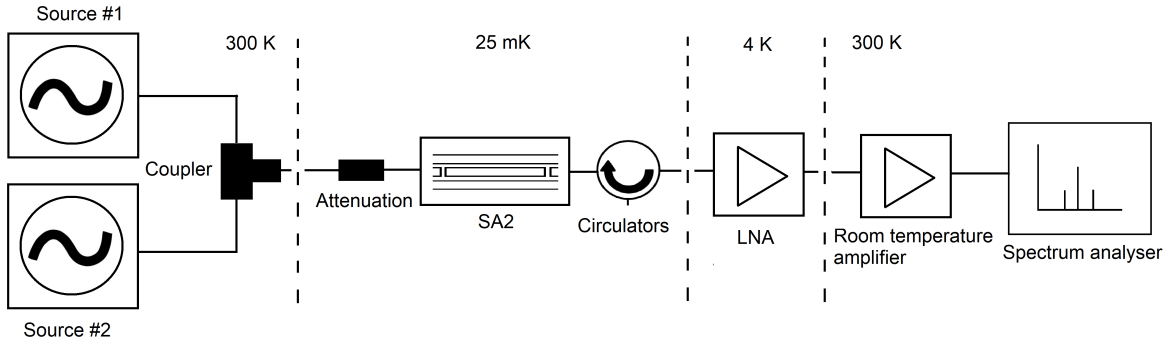

Figure 6.36: SA2 - coupled mode measurement set-up for probing the response of the second mode when driving the sigma mode.

For this measurement one of the CW sources will serve as a probe tone whose amplitude will be measured. The second CW source will act a drive tone which will vary in frequency and power over the course of the measurement. The probe tone is positioned close to the resonant frequency of the second mode at $f_p = 3.5466$ GHz. The power of the probe

tone, P_{probe}, will be kept constant throughout the measurement. The spectrum analyser, with a narrow acquisition window, captures the probe tone so that its amplitude can be determined using a non-linear least squares fit. The drive tone, provided by the second CW source, is positioned around the sigma mode starting at a frequency of the 3.515 GHz. The power is then increased from −100 dB to −67 dBm, measuring the amplitude of probe tone at each individual power level. The frequency of the drive tone is then incremented and the process repeats. Fig. 6.37, show the relative change of a probe tone at frequency $f_p = 3.5466$ GHz and power $P_{probe} = -107$ dBm as a function of the drive tone power and frequency. Fig. 6.38 shows the response when the probe tone power is reduced to $P_{probe} = -117$ dBm.

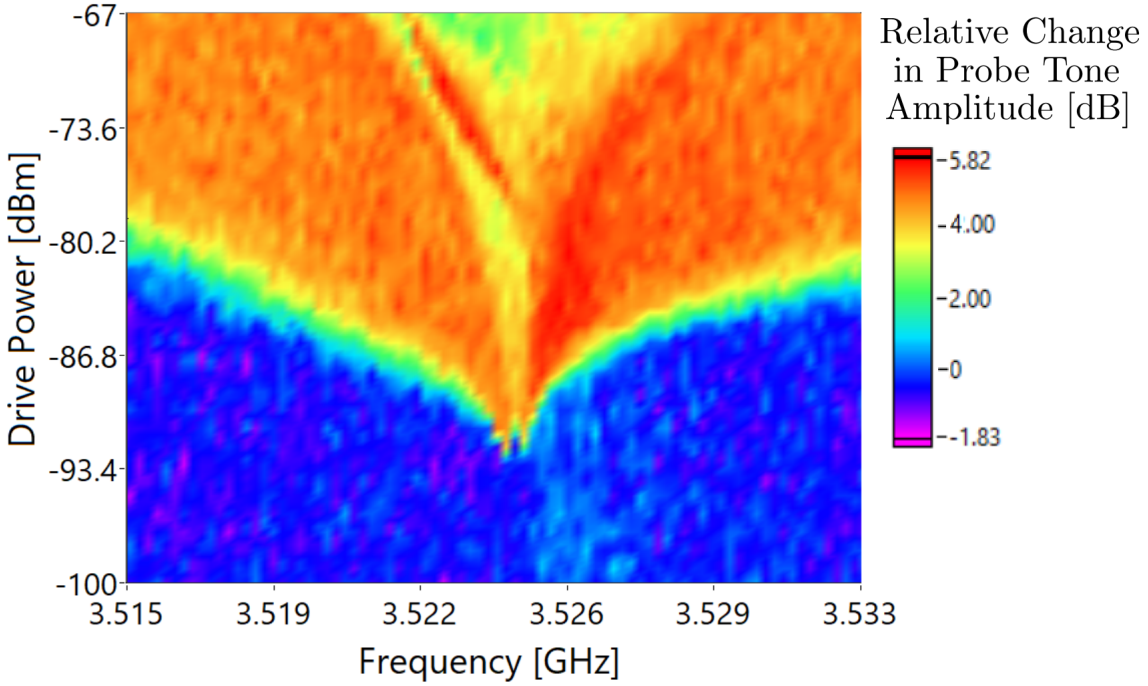

Figure 6.37: Relative change in the amplitude of the probe tone $f_p = 3.5466$ GHz $P_{probe} = -107$ dBm as a function of the power and frequency of the drive tone sweeping the area around the sigma mode.

The amplitude of the probe tone for both $P_{probe} = -107$ dBm and $P_{probe} = -117$ dBm shows a clear response to the driving tone centred around the location of the sigma mode at 3.525 GHz. The first significant change in the amplitude of the probe tone is observed when driving around 3.525 GHz at approximately −92 dBm, corresponding to the sigma modes appearance in the spectrum noted in S_{21} measurements (Fig. 6.16). At slightly higher powers around −86.5 dBm a change of order 6 dB can be noted in the probe signal around 3.526 GHz, corresponding to a maximum in the sigma modes Fano line-shape. At higher drive powers, above −86 dBm, a high amplitude state can be seen moving from

around 3.526 GHz to 3.522 GHz, this frequency range correspond to the splitting of the sigma mode with an additional mode moving to lower frequencies, shown in Fig. 6.32.

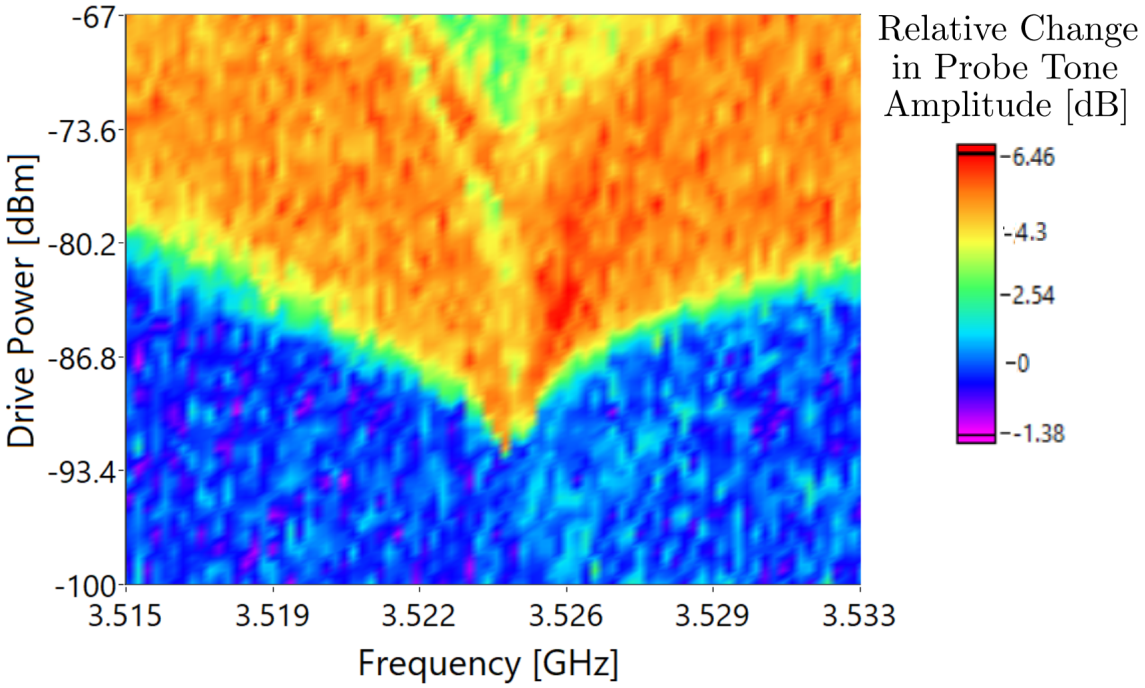

Figure 6.38: Relative change in the amplitude of the probe tone $f_p = 3.5466$ GHz $P_{probe} = -117$ dBm as a function of the power and frequency of the drive tone sweeping the area around the sigma mode.

The implications of these measurements are quite clear; driving the sigma mode results in an excitation of the second mode of the CPW resonator, suggesting the oscillations are coupled. Coupled oscillators were introduced to describe the Fano resonance in Chapter 2.1.4. In that case two mechanic oscillators where coupled with a spring such the amplitude response of each oscillator was dependent on the other as the driving force was swept through the oscillators resonant frequencies. This situation is analogous, we are measuring the oscillating state of the second mode and seeing an increase in the amplitude of the oscillation as we move the drive through the resonant frequency of the sigma mode. An interesting consequence of the coupling of two oscillators is the detuning of their respective resonant frequencies as a function of the coupling parameter ν_{12}. At approximately -92 dB when the sigma mode appears in the spectrum a 7 kHz shift in the resonant frequency of the second mode is observed (Fig. 6.24). In this light this could represent a shift due to the establishment of the sigma mode and subsequent coupling between the oscillators. Prior to the sigma modes onset around a power level of -105 dBm, there was a much larger increase of approximately 100 kHz in the resonant frequency of the second mode, which is possibly similar in relation. However the question remains regarding the nature

of the coupling of the oscillations and the relation to the Al junction at the centre of the resonator.

6.3.8 Third mode

Although we have primarily focussed on the response of the resonator around the second mode the majority of measurements of SA2 were dedicated to probing the third mode. Similarly to fundamental of SA1, the third mode of SA2 was absent from the spectrum. It was suspected of being dampened even at low power levels powers due to the junction being over driven by the current anti-node of the third mode centred around the junctions location at the $l/2$ point. Although the power dependence of the second mode is very interesting and exhibits numerous phenomena, the location of the current node around the junctions location makes the situation very ambiguous. The region of the spectrum around 5.3 GHz was intensely searched over a wide frequency and power space to attempt to observe the third mode without significantly perturbing the junction. Such as with SA1 numerous methodologies where attempted including attempting to drive the junction via the fundamental (1.8 GHz) and higher odd modes (9 GHz) while looking for a response around the expected resonant frequency of the third mode.

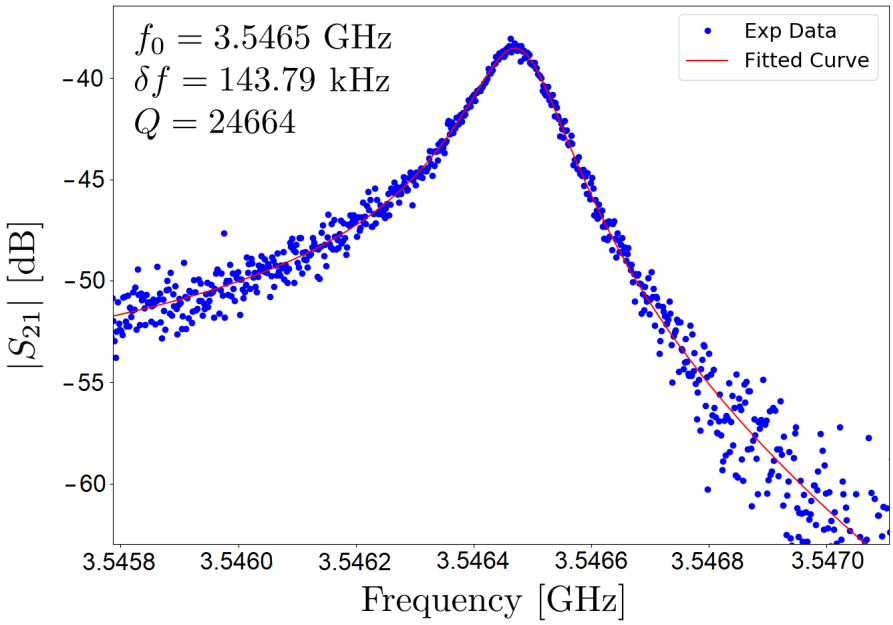

Figure 6.39: $|S_{21}|$ as a function of frequency around the second mode for power level of -120 dBm. Fitted with a Lorentzian function.

Dielectric losses at low input powers may also factor into the difficulty of observing the third mode. The second mode showed no significant power dependence (mode splitting or shift in the resonant frequency) below -107 dB. However, there was a drop in the quality factor at lower powers, shown in Fig. 6.39. For a power level of -120 dBm the quality

factor of the mode is reduced from 45000 at −107 dBm to 25000. This is indicative of dielectric losses, discussed in Chapter 2.1.3.

Given a suspected relation between the junction and the sigma mode several experiments attempted to perturb the sigma mode by driving at the fundamental mode and third mode of the resonator, attempting to overdrive the junction while measuring the response of the sigma mode. The measurements showed no change in the state of the sigma mode when driving around the expected location of the fundamental mode or odd harmonics. However given that the location of the fundamental or the third mode was never observed it is hard to know if these measurements resulted in the junction being sufficiently driven.

6.3.9 Summary

Unfortunately the measurement of SA2 were interrupted by a failure of the dilution refrigerator. Although the behaviour of SA2 is complex such that it cannot be easily modelled, the power dependent behaviour of the second mode observed at a power level around −106 dBm (Fig. 6.17), the subsequent appearance of the sigma mode around −92 dBm (Fig. 6.28) and the bifurcation like behaviour observed at the extremities of the second mode at a power level −78 dBm (Fig. 6.23) all point to a highly reactive non-linear element with a significant power dependence.

Although these effects could be attributed to the presence of the low I_c Josephson junction, the exact nature of how the Josephson junction would lead to the appearance of the sigma mode in the spectrum is unclear. It is possible that this is a consequence of the junction integration with the CPW resonator. When discussing measurement of SA1 at 4.18 K a similar unknown component was encountered (Fig. 6.3 (A)), which was referred to as the LHS mode centred close to the second mode of the resonator. Several arguments were made regarding the nature of this secondary component and its implications, the biggest concern being an impedance mismatch induced due to the modification of the CPW geometry at the point of the integration of the Al junction. Several changes were made to the SA1 design when fabricating SA2 to mitigate this concern, and no LHS component was observed above 0.45 K. However, although the relation of the LHS mode of SA1 and the sigma mode of SA2 maybe unclear (or non-existent), a similar argument can be applied, that an change in the impedance, in this case dependent on the state of the Josephson junction, allows the sigma mode to be supported by the cavity, with modes coupled via their interaction with the junction.

Chapter 7

Measurements of Nb nanobridge RF SQUID CPW resonators

This chapter details initial measurements of Nb CPW resonators with nanobridge constrictions etched in the central conductor. All devices detailed in this chapter were fabricated as summarised in Chapter 5 and an example recipe is given in appendix A.3. As previously mentioned, fabrication of nanobridges was not an initial aim of this project, however, their fabrication developed naturally from the process of etching EBL defined segments in Nb resonators intended for Al integration. The process of fabricating these constrictions was non-trivial, however, the advantages of such components motivated development. Nanobridges are inherently interesting structures and have typically avoided comprehensive study due to the extremes of their geometries and the prevalence of tunnel junction technology. As noted in Chapter 2.2.2, they are innately very different to tunnel junctions and lack any form of capacitance, with a current-phase relation highly dependent on their geometry. These reasons alone motive study.

Although the Al/AlO_x/Al tunnel junctions offer very low critical currents, they required low temperatures to operate necessitating measurement in a dilution refrigerator. Although low temperature measurements are often required, it is also restrictive, generally with a long turn around times between measurement of individual samples. The time investment and possibility of complications also constrains sample design. Nb nanobridges can exhibit the Josephson effect at liquid He temperatures owing to the higher T_c of Nb. This was a great motivation to produce these structures. Allowing for a quick sample design and fabrication cycle. Experimentation with these non-linearities and CPW resonators could also allow for inferences regarding the behaviour exhibited by SA1 and SA2, and provide insight into future sample design.

7.1 Nanobridge RF SQUIDs

When discussing sample design of the SA1 in Chapter 6.1 a primary consideration was which order of non-linearity to promote, specifically whether or not to adopt an RF SQUID

configuration. In the case of the Al integrated samples, a single junction was preferred due to the low critical current estimates of test junction iterations. An RF SQUID design was considered, however, due to the expected low critical current of the Al junctions the geometric inductance required such that the SQUID screening parameter $\beta_L \approx 1$ was too large to practically implement due to constraints imposed by the Nb CPW geometry of the R1, R3 and R5 design resonators.

The critical current of Nb nanobridges is reported to be in the range 100 μA to several mA [68], depending strongly on the geometry of the constriction. In the case of an RF SQUID employing a Nb nanobridge with $I_c = 1$ mA, a geometric inductance of 2×10^{-13} H would give $\beta_L \approx 0.7$. From a fabrication standpoint this is straight forward to achieve within the constraints of the CPW geometry. Furthermore, by employing an RF SQUID the magnitude of the non-linearity is dictated by β_L, the product of the geometric inductance and the critical current of the junction, discussed in Chapter 2.2.2. As such, although a Nb nanobridge may have a high I_c in comparison with a small Al junction, using the RF SQUID geometry avoids these limitations allowing for a significant response when β_L is close to unity. Furthermore, it was suspected that the single junction design, employed in SA1 and SA2, resulted in a change in the impedance of the Nb resonator due to the modification of the central conductors width and ground plane separation at the point of the junction integration. Using an RF SQUID geometry the central conductor and ground plane separation can be approximately maintained along the length of the resonator, mitigating these concerns.

In this chapter we will focus on two Nb CPW resonator samples employing etched Nb nanobridge RF SQUIDs, designated SN1 and SN2, respectively.

7.2 SN1

7.2.1 Sample design

SN1, shown in Fig. 7.1, was a prototype sample to assess the behaviour of the nanobridge structures fabricated using the methods detailed in Chapter 5.4. SN1 features an array of nine nanobridge RF SQUIDs each with an identical intended geometric inductance (SQUID loop) of approximately 3×10^{-12} H, using a 5 μm $\times$ 12 μm rectangular geometry. The sample is fabricated as detailed in Chapter 5.4, where the nanobridge constrictions and SQUID loops are defined in a R3 Nb CPW resonator using EBL and etching using a SF_6/Ar RIE process. The bridge constriction width was measured via SEM imaging. All of the nanobridges in the array had constriction widths of approximately 60 nm.

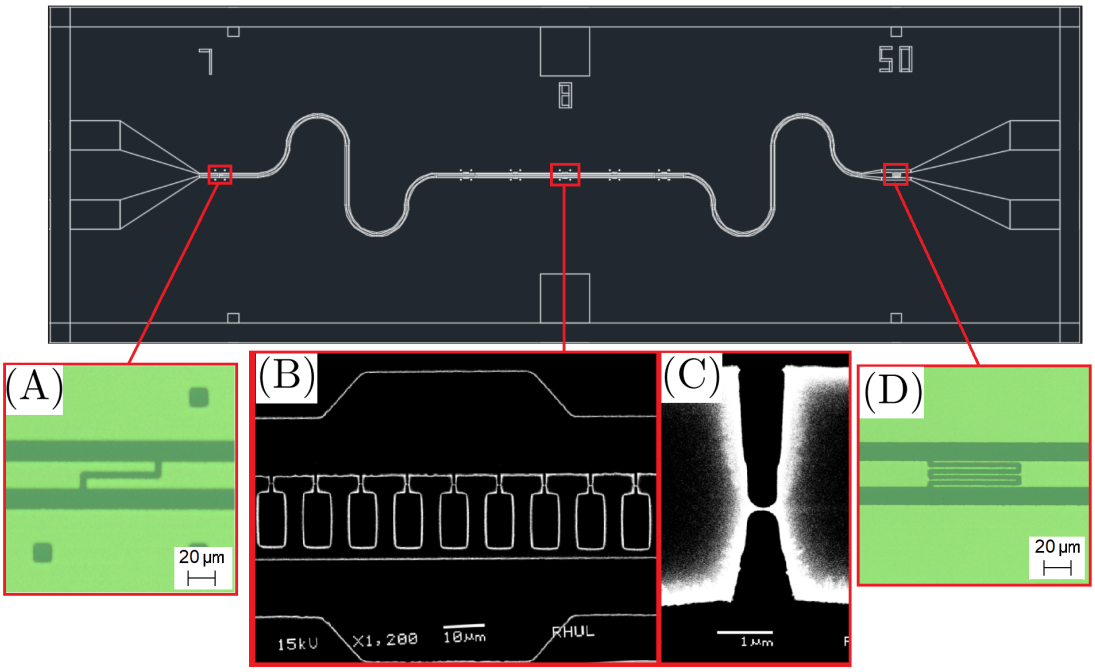

Figure 7.1: SN1. The sample uses the same R3 resonator design as SA1. Optical images of the coupling capacitors can be seen in (A) and (D). (B) A SEM image of the RF SQUID array located at the $l/2$ point of the resonator. (C) A SEM image of one of the nanobridge constrictions in the array, measuring approximately 60 nm.

The sample design of SN1 assumes that the non-linearity is weak, given the unknown critical currents of the fabricated constrictions, as such an array of nanobridge RF SQUIDs is used to maximise the non-linear interaction. The array is placed at the central position in the resonator ($l/2$), where l is the length of the resonator, located at the current antinode of the fundamental mode (6 GHz), allowing the RF SQUID array to be driven at higher powers.

SN1 was measured at 4.18 K using an RF probe immersed in liquid He. Although this measurement probe is versatile it does not provide a source of flux bias. As such the measurements of SN1 and SN2 detailed in this chapter will be in the absence of an externally controlled flux, such that the flux threading the SQUID is unknown. We could assume that the external flux threading the SQUID loop is zero. However, although the sample is enclosed in an electromagnetic shield, flux from ambient field threading the SQUID loop can be trapped as the Nb transitions from the normal to superconducting state. The trapped flux can result in a DC phase offset, ϕ_{dc}, over the nanobridge in the absence of an applied field. Although the DC phase offset cannot be directly controlled, as discussed in Chapter 2.3.6 it dictates the magnitude of the non-linear terms. As such the non-linear phenomena it will exhibit, depending on the driving power, will directly relate to the DC phase offset over the nanobridge. If we assume $\Phi_e/\Phi_o \approx 0$, then we would expect to observe FWM and bifurcation phenomena associated with the cubic non-linear

term. However, if there is a non-zero DC phase offset over the junction we would also expect to manifest TWM under the right circumstances.

7.2.2 Fundamental mode

A $|S_{21}|$ measurement of the fundamental mode of SN1 for a drive power of -50 dBm at 4.18 K is shown in Fig. 7.2. The quality factor of mode is approximately 7500, close to the expected quality factor of an unmodified R3 resonator at 4.18 K. This indicates that the process of etching the constrictions and SQUID loops in the central conductor has not resulted in the addition of significant loss due to generation of defects from the further fabrication processes.

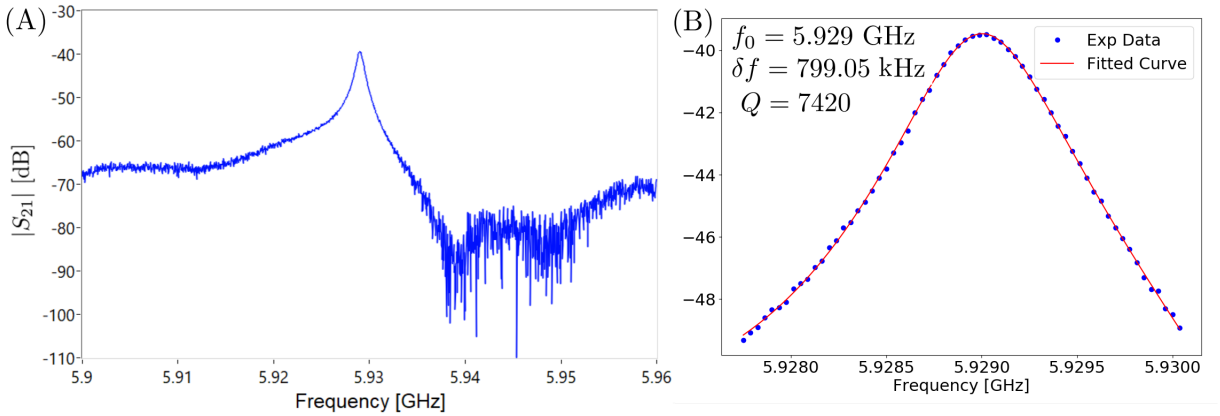

Figure 7.2: (A) $|S_{21}|$ as a function of frequency measurement at a power level of -50 dBm of the fundamental mode of SN1 at 4.18 K. (B) $|S_{21}|$ measurement fitted with a Lorentzian function.

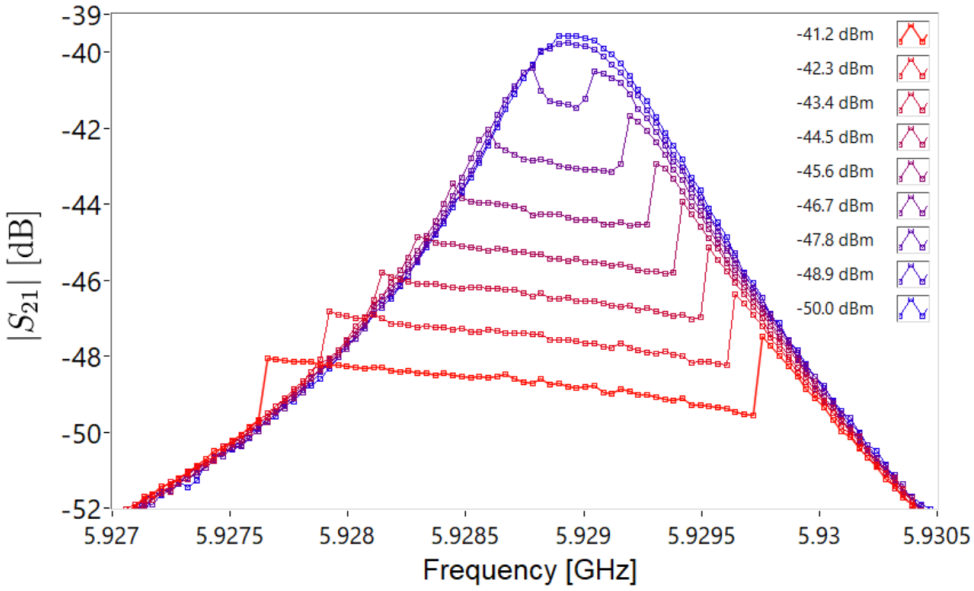

Figure 7.3: $|S_{21}|$ as a function of frequency for several different drive powers around the fundamental mode of SN1. The measurements have been overlaid for comparison.

As the drive power is increased a significant non-linear response is observed at around -48 dBm, shown in Fig. 7.3. The mode seems to split into two frequency components pulling to higher (RHS) and lower frequencies (LHS) respectively with increasing power. The LHS response is indicative of an amplitude bifurcation due to a cubic non-linear restoring force acting on the mode of oscillation. This can be attributed to the modulation of the non-linear inductance presented by the array of nanobridge RF SQUIDs, analogous to the phenomena observed in Josephson junction based bifurcation detectors, discussed in Chapter 2.3.7. The frequency pulling towards lower frequencies suggests the Josephson inductance of the nanobridge RF SQUIDs is increasing for higher driving powers. The origin of the RHS component of the resonance however is more ambiguous, moving towards higher frequencies with increasing powers.

There are several considerations to make regarding the behaviour of the RHS component moving to higher frequencies with increasing powers. Referring to Fig. 7.3, it is constructive to consider the observed $|S_{21}|$ as a function of frequency at a power level of -42.2 dBm shown in red, in comparison with the response at a power level of -50 dBm shown in blue. At lower frequencies from 5.927 GHz to 5.275 GHz, the amplitude response as a function of frequency at a power level of -41.2 dBm follows the amplitude response of the mode when measured at lower power levels (-50 dBm blue). Around 5.9277 GHz, the amplitude jumps into a higher amplitude state, which we will assume is due the driving of the nanobridge RF SQUID array at a critical power, bending (and bifurcating) the resonance towards lower frequencies. As we continue towards higher frequencies passing through the resonant frequency of the mode (5.929 GHz at a power level of -50 dBm) we remain in this bifurcated state. Around 5.9297 GHz the amplitude switches back to approximately the same amplitude state as the case of low powers (-50 dBm). As the frequency is increased further the amplitude response increases, close to the response at low powers, coming into good agreement around 5.93 GHz.

We could explain this as follows, the mode bifurcates at lower frequencies (LHS) due to the nanobridge RF SQUID array being sufficiently driven by the RF bias. As the frequency is further increased past the resonance the bias over the nanobridge RF SQUID array begins to reduce. At a certain frequency (5.9297 GHz) the nanobridge RF SQUID array is no longer sufficiently driven and the bifurcated state of oscillation can no longer be supported ($F < F_c$) and the amplitude response sharply changes. Although at this frequency the driving force is not sufficient to manifest a bifurcation, there is still sufficient bias such that the nanobridge RF SQUID array still has a non-negligible inductive contribution and the amplitude response does not initially rejoin the resonant line-shape observed at low powers (-50 dBm). As the frequency is further increased the bias over the nanobridge array reduces further such that its inductive contribution becomes negligible and the amplitude response at higher powers comes into good agreement with the response at lower powers as the frequency is further detuned from resonance (5.93 GHz).

This would explain why the RHS component moves to higher frequencies for increasing powers. Fig. 7.4 shows S_{21} for a for multiple power levels from -51 dBm to -41 dBm.

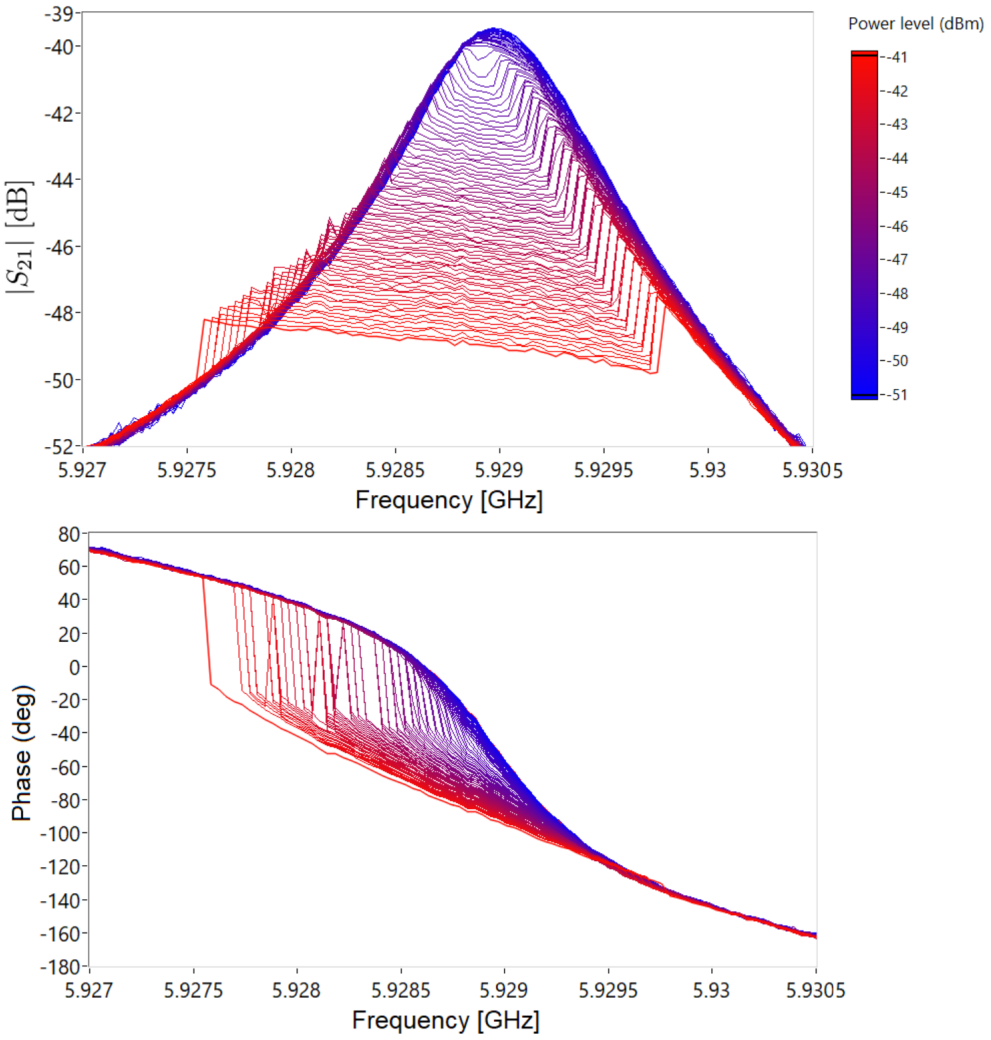

Figure 7.4: $|S_{21}|$ as a function of frequency measurements centred around the fundamental mode of SN1 for several different power levels, ranging from -51 dBm to -41 dBm in 0.1 dBm intervals. The measurements have been overlaid for comparison.

An alternative explanation for the observed two component nature of the power dependence observed in Fig. 7.3 could be given by considering the suspected current-phase relation of the nanobridges formed in the central conductor of SN1. Recalling Chapter 2.2.2, the current-phase relation of a nanobridge junction can differ in functionality depending on its geometry, compared with the well-defined sinusoidal current-phase relation in tunnel junctions. It has been reported that the current-phase relation of a nanobridge can vary from a distorted sinusoid to an almost linear function in extreme situations ($I \propto \delta$) [42]. It could be the current-phase relation of the nanobridges in SN1 is non-linear but also hysteretic, such that a discontinuous switching of the phase over the nanobridge is responsible for the RHS component observed in Fig. 7.3. Measurements of

the current-phase relation of these nanobridge geometries would be of great interest for further development of devices based on these constrictions.

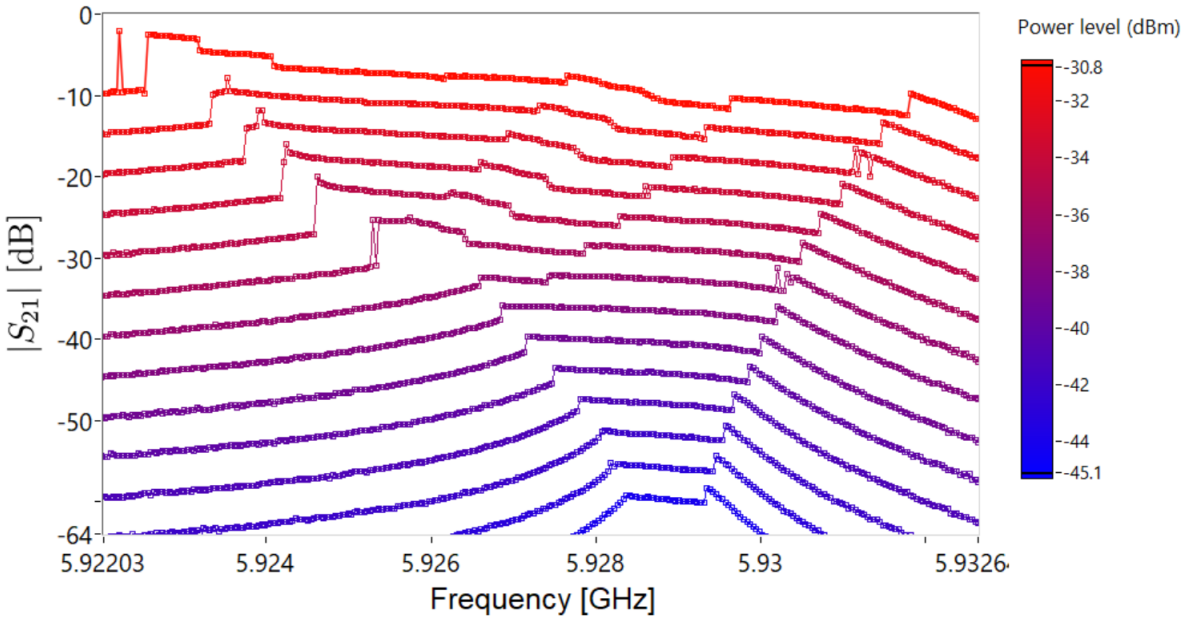

Figure 7.5: $|S_{21}|$ as a function of frequency measurements centred around the fundamental mode of SN1 for several different power levels, ranging from -45.1 dBm to -30.8 dBm in approximately 1 dBm intervals. Each power level is offset $+5$ dB from the previous for clarity.

As the power level is increased further, shown in Fig. 7.5 the LHS and RHS components continue to diverge towards lower and higher frequencies respectively. At a power level of approximately -38 dBm additional bifurcations appear to occur with a similar two component nature observed in Fig. 7.3. Around this power level the difference in high and low amplitude state of the initial LHS bifurcation also increases.

Fig. 7.6 shows $|S_{21}|$ measurements for a power level range of -54 dBm to -24 dBm in 0.1 dBm steps plotted as a function of power level and frequency. The additional bifurcations noted after the initial bifurcations around -48 dBm could relate to the response of the individual nanobridge RF SQUIDs comprising the array at the $l/2$ point. Although SEM imaging observed that the nanobridge constrictions where approximately identical, small variations could result in the constrictions having differing critical currents. If each of the RF SQUID are unique such that their individual responses to the perturbation of the driving tone is different then they could bifurcate at differing power level as a function of frequency. Variation in the inductance L_G and the trapped flux of each individual SQUID loop could similarly result in each SQUID responding differently to the drive tone. Given the previous argument regarding the RHS bifurcation observed in Fig 7.3 we would also expect that these additional bifurcations onset at differing critical powers dependent on drive frequency to also have RHS components as the driving frequency

increases and the bias over the individual RF SQUID is reduced. Although this is supported by Fig. 7.6 the power space over which these additional bifurcation occur is quite large with secondary events noted as high as −25 dBm. As such it is worth considering other possibilities. Dissipation maybe expected from over-driving the RF SQUIDs such that the critical current of the nanobridge's is exceeded for higher drive powers. As such these secondary events may relate to switching of the amplitude state due to entering a dissipative regime at higher powers as a function of the driving frequency.

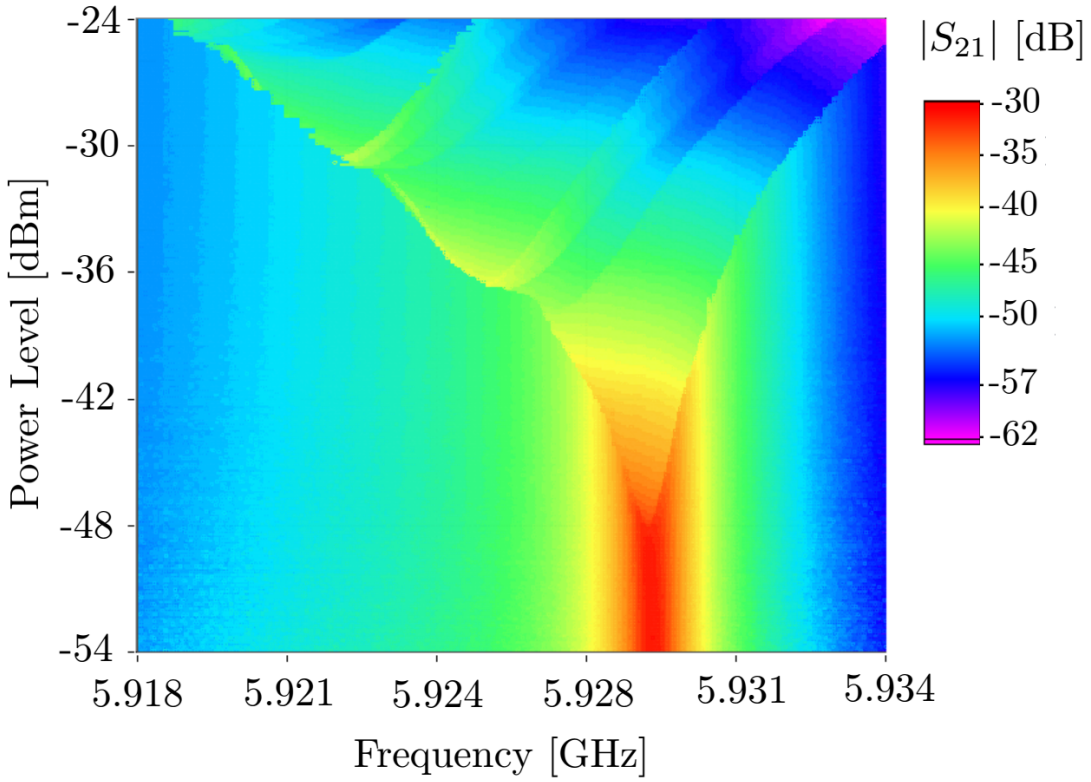

Figure 7.6: $|S_{21}|$ as a function of frequency and power level centred around the fundamental mode of SN1. At low powers the peak of the resonance can be seen centred around approximately 5.93 GHz. At a power level of approximately −48 dBm the mode splits into the two bifurcated components observed in Fig. 7.3, moving towards lower and higher frequencies, similar behaviour can be seen around a power level of −38 dBm and −31 dBm. Several other subtler branching features can be observed.

7.2.3 Second mode

The second mode of the SN1 shows no power dependence even at the highest power levels, illustrated in Fig. 7.7. This is expected given the node in the current distribution of the second mode at the $l/2$ point where the nanobridge RF SQUID array is located. In the case of SA2 the power dependence was suspected primarily due to the presence of a low I_c highly reactive tunnel junction.

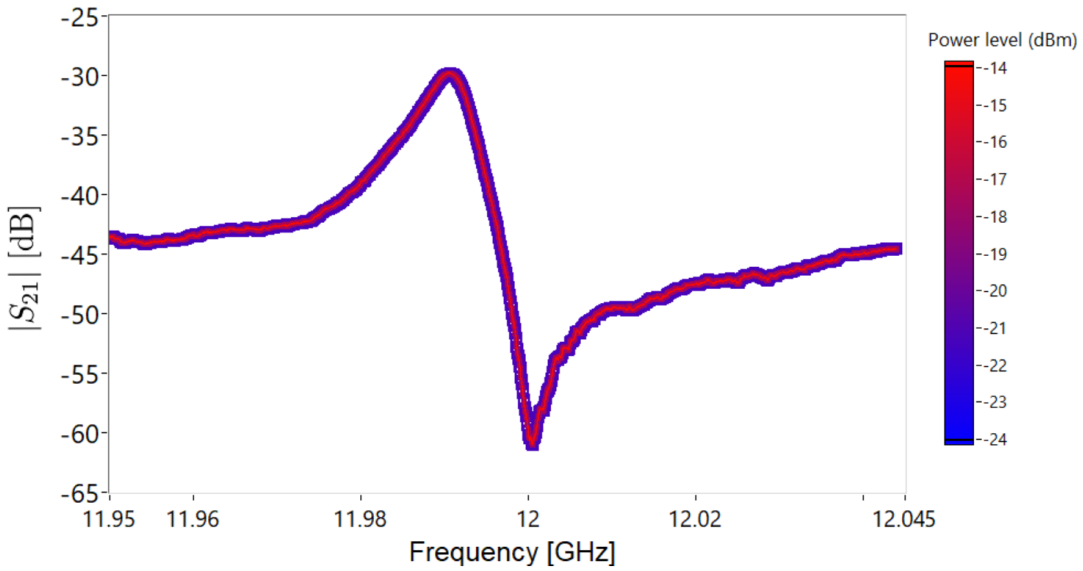

Figure 7.7: $|S_{21}|$ as a function of frequency measurements centred around the second mode of SN1 for several different power levels, ranging from -14 dBm to -24 dBm in approximately 1 dBm intervals. The measurements are overlaid to illustrate the lack of any change in the resonant mode over the power level range.

7.2.4 Summary

The power dependence exhibited by SN1 appears characteristic of a cubic Duffing like non-linearity, correlated to the etched RF SQUID nanobridge array located at the $l/2$ point of the Nb CPW resonator. Ambiguity remains regarding the DC phase offset of each individual SQUID without the ability to flux bias the array, similarly limiting the ability to tune the magnitude and order of the non-linearity such as to fully exploit the possible mixing regimes.

Although the array of nanobridge RF SQUIDs has imparted a significant non-linear response to the Nb CPW resonator it increases the complexity involved in understanding the characteristics of the individual Nb nanobridges and their cumulative behaviour. Additional bifurcations noted at higher powers could relate to individual elements of the array responding at differing drive frequencies/powers due to variations in geometry of the nanobridge constrictions and inductance of the SQUID loops. As such the elements of the array could be acting independently. Another possibility could relate to how the array and loop inductances were formed. The RF SQUID array could be coupled via the shared conductor forming each SQUID loop (Fig. 7.1) [69]. For a non-zero flux bias (or trapped flux) this results in a spread of the flux threading each SQUID loop, giving rise to a range in the magnitudes of the even and odd non-linear terms.

7.3 SN2

7.3.1 Sample design

In order to explore the non-linear properties of Nb nanobridges further a new sample design was employed, shown in Fig. 7.8. In this case two nanobridge RF SQUIDs are separately positioned in the locations corresponding to $l/3$ and $l/2$, where l the total length of the resonator. This design was adopted due to its versatility, allowing for a variety of operational modes by controlling the external flux threading the RF SQUID loops. The position of the RF SQUIDs also determines the modes of the CPW resonator that can interact with the parametric non-linearity provided by the RF SQUIDs, which mediates interactions between them.

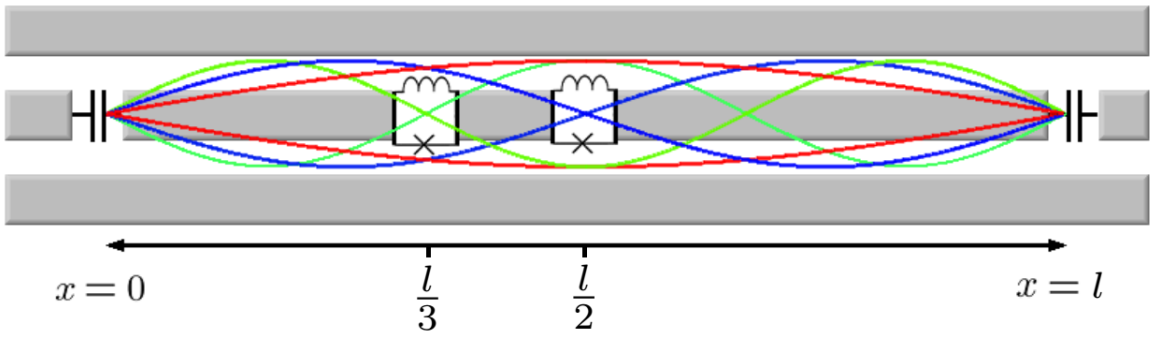

Figure 7.8: Representation of Nb $\lambda/2$ CPW resonator with etched nanobridge RF SQUIDs. Current distribution of the fundamental (red), second (blue) and third mode (green).

If TWM is desired then the appropriate external flux could be applied to maximise the quadratic non-linear coefficient and minimise the cubic coefficient ($\Phi_e/\Phi_0 \approx 0.4$ for $\beta_L = 0.7$). At this position of flux TWM mixing and period doubling could be mediated by the RF SQUID located at the $l/3$ position coupled to the fundamental and second mode of the resonator, as seen in the PD sample discussed in Chapter 4. The RF SQUID at the $l/2$ position would also present a quadratic non-linear medium to support the aforementioned mixing regimes, however due to the current node of the second mode at the $l/2$ position, the fundamental and second mode are uncoupled. Although the fundamental and the third mode have a current antinode at the $l/2$ position mixing between them wouldn't be realised as the cubic coefficient at this position of flux would be minimised ($\gamma = 0$) such that FWM or third harmonic conversion would not be supported.

If FWM is desired then zero/integer flux can be applied to the RF SQUIDs ($\Phi_e/\Phi_0 = n\Phi_0$ where $n = 1, 2...$). In this case the cubic non-linear coefficient is maximised and the quadratic coefficient is minimised. The medium can then support FWM and third harmonic generation mediated by the RF SQUID located at the $l/2$ position coupled to the fundamental and third mode of the resonator. For this flux bias the RF SQUID

located at the $l/3$ position would be uncoupled from the third mode and unable to support mixing of the fundamental mode and the second mode due to the quadratic coefficient being minimised at this position of flux ($\beta = 0$).

This design is also useful for testing the behaviour of the etched nanobridge RF SQUIDs employed in SN1. Given their respective locations the RF SQUIDs can be interrogated independently via the second and third mode, given the corresponding current node and antinode at the respective locations of the RF SQUIDs. Both RF SQUIDs can also be probed via the fundamental mode of the resonator

7.3.2 Trial iterations

Before discussing SA2 it is worth briefly reviewing an early iteration of this sample design shown in Fig. 7.9. An etched RF nanobridge SQUID is positioned at approximately $l/3$ and $l/2$.

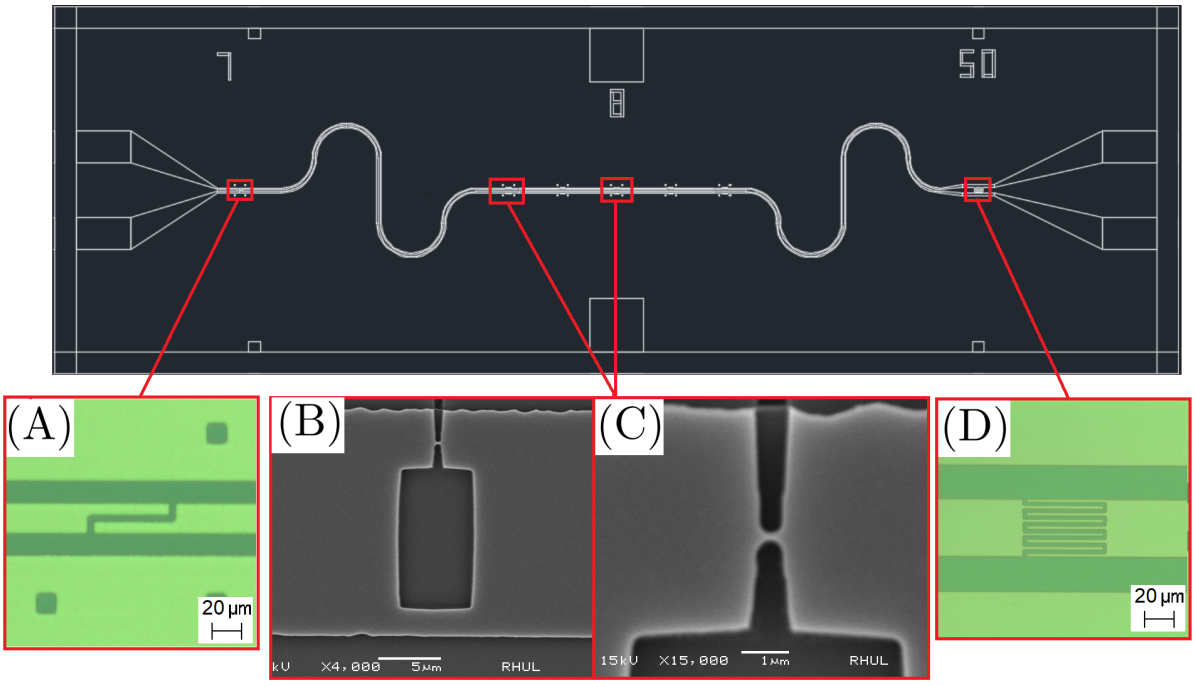

Figure 7.9: Trial iteration of SA2. A R5 resonator is used with coupling capacitors shown in (A) and (D). Two RF SQUIDs are etched at the location corresponding to approximately $1/3^{\text{rd}}$ and $1/2^{\text{th}}$ the total length of the resonator. SEM images of the RF SQUID position at $1/2^{th}$ are also shown in (B) and (C). The nanobridge constrictions where measured to be approximately 100 nm wide.

Due to variance in the clean room environment the nanobridge constrictions etched in this sample were approximately 100 nm wide, considerably larger that the constrictions employed in SN1. The sample was measured at 4.18 K to assess the wider constrictions effect on the modes of the resonator. Fig. 7.10 shows $|S_{21}|$ as a function of frequency

measurements centred around the fundamental and second mode the sample for a range of power levels.

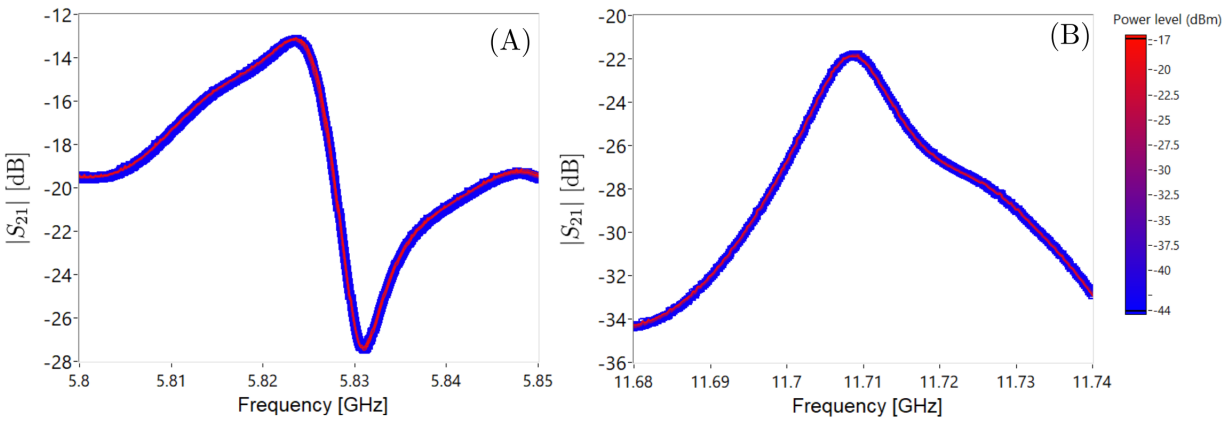

Figure 7.10: $|S_{21}|$ as a function of frequency measurements of a test iteration sample with 100 nm nanobridges centred around (A) the fundamental mode (B) the second mode for several different power levels, ranging from -44 dBm to -17 dBm in approximately 1 dBm intervals. Measurements for each power level are overlaid to illustrate the lack of power dependence.

In this case no power dependence is noted on the fundamental or second mode of the test iteration with 100 nm wide constrictions. It should be noted that both this test iteration and SA2, which will be introduced in the subsequent section, use an R5 design Nb resonator design, as detailed in Chapter 5.1.1. Ideally a R3 design resonator would be used given the higher loaded quality factor, however due to a shortage of Nb film unused R5 resonators were utilised. The unmodified R5 design Nb CPW resonators have a quality factor of approximately 600 to 800 at 4.18 K, limiting the interaction time with an embedded non-linear element, increasing the driving power required to elicit a significant non-linear response. The lower loaded quality factor also applies to the higher harmonic modes of the resonator, this is especially relevant regarding the mixing of the respective modes. Regardless of the quality factor of the R5 design it is assumed that this test iteration showed no power dependence due to the increased width of the nanobridges.

7.3.3 Fundamental mode

SN2 is shown in Fig. 7.11. The design is identical to that of the test iteration discussed in the previous section, using the same R5 resonator design. An etched RF nanobridge SQUID is position at approximately $1/3^{\text{rd}}$ and $l/2^{\text{th}}$ the length of the resonator. The width of the etched nanobridges are approximately 60 nm, inferred by SEM imaging. Fig. 7.12 shows the fundamental mode of SN1 at a power level of -72 dBm. Due to the R5 resonator design used, the fundamental mode in this case is relatively broad with a quality factor of approximately 600.

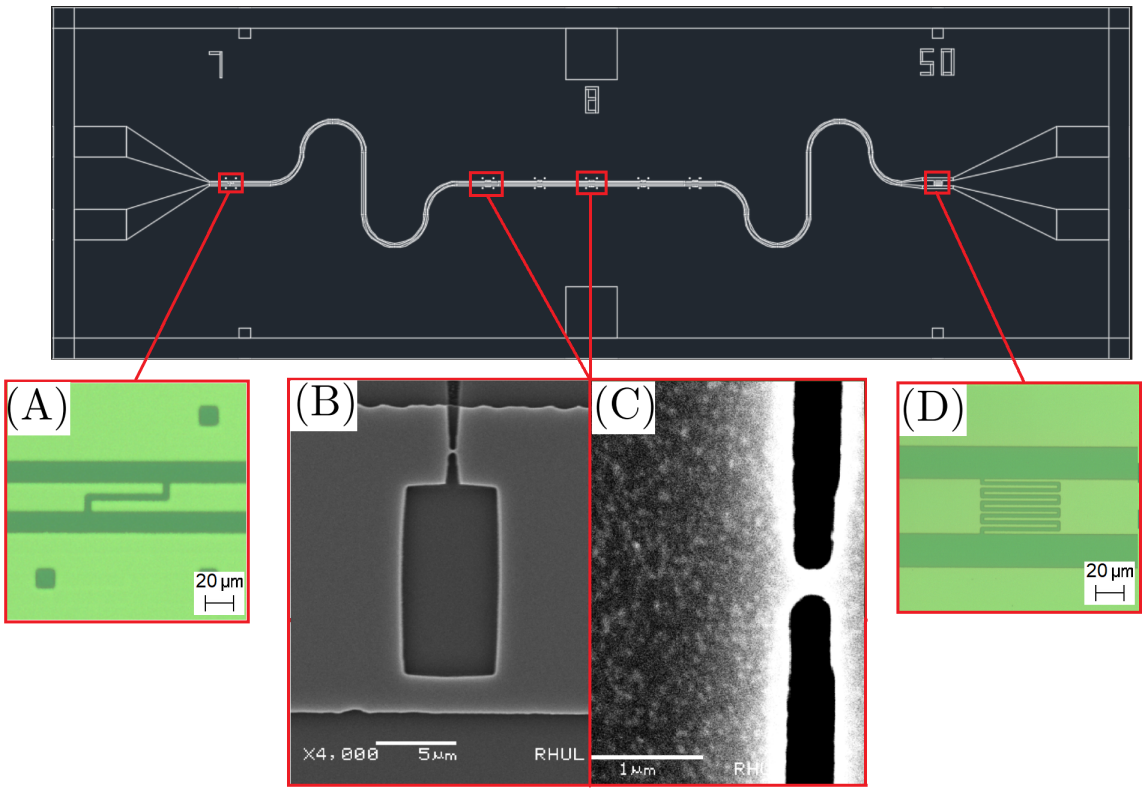

Figure 7.11: SN2 - $\lambda/2$ Nb CPW resonator with two etched nanobridge RF SQUIDs located at the positions corresponding to approximately $1/3^{\text{rd}}$ and $1/2^{\text{th}}$ the total length of the resonator. (A) and (D) show optical images of the coupling capacitors. (B) SEM image of a test device representative of the RF SQUID loop used in SN2. (C) SEM image of the etched nanobridge located at the $\lambda/2$ point of SN2.

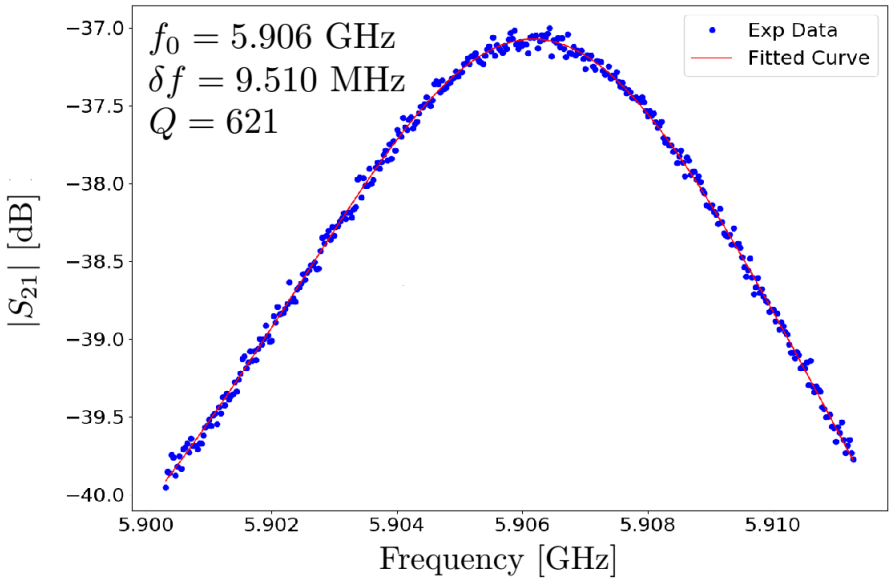

Figure 7.12: $|S_{21}|$ as a function of frequency measurement of the fundamental mode of SN2 at a power level of -72 dBm, fit with a Lorentzian function.

At a power level of approximately −49 dBm the fundamental mode appears to split into two separate components (LHS and RHS) moving to lower and higher frequencies respectively, shown in Fig 7.13. Although initially this appears similar to the two component behaviour observed when measuring SN1 around a similar power level (Fig. 7.3), upon closer inspection no significant frequency pulling can be observed with increasing powers with respect the LHS component. The response in this case seems to appear dissipative with the transmission amplitude significantly reduced in the region of the resonant frequency.

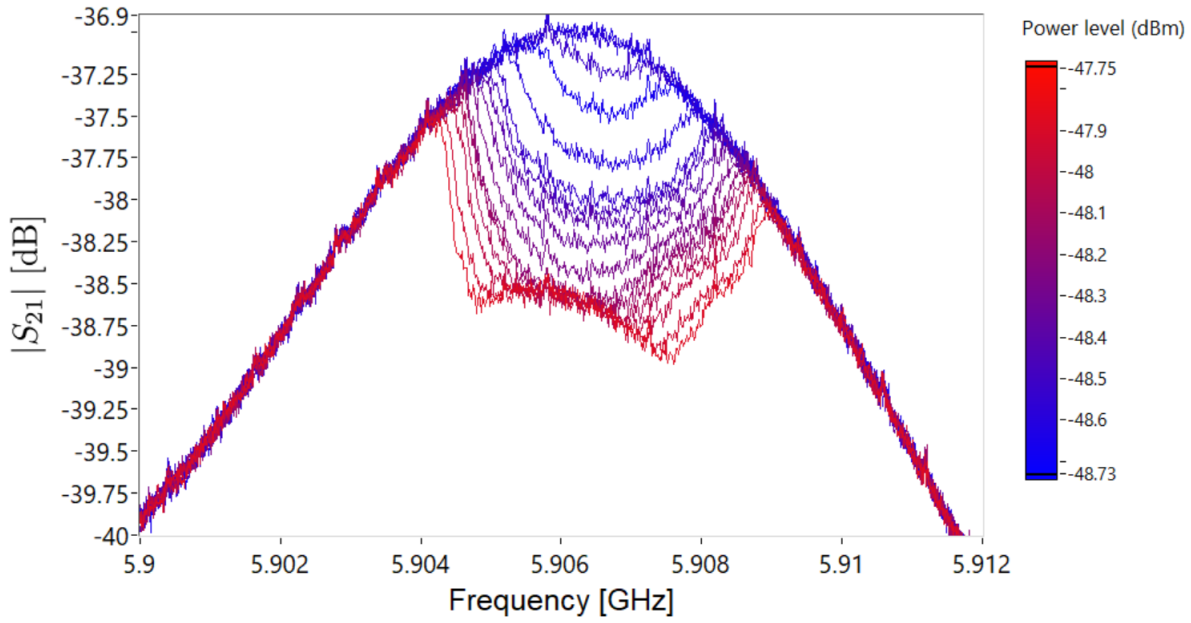

Figure 7.13: $|S_{21}|$ as a function of frequency measurements centred around the fundamental mode of SN2 for several different power levels, ranging from −48.73 dBm to −47.75 dBm in approximately 0.5 dBm intervals. The measurements at individual power levels are overlaid for comparison.

Fig 7.14 show $|S_{21}|$ as a function of frequency measurements of the fundamental mode over a wider power range of approximately −49 dBm to −43 dBm. As the power is increased the LHS and RHS components continue to move towards lower and higher frequencies. At a power level of approximately −48 dBm the resonant line-shape appears to recover although significantly damped and shifter to a slightly lower frequency indicating a small increase in inductance in this dissipative state. At higher powers around −44 dBm the RHS component, now positioned around 5.8987 GHz is observed to switch between two amplitude states of oscillation, indicative of an unstable amplitude bifurcation. At a power level of approximately −43 dBm the fundamental mode of SN2 has a quality factor of approximately 500 with a centre frequency of 5.904 GHz, detuned approximately 2.4 MHz from its original position at a power level of −72 dBm.

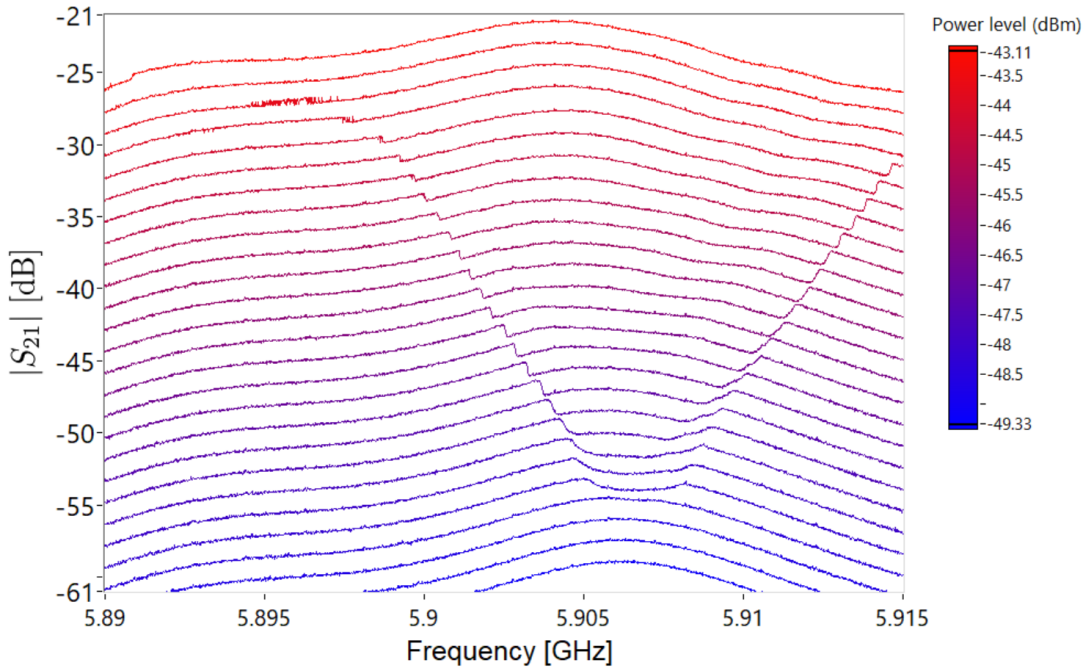

Figure 7.14: $|S_{21}|$ as a function of frequency measurements centred around the fundamental mode of SN2 for several different power levels, ranging from -49.33 dBm to -43.11 dBm in approximately 0.2 dBm intervals. The measurements at individual power levels have been offset approximately $+2$ dB for clarity.

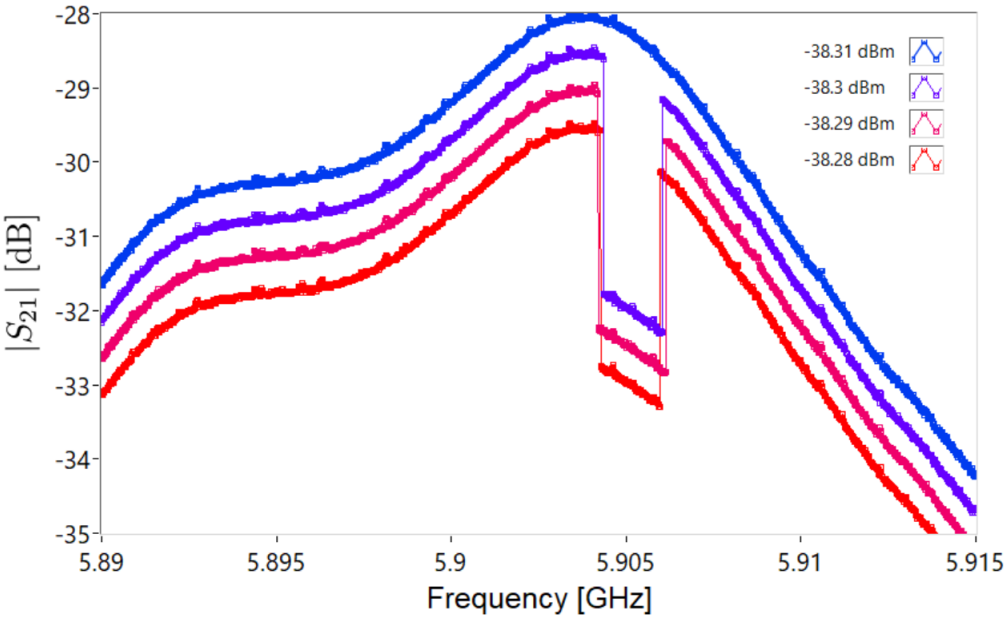

Figure 7.15: $|S_{21}|$ as a function of frequency measurements centred around the fundamental mode of SN2 for several different power levels, ranging from -38.31 dBm to -38.28 dBm in 0.01 dBm intervals. The measurements at individual power levels have been offset -0.5 dB for clarity (this is the only time a negative offset will be used as it suits the volcano bifurcation).

At a power level of approximately −38.3 dBm an extreme response in the state of oscillation is observed, shown in Fig 7.15. In this case the mode appears to spontaneously bifurcate, dropping into a reduced amplitude state and then switching back soon after. This phenomenon has been observed in other SCPW resonators employing weak link constrictions and is commonly referred to as a volcano bifurcation [70], [71]. It is associated with a current-dependent resistance of the nanobridge constrictions at a threshold current bias. Hysteresis of the volcano non-linearity can also be observed at power levels around the onset of the event, shown in Fig 7.16.

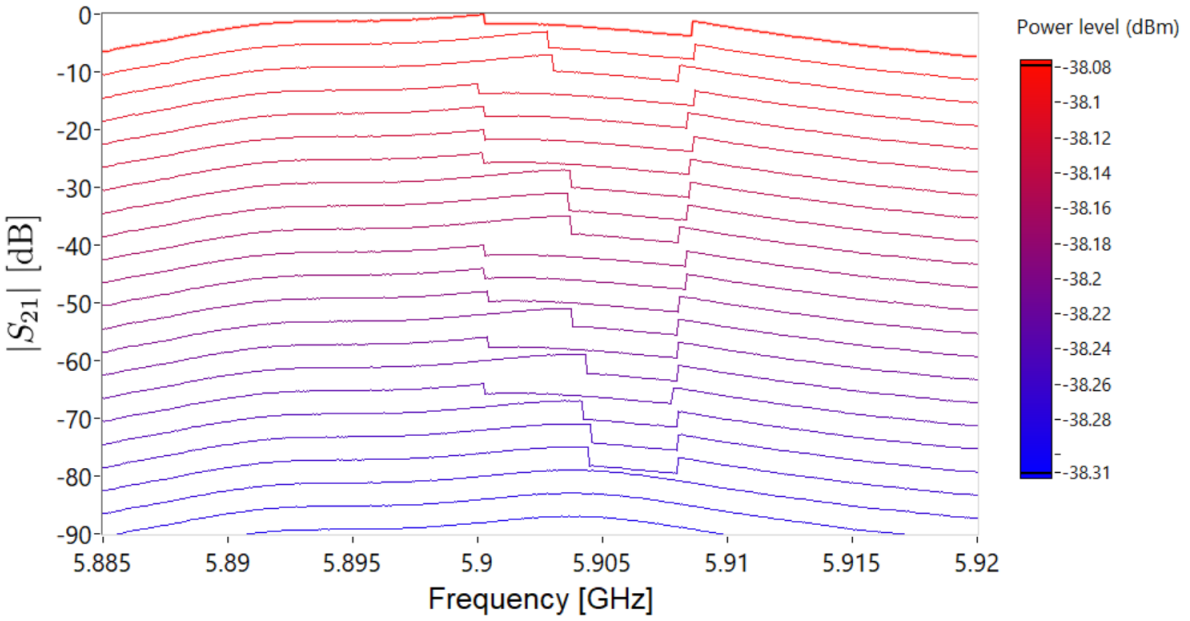

Figure 7.16: $|S_{21}|$ as a function of frequency measurements centred around the fundamental mode of SN2 for several different power levels, ranging from −38.31 dBm to −38.08 dBm in 0.01 dBm intervals. The measurements at individual power levels have been offset +4 dB for clarity.

At higher power levels the fundamental mode of SN2 is considerately damped, a comparison of the fundamental at a power level of −48.5 dBm and −24 dBm is shown in Fig 7.17. Although the mode is damped it is also shifted to lower frequencies indicating an inductive contribution even in this dissipative state. A bifurcation is still observed at a power level of −24 dBm located at lower frequency of 5.85 GHz.

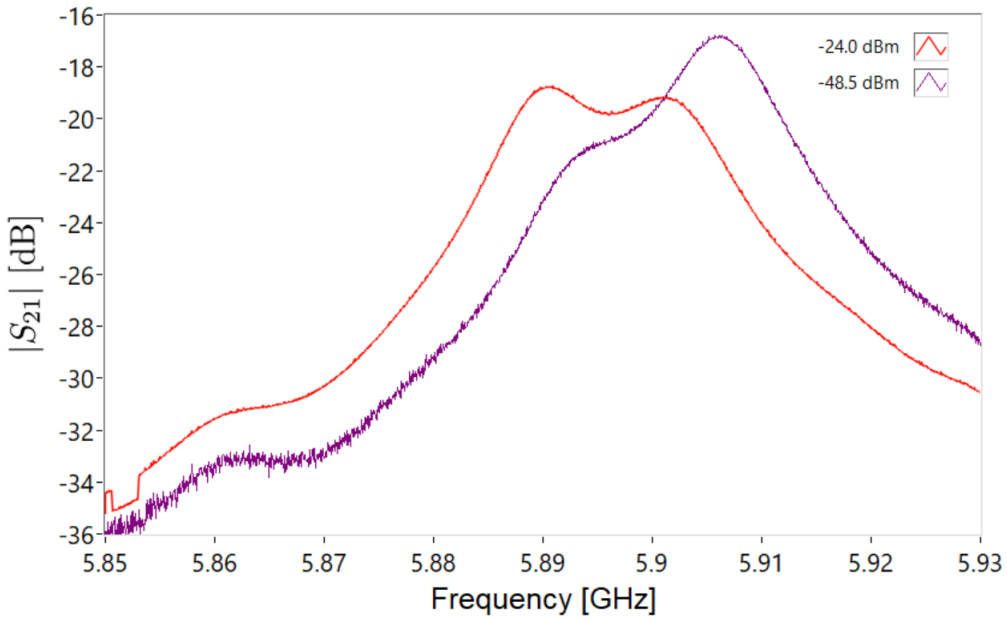

Figure 7.17: $|S_{21}|$ as a function of frequency measurements centred around the fundamental mode of SN2 for a power level of -24 dBm and -48.5 dBm.

Volcano bifurcation like events can also be observed when driving the second mode of the resonator. Shown in Fig 7.18 in this case at an onset power of -40.2 dBm.

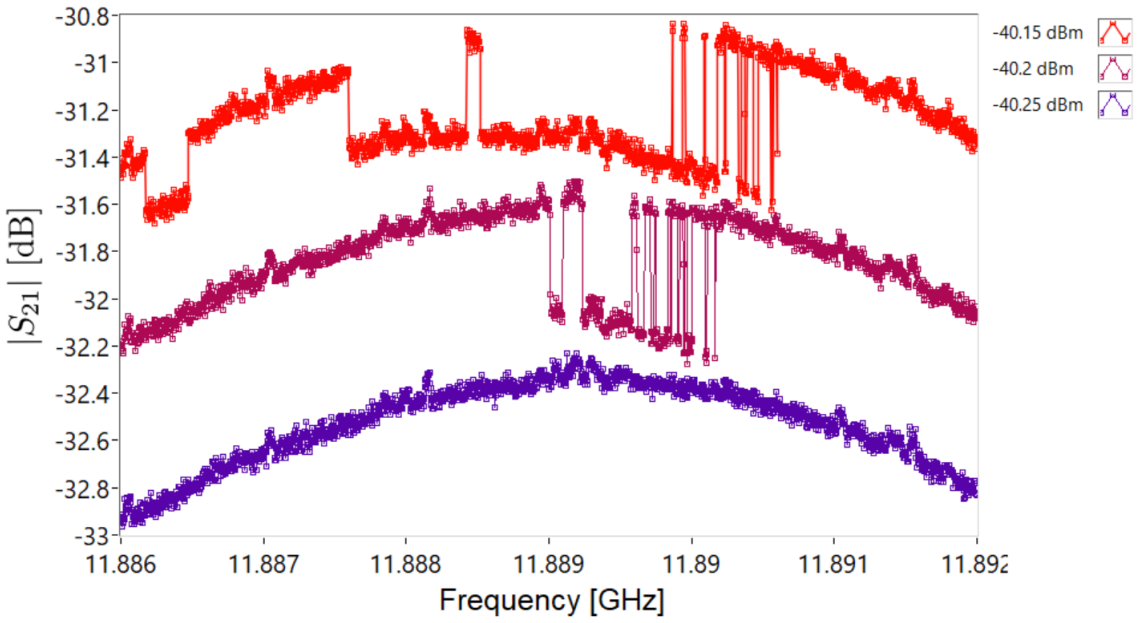

Figure 7.18: $|S_{21}|$ as a function of frequency measurements centred around the second mode of SN2 for a range of power levels.

The response of the second mode at this power level is comparable with the volcano bifurcation observed on the fundamental mode at a power level of -38.31 dBm (Fig.

7.15). The event is less abrupt with the amplitude fluctuating between a high and low state, this could be due to the lower quality factor of the second mode interacting with the SQUID at the $l/3$ position in the resonator.

Due to the location of the RF SQUIDs in the resonator their interaction with the resonant modes of the CPW is constrained. The fundamental mode interacts with both RF SQUIDs with a maximum in the current distribution at the position of the RF SQUID located a $l/2$ the total length of the cavity. As such, assuming the RF SQUIDs are approximately identical, we would expect a response from the RF SQUID at the $l/2$ position at lower power levels, followed by a response at higher powers from the RF SQUID at $l/3$ when driving the fundamental mode. This could explain the two events noted when driving the fundamental mode at a power level of approximately -48 dBm (Fig. 7.13) and the second event at a higher power level of approximately -38 dBm (Fig. 7.15), correlating to the individual RF SQUIDs positioned at $l/2$ and $l/3$ the length of the resonator. When driving the second mode we would only expect a response from the RF SQUID located at the $l/3$ position due to node in the current distribution of the second mode at the position of the RF SQUID at $l/2$. The second mode appears to bifurcate in the same manner as the fundamental mode at a power level of approximately -38 dBm (Fig. 7.18), however at a lower power level of approximately -40 dBm. Indicating that the RF SQUID located at the $l/3$ position is responsible for the behaviour of the fundamental mode around -38 dBm.

7.3.4 Four-wave mixing

The volcano bifurcation observed in SA2 is an interesting consequence of the etched nanobridge constrictions becoming dissipative at a critical driving power. However, it confuses inferences regarding the nature of the non-linearity they present. As such it is constructive to try to observe their non-linearity in a different manner. Given we expect a cubic non-linearity, assuming $\Phi_e \approx 0$, then FWM should be realised. In order to investigate this further two continuous wave (CW) sources are used in conjunction with a spectrum analyser as shown in Fig 7.19.

The experimental set-up is similar to that used when studying the different wave mixing regimes exhibited by the period doubling (PD) sample in Chapter 4. In this case one of the CW sources provides a signal tone set at a constant frequency of $\omega_s = 5.906$ GHz at a constant power level P_{signal}. The second CW source acts as a pump tone (ω_p) set to a slightly lower frequency of $\omega_p = 5.900$ GHz. The frequency of the pump tone is fixed and the power P_{pump} is incremented over the course of the measurement. The spectrum analyser captures a frequency window centred around the respective tones. Fig. 7.20 illustrates the mixing products that result around the fundamental mode of SN2 for a constant signal power $P_{signal} = -38$ dBm, as the pump power P_{pump} is incremented.

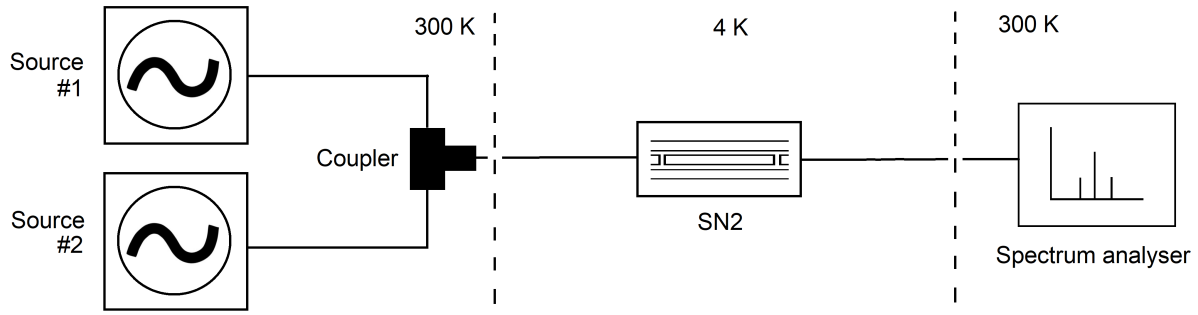

Figure 7.19: Two continuous wave (CW) sources are used to provide the signal and pump tone to the sample input. The output is measured using a spectrum analyser.

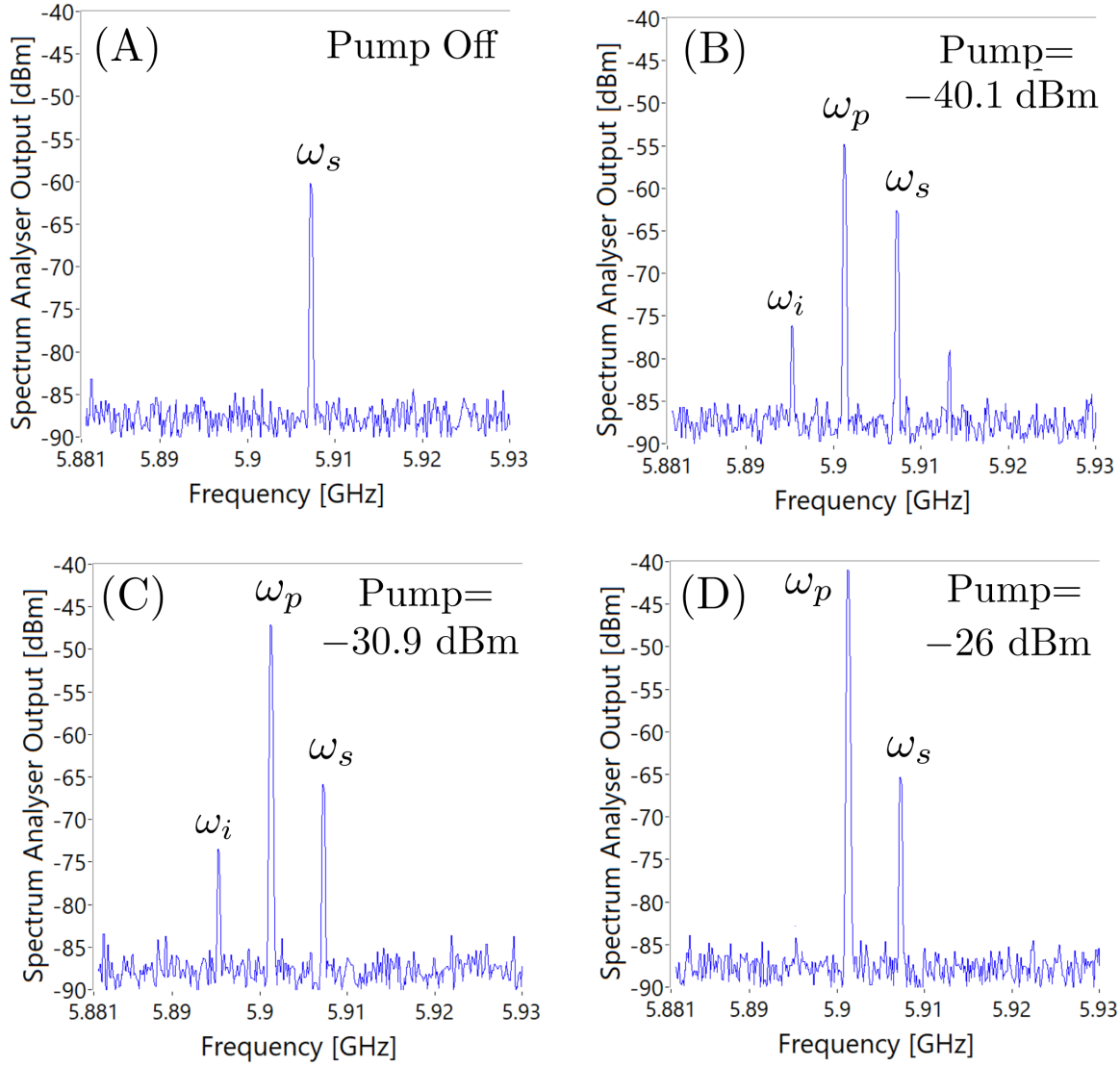

Figure 7.20: Spectrum analyser data, centred around the fundamental mode, at various pump powers. (A) Pump output off - no mixing (B) $P_{pump} = -40.1$ dBm - non-degenerate FWM (C) $P_{pump} = -30.9$ dBm - degenerate FWM (D) $P_{pump} = -26$ dBm - no mixing.

As P_{pump} is increased different regimes of FWM are encountered. Non degenerate FWM is encounter at lower pump powers with degenerate FWM becoming the dominant mixing regime at higher pump powers. This could correlate with the individual RF SQUIDs interaction with the signal and pump tone given their differing position in respect to the current distribution of the fundamental mode of the CPW resonator. The amplitude of the spectrum analyser output as a function of pump power P_{pump} and frequency is shown in Fig 7.21 for several different constant signal powers.

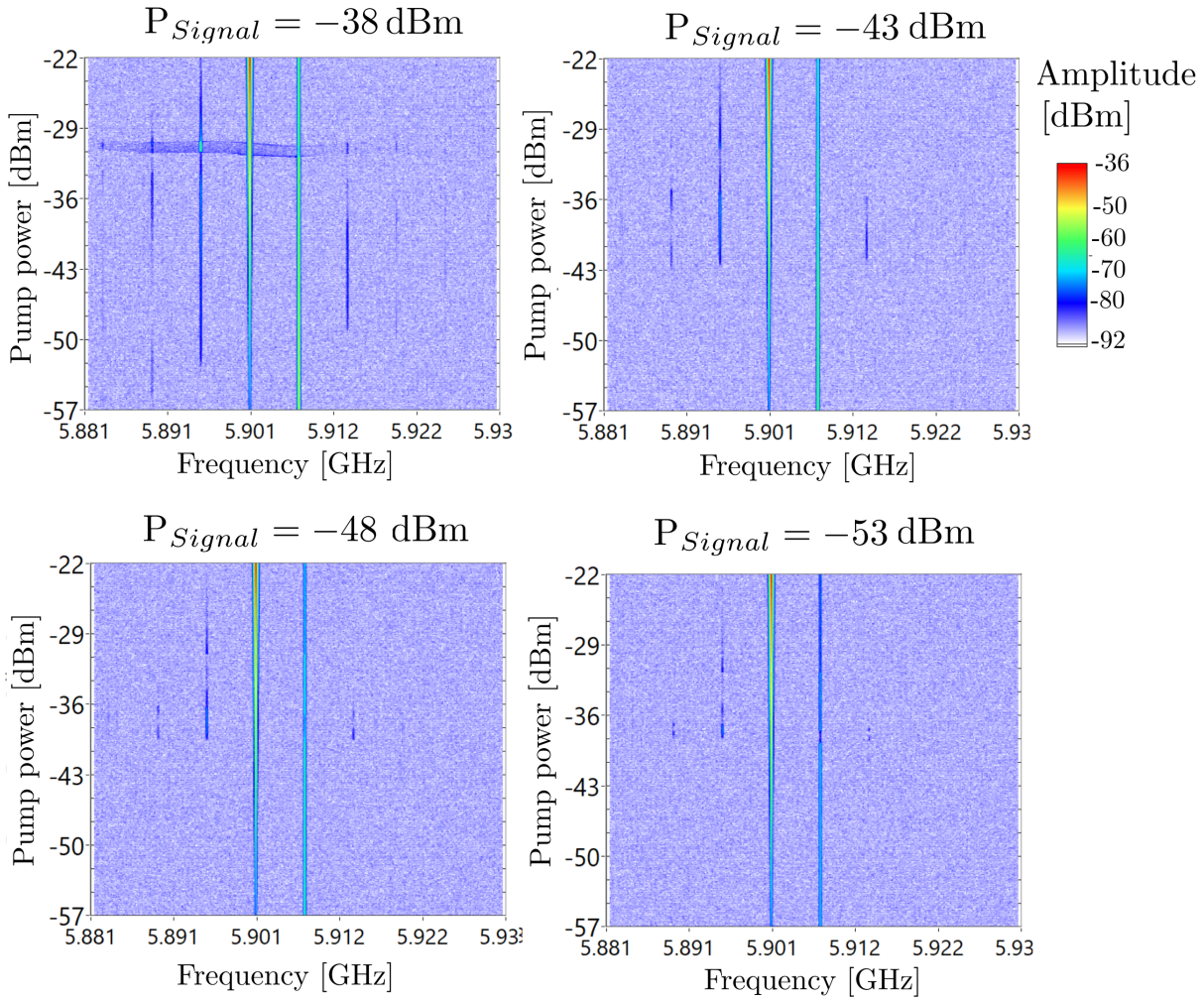

Figure 7.21: Spectrum analyser output centred around the fundamental mode of SN2 as a function of pump power and frequency for several different signal powers (P_{signal}).

7.3.5 Summary

Both SN1 and SN2 have been demonstrated to manifest a cubic non-linearity. In the case of SN1, where an array was utilised, the response was analogous to a Duffing like non-linearity with the resonance bending to lower frequencies at higher powers and the amplitude state bifurcating. This behaviour is consistent with a current dependent Josephson inductance, although it is expected that the current-phase relation of the fabricated

nanobridges could be quite different to the sinusoidal relation found in Josephson tunnel junctions. SN2 however, although capable of supporting FWM exhibits a notably different response for increasing drive powers. In this case dissipation is observed in combination with a volcano non-linearity associated with a current-dependent resistance at a critical driving power. This is an interesting phenomenon, although not necessarily favourable for a practical device. Although SEM imaging of the respective samples showed them to have approximately identical widths and electrode separation, given these structures reported sensitivity to their dimensions even a slight variance may result in differing characteristics. These measurements represent a first step in understanding the characteristics of the RHUL etched nanobridges using the fabrication methodology outline in Chapter 5. I hope continued exploration of these devices will be considered.

Chapter 8

Conclusions

Josephson junction embedded Nb CPW resonators

Addressing the measurements of the Nb $\lambda/2$ CPW resonator with an embedded Al/AlO_x/Al tunnel junction designated SA2. Although this device was never observed in its intended mode of operation, the observation of significant power dependence in the form of mode splitting, frequency pulling and bifurcation of the amplitude state when driving the second mode of the resonator is indicative of the response of a low I_c Josephson junction whose inductance is being modulated. When driven at higher power levels the quality factor of the mode begins to reduce substantially indicating dissipation. This can be attributed to over-driving of the junction. The most surprising behaviour observed by SA2 was the appearance of the "sigma mode". A mode at a slightly lower frequency with respect to the second mode, appeared in the spectrum at a power level of -92 dBm.

The origin of the sigma mode is related to the Josephson junction. A primary indication of this is the damping of the mode after its onset, correlating with damping of the second mode around the same power level. This would suggest that the sigma mode is also over-driving the Josephson junction although it is far from the resonant frequency of the Nb CPW resonator. This can also be inferred from the mode splitting and frequency pulling of the sigma mode after its onset. Coupling between the sigma mode and the second mode was also observed, such that a change in the amplitude state of the sigma mode results in a response in the amplitude of the second mode. This could be mediated by their shared interaction with the junction. To my knowledge this phenomenon is unique. Thus far, it is not fully understood and as such warrants further study.

A primary motivation of this project was the development of the fabrication of Al/AlO_x/Al junction integrated CPW resonators using the RHUL facilities. Such as to establish the technology required for the design and development of superconducting nano-fabricated quantum devices, such as parametric amplifiers. Although analysis of measurements of SA2 is complicated due the position of the junction with respect to the spatial current distribution of the second mode, the behaviour exhibited would suggest that the junction fabrication and subsequent integration with the Nb CPW resonator has been largely

successful. Low I_c tunnel junction technology is extremely powerful with numerous applications spread over several fields. Although only a single sample design was explored in this work the same technology can be applied to produce a wide range of cQED devices; including qubits, single photon sources and quantum limited amplifiers. As such I hope development of the fabrication methods outlined in Chapter 5 continues.

This work has focussed on the development of resonant based devices where the interaction time with a non-linear element has been extended due to the boundary conditions imposed by the capacitive coupling of the CPW resonator to the input and output line. This approach can be used to produce parametric amplifiers with high gain, near if not achieving quantum limited sensitivity and the ability to squeeze the quantum noise of the electromagnetic vacuum [7]. However, the resonant architecture imposes fundamental limitations on the bandwidth of such an amplifier, relevant when considering practical applications. In Chapter 2.3.6 we discussed non-linear transmission lines, in this case no resonant geometry is employed, a transmission line itself is embedded with non-linear elements to produce a non-linear microwave medium (travelling-wave parametric amplifier). The interaction time between the signals traversing the transmission line and the effective non-linearity is dependent on the magnitude of non-linearity per unit length and the interaction length. In practice this requires a large number of consistent nano-fabricated non-linear elements (e.g. Josephson junctions) over a "long" length of transmission line. Although more demanding to fabricated than a resonant based amplifier, recent advances in fabrication technologies and techniques have made this task far easier.

The travelling-wave approach removes the bandwidth constraints imposed in resonant based parametric amplifiers, however, the extended interaction length poses additional considerations for achieving optimum performance. The operation of several travelling-wave parametric amplifiers based on Josephson junctions have been reported ([8], [72], [73]), showing high gain and near quantum limited performance. However, these devices employ a cubic 4MW regime (discussed in Chapter 2.3.4) and with that are subject to self and cross phase modulation, where the phase relation of the waves traversing the medium is dependent on the power of the respective components. As such, travelling-wave parametric amplifiers based on a 4WM regime typically require additional engineering to ensure phase matching of the signals to be mixed along the length of the interaction to achieve optimum performance. This additional engineering increases the difficulty of fabricating such devices. As discussed in Chapter 2.3.6 a way of avoiding self and cross phase modulation is to use a 3WM regime, achievable with a RF SQUID based non-linear transmission line, as proposed by A. Zorin [56]. The RF SQUID, when biased appropriately with an external flux, can be used to realise a quadratic non-linearity. Operating in the 3WM regime avoids the complications of self and cross phase modulation, with the added advantages of shifting the pump far from the signal frequency ($\omega_p = 2\omega_s$

in the degenerate case) and an inherently stronger interaction between the signals coupled by the parametric non-linearity, in comparison to the higher-order cubic interaction.

Such a travelling-wave parametric amplifier based on 3WM using RF SQUIDs has been recently demonstrated by A. Zorin et al. [74] and shown in Fig. 8.1. The measured device employs 272 cells, each comprised of six RF SQUIDs (Fig. 8.1(C)) using Nb/AlO_x/Nb trilayer Josephson junctions ($I_c = 12\ \mu$A), with a SQUID screening parameter $\beta_L \approx 0.85$. This amplifier demonstrated a maximum gain of 11 dB, with a gain $\geq$ 10 dB over a frequency range of 4.8 GHz to 7.8 GHz. I predict that the gain and noise performance of this class of travelling-wave parametric amplifiers will continue to improve as device parameters are tuned to their optimal values.

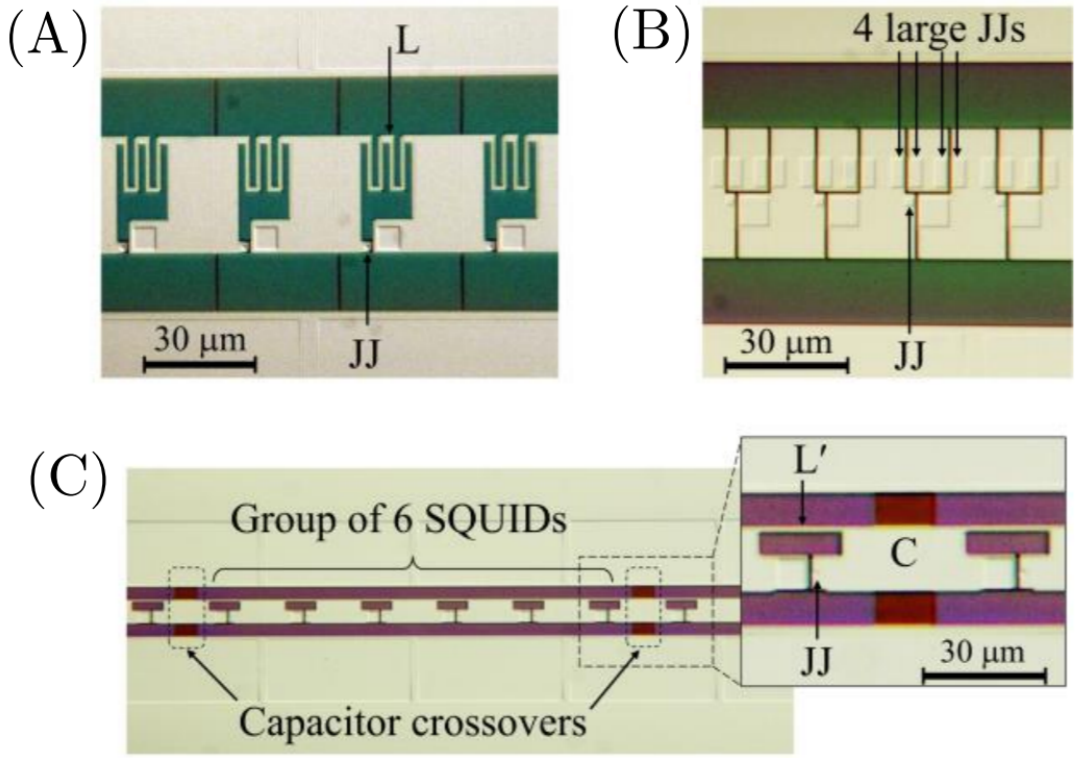

Figure 8.1: Taken from [74]. Images of various sections of travelling-wave parametric amplifiers, of different designs, based on a RF SQUID embedded CPW transmission lines. Two difference methods of producing the shunting inductance to give the desired β_L for the RF SQUID elements are shown in (A) and (B). The method employed in (A) uses the geometric inductance (L) of a superconducting wire, whereas in (B) the kinetic inductance of 4 large Josephson junctions (L') provides the shunting capacitance. (C) shows an array of six RF SQUIDs with a capacitance separating one array from the next. This configuration results in a cell (formed by the array of RF SQUIDs) with an effective inductance much greater than that of a single SQUID, allowing for a reduction in the cut-off frequency of the transmission line, while maintaining a 50 Ω impedance.

Nb nanobridges

The fabrication of CPW resonators incorporating nanobrdiges was largely successful, with the demonstration of a significant non-linearity imparted to a Nb CPW resonator using an array of RF SQUIDs formed by etching nanobridge constrictions and SQUID loops in the central conductor (SN1). In this case a Duffing like bifurcation was observed as the inductance of the nanobridge RF SQUID array was modulated via driving the fundamental mode of the resonator. Although further characterisation of these devices is required, in principle the presence of the Duffing like non-linearity allows SN1 to be operated as a bifurcation based photon detector or FWM parametric amplifier. A DC SQUID geometry employing nanobridges would also be interesting to explore in the case that a quadratic non-linearity was not desired.

SN2, featuring a single RF SQUID at $1/3^{\text{rd}}$ and $1/2^{\text{th}}$ the length of the resonator, showed different behaviour to SN1. At a critical power a volcano type non-linearity was observed. In this case an inductive response is observed in a dissipative regime. Although quite different to the Duffing like non-linearity encountered in SN1, it was shown that the devices supports FWM such that parametric amplification can also be realised using this non-linearity. However, given the dissipation encountered, a Duffing like non-linearity would be preferred. Given the absence of flux bias from these measurements the full extent of what is capable with the SN2 sample design could not fully be explored, primarily the TWM regime. An interesting experiment would be to combine the SN1 and SN2 design, employing arrays of RF SQUIDs at $1/3^{\text{rd}}$ and $1/2^{\text{th}}$ the length of a high quality factor resonator to enhance the non-linearity. This should allow for a strong non-linearity whose order and strength can be controlled via an external flux to realise a very flexible amplifier able to operate in both a TWM and FWM regime, capable of operating in a temperature range inaccessible to Al tunnel junction based devices.

Similarly to the Al Josephson junctions, the Nb nanobridges represent an extremely applicable technology. Although thermal hystersis and dissipation maybe of concern in certain applications [75]. If a significant non-linear response is manifested below I_c, such as that observed in SN1, then this would allow for the development of a parametric amplifier. A major advantage to the Nb nanobridges developed in this work is the relative ease of fabrication. The nanobridges where fabricated without using high resolution electron-beam lithography or focussed ion beam (FIB) technology. The method developed relies on the correct dosing of a PMMA/copolymer resist bilayer and RIE. Due to the simplicity of their design they could be produced in large numbers in a straight forward manner. As such they may be used for the basis of devices employing multiple non-linear elements, such as a Josephson parametric travelling-wave amplifier. To optimise the etched nanobridges further for this particular application it would be worth studying their geometry and its influences on the current-phase relation of the weak link, such as to realise

the maximal non-linearity, required for efficient amplification.

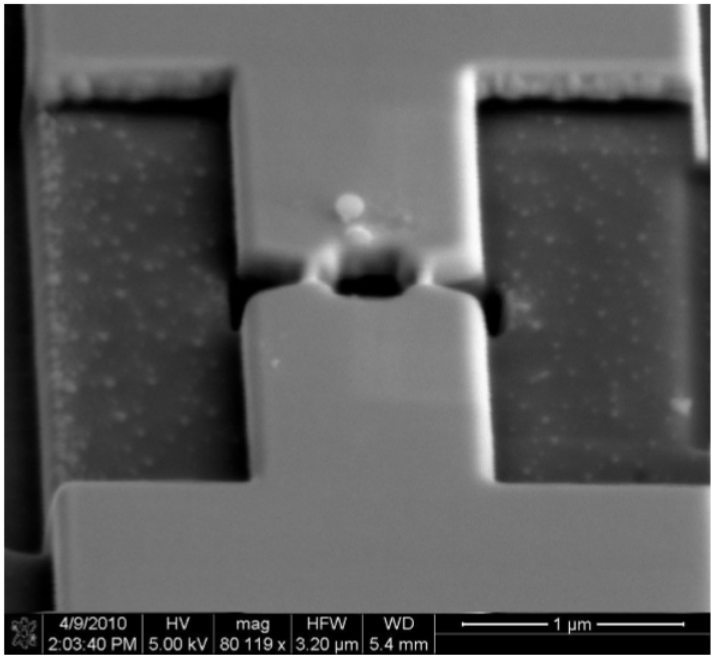

Figure 8.2: Taken from [77]. A SEM image of a nano-SQUID with a loop diameter of approximately 350 nm and nanobridges of dimensions 50 nm × 80 nm. The nano-SQUID is fabricated using gallium FIB milling. A single magnetic particle (diameter ≈ 120 nm) can be seen positioned on the top of the SQUID loop. The magnetic particle is deposited onto the nano-SQUID using a sharpened carbon fibre tip controlled via a micro-manipulator operated in a SEM to "pick up" the particle and place it at the desired location on the SQUID loop.

We have primarily focussed on nanobridges as non-linear elements for manifesting parametric interactions and realising non-linear oscillators. However, a primary attraction of nanobridges is their geometrical dimensions in comparison to Josephson tunnel junctions. Nanobridges can be used to readily realise SQUID geometries with loop diameters of the order 200 nm [76], commonly referred to as nano-SQUIDs. One of the most interesting applications of nano-SQUIDs is as a nanomagnetic particle detector (Fig. 8.2), where the reduced loop area of the nano-SQUID, corresponding to a reduced inductance, allows for near quantum limited energy sensitivity. However, the smaller loop area results in a reduced coupling to external magnetic fields. This places constraints on the requirements of coupling the field of interest to the nano-SQUID, often requiring the sample to be measured to be in close proximity or inside the SQUID loop itself. The electric spin sensitivity, S_n, in units of spins per $\sqrt{\text{Hz}}$, of a SQUID is given as

$$S_n = d\frac{S_\Phi}{2\pi\mu_B\mu_o} \tag{8.0.1}$$

where S_Φ is the power spectral density of the flux noise, related to the inductance of the SQUID loop and d is the dimension of the loop scaled by a geometric parameter. With the appropriate SQUID dimensions ($d \approx 200$ nm) the detection of single electronic spin flips should be achievable. Such a device would find wide reaching applications in the field of spintronics and quantum information processing.

The nano-SQUID shown in Fig. 8.2 is fabricated using gallium FIB milling. This technique allows for the definition of nano-scale structures below 50 nm, however it has been reported that the implantation of Ga ions can result in the poisoning of superconducting films [78]. As such, it would be interesting to compare nanobridges fabricated using EBL and RIE (as detailed in Chapter 5.4) with Ga FIB fabricated nanobridges.

Closing remarks

In this project two distinct Josephson elements have been produced and integrated into Nb CPW resonators. These devices have been measured and have exhibited some unique phenomena. The behaviour of these devices has been discussed in regard to the potential applicability for the development of a wide variety of non-linear devices. The next step is to implement these elements into devices with practical applications.

Appendix A

Fabrication recipes

A.1 - Fabrication of Nb CPW resonator

Table A.1: CPW resonator fabrication. Substrate: 200nm sputtered Nb on oxidised Si substrate

Step	Process	Equipment and Parameters	Comments
1	Sustrate preparation	Acetone at 60°C 5 mins. Rinse IPA, N_2 blow dry.	
2	Sustrate preparation	RIE - 100 SCCM O_2. Power = 100 W. Pressure = 100 mtorr. Time = 2mins. Rinse with IPA, N_2 blow dry.	Noted to reduce resist residue
3	Resist application	S1813 novolak resist. Spin speed = 4500 rpm. Hot plate 110°C 5 mins.	Saturate substrate surface to avoid beading with resist
4	Exposure	Optical Mask aligner, exposure time: 15 s.	If beading is an issue strip reset and restart
5	Development	Microposit MF319, 60 s. Rinse with dI water and N_2 blow dry.	
6	Inspection	Optical microscope.	Inspect for mask quality prior to etching, develop for a further 20 s if necessary
7	Etch	RIE - 20 SCCM SF_6 , 10 SCCM Ar. Time = 10-12 mins.	Observe plasma for glow discharge during etching
8	Inspection	Optical microscope.	Check if Nb has been fully etched, return to RIE if required

9	Mask removal	Acetone at 60°C 5 mins. Rinse with IPA N_2 blow dry.	
10	Postior etch	RIE - 20 SCCM SF_6 , 10 SCCM Ar. Time 30 s. Rinse with IPA, N_2 blow dry.	Can be skipped if a secondary etch is required
11	Inspection	Optical microscope.	

A.1 - Fabrication of Nb CPW with integrated Al JJ

Table A.2: Nb CPW with integrated Al junction. Substrate: Nb CPW resonator

Step	**Process**	**Equipment and Parameters**	**Comments**
1	Substrate preparation	Acetone at 60°C 5 min. Rinse IPA , N_2 blow dry.	If necessary
2	Etch	RIE - 100 SCCM O_2. Power = 100 W. Pressure = 100 mtorr, Time = 2 mins. Rinse with IPA, N_2 blow dry.	If required
3	Resist application	Copolymer 13%, 4000rpm, bake 5 mins at 150°C.	Beading is not a concern for EBL, use minimal resist
4	Inspection	Optical microscope.	Ensure no diffraction pattern around sample space
5	EBL lithography	EBL - acc. Voltage = 30 keV, beam current 15 pA, WD 10 mm.	Exposure area intended for the Al junction to be positioned
6	Development	7% H_2O, 93% IPA, 2 minutes. Rinse with IPA blow dry.	
7	Inspection	Optical microscope.	Check pattern
8	Etch	RIE - 40 SCCM SF_6, 50 SCCM O_2, time 10-12 minutes.	Observe glow discharge during etching
9	Inspection	Optical microscope.	Check if Nb has been fully etched, return to RIE if required

10	Mask removal	Microposit 1165 resist remover, hot plate 60°C. Rinse with IPA N_2 blow dry.	
11	Posterior etch	RIE - 20 SCCM SF_6, 10 SCCM Ar. Time = 30 seconds. Rinse with IPA, N_2 blow dry.	
12	Resist application	13% Copolymer 4500 rpm bake 150°C 5 mins, 4% PMMA, 4500 rpm ,bake 150°C 5mins.	
13	Inspection	Optical microscope.	Ensure no diffraction pattern around intended EBL location
14	EBL lithography	EBL - 30 keV, 15 pA beam current, WD 10 mm.	Define junction
15	Development	7% H_2O, 93% IPA, 2.5 minutes, Rinse with IPA, N_2 bow dry.	
16	Inspection	Optical microscope.	Check pattern for suitably for deposition
17	Deposition Ar etch	Thermal evaporator - 1.5 SCCM Ar plasma etch. Time = 3.5 minutes.	
18	Depositon First layer	Thermal evaporator - Al - angle 60°, thickness 60 nm, rate 1 nm/s.	
19	Deposition Oxidation	Thermal evaporator - O_2, 950 mtorr, 5 mins.	
20	Deposition Second layer	Thermal evaporator - Al - angle 0° thickness 100 nm rate 1 nm/s.	
21	Lift off	Microposit 1165 resist remover hot plate 60°C time 15 mins. Rinse with IPA, N_2 blow dry.	
22	Lift off (extended)	Microposit 1165 resist remover hot plate 70°C, time = 3 hours. Rinse with IPA, N_2 blow dry.	Optional - known to anneal junction and be beneficial
23	Inspection	Optical microscope.	

24	Etch	RIE - 100 SCCM O_2. Power = 100 W. Pressure = 100 mtorr, Time = 2 mins. Rinse with IPA, N_2 blow dry.	If required
25	Inspection	Optical microscope.	

A.2 - Fabrication of Nb CPW with etched nanobridges

Table A.3: Nb CPW with etched nanobridges. Substrate: Nb CPW resonator

Step	Process	Equipment and Parameters	Comments
1	Substrate preparation	Acetone at 60°C 5 mins, rinse IPA, N_2 blow dry.	If necessary
2	Resist application	copolymer 13% 4000 rpm bake 5 mins at 150°C.	Beading is not a concern for EBL, use minial resist
3	Resist application	13% Copolymer, 4500 rpm bake 150°C 5 mins 4%, PMMA 4500 rpm bake 150°C 5 mins.	
4	Inspection	Optical microscope.	Ensure no diffraction pattern around intended EBL location
5	EBL lithography	EBL - 30 keV, 15 pA beam current, WD = 10 mm.	Define nanobridges and addition geometries to be etched
6	Development	7% H_2O, 93% IPA, 2.5 minutes. Rinse with IPA N_2, blow dry.	
7	Inspection	Optical microscope.	Check pattern for suitability for etching
8	Etch	RIE - 20 SCCM SF_6 , 10 SCCM Ar. Time 10 - 12 mins. Rinse with IPA, N_2 blow dry.	
9	Inspection	Optical microscope.	Check if Nb has been fully etched, return to RIE if required.
10	Mask removal	Microposit 1165 resist remover hot plate 60°C. Rinse with IPA, N_2 blow dry.	

11	Posterior etch	RIE - 20 SCCM SF_6 , 10 SCCM Ar. Time 15-30 seconds. Rinse with IPA, N_2, blow dry.	
12	Inspection	Optical microscope.	

Bibliography

[1] Y. Nakamura, Yu. A. Pashkin and J. S. Tsai. Coherent control of macroscopic quantum states in a single-Cooper-pair box. Nature 398, 786-788 (1999). DOI: 10.1038/19718

[2] D. Vion, A. Aassime, A. Cottet, P. Joyez, H. Pothier, C. Urbina, D. Esteve, M. H. Devoret. Manipulating the quantum state of an electrical circuit. Science 296, 5569, 886-889 (2002). DOI: 10.1126/science.1069372

[3] I. Chiorescu, Y. Nakamura, C. J. P. M. Harmans, and J. E. Mooij. Coherent quantum dynamics of a superconducting flux qubit. Science 299, 5614, 1869-1871 (2003). DOI: 10.1126/science.1081045

[4] M. J. Martinis, S. Nam, J. Aumentado and C. Urbina. Rabi oscillations in a large Josephson junction qubit. Phys. Rev. Lett. 89, 117901 (2002). DOI: /10.1103/PhysRevLett.89.117901

[5] M. Metcalfe. A new microwave resonator readout for superconducting qubits. PhD thesis. Yale University (2008).

[6] M. Metcalfe, E. Boaknin, V. Manucharyan, R. Vijay, I. Siddiqi, C. Rigetti, L. Frunzio, R. J. Schoelkopf, and M. H. Devoret. Measuring the decoherence of a quantronium qubit with the cavity bifurcation amplifier. Phys. Rev. B 76, 174516 (2007). DOI: /10.1103/PhysRevB.76.174516

[7] M. A. Castellanos-Beltran, K. D. Irwin, G. C. Hilton, L. R. Vale and K. W. Lehnert. Amplification and squeezing of quantum noise with a tunable Josephson metamaterial. Nature physics 4, 928-931 (2008). DOI:10.1038/nphys1090

[8] T. C. White, J. Y. Mutus, I. C. Hoi, R. Barends, B. Campbell, Y. Chen, Z. Chen, B. Chiaro, A. Dunsworth, E. Jeffrey, J. Kelly, A. Megrant, C. Neill, P. J. J. O'Malley, P. Roushan, D. Sank, A. Vainsencher, J. Wenner, S. Chaudhuri, J. Gao, and J. M. Martinis. Travelling wave parametric amplifier with Josephson junctions using minimal resonator phase matching. Appl. Phys. Lett. 106, 242601 (2015). DOI: 10.1063/1.4922348

[9] A. S. Gilmour. Microwave tubes. Artech House Publishers (1986). ISBN: 9780890061817

[10] C. P. Wen. Coplanar waveguide: a surface strip transmission line suitable for nonreciprocal gyromagnetic device applications. IEEE Transactions on Microwave Theory and Techniques 17, 12, 1087-1090 (1969). DOI: 10.1109/TMTT.1969.1127105

[11] E. Carlsson and S. Gevorgian. Conformal mapping of the field and charge distributions in multilayered substrate CPWs. IEEE Transactions on Microwave Theory and Techniques 47, 8, 1544-1552 (1999). DOI: 10.1109/22.780407

[12] K. C. Gupta. Microstrip lines and slotlines, second edition. Artech House Publishers (1996). ISBN: 089006766X

[13] M. Goano, F. Bertazzi, P. Caravelli, G. Ghione and T. A. Driscoll. A general conformal-mapping approach to the optimum electrode design of coplanar waveguides with arbitrary cross section. IEEE Transactions on Microwave Theory and Techniques 49, 9, 1573 - 1580 (2001). DOI: 10.1109/22.942569.

[14] R. J. Schoelkopf and S. M. Girvin. Wiring up quantum systems. Nature 451, 664669 (2008). DOI: 10.1038/451664a

[15] P. J. Petersan and S. M. Anlage. Measurement of resonant frequency and quality factor of microwave resonators: Comparison of methods. Journal of Applied Physics 84, 6, 3392-3402 (1998). DOI: 10.1063/1.368498

[16] D. M. Pozar. Microwave engineering, third edition. Wiley (2007). ISBN: 9788126510498

[17] M. Göppla, A. Fragner, M. Baur, R. Bianchetti, S. Filipp, J. M. Fink, P. J. Leek, G. Puebla, L. Steffen, and A. Wallraff. Coplanar waveguide resonators for circuit quantum electrodynamics. Journal of Applied Physics 104, 113904 (2008). DOI: 10.1063/1.3010859

[18] J. Bardeen, L. N. Cooper and J. R. Schrieffer. Theory of Superconductivity. Phys. Rev. 108, 5, 1175-1204 (1957). DOI: 10.1103/PhysRev.108.1175

[19] G. C. O'Neil. Improving NIS tunnel junction refrigerators: modelling, materials and trap. PHD thesis. University of Colorado (2011). UMI Number: 3453766.

[20] T. P. Orlando, E. J. McNiff, S. Foner and M. R. Beasley. Critical fields, Pauli paramagnetic limiting, and material parameters of Nb_3Sn and V_3Si. Phys. Rev. B, 19, 4545-4561 (1979). DOI: 10.1103/PhysRevB.19.4545

[21] M. Tinkham. Introduction to superconductivity, second edition. Dover Publications (1996). ISBN: 97804864350391

[22] D. C. Mattis and J. Bardeen. Theory of the anomalous skin effect in normal and superconducting metals. Phys. Rev. 111, 2, 412-417 (1958). DOI: 10.1103/PhysRev.111.412

[23] K. Watanabe, K. Yoshida, T. Aoki and S. Kohjiro. Kinetic inductance of superconducting coplanar waveguides. Jpn. J. Appl. Phys. 33, 5708-5712 (1994). DOI: 10.1143/JJAP.33.5708

[24] J. Gao, J. Zmuidzinas, B. A. Mazin, H. G. LeDuc and P. K. Day. Noise properties of superconducting coplanar waveguide microwave resonators. Appl. Phys. Lett. 90, 102507102507 (2007). DOI: 10.1063/1.2711770

[25] J. Gao, M. Daal, A. Vayonakis, S. Kumar, J. Zmuidzinas, B. Sadoulet, B. A. Mazin, P. K. Day, and H. G. Leduc. Experimental evidence for a surface distribution of two-level systems in superconducting lithographed microwave resonators. Appl. Phys. Lett. 92, 152505 (2008). DOI: 10.1063/1.2906373

[26] R. Barends, N. Vercruyssen, A. Endo, P. J. de Visser, T. Zijlstra, T. M. Klapwijk, P. Diener, S. J. C. Yates, and J. J. A. Baselmans. Minimal resonator loss for circuit quantum electrodynamics. Appl. Phys. Lett. 97, 023508 (2010). DOI: 10.1063/1.3458705

[27] J. M. Sage, V. Bolkhovsky, W. D. Oliver, B. Turek, and P. B. Welander. Study of loss in superconducting coplanar waveguide resonators. Journal of Applied Physics 109, 063915 (2011). DOI: 10.1063/1.3552890

[28] P. W Anderson, B. Halperin and C. M. Varma. Anomalous low-temperature thermal properties of glasses and spin glasses. Philos. Mag. 25, 19 (1972). DOI: 10.1080/14786437208229210

[29] W. A. Phillips. Tunneling states in amorphous solids. Journal of Low Temp. Phys. 7, 3-4, 351360 (1972). DOI: 10.1007/BF00660072

[30] J. Burnett, L. Faoro, I. Wisby, V. L. Gurtovoi, A. V. Chernykh, G. M. Mikhailov, V. A. Tulin, R. Shaikhaidarov, V. Antonov, P. J. Meeson, A. Ya. Tzalenchuk and T. Lindström. Evidence for interacting two-level systems from the 1/f noise of a superconducting resonator. Nature Communications 5, 4119 (2014). DOI: 10.1038/ncomms5119

[31] S. E. de Graaf , L. Faoro, J. Burnett, A. Adamyan, A. Tzalenchuk, S. Kubatkin, T. Lindström and A.V. Danilov. Suppression of low-frequency charge noise in superconducting resonators by surface spin desorption. Nature Communications 9, 1143 (2018). DOI: 10.1038/s41467-018-03577-2 45

[32] U. Fano. Effects of configuration interaction on intensities and phase shifts. Phys. Rev. 124, 6, 1866-1878 (1961). DOI: 10.1103/PhysRev.124.1866

[33] C. Wu, A. B. Khanikaev, R. Adato, N. Arju, A. A. Yanik, H. Altug and G. Shvets. Fano-resonant asymmetric metamaterials for ultrasensitive spectroscopy and identification of molecular monolayers. Nature Materials 11, 69-75 (2012). DOI: 10.1038/nmat3161.

[34] I. Stern, M. Grajower and U. Levy. Fano resonances and all-optical switching in a resonantly coupled plasmonicatomic system. Nature Communications 5, 4865 (2014). DOI: 10.1038/ncomms5865

[35] J. F. Song, Y. Ochiai and J. P. Bird. Fano resonances in open quantum dots and their application as spin filters. Appl. Phys. Lett. 82, 45613 (2003). DOI: 10.1063/1.1586788

[36] Y. S. Joe, A. M. Satanin and C. S. Kim. Classical analogy of Fano resonances. Physica Scripta 74, 2, 259266 (2006). DOI:10.1088/0031-8949/74/2/020

[37] F. Chen, A. J. Sirois, R. W. Simmonds, and A. J. Rimberg. Introduction of a dc bias into a high-Q superconducting microwave cavity. Appl. Phys. Lett. 98, 132509 (2011). DOI: 10.1063/1.3573824

[38] B. D. Josephson. Possible new effects in superconductive tunnelling. Phys. Lett. 1, 7, 251-253 (1962). DOI: 10.1016/0031-9163(62)91369-0

[39] J. M. Martinis and K. Osborne. Superconducting qubits and the physics of Josephson junction. arXiv:cond-mat/0402415 [cond-mat.supr-con]. Submitted: 16 Feb 2004.

[40] K. K. Likharev. Superconducting weak links. Rev. Mod. Phys. 51, 101-159 (1979). DOI: 10.1103/RevModPhys.51.101

[41] R. F. Voss, R. B. Laibowitz, and A. N. Broers. Niobium nanobridge dc SQUID. Appl. Phys. Lett. 37, 656-658 (1980); DOI: 10.1063/1.92026

[42] R. Vijay, J. D. Sau, Marvin L. Cohen, and I. Siddiqi. Optimizing anharmonicity in nanoscale weak link Josephson junction oscillators. Phys. Rev. Lett. 103, 8, 087003 (2009). DOI: 10.1103/PhysRevLett.103.087003

[43] C. D. Shelly, P. See, I. Rungger, J. M. Williams. Existence of shapiro steps in the dissipative regime in superconducting weak links. arXiv:1806.10420 [cond-mat.supr-con]. Submitted: 27 Jun 2018.

[44] J. Clarke and A. I. Braginski. The SQUID Handbook, Vol 1. Wiley Online Library (2004). ISBN: 3527402292

[45] D. E. McCumber. Effect of ac impedance on dc voltage-current characteristics of superconductor weak-link junctions. Journal of Applied Physics 39, 3113 (1968). DOI: 10.1063/1.1656743

[46] W. C. Stewart. Current-voltage characteristics of Josephson junctions. Appl. Phys. Lett. 12, 277 (1968). DOI: 10.1063/1.1651991

[47] G. Aviv, Ben-Gurion University of the Negev. Experimental physics course (2008). physics.bgu.ac.il/ gal/Gal%20Aviv˙files/SQUID˙Gal˙Aviv˙paper.pdf (Last accessed: 21/09/2018)

[48] M. R. Vissers, R. P. Erickson, H. S. Ku, L. Vale, X. Wu, G. C. Hilton, and D. P. Pappas. Low-noise kinetic inductance traveling-wave amplifier using three-wave mixing. Appl. Phys. Lett. 108, 012601 (2016). DOI: 10.1063/1.4937922

[49] J. Zmuidzinas. Superconducting microresonators: physics and applications. Annual Review of Condensed Matter Physics 3, 169-214 (2012). DOI: 10.1146/annurev-conmatphys-020911-125022

[50] B. H. Eom, P. K. Day, H. G. LeDuc and J. Zmuidzinas. A wideband low-noise superconducting amplifier with high dynamic range. Nature Physics 8, 623-627 (2012). DOI: 10.1038/nphys2356

[51] R. W. Boyd. Nonlinear Optics, third edition. Academic Press Inc. (2008). ISBN: 9780123694706

[52] B. E. A. Saleh and M. C. Teich. Fundamentals of photonics. John Wiley and Sons Inc. (1991). ISBN: 0471839655

[53] A. Yariv. Quantum Electronics, third edition. Wiley (1988). ISBN: 9780471609971

[54] O. Yaakobi, L. Friedland, C. Macklin, and I. Siddiqi. Parametric amplification in Josephson junction embedded transmission lines. Phys. Rev. B 87, 144301 (2013). DOI: 10.1103/PhysRevB.87.144301

[55] M. A. Castellanos-Beltran and K. W. Lehnert. Widely tunable parametric amplifier based on a superconducting quantum interference device array resonator. Appl. Phys. Lett. 91, 083509 (2007). DOI: 10.1063/1.2773988

[56] A. B. Zorin. Josephson traveling-wave parametric amplifier with three-wave mixing. Phys. Rev. Appl. 6, 034006 (2016). DOI: 10.1103/PhysRevApplied.6.034006

[57] A. B. Zorin and Y. Makhlin. Period-doubling bifurcation readout for a Josephson qubit. Phys. Rev. B 83, 224506 (2011). DOI: 10.1103/PhysRevB.83.224506

[58] K. Porsch. Exploring the period doubling bifurcation. PhD thesis. Royal Holloway University of London (2017).

[59] L. E. M. Lifshitz. Mechanics, third edition. Butterworth-Heinemann (1982). ISBN: 9780750628969

[60] R. Vijayaraghavan. Josephson bifurcation amplier: amplifying quantum signals using a dynamical bifurcation. PhD thesis. Yale University (2008).

[61] S. Schmidlin. Physics and Technology of small Josephson junctions. PhD thesis. Royal Holloway University of London (2013).

[62] Cryogenic Low Noise Amplifier (LNF-LNC4.8C s/n 725H, 4-8 GHz) dataset provided with purchase from Low Noise Factory. www.lownoisefactory.com

[63] Q. Zhong, W. Cao, J. Li, Y. Zhong and X. Wang. Study of dry etching process using SF_6 and $CF4/O_2$ for Nb/NbSi/Nb Josephson-junction fabrication. Conference on Precision electromagnetic Measurements, Washington DC, 46-47 (2012). DOI: 10.1109/CPEM.2012.6250653

[64] G. Tancredi. Superconducting tunable resonator. PhD thesis. Royal Holloway University of London (2010).

[65] I. M. Pop, T. Fournier, T. Crozes, F. Lecocq, I. Matei, B. Pannetier, O. Buisson, W. Guichard. Fabrication of stable and reproducible sub-micron tunnel junctions. Journal of Vacuum Science and Technology B 30, 1, 010607 (2012). DOI: 10.1116/1.3673790

[66] J. S. Kelly. Fault-tolerant superconducting qubits. PhD thesis. University of California, Santa Barbara (2015).

[67] V. Ambegaokar and A. Baratoff. Tunneling between superconductors. Phys. Rev. Lett. 10, 486489 (1963). DIO: 10.1103/PhysRevLett.10.486

[68] C. D Shelly, P. See, J. Ireland, E. J. Romans and J. M. Williams. Weak link nanobridges as single flux quantum elements. Supercond. Sci. Technol. 30, 095013 (2017). DOI: 10.1088/1361-6668/aa80cd

[69] A private communication with Jacob Dunstan.

[70] E. Tholèn. Intermodulation in microresonators. PhD Thesis. KTH School of Engineering Sciences Stockholm, Sweden (2009).

[71] S. J. Hedges, M. J. Adams, B. F. Nicholson, and N. G. Chew. Power dependent effects observed for a superconducting stripline resonator. Electron. Lett. 26(14), 977 (1990). DOI: 10.1049/el:19900636

[72] C. Macklin, K. O'Brien, D. Hover, M. E. Schwartz, V. Bolkhovsky, X. Zhang, W. D. Oliver and I. Siddiqi. A near-quantum-limited Josephson travelling-wave parametric amplifier. Science 350, 6258, 307-310 (2015). DOI: 10.1126/science.aaa8525

[73] M. T. Bell and A. Samolov. Traveling-wave parametric amplifier based on a chain of coupled asymmetric SQUIDs. Phys. Rev. Applied 4, 024014 (2015). DOI: 10.1103/PhysRevApplied.4.024014

[74] A. B. Zorin, M. Khabipov, J. Dietel and R. Dolata. Traveling-wave parametric amplifier based on three-wave mixing in a Josephson metamaterial. 16th International Superconductive Electronics Conference (ISEC), 1-3, Naples (2017). DOI: 10.1109/ISEC.2017.8314196

[75] D. Hazra, L. M. A. Pascal, H. Courtois and A. K. Gupta. Hysteresis in superconducting short weak links and μ-SQUIDs. Phys. Rev. B 82, 184530 (2010). DOI: 10.1103/PhysRevB.82.184530

[76] L. Hao. Quantum detection applications of nanoSQUIDs fabricated by focussed ion beam. Journal of Physics: Conference Series 286, 1, 012013 (2011). DOI: 10.1088/1742-6596/286/1/012013

[77] L. Hao, D. Cox, P. See, J. C. Gallop and O. Kazakova. Magnetic nanoparticle detection using nano-SQUID sensors. Journal of Physics D: Applied Physics 43, 47, 474004 (2010). DOI: 10.1088/0022-3727/43/47/474004

[78] L. Hao, D. C. Cox and J. C. Gallop. Characteristics of focused ion beam nanoscale Josephson devices. Superconductor Science and Technology 22, 6, 064011 (2009). DOI: 10.1088/0953-2048/22/6/064011